



## Novel Heterogeneous Catalysts with Nano-Engineered Porosity

**Zacho, Simone Louise**

*Publication date:*  
2020

*Document Version*  
Publisher's PDF, also known as Version of record

[Link back to DTU Orbit](#)

*Citation (APA):*  
Zacho, S. L. (2020). *Novel Heterogeneous Catalysts with Nano-Engineered Porosity*. Technical University of Denmark.

---

### General rights

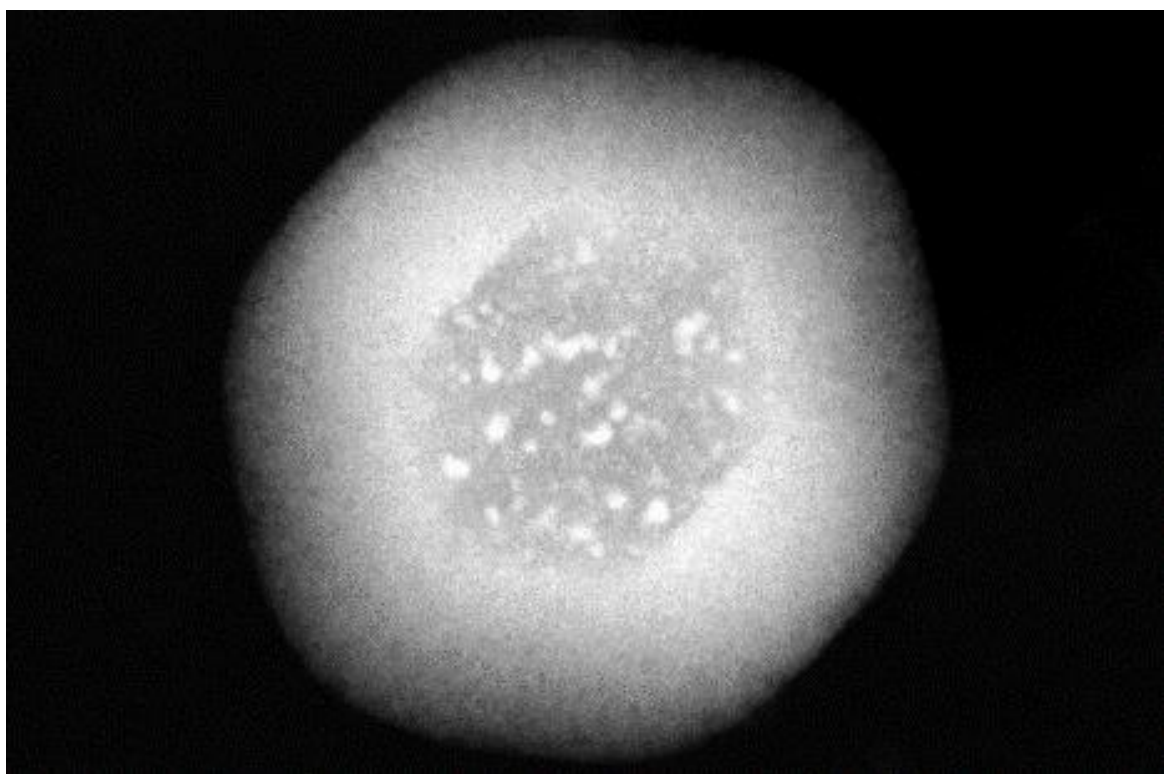
Copyright and moral rights for the publications made accessible in the public portal are retained by the authors and/or other copyright owners and it is a condition of accessing publications that users recognise and abide by the legal requirements associated with these rights.

- Users may download and print one copy of any publication from the public portal for the purpose of private study or research.
- You may not further distribute the material or use it for any profit-making activity or commercial gain
- You may freely distribute the URL identifying the publication in the public portal

If you believe that this document breaches copyright please contact us providing details, and we will remove access to the work immediately and investigate your claim.

# **Novel Heterogeneous Catalysts with Nano-Engineered Porosity**

---



**PhD dissertation by Simone Louise Zacho, M.Sc.**

February 2020

**DTU Chemistry**

**Simone Louise Zacho**

*Novel heterogeneous catalysts with nano-engineered porosity*

PhD dissertation, February 2020

Technical University of Denmark

E-mail address: simolo@kemi.dtu.dk

*Simone Louise Zacho*

*Cover photo:*

*Projected STEM-HAADF image of a nanorattle catalyst comprised of Co nanoparticles encapsulated within a SiO<sub>2</sub> shell. The image is described in Chapter 4.3.5 and reproduced by permission of Elsevier from Zacho et al.<sup>1</sup>*

## Preface

This PhD dissertation is based on research carried out at the Technical University of Denmark (DTU) from March 1<sup>st</sup> 2017 to February 29<sup>th</sup> 2020. The work was conducted at the Centre for Catalysis and Sustainable Chemistry (CSC) at DTU Chemistry under the supervision of Professor Søren Kegnæs and co-supervision of Senior Researcher Dr. Jerrik Mielby. Research from an external stay at Friedrich-Alexander University (FAU), Erlangen, Germany, from September 17<sup>th</sup> 2018 to December 14<sup>th</sup> 2018 is included in this dissertation. The research during the external stay was performed in the group of Professor Peter Wasserscheid under the supervision of Dr. Ing. Jakob Albert at the Institute of Chemical Engineering. Additionally, this dissertation includes work performed in collaboration with PhD student Joachim Thrane, Assistant Professor Martin Høj and Professor Anker Degn Jensen from DTU Chemical Engineering. The project was funded by the Independent Research Fund Denmark with grant no. 6111-00237.

This PhD dissertation consists of seven chapters, where Chapter 1 provides an introduction to heterogeneous catalysis and advanced nanomaterials. Moreover, the aim of this dissertation is described in this chapter. Chapter 2 presents the characterization techniques used and describes the general experimental details. Chapter 3 describes the preparation of Co nanoparticles in nitrogen-doped carbon materials investigated as catalysts in the hydrolytic dehydrogenation of ammonia borane. In Chapter 4 the preparation of Co<sub>3</sub>O<sub>4</sub> nanoparticles encapsulated in mesoporous SiO<sub>2</sub> shells is presented, which were tested as nanorattle catalysts in a CO oxidation reaction. Chapter 5 includes the preparation of encapsulated iron molybdate catalysts in nano-engineered porous materials examined as catalysts for the selective oxidation of methanol to formaldehyde. In Chapter 6, the preparation of encapsulated heteropolyoxometalates in nano-engineered porous materials is described. Catalytic tests are also described, including a phenyl acetate Fries rearrangement reaction and the selective oxidation of biomass to formic acid. The results from each project are summarized in Chapter 7, which offers an additional final conclusion.

All tables, schemes and figures presented in this dissertation were prepared by the author unless otherwise stated. Some of the results obtained during this project have already been published in international and peer-reviewed journals, in which cases they are clearly referenced.

Simone Louise Zacho, Kgs. Lyngby, Denmark, February 2020



## Acknowledgements

During my three years at DTU, so many people have kindly supported me, helped me and contributed to a pleasant work atmosphere. I will try to mention as many people as possible since I deeply appreciate all the help I have received and the time spent together.

I want to extend my sincere gratitude to my supervisor Professor Søren Kegnæs who has been guiding me for more than five years, starting with my BSc project. He is the reason my interest within catalysis blossomed. From the beginning of our collaboration, he has included me in his research group, for which I am truly grateful. Therefore, I was eager to begin a PhD project under his kind supervision and immense knowledge within catalysis. I will truly miss working in his group.

I will also like to thank my co-supervisor Senior Researcher Dr. Jerrik Mielby, who is one of my closest colleagues. He has been a mentor and a friend who has supported, guided and helped me with various tasks during my PhD studies. I will never stop appreciating the time and effort he has put into our collaborative research. I wish the best for him in the future.

The three years of work at DTU would not have been the same without my colleagues who, besides making working at the Department of Chemistry more fun, also have assisted me with their knowledge. A special thanks to my officemates David B. Christensen, Mikkel B. Buendia, Kristoffer H. Møller and Kai Gao with who I have had fruitful discussions about research results, but also life in general. Moreover, I would like to thank Niklas R. Bennedsen, Farnoosh Goodarzi, Rouzana P. Thumbayil, Faliu Yang and Søren Kramer from Søren Kegnæs' group for their assistance and their contagious good moods.

As part of my external research stay, a great deal of people from FAU in Erlangen, Germany helped me and made me feel welcome. Thanks to Professor Peter Wasserscheid for letting me visit his research group. I would also like to thank my external supervisor Dr. Ing. Jakob Albert, who besides guiding me with the collaborative project abroad, has become a friend of mine. I am thankful for the effort he has made to make me feel welcome in his group. In my collaboration with DTU Chemical Engineering, I have worked together with Joachim Thrane, Assistant Professor Martin Høj and Professor Anker D. Jensen, who I would like to thank for the assistance with the

project. Moreover, I would like to thank Dr. Kristian R. Viegard, who helped me at the beginning of this collaboration.

I am greatly thankful to the people from the CSC group, the people from the Department of Chemistry and the people who have helped me performing specialized instrumental characterizations. Some of these people include Dr. Kasper Enemark-Rasmussen, Lise Lotte Berring, Lise-Lotte Jespersen, Jes Æ. Hyllested, Senior Researcher Dr. Takeshi Kasama and Dr. Nicola Taccardi.

A special thanks to Dr. Amalie Modvig, Anna Bukowski, Dorothea Voss and Alexander Søgaaard, who I have gotten to know as my close friends due to our time spent together either at DTU and/or FAU. Thank you for your assistance with my work and all the great times we have had. Moreover, I am grateful for the support I have received from my long time friend Dr. Alexandru Vlasceanu who has advised me and helped me during the writing of this dissertation.

Finally, I would like to extend my deepest gratitude to my friends Mads T. Jensen, Camilla J. Jacobsen, Rose Fjeldberg, Emily S. B. Winter, Sofie B. Hansen and Sif C. Olsen for their patience and support during the last months, as I have not been around as much as I wanted. This also applies to my family, which I am truly grateful for the never-ending support and belief in me. Last but not least, I am so lucky to have the best boyfriend, Klaus B. M. Kragh, who has been the greatest support for the last three years. Thank you for putting up with me in the difficult times and always believing in me.



## Abstract

Roughly 90% of all industrial chemical processes are using a catalyst. In the industry, a heterogeneous catalyst is often chosen rather than a homogeneous catalyst because of the easy separation and recycling of heterogeneous catalysts. However, it is often more difficult to achieve a high catalytic activity and selectivity by using a heterogeneous catalyst.

A major challenge in the development of robust heterogeneous catalysts is to design a catalyst with high catalytic activity and selectivity while ensuring sufficient catalyst stability. As the reaction conditions in industrial processes are often detrimental to the catalyst, the catalyst has to be highly thermally stable without leaching of the active metals. Today it is possible to prepare advanced nanostructured materials with pore systems designed with high precision. Encapsulation of catalytically active metals in nanostructured porous materials has proven to hold great potential for the development of size-selective and stable metal catalysts. The highly controlled encapsulation of catalytically active metals opens up the possibility to design robust heterogeneous catalysts with improved thermal stabilities and no leaching while maintaining the catalytic activities.

In this dissertation, the aim was to prepare novel heterogeneous catalysts with low metal sintering and leaching. The prepared catalysts were tested in different existing catalytic processes. The catalysts were prepared by encapsulation of the active metals in nano-engineered porous materials by the use of sacrificial metal precursors or by metal impregnation.

Chapter 3 describes how the metal-organic frameworks, Co-based ZIF-67 and Zn-based ZIF-8, were used as sacrificial metal precursors to create Co nanoparticles encapsulated in porous nitrogen-doped carbon matrices. Different thermally stable catalysts were prepared by varying the synthetic parameters and the metal ion composition (ZIF-67/ZIF-8). The catalyst prepared from ZIF-67/8 crystal precursors at a low temperature was found to have higher stability and activity in the hydrolytic dehydrogenation of ammonia borane. In Chapter 4, the concept of using metal-organic frameworks as sacrificial metal precursors was further investigated to design nanorattle catalysts consisting of  $\text{Co}_3\text{O}_4$  nanoparticles in mesoporous  $\text{SiO}_2$  shells. The thermal treatments (carbonization and/or calcination) and the Co/Zn ratios of the ZIF-67/8 precursors were optimized to give low-sintering catalytically active catalysts. These nanorattle catalysts were thermally stable and active when tested in a CO oxidation reaction. Chapter 5

describes how the concept of encapsulation was further extended to encapsulate iron molybdate catalysts in modified porous SiO<sub>2</sub> shells and zeolites. The encapsulated iron molybdate catalysts were prepared by vacuum impregnation of the modified porous supports. Here, the pore size of the supports was varied in order to ensure complete confinement of the active metals. The iron molybdate catalyst encapsulated in desilicated silicalite-1 zeolites was found to maintain a high catalytic activity with minimized metal leaching when tested for the selective oxidation of methanol to formaldehyde. However, the metal impregnation procedure was challenging to reproduce. In Chapter 6, the encapsulation of heteropolyoxometalates in modified zeolites is described. The encapsulation was performed by vacuum impregnation of the zeolite support. Here, the pore size of the zeolite support was designed to limit the leaching of the active metals in polar media. The encapsulation of W-based heteropolyoxometalates in recrystallized silicalite-1 zeolites was found to prevent metal leaching in the tested phenyl acetate Fries rearrangement reaction. However, it was found that encapsulation of the more unstable V substituted Mo-based heteropolyoxometalates was more challenging and the catalyst suffered from metal leaching when tested for the selective oxidation of biomass to formic acid process in water. All prepared catalysts were characterized by several analytical techniques, which are described in Chapter 2.

In this dissertation, ZIF-67/8 crystals were successfully used as sacrificial metal precursors in the design of thermally stable heterogeneous catalysts with maintained high catalytic activities when tested in catalytic processes. In addition, it was found, that the encapsulation of iron molybdate catalysts and heteropolyoxometalates, by metal impregnation of nano-engineered porous materials, could be used to design non-leaching heterogeneous catalysts with maintained catalytic activities. However, especially when encapsulating heteropolyoxometalates, the catalytic activities were decreased due to a limited mass diffusion. The introduction of active metals into porous supports by metal impregnation was often found to be challenging in terms of achieving high metal loadings or reproducible metal loadings. It was found, that these challenges could be overcome, by using a sacrificial metal precursor to introduce the active metals.

## Resumé

Omkring 90% af alle industrielle kemiske processer benytter en katalysator. I industrien vælges oftest en heterogen katalysator over en homogen katalysator på grund af den lette separation og genanvendelse af heterogene katalysatorer. Det er imidlertid ofte mere svært at opnå en høj katalytisk aktivitet og selektivitet ved at anvende en heterogen katalysator.

En af de største udfordringer i udviklingen af robuste heterogene katalysatorer er at designe en katalysator med høj katalytisk aktivitet og selektivitet, som samtidig har en tilstrækkelig høj stabilitet. Da reaktionsbetingelserne i industrielle processer ofte er skadelige for katalysatoren, er det nødvendigt at den benyttede katalysator er termisk stabil og at de aktive metaller ikke udvaskes nemt. I dag er det muligt at fremstille avancerede materialer af nanostrukturer som indeholder poresystemer designet med høj præcision. Indkapslingen af katalytisk aktive metaller i avancerede nanostrukturerede porøse materialer har vist sig, at have stort potentiale i udviklingen af størrelses-selektive og stabile metalkatalysatorer. Potentielt kan robuste heterogene katalysatorer med forbedret termisk stabilitet, ingen metal-udvaskning og bibeholdt katalytisk aktivitet, fremstilles i en kontrolleret indkapsling af de katalytisk aktive metaller.

Formålet med denne afhandling var at fremstille nye heterogene katalysatorer uden sintring og udvaskning af de aktive metaller. Dette blev undersøgt i forskellige eksisterende katalytiske processer. Katalysatorerne blev fremstillet ved at indkapsle de aktive metaller i designede nanoporøse materialer ved brug af (selv)dekomponerende metalskabeloner eller metalimprægnering.

I Kapitel 3 beskrives, hvordan de metal-organiske strukturer, Co-baserede ZIF-67 og Zn-baserede ZIF-8 krystaller, blev brugt som (selv)dekomponerende metalskabeloner til fremstillingen af Co nanopartikler indkapslet i porøse nitrogen-dopede kulstofmaterialer. Forskellige termostabile katalysatorer blev fremstillet ved at variere syntese parametre og kompositionen af metal ionerne (ZIF-67/8). Katalysatoren fremstillet fra ZIF-67/8 krystaller ved lave temperaturer viste sig, at have en højere stabilitet og aktivitet i den hydrolytiske dehydrogenering af ammoniakboran. I Kapitel 4 blev anvendelsen af metal-organiske strukturer som (selv)dekomponerende metalskabeloner yderligere udviklet til design af nanorattle-katalysatorer bestående af  $\text{Co}_3\text{O}_4$  nanopartikler i mesoporøse  $\text{SiO}_2$  skaller. De termiske behandlinger (karbonisering og/eller kalcinering) og Co/Zn-forholdet af ZIF-67/8 krystallerne blev optimeret til at

fremstille katalytiske aktive katalysatorer med lav metal-sintring. Disse nanorattle-katalysatorer viste sig at være termisk stabile og katalytisk aktive i den testede CO oxidations-reaktion. I Kapitel 5 beskrives, hvordan konceptet med indkapsling yderligere blev udvidet til at indkapsle jernmolybdat-katalysatorer i modificerede porøse SiO<sub>2</sub>-skaller og zeolitter. De indkapslede jernmolybdat-katalysatorer blev fremstillet ved at imprægnere de modificerede porøse bærematerialer under vakuum. Bærematerialernes gennemsnitlige porestørrelse blev modificeret til at sikre en fuldstændig indespærring af de aktive metaller. Den indkapslede jernmolybdat-katalysator i desilikeret silicalit-1 zeolitter viste sig at bibeholde en høj aktivitet med en formindsket metal-udvaskning i den testede selektive oxidation af metanol til formaldehyd-reaktion. At reproducere katalysatorerne ved brug af metal-imprægnerings-proceduren viste sig at være udfordrende. I Kapitel 6 blev indkapslingen af heteropolysyre i modificerede zeolitter beskrevet. Indkapslingen blev udført ved at metalimprægnere zeolit-bærematerialet under vakuum. Zeolit-bærematerialet blev fremstillet med porestørrelser der skulle minimere udvaskningen af de aktive metaller i polære medier. Indkapslingen af W-baserede heteropolysyre i omkrystalliseret silicalit-1 zeolitter viste sig at hindre udvaskningen af det aktive metal, i den testede Fries ombytning af phenylacetat. Det blev vist at indkapslingen af de mere ustabile V-substituerede Mo-baserede heteropolysyre var mere udfordrende, da katalysatorerne led under udvaskning af de aktive metaller i den testede selektive oxidation af biomasse til myresyre i vand. Alle de fremstillede katalysatorer blev karakteriseret ved hjælp af adskillige analytiske teknikker, som er beskrevet i Kapitel 2.

I denne afhandling blev det beskrevet hvordan ZIF-67/8 krystaller kan bruges som (selv)dekomponerende metalskabeloner til at designe termostabile heterogene katalysatorer med bevaret katalytisk aktivitet i katalytiske reaktionstest. Derudover blev det vist, at indkapslingen af jernmolybdat-katalysatorer og heteropolysyre fremstillet ved metalimprægnering af nanometerskala-designede porøse materialer kan anvendes til at udvikle heterogene katalysatorer med en hindret udvaskning af de aktive metaller og en bibeholdt katalytisk aktivitet. I nogle tilfælde blev den katalytiske aktivitet dårligere i den testede reaktion på grund af en begrænset massediffusion. Dette var specielt tilfældet med de indkapslede heteropolysyre. Brugen af metalimprægnering til at introducere de aktive metaller i porøse bærematerialer viste sig ofte, at være enten udfordrende i forhold til at opnå et højt metalindhold eller et reproducerbart metalindhold. Det blev fundet, at disse udfordringer kan overvindes ved brug af (selv)dekomponerende metalskabeloner til at introducere de aktive metaller.

## Abbreviations

DTU	Technical University of Denmark
CSC	Centre for Catalysis and Sustainable Chemistry
FAU	Friedrich-Alexander University
TOF	Turnover Frequency
STY	Site-Time Yield
MOF	Metal-Organic Framework
CSD	Cambridge Structural Database
CTAB	Hexadecyltrimethylammonium Bromide
IZA	International Zeolite Association
SDA	Structure-Directing Agent
MOFMS	Metal-Organic Framework Mediated Synthesis
ZIF	Zeolitic Imidazolate Framework
N-doped	Nitrogen-doped
CRT	Lehrstuhl für Chemische Reaktionstechnik
OxFA	Oxidative conversion of biomass to Formic Acid
XRF	X-Ray Fluorescence Spectroscopy
XRD	X-Ray Diffraction
XRPD	X-Ray Powder Diffraction
ICDD	Centre for Diffraction Data



FTIR	Fourier-Transform Infrared Spectroscopy
POM	Polyoxometalate
XPS	X-Ray Photoelectron Spectroscopy
N <sub>2</sub> Physisorption	Nitrogen Physisorption
$p/p^0$	Relative Pressure
IUPAC	International Union of Pure and Applied Chemistry
BET	Brunauer-Emmett-Teller
DFT	Density Functional Theory
SEM	Scanning Electron Microscopy
SE	Secondary Electrons
BSE	Backscattered Electrons
TEM	Transmission Electron Microscopy
FEG	Field Emission Gun
CCD	Charge Coupled Device
BF	Bright Field
DF	Dark Field
STEM	Scanning Transmission Electron Microscopy
HAADF	High Angle Annular Dark Field
EDS	Energy Dispersive Spectrometer
SIRT	Simultaneous Iterative Reconstruction Technique

SS-NMR	Solid-State Nuclear Magnetic Resonance
LS-NMR	Liquid-State Nuclear Magnetic Resonance
MAS	Magic-Angle Spinning
AAS	Atomic Absorption Spectroscopy
TGA	Thermal Gravimetric Analysis
ZIF-67	ZIF based on Co
ZIF-8	ZIF based on Zn
ZIF-67/8	ZIF based on Co/Zn
Co/NC	Co nanoparticles in N-doped C
CoZn/NC	Co and Zn nanoparticles in N-doped C
TWC	Three-Way-Catalyst
TEOS	Tetraethyl Orthosilicate
ZIF-67@SiO <sub>2</sub>	Monometallic precursor based on ZIF-67 inside a SiO <sub>2</sub> shell
Co <sub>x</sub> @SiO <sub>2</sub> (Zn <sub>y</sub> )	Nanorattle catalyst with a Co/Zn ratio of x:y
Co <sub>x</sub> /NC@SiO <sub>2</sub> (Zn <sub>y</sub> )	Nanorattle catalyst with a C core and a Co/Zn ratio of x:y
Co <sub>x</sub> /SiO <sub>2</sub> (Zn <sub>y</sub> )	SiO <sub>2</sub> supported catalyst with a Co/Zn ratio of x:y
TPAOH	Tetrapropylammonium Hydroxide
D S1	Desilicated Silicalite-1
FeMo	Iron Molybdate (Fe <sub>2</sub> (MoO <sub>4</sub> ) <sub>3</sub> + MoO <sub>3</sub> )
ICP	Inductively Coupled Plasma mass spectrometry

FeMo/SiO <sub>2</sub>	SiO <sub>2</sub> supported catalyst with iron molybdate
FeMo@SiO <sub>2</sub>	Iron Molybdate encapsulated in SiO <sub>2</sub>
FeMo@D S1	Iron Molybdate encapsulated in Desilicated Silicalite-1
TOS	Time On Stream
DME	Dimethyl Ether
DMM	1,1-dimethoxymethane
MF	Methyl Formate
HPA	Heteropoly acid
IPA	Isopoly acid
HPW	H <sub>3</sub> PW <sub>12</sub> O <sub>40</sub>
HPA-n	Heteropoly acid with n amount of substituted V
HPA-0	H <sub>3</sub> PMo <sub>12</sub> O <sub>40</sub>
HPA-5	H <sub>8</sub> PV <sub>5</sub> Mo <sub>7</sub> O <sub>40</sub>
HPA-2	H <sub>8</sub> PV <sub>2</sub> Mo <sub>10</sub> O <sub>40</sub>
PhOAc	Phenyl Acetate
2HAP	2-hydroxyacetophenone
PhOH	Phenol
4AAP	4-acetoxyacetophenone
4HAP	4-hydroxyacetophenone
GC	Gas Chromatography

HPLC	High-Performance Liquid Chromatography
Recryst S1	Recrystallized Silicalite-1
HPA@Recryst S1	Heteropoly acid encapsulated in Recryst S1
PhNO <sub>2</sub>	Nitrobenzene
FA	Formic Acid



## Table of Contents

Chapter 1.	Introduction .....	5
1.1	Heterogeneous Catalysis .....	6
1.2	Advanced Nanomaterials.....	9
1.2.1	Porous Materials.....	10
1.2.2	Metal Incorporation Methods .....	15
1.3	Aim and Outline of the Dissertation .....	17
Chapter 2.	Characterization of Catalysts .....	19
2.1	X-Ray Fluorescence Spectroscopy .....	20
2.2	X-Ray Diffraction .....	21
2.3	Fourier-Transform Infrared Spectroscopy .....	22
2.4	X-Ray Photoelectron Spectroscopy .....	22
2.5	Nitrogen Physisorption .....	23
2.6	Electron Microscopy .....	27
2.6.1	Scanning Electron Microscopy.....	28
2.6.2	Transmission Electron Microscopy .....	29
2.6.3	Scanning Transmission Electron Microscopy .....	31
2.6.4	Electron Tomography .....	32
2.7	Solid-State Nuclear Magnetic Resonance.....	33
Chapter 3.	Hydrolytic Dehydrogenation of Ammonia Borane .....	35
3.1	Introduction .....	36
3.2	Experimental Details.....	38
3.2.1	Material Preparations.....	38
3.2.2	Characterization Methods .....	40
3.2.3	Catalytic Test Procedure .....	40
3.3	Results and Discussion .....	41
3.3.1	AAS and XRF .....	41
3.3.2	XRPD.....	42
3.3.3	N <sub>2</sub> Physisorption .....	43
3.3.4	SEM .....	46
3.3.5	TEM and TGA .....	47
3.3.6	The Hydrolytic Dehydrogenation of Ammonia Borane .....	50
3.4	Summary .....	54
Chapter 4.	Carbon Monoxide Oxidation .....	57
4.1	Introduction .....	58

---

4.2	Experimental Details .....	60
4.2.1	Material Preparations .....	60
4.2.2	Characterization Methods .....	62
4.2.3	Catalytic Test Procedure .....	62
4.3	Results and Discussion .....	63
4.3.1	XRF and TGA .....	63
4.3.2	XRPD and XPS .....	65
4.3.3	N <sub>2</sub> Physisorption .....	67
4.3.4	SEM and TEM .....	69
4.3.5	Electron Tomography and EDS .....	73
4.3.6	The Carbon Monoxide Oxidation .....	75
4.4	Summary .....	80
Chapter 5.	Selective Oxidation of Methanol to Formaldehyde .....	83
5.1	Introduction .....	84
5.2	Experimental Details .....	86
5.2.1	Material Preparations .....	86
5.2.2	Characterization Methods .....	89
5.2.3	Catalytic Test Procedure .....	89
5.3	Results and Discussion .....	90
5.3.1	Catalytic Test Procedure .....	90
5.3.2	XRPD and Raman spectroscopy .....	90
5.3.3	N <sub>2</sub> Physisorption .....	93
5.3.4	SEM and TEM .....	94
5.3.5	The Selective Oxidation of Methanol to Formaldehyde .....	96
5.4	Summary .....	99
Chapter 6.	Phenyl Acetate Fries Rearrangement and OxFA Process .....	101
6.1	Introduction .....	102
6.2	Experimental Details .....	109
6.2.1	Material Preparations .....	109
6.2.2	Characterization Methods .....	111
6.2.3	Catalytic Test Procedure .....	112
6.3	Results and Discussion .....	113
6.3.1	XRF and XPS .....	113
6.3.2	XRPD and FTIR .....	114
6.3.3	Solid-State NMR .....	117
6.3.4	N <sub>2</sub> Physisorption .....	120
6.3.5	STEM and EDS .....	122
6.3.6	The Phenyl Acetate Fries Rearrangement .....	124
6.3.7	The OxFA Process .....	126
6.4	Summary .....	127

Chapter 7.	Conclusion .....	129
<b>Bibliography</b>		133
Appendix A	Supporting information, Chapter 3 .....	150
Appendix B	Supporting information, Chapter 4 .....	151
Appendix C	Supporting information, Chapter 5 .....	155
Appendix D	Supporting information, Chapter 6 .....	160
Appendix E	Disseminations .....	164





## **Chapter 1.      Introduction**

---

This chapter offers an introduction to heterogeneous catalysis and advanced nanomaterials for catalysis. Here, I describe the different methods to synthesize porous materials and incorporate active metals, which will lay the foundation of my dissertation's experimental work. At the end of the chapter, I present the overall aim and outline of my dissertation.

---

## 1.1 Heterogeneous Catalysis

Heterogeneous catalysts are indispensable in the chemical industry. If the chemical industry was to rely on stoichiometric, non-catalytic, reactions alone it could not have developed to its present status. This is simply because many reactions would not be possible due to kinetic limitations and others would not be economically feasible in regards to reaction conditions.<sup>2</sup> Roughly, 90% of the current industrial processes in the chemical industry use a catalyst.<sup>3</sup> Thus, more than 800 000 tons of catalysts are manufactured worldwide every year.<sup>3</sup> The economic significance of catalyst production is immense, where currently over 15 international companies have specialized in the manufacturing of catalysts for various industrial applications. Moreover, a large number of books, dedicated journals and thousands of research papers on heterogeneous catalysis exist with more to come.<sup>4</sup>

“A catalyst is a substance that changes the rate, but not the thermodynamics of a chemical reaction”.<sup>4</sup> This is the classical definition of a catalyst, which is based on Ostwald’s definition from 1894.<sup>5</sup> The catalyst increases the reaction rate  $k$  by lowering the activation energy  $E_a$  of the reaction by offering a different reaction pathway. The reaction rate depends on the pre-exponential factor  $A$ , the universal gas constant  $R$  and the temperature  $T$ , as described by the Arrhenius equation, Equation 1.1.<sup>6</sup>

$$k = Ae^{-E_a/RT} \tag{1.1}$$

The catalyst offers an alternative and more energetically favorable mechanism. Thus, enabling economically unfeasible reactions to be carried out under industrially feasible temperatures and pressures. The Haber-Bosch Ammonia synthesis, the methanol synthesis and the Fischer-Tropsch process are examples of industrial reactions that are made feasible due to the introduction of a catalyst.<sup>3</sup>

In heterogeneous catalysis, the catalyst and the reactants are in different phases. In most cases, the catalyst is a solid such as a metal, metal salt, oxide or sulfide, while the reactants are gases or liquids.<sup>4</sup> The huge reactors at plant facilities demand advanced engineering to run the plant without complications. The catalysis taking place inside these reactors may seem simple at first, with reactants entering the reactor and the products leaving it, but the complexity of the catalysis is just as significant. The catalysis

is carefully designed in various length scales from the macroscopic level of the catalyst bed, through the mesoscopic level with the shaped catalyst particles, down to the microscopic level of the actual catalytically active surface, see Figure 1.1.<sup>2</sup>

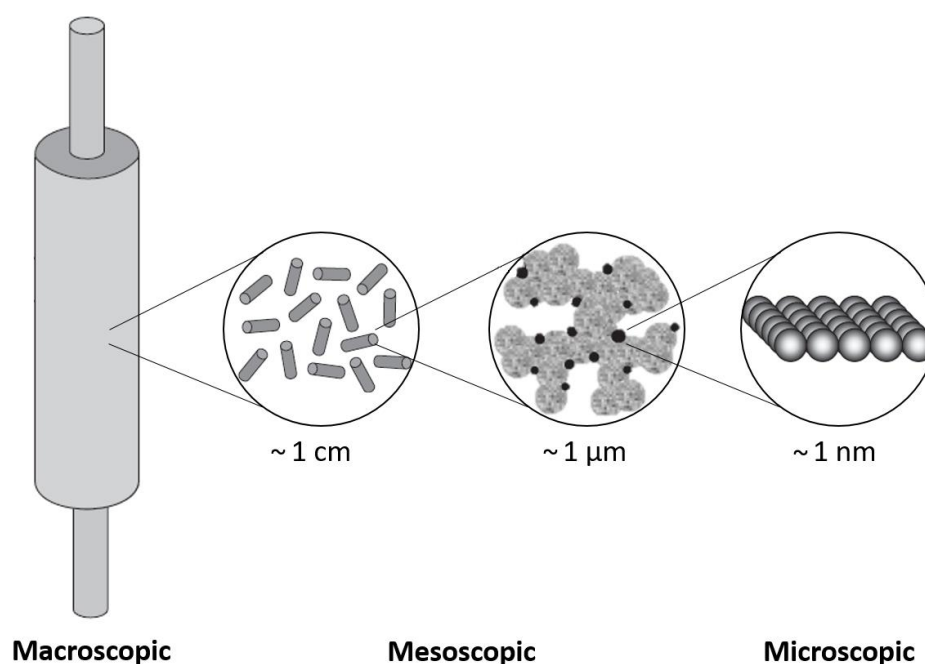


**Figure 1.1.:** *The length scales involved in the design of a solid heterogeneous catalyst. Here, the reactor bed, the catalyst pellets, the support and active sites are visualized. Adapted from Chorkendorff et al.<sup>2</sup>*

Consider a solid porous catalyst in a gas-phase reaction: In a successful catalytic reaction, the reactants have to diffuse through the boundary layer of the catalyst. Next is the diffusion into the pores and then adsorption of the reactants on the surface of the catalyst. The catalytic reaction at the active sites of the surface takes place, followed by desorption of the products from the surface. Then diffusion of the products out of the pores takes place and finally, in the last step, the products diffuse out of the boundary layer to the gas-phase.<sup>6</sup>

This adsorption can proceed by either physisorption (weak van der Waals or chemical bonds). Here, three mechanisms, the Langmuir-Hinshelwood, the Eley-Rideal or the Mars-van-Krevelen mechanism, are generally used to explain different adsorption scenarios. The Langmuir-Hinshelwood is the most common scenario, where two

reactants independently are adsorbed on the catalyst surface before they finally react to give the product. In the Eley-Rideal mechanism, only one reactant adsorbs on the catalyst surface, which reacts with the other reactant still in the gas-phase to give the product. The Mars-van-Krevelens mechanism exemplifies a scenario where the surface itself plays a significant part in the mechanism. In this case, one reactant is adsorbed on the catalyst surface to give a thin film, acting as the active site, which leaves the surface inactive after reaction. Thus, the catalyst has to be regenerated subsequently.<sup>6-9</sup>

Adsorption of reactants plays a vital role in heterogeneous catalysis. Sabatier's principle describes that the interaction between the reactants and the surface should be "just right". It is important that after the reactants have formed the products, that the products can also detach from the active sites of the catalyst surface. In an ideal case, all active sites should be identical with an equal distribution throughout the catalyst. However, this is rarely the case. It has been discovered by the aid of modern characterization techniques at atomic level, such as *in situ* Transmission Electron Microscopy, that often the active sites are irregularities found in the catalyst surface.<sup>6</sup> The active sites are primarily under-coordinated surface atoms with free valences consisting of corners, edges and lattice defects, see Figure 1.2.<sup>3</sup>

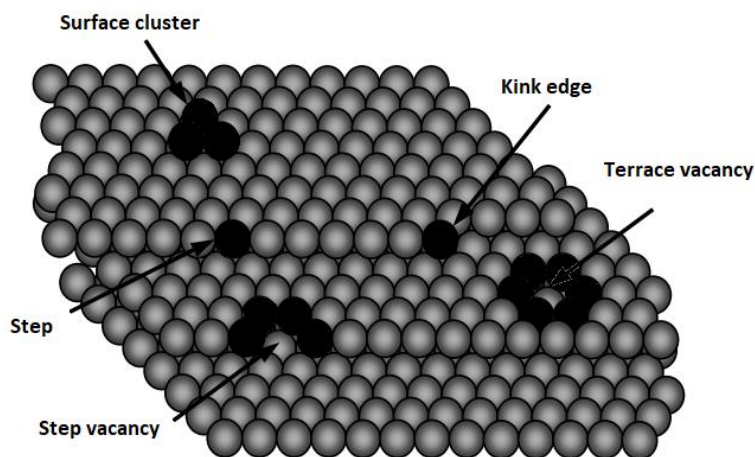


**Figure 1.2.:** Examples of irregularities found in heterogeneous catalyst surfaces.  
Adapted from Rothenberg et al.<sup>3</sup>

To have as many active sites as possible, we wish to have as much active surface area as possible. The synthesis of small-sized catalyst particles from nm-size to single atoms is therefore of great importance in the research field of heterogeneous catalysis. It can be

difficult to compare the catalytic activities of different catalysts in the literature. Thus, the activity is frequently reported as the turnover frequency (TOF), Equation 1.2.<sup>4</sup>

$$\text{TOF} = \frac{\text{moles of substrate converted}}{\text{moles of active sites} \times \text{time}} \quad (1.2)$$

The TOF is based on the moles of active sites, which can be defined from sorption methods. However, since the number of active sites is difficult to quantify in heterogeneous catalysts as in a supported metal catalyst, the catalytic activity can be normalized by the total number of moles metal atoms. The activity can also be reported as the site-time yield (STY), which is the moles of a product made per unit volume of reactor per unit time.<sup>10</sup>

An industrial catalyst should ideally have a long lifetime. Thus, the catalyst should be sufficiently stable.<sup>4</sup> Deactivation of the catalyst could be a result of many things, such as changes in the catalyst structure (e.g. metal sintering) or products of side reactions inhibiting further catalysis (e.g. coke formation). In heterogeneous catalysis, metal nanoparticles often contribute as the active sites doing the actual catalysis. Nanoparticles are commonly supported on porous supports with high surface areas.<sup>3</sup> By using high surface area materials as supports several deactivation routes can be diminished and optimization of the catalytic stability and performance can be achieved.

## 1.2 Advanced Nanomaterials

In the search for novel heterogeneous catalysts with specific desirable properties, the design of advanced materials plays a central role in present research. Even though the level of understanding in heterogeneous catalysis is not as high as in molecular catalysis, it is possible to control multiple parameters such as the size, the shape, the morphology and the composition of catalysts with high precision at the nanometer scale.<sup>11,12</sup> Today several advanced nanostructures, including graphene or carbon nanotubes, have already been incorporated into more than ten thousand commercial products with the prospect of more.<sup>12,13</sup> It is of course not only in the field of catalysis that advanced nanostructured materials are used. In fields like drug delivery and batteries several

advanced systems already exists, which might prove valuable in the design of new catalysts.<sup>11</sup>

There are several sophisticated techniques to create “smart” or advanced catalysts. Here, selective catalysis using the encapsulation of active metals in porous- or hollow materials has been in focus. The porous materials utilized for the advanced catalyst designs include metal-organic frameworks (MOFs), mesoporous silica, zeolites and porous carbon. It should be mentioned, that in industry, some of these porous materials are not only used as supports but typically used as catalysts themselves. MOFs are used in gas storage and can have incorporated magnetic properties.<sup>14</sup> Zeolites can contain both Brønsted or Lewis acidity and are well-known in catalytic cracking in the petrochemical industry. However, in this work, the porous materials have been used as supports to encapsulate the active metals, where the morphology and the capacity of the inner voids can be controlled. The chosen porous materials are similar in their large surface areas, large pore volumes and low densities, which can increase the number of exposed active sites of the encapsulated active metals.<sup>13</sup> These can be used to make shape-selective, thermal- and leaching stable catalysts. In the design of the catalysts manufactured in this dissertation, I attempt to incorporate some of these features.

To explain the synthetic strategies used in the experimental section, the porous support materials and the general experimental procedures will be introduced in Chapter 1.2.1, followed by the methods to incorporate active metals in these porous materials in Chapter 1.2.2.

### **1.2.1 Porous Materials**

Porous materials consist of micropores, mesopores and/or macropores. Micropores are classified as pores below <2 nm in diameter, where mesopores are between 2-50 nm and macropores are above >50 nm. The pore systems can be of disordered character or ordered character with multiple morphologies, which is essential for the application of the material.

Shape selectivity is one of the features that a porous support can introduce, which depends solely on the specific pore system. Shape selectivity can be either in the form of reactant, transition-state or product selectivity, also entitled molecular sieving.

Hence, the reactants entering, the products formed inside or the products leaving the molecular sieve are restricted to the size of the smallest pores of the catalyst material.<sup>15</sup> Additionally, increased thermal stability of metal nanoparticles can be achieved by encapsulation in porous supports. Metal nanoparticles are prone to agglomeration and sintering upon heating. This can be significantly diminished when the nanoparticles are distributed inside a high surface area support, as in a micro- or mesoporous network, where they are separated from each other. Sintering, which is the growth of larger metal nanoparticles from smaller ones, can be caused by particle migration and coalescence or Ostwald ripening, see Figure 1.3. Particle migration is when smaller metal nanoparticles moves in a Brownian-like motion on the surface of the support to form larger metal nanoparticles. In Ostwald ripening it is the migration of adatoms, which are induced by the difference in free energy to form larger metal nanoparticles.<sup>16</sup> Finally, leaching of the active metals from catalysts can be a huge problem resulting in a limited lifetime of the catalyst. Several industrial catalysts suffer from leaching of the active metals due to the harsh reaction conditions.<sup>17</sup> Here, encapsulation of the metal catalyst in porous materials might hinder leaching as well as sintering if the porous structure is designed properly. The challenges here include the introduction of the active metals into the porous structure while simultaneously ensuring the pore sizes of the structure are small enough to keep the active metals from leaching out during the reaction. Thus, the nano-engineering of porous materials can enhance the catalytic performance of advanced nanomaterials.

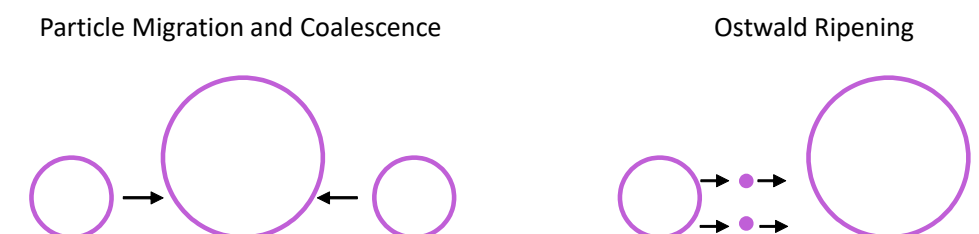


**Figure 1.3.:** *Sintering by particle migration and coalescence or Ostwald ripening where small nanoparticles or adatoms form larger nanoparticles, respectively.*

The use of templates is a common way to manufacture all sorts of porous materials. Templates are used to implement morphologies of different sizes and shapes in materials. There are two common approaches, the hard and the soft template method. The hard templating method is where the porous material is built around a well-defined solid template. After the synthesis, the template has to be removed, often by a reactive step, to give rise to the porosity with the character of the absent solid structure. The



soft templating method is where the porous material is built by flexible components, which could be liquids or gases, used as molds to implement characteristic morphologies. Subsequently, this method also requires removal of the template. The subsequent removal of hard and soft templates can be time and cost consuming, and this is why template-free syntheses of porous materials also exists to some extent.

## Metal-Organic Framework Materials

MOFs are porous crystalline materials consisting of metal ions and organic linkers, which form one-, two-, or three-dimensional frameworks. The pore sizes are in the microporous range and the porosity is a result of the long organic linkers that give rise to cavities and multiple adsorption sites, see Figure 1.4.<sup>18,19</sup> According to the Cambridge Structural Database (CSD) more than 54000 MOFs exist, offering a large number of frameworks with different compositions.<sup>11</sup> Their typical surface areas are in the range of 1000- 10000 m<sup>2</sup>/g, which is some of the highest for porous materials.<sup>20</sup>

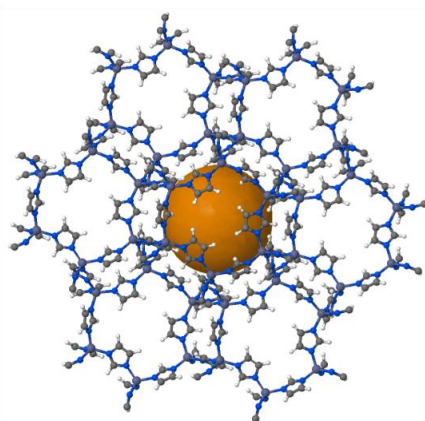


**Figure 1.4.:** *Cavities and channels in the framework of ZIF-8 constructed from 2-methylimidazole and Zn ions. The orange sphere is to guide the eye.*<sup>21</sup>

The formation of the dative bonds in the MOFs are usually done from a one-pot synthesis of the metal precursor and the organic linker.<sup>22</sup> The reaction conditions are simple and at low temperatures using a solvothermal synthesis. Other methods include microwave-assisted and electrochemical synthesis.<sup>23</sup> Additionally, it is possible to carbonize the MOFs, heating the organic structure under an inert atmosphere until it decomposes, yielding a porous carbon material. Thus, the MOFs can be used as a sacrificial template for porous carbon structures.<sup>24,25</sup>

## Mesoporous Silica Materials

Mesoporous silica materials have amorphous structures. These materials can be easily controlled to obtain highly uniform porous structures with well-defined pore shapes. Their surface areas are typically in the range of 300-1000 m<sup>2</sup>/g.<sup>26</sup>

Mesoporous silica materials can be synthesized by soft templating, gelation of silica solutions or etching. The soft templating offers the most control of the pore architecture by the use of a surfactant. The method is simple and only requires a soft template, a silica precursor, solvent and a base to catalyze the condensation and polymerization. The soft template is typically composed of surfactant micelles, which are removed after the polymerization to form the porous structure, which can be done by heating in air, i.e. by calcination. The size and the shape of the pores are replicas of the surfactant aggregates, which means they can be altered by changing the surfactant. The surfactant consists of a hydrophilic part and a hydrophobic part (a headgroup and a tail), thus when forming these micelle aggregations, the hydrophobic part usually controls the pore size. For instance, the surfactant template Hexadecyltrimethylammonium bromide (CTAB) results in pore sizes of 2-3nm due to the length of its hydrophobic tail.<sup>19</sup>

## Synthetic Silica Zeolites

Zeolites are crystalline uniform microporous (alumino)silicates. They are three-dimensional networks of silicon and/or aluminium oxide tetrahedra linked together by oxygens, TO<sub>4</sub> units (T=Si(+IV) or Al(+III)). Zeolites have channels and cavities at the molecular level, which gives them shape-selective and adsorption properties. The pore systems can be composed of different ring sizes built by the T units, see Figure 1.5. Small ( $\leq 8$  atoms), medium ( $\geq 10$  atoms), large ( $\geq 12$  atoms) and extra-large ( $\geq 14$  atoms) zeolite pore systems. There exist around 248 zeolite framework types. These have a unique three-letter code confirming the framework, but not the chemical composition. The codes and their characteristics can be found at the homepage of The International Zeolite Association (IZA).<sup>27</sup> Zeolites typically have surface areas in the range of 200-900 m<sup>2</sup>/g and they have high thermal and mechanical stabilities,<sup>28</sup> depending on their chemical composition.<sup>15,29</sup>

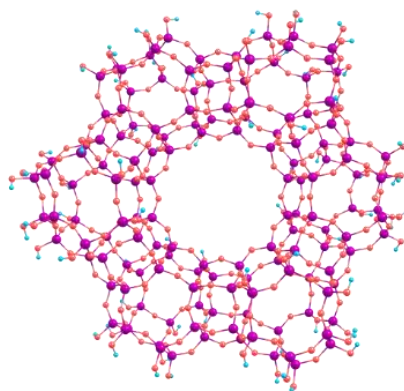


**Figure 1.5.:** *Cavities and channels in the zeolite faujasite (FAU) framework.*<sup>30</sup>

One difficult task in zeolite synthesis is to obtain the correct “phase” that crystallizes. The crystallization depends on different conditions such as the gel composition, the temperature, the pH, the time and the stirring, among other things. The crystallization is a hydrothermal self-assembly where often a structure-directing agent (SDA), is used to obtain a desired morphology. These SDA’s can be of inorganic or organic character. Additionally, mesopores can be introduced to the zeolite’s microporous structure resulting in hierarchical zeolites. The introduction of mesopores can decrease diffusion limitations to the active sites, change selectivity or decrease deactivation from coke formation in the micropores. The synthesis strategies for hierarchical zeolites are divided into the Top-down and the Bottom-up approach. The Top-down approach involves post-synthesis treatments of the already crystallized zeolite. Examples include desilication and dealumination of the microporous zeolite structure. The Bottom-up approach involves a soft or a hard template introduced during the zeolite crystallization. The soft templates usually involve a surfactant (micelles), where the hard template often is a carbon-based template. However, template-free strategies to create intercrystalline mesoporosity have also been developed.<sup>15</sup>

## Porous Carbon Materials

Porous carbon materials are amorphous non-oxides, typically with non-ordered porosities. They have high thermal and mechanical stabilities. Additionally, these materials have adsorption properties. Their surface areas are typically very diverse in the range of 300-3000 m<sup>2</sup>/g.<sup>31,32</sup>

Porous carbon materials are often obtained by the carbonization of organic precursors with natural or synthetic origin. Thus, the porous carbon materials can have very different morphologies depending on their precursor material. Carbonization often results in non-ordered porosities with wide pore size distributions. Higher carbonization temperatures can result in graphitic domains. Hard and soft templates allow the preparation of ordered porous carbon materials with narrow size distributions. Soft templates could be surfactant micelles or polymers and hard templates could be MOFs or zeolites.<sup>19</sup>

### 1.2.2 Metal Incorporation Methods

Since the actual catalysis is often taking place at the surface of the active metals, the metal choice is of great importance when designing a catalyst. Noble metals, such as Au, Ag, Pd and Pt, are generally the more active metals in many catalytic reactions. Noble metals are less prone to oxidation by atmospheric oxygen, but their scarcity and cost make the use of noble metals less desirable. Here, base metals, such as Ni, Co, Fe and Mo, can often replace the noble metals due to their abundance and lower cost.<sup>33</sup> It is typically more difficult to obtain small nanoparticles with a narrow size distribution with base metals, but other features such as ferromagnetism might come in handy in separation and recycling of the catalyst. This could be by using the ferromagnetic Fe or Co. The focus of this dissertation has been to utilize base metals in the design of the advanced nanomaterials due to their abundance.

The introduction of the base metal into the porous support can be done in numerous ways. In general the approaches can be divided into physical (e.g. sonication or microwave irradiation), chemical (e.g. impregnation, coprecipitation or deposition-precipitation) and physiochemical (e.g. frame spray pyrolysis) techniques.<sup>34</sup>

The common strategy is to use a chemical technique as impregnation of supported catalysts, where the already synthesized porous support is impregnated with a metal of choice.<sup>2,3</sup> Alternatively, the creation of the porous support with the encapsulated metals can be done in one-step by the use of a sacrificial metal precursor and template. Since the introduction method plays a vital role in the size and distribution of the metal nanoparticles, it also ultimately regulates the catalytic activity. The focus in this

dissertation will be on the metal impregnation and the sacrificial metal precursor techniques.

## **Metal Impregnation**

This technique involves the porous support and the metal precursor in solution with the desired concentration. Here, the metal precursor is often a metal salt dissolved in a solvent. There are in general three different methods to impregnate the support according to Rothenberg *et al.*<sup>3</sup>; wet impregnation, incipient wetness impregnation and vacuum pore impregnation. In wet impregnation, the porous support is immersed in the metal precursor solution. As the name indicates, it involves a lot of liquid waste. The metal precursor is here adsorbed or precipitated on the support, followed by filtration, drying and calcination. Subsequently, it may be necessary to reduce the metal in an appropriate gas. These last steps are relevant in all of the impregnation techniques. In incipient wetness impregnation, the liquid waste is limited. Here, the volume of the metal precursor solution is adjusted (calculated) to the pore volume of the porous material. The metal precursor solution is added to the pre-dried powder support until the pores are filled. This can be observed as a change from dry powder to a “sticky paste” of the powder. In a vacuum pore impregnation, the porous support is pre-dried in vacuum to empty the pores of air. The mix between the porous support and the metal precursor solution is completed in vacuum to fill the pores with the adjusted metal precursor solution.<sup>3</sup> In this method, it is possible to obtain relatively large metal loadings, since the impregnation procedure can be repeated. However, it can be difficult to obtain homogeneous quality and high reproducibility of the impregnated materials. The size and distribution of the metal is highly dependent on the metal, the support and the loading.<sup>34</sup>

## **Sacrificial Metal Precursor**

Sacrificial templating is where a template is removed or rearranged in the synthesis of a porous material. The sacrificial template method might also fit the definition of the hard template method. However, if the removal of the (sacrificial) hard template not only yields the porous support, but also introduces metal nanoparticles, it additionally acts as a sacrificial metal precursor. A good example is the use of MOFs as a sacrificial template and metal precursor, also called a MOF mediated synthesis (MOFMS).<sup>25</sup> MOFs can yield a variety of advanced catalytic materials depending on their heat treatment or post treatment. In general MOFMS can yield three types of advanced materials. These

include metal nanoparticles in porous carbons, nanostructured carbons and unsupported metal oxides, which features are dependent on the parent MOF.<sup>25,35–38</sup> Here, especially the subclass Zeolitic Imidazolate Frameworks (ZIFs), is interesting for the development of metal nanoparticle catalysts with nanoporosity.<sup>11</sup> The derived catalyst is typically produced by a thermal decomposition of the parent ZIF under a gaseous atmosphere (e.g. Ar or N<sub>2</sub>) at high temperatures (e.g. 500-900°C) to obtain different properties of the material.<sup>39</sup> The benefits of using ZIFs as sacrificial metal precursors are the numerous structures containing different metals. Since the structure already includes metal ions equally distributed in the structure, the decomposed material upon carbonization often yields a uniform distribution of small metal nanoparticles in a hierarchical porous carbon matrix. The derived porous carbon matrix often maintains part of the morphology of the ZIF framework. The metal nanoparticles derives from the carbothermally reduced ZIF metal ions. Simoultaneously, the carbon originating from the decomposed ZIF is oxidized to CO and CO<sub>2</sub>.<sup>40,41</sup> ZIFs are built up by 2-methylimidazole as the organic linker, which means the resulting carbon is nitrogen-doped (N-doped). N-doped carbons can have some beneficial properties especially in electrochemical reactions. The temperature at which these ZIFs will be carbonized at will have an influence on both the graphitization of the carbon and the amount of N present in the carbon matrix. In general, the higher the carbonization temperature the more graphitic like the structure becomes and the less pyrrolic/pyridinic N are present in the carbon matrix.<sup>25</sup>

### 1.3 Aim and Outline of the Dissertation

This dissertation aims to prepare and investigate different novel heterogeneous catalysts with nano-engineered porosity. The synthesized catalysts are all solid catalysts, which consist of the active metal species encapsulated in porous or hollow supports. The research results in this dissertation are divided into two parts consisting of four chapters; the catalysts prepared by a sacrificial metal precursor **Chapter 3** and **Chapter 4** for increased thermal stability and the catalysts prepared by metal impregnation **Chapter 5** and **Chapter 6** for increased stability towards leaching.

**Chapter 3** Introduces the use of cobalt nanoparticles encapsulated in nitrogen-doped porous carbon materials manufactured from ZIFs. The catalysts have been tested in the

hydrolytic dehydrogenation of ammonia borane. The chapter is based on the work published as Zacho *et al. Catalysis Science and Technology*. **8**(18), 4741–4746 (2018).<sup>42</sup>

**Chapter 4** Describes the work completed with cobalt oxide nanoparticles encapsulated in mesoporous silica nanorattles prepared from ZIFs. The catalysts were tested in a carbon monoxide oxidation reaction. The chapter is built on the work published as Zacho *et al. Catalysis Communications*. **125**, 6-9 (2019).<sup>1</sup> and Zacho *et al. Topics in Catalysis*. (2019).<sup>43</sup>

**Chapter 5** Presents the work done with iron molybdate catalysts encapsulated in mesoporous silica and zeolites in collaboration with PhD student Joachim Thrane, Assistant Professor Martin Høj and Professor Anker Degn Jensen from DTU Chemical Engineering, Department of Chemical and Biochemical Engineering. The catalysts have been tested for the selective oxidation of methanol to formaldehyde.

**Chapter 6** Describes the results obtained with heteropolyoxometalates encapsulated in mesoporous silica and zeolites. The work was performed in the group of Professor Peter Wasserscheid in collaboration with PhD student Anna Bukowski, PhD student Dorothea Voss and Dr. Ing. Jakob Albert at the Institute of Chemical Engineering (Lehrstuhl für Chemische Reaktionstechnik (CRT)), Friedrich-Alexander University (FAU), in Erlangen Germany. The catalytic tests include phenyl acetate Fries rearrangement and production of formic acid from biomass by catalytic oxidation (the OxFA reaction).

## **Chapter 2. Characterization of Catalysts**

---

In this chapter, I discuss the different methods I used to characterize the synthesized catalysts, including X-Ray Fluorescence Spectroscopy, X-Ray Diffraction, Fourier-Transform Infrared Spectroscopy, X-Ray Photoelectron Spectroscopy, Nitrogen Physisorption, Electron Microscopy and Solid-State Nuclear Magnetic Resonance. In each subsection, I also describe the experimental details, the instrumental settings and the typical sample preparation.

---



## 2.1 X-Ray Fluorescence Spectroscopy

X-Ray Fluorescence (XRF) spectroscopy is a non-destructive method to determine the elemental compositions of samples with high accuracy. The technique is suitable for liquids, powders or solids. In this dissertation, XRF was used to determine the metal loadings of the synthesized powder samples. XRF spectroscopy can provide qualitative and quantitative data of samples with a broad analytical concentration range of elements from 100% to sub-ppm levels. The X-ray source is usually a Coolidge tube where electrons are emitted from the cathode, a heated W filament, accelerated by high voltage to the anode, e.g. Cr, Ag, Co or Mo.<sup>44</sup> Depending on the instrument the XRF technique is usually restricted to elements of atomic numbers from 11 (Na) to 92 (U) due to the poor quality of the spectra for the lighter elements.<sup>45</sup> In this case elements lighter than Na will not be measured. Samples can be measured without preparation. However, the samples can also be pre-treated in several ways to give higher degree of homogeneity. This includes transformation of powder samples to glass disks using a fusion oven or pressing the powder samples to pellets using a wax. In XRF spectroscopy, the X-rays from the tube irradiate the sample, which results in the emission of fluorescent X-rays from the sample. An energy-dispersive detector quantifies the fluorescent X-rays emitted and the composition of the sample is determined from the characteristic discrete energies for each element in the sample.<sup>46</sup>

### Experimentals

XRF measurements were obtained with a PANalytical Epsilon3-XL instrument with an analysis range from 9 (F) to 92 (U). The anode materials were Rh, Ag and Mo and the system was equipped with a high-resolution Si drift detector. Some powder samples were measured directly in the apparatus without further preparation. Alternatively, a Claisse LeNeo Fluxer instrument was used to make glass disks of other powder samples by fusion at a temperature of 1050°C. The samples were prepared by mixing 50 mg of the sample with a flux of 10.500 g lithium borate (67%  $\text{Li}_2\text{B}_4\text{O}_7$ , 33%  $\text{LiBO}_2$ ) and 60 mg of the non-wetting agent LiBr. The samples were either quantified from a multi-element calibration with the Omnian application present in the Epsilon software or by a calibration line made from measurements of self-made standards.

## 2.2 X-Ray Diffraction

X-Ray Diffraction (XRD) is a technique applied to identify and solve unknown crystalline structures. XRD makes it possible to determine the degree of crystallinity, the crystalline phases and estimate particle sizes in a sample. If the sample is a polycrystalline powder, it is termed X-Ray Powder Diffraction (XRPD). In this dissertation, XRPD was used to identify the crystalline structures of the porous supports and metal nanoparticles. In XRD, the sample is irradiated with a beam of X-rays at a wavelength  $\lambda$  between 0.5-2 Å.<sup>3</sup> If the sample's atoms are organized in a periodic lattice with the distance  $d$  between the lattice planes then coherent scattering causes diffraction. This is called constructive interference and occurs when Bragg's law is fulfilled, where  $n$  is an integer and  $\theta$  is the diffraction angle, see Equation 2.1 and Figure 2.1.<sup>47</sup>

$$n\lambda = 2d\sin\theta$$

(2.1)

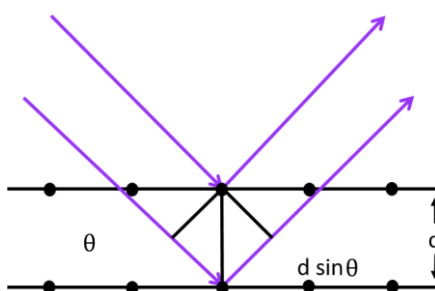


**Figure 2.1.:** *The geometry of Bragg diffraction.*

The diffraction results in a unique diffraction pattern, which can be compared to existing patterns in the International Centre for Diffraction Data (ICDD) database or for zeolites in the Database of Zeolite Structures by the International Zeolite Association (IZA). If the sample is a polycrystalline powder it can be necessary to rotate the sample during measurements. Otherwise, the diffraction pattern will only be created from a small fraction of the crystal orientations.<sup>47</sup> XRD cannot be used to detect very small particles and amorphous samples provides diffraction patterns with broad and weak diffraction peaks.<sup>3</sup>

## Experimentals

All samples were measured with a Huber G670 diffractometer operated in transmission mode. The apparatus used CuK $\alpha$ 1 X-ray irradiation from a focusing quartz monochromator. The samples were prepared by placing a thin layer of the powder on a piece of scotch tape fixed to a gold plated sample holder. The XRD patterns of the samples were measured with the help of laboratory technicians Lise Lotte Berring and Lise-Lotte Jespersen for 10-60 min with a wavelength of 1.54060 Å in the  $2\theta$  interval 3-100°.

## 2.3 Fourier-Transform Infrared Spectroscopy

Fourier-Transform Infrared (FTIR) spectroscopy is a fast and non-destructive technique to identify chemical compounds. In this dissertation, FTIR spectroscopy was used to examine and identify the synthesized polyoxometalate (POM) structures. The sample, which can be a solid, liquid or gas is irradiated with an infrared beam and the transmitted radiation by the sample is then measured. Because different chemical compounds absorb infrared radiation at different frequencies, the measurements can be used to characterize the molecules present in the sample. From the measured absorbed radiation a spectrum can be produced.<sup>44</sup> The spectrum is visualized as a graph with the frequency as a function of absorption. From reference materials or available reference spectra libraries it is then possible to determine the identity of a particular chemical structure from the absorbed radiation at a specific frequency. The technique can also be used to detect impurities in a sample.<sup>48</sup>

## Experimentals

All samples were measured at ambient conditions with a Jasco FT/IR-4100 spectrometer equipped with a PIKE GladiATR ATR-accessory with a resolution of 4 cm<sup>-1</sup>. The samples were powders recorded without further preparation in the range 4000-400 cm<sup>-1</sup>.

## 2.4 X-Ray Photoelectron Spectroscopy

X-Ray Photoelectron Spectroscopy (XPS) is a surface-sensitive technique, which provides information about the surface elemental composition and the chemical/electronic state

of a sample. In this dissertation, XPS was used to verify the encapsulation of metal nanoparticles and identify the oxidation states of the metals. The method is based on the photoelectric effect, where it uses photons from an X-ray source, usually Al K $\alpha$  or Mg K $\alpha$  radiation, which penetrates the outer atomic layers of a sample's surface. The mean free path is usually less than 2 nm.<sup>47</sup> Here, the energy of the photon is absorbed by the atoms of the sample and an electron with a specific kinetic energy is ejected. The binding energy is calculated as the difference between these energies, which is characteristic for the element. The obtained binding energies can be compared to reference tables. It is possible to analyze the concentrations of each element at the surface for all elements except H<sub>2</sub> and He. The technique requires ultrahigh vacuum conditions for the analysis.<sup>3</sup>

## Experimentals

The measurements were made with a Thermo Scientific K-Alpha X-ray photoelectron spectrometer equipped with a hemispherical analyzer and an Al K $\alpha$  micro-focused monochromator. The pass energy of the analyzer was put to 100 eV for survey scans and 50 eV for narrow scans. The pressure was less than  $2 \cdot 10^{-7}$  Pa in the analysis chamber during experiments. The XPS spectra of the samples were measured with the help of fellow PhD students Kristoffer Hauberg Møller and David Bejamin Christensen. All spectra were subsequently corrected with binding energies C 1s at 284.8 eV or Si 2p at 103.4 eV to account for charging effects. The software "Avantage" was used to process the measured data.

## 2.5 Nitrogen Physisorption

Nitrogen (N<sub>2</sub>) physisorption is a technique to determine the surface area, porosity and pore size distribution of porous solids or fine powder samples with physical adsorption of N<sub>2</sub>. All samples in this dissertation were studied with N<sub>2</sub> physisorption to identify the porosities and other characteristics of the synthesized supports. N<sub>2</sub> physisorption is done by the adsorption of the inert gas (N<sub>2</sub>) at liquid N<sub>2</sub> temperature (77K), a temperature close to the boiling point, in monolayer, bilayer and finally multilayer coverage of the material surface. It is also possible to measure physisorption with Ar at a liquid Ar temperature of 84K.<sup>3,49</sup>

Traditionally, there are six types of adsorption isotherms (Type I-VI). However, since 2015 two additional isotherm types have been added by the International Union of Pure and Applied Chemistry (IUPAC) due to recent advances in the field. The Type I and IV now have an (a) and (b) form, which makes it possible to identify eight different types of adsorption isotherms by N<sub>2</sub> physisorption analysis, see Figure 2.2 (left). An adsorption isotherm is presented as a graph, which presents how the amounts of N<sub>2</sub> a sample has adsorbed (mol g<sup>-1</sup>) depends on the relative pressure ( $p/p^0$ ), at the operational temperature (77K). In an isotherm, the onward process of adsorption is defined as the adsorption branch and the opposite process is defined as the desorption branch. Hysteresis arises due to delayed condensation, which is seen as a difference between the adsorption and desorption curve of the isotherm, see Figure 2.2 (right).<sup>50</sup>

## Adsorption Isotherms

*Type I:* This isotherm is known as the Langmuir isotherm.<sup>3</sup> It is typical for microporous materials with relatively small external surfaces, e.g. molecular sieve zeolites and ultrahigh surface area activated carbons. The adsorption is typically a monolayer, since the micropores restrict the formation of multilayers. The reason for the high increase in adsorption at low pressures is because of the enhanced adsorbent-adsorptive interaction in the narrow micropores, which makes them fill up already at low pressures. Here, capillary or pore condensation occurs, where the gas is condensed to a liquid-like phase inside the pores at a pressure less than the saturation pressure ( $p/p^0=1$ ). Type I (a) is typical for materials with micropores of narrow widths <1 nm, where Type I (b) materials typically have wide microporous or narrow mesoporous widths <2.5 nm.

*Type II:* The isotherm is characteristic of nonporous or macroporous materials. The monolayer is filled at rather low relative pressures, which is equal to the Langmuir isotherm. At higher relative pressures, a second layer begins to form, until it reaches unrestricted multilayer formation, equivalent to the previously defined capillary condensation. If point B “the knee” is sharp it indicates the completion of the monolayer and if not it indicates overlap between the adsorption of the monolayer and the multilayer, see Figure 2.2.

*Type III:* The isotherm is usually a nonporous or macroporous material, as for Type II. Here the adsorbent-adsorbate interactions are weak and the molecules prefer to adsorb on another adsorbed molecule, which is the equivalent of no monolayer formation.

*Type IV:* The isotherm is typical for mesoporous materials.<sup>3</sup> In this type a monolayer is formed at low pressures, followed by multilayers until capillary condensation arises and restricts further adsorption. In this case a hysteresis loop will form due to capillary

forces, where the gas leaving the pores has a lower equilibrium pressure than when entered.<sup>49</sup> Type IV(a) isotherms exhibit hysteresis due to capillary condensation. Hysteresis arises when the pores exceed  $\sim 4$  nm in diameter and their widths become critical for the emptying of the pores. Type IV(b) isotherms have mesopores with smaller widths. Thus, the pores can be emptied and a reversible isotherm is acquired. The Type IV isotherm often reaches a final saturation plateau, which can be of different length.

*Type V:* The isotherm's shape is similar to Type III due to its weak adsorbent-adsorbate interactions. Thus, the weak interactions result in no pore filling until higher relative pressures. This type of isotherm could be present for water adsorption on hydrophobic materials or some mesoporous materials.

*Type VI:* The isotherm is typical for uniform nonporous materials with layer-by-layer adsorption. Every step increase "knee" indicates the adsorption capacity of the related layer.<sup>50</sup>

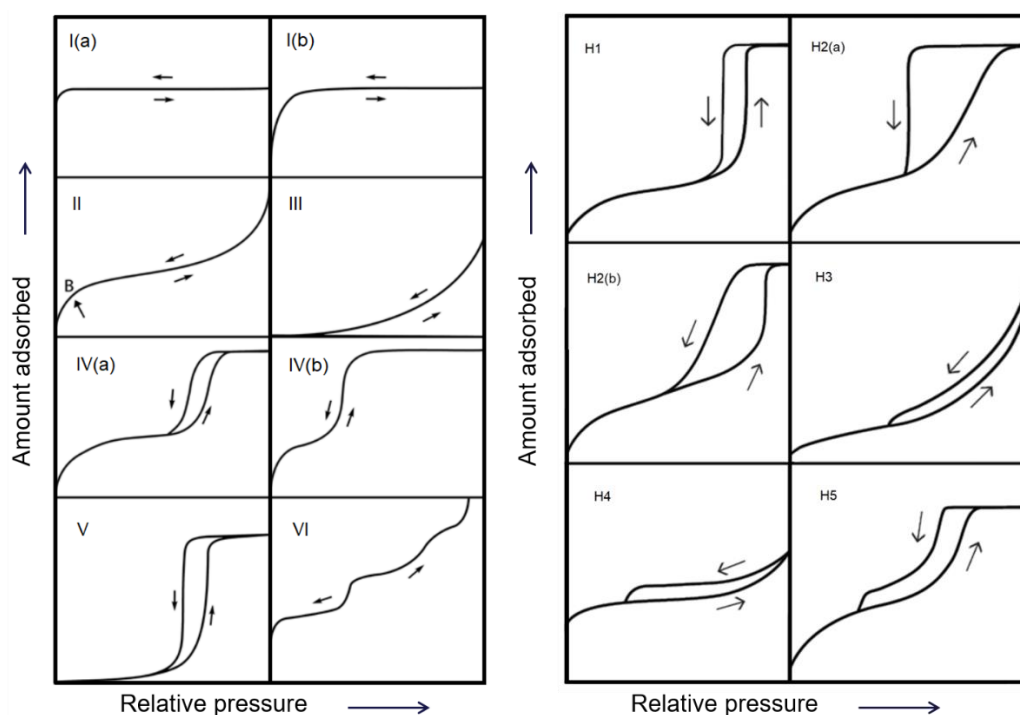


**Figure 2.2.:** (Left) the different Types of adsorption isotherms and (right) Hysteresis loops classified by IUPAC. Adapted from Thommes et al.<sup>50</sup>

## Hysteresis Loops

As mentioned in the Type IV adsorption isotherm section, Hysteresis loops can occur due to capillary forces. Six types of Hysteresis loops are classified by IUPAC, where two of these types were added in 2015 due to the revision. The Types include H1, H2(a), H2(b), H3, H4, H5, see Figure 2.2. above.

*H1:* The Hysteresis loop H1 occurs for materials with uniform mesopores of narrow character. Type H1 includes templated silicas and mesoporous carbons. The steep but narrow loop is a result of delayed condensation.

*H2:* The Hysteresis loop H2 is found in complex pore structures. Type H2 includes silica gels or mesocellular silica foams. Type H2(a) loops have very steep desorption branches due to pore-blocking in narrow range pore necks or cavitation-induced evaporation. Type H2(b) loops have fewer steep branches, which is a result of a broad size distribution of widths of the blocked pore necks.

*H3:* The Hysteresis loop H3 has a similar shape of the Type II isotherm. Type H3 includes clays or materials where the macroporous networks are only half-full with pore condensate.

*H4:* The Hysteresis loop H4 has a combined shape of Type I and II isotherm. The adsorption at lower relative pressures in Type H4 arises from the micropores. Type H4 includes mesoporous or aggregate crystals of zeolites and micro-mesoporous carbons.

*H5:* The Hysteresis loop H5 is unusual and arises in materials with mesopores of open and partially blocked origin.

The closure point of the desorption branches of H3-H5 is usually located in the relative pressure area ( $p/p^0$ ) 0.4-0.5, which is characteristic for the adsorbate,  $N_2$  at 77K.<sup>50</sup>

## Data Analysis

The surface area of a sample can be determined based on the volume of gas adsorbed on the sample's surface at a specific temperature and pressure. The Brunauer-Emmett-Teller (BET) method is the most common procedure to use for surface area calculations, which is an extended version of the Langmuir equation.<sup>51</sup> In comparison to the Langmuir equation, the BET equation is not limited to monolayer adsorption, but is extended to multilayer adsorption, see the BET Equation 2.2.<sup>52</sup>

$$V = V_m \frac{C \frac{p}{p^0}}{\left(1 - \frac{p}{p^0}\right) \left\{1 - (1 - C) \frac{p}{p^0}\right\}} \quad (2.2)$$

Here,  $V$  is the volume of gas adsorbed,  $V_m$  is the volume equivalent to one adsorbed monolayer,  $p$  is the equilibrium pressure of the gas,  $p^0$  is the saturation pressure and  $C$  is the BET constant.<sup>52</sup> However, as the calculations from the BET method are built on certain assumptions, which are not always true, unreliable results can be derived.<sup>49,50,53</sup> Data obtained with the physisorption analysis can be used for the calculation of several additional characteristics of porous materials as the micropore volume and the external surface area calculated by the t-plot method<sup>54</sup> or the pore size distribution calculated by the Density Functional Theory (DFT) method.<sup>55</sup>

## Experimentals

The N<sub>2</sub> physisorption analysis was performed with a Micromeritics 3Flex instrument at liquid nitrogen temperature (77K). The samples were degassed in vacuum prior to analysis at 200°C for 20 h. The BET method was used to calculate the specific surface area ( $S_{\text{BET}}$ ). The t-plot method was used to calculate the micropore volume ( $V_{\text{micro}}$ ) and the external surface area ( $S_{\text{ext}}$ ). From the isotherm adsorption branch, the total pore volume ( $V_{\text{total}}$ ) was determined by a single point read at the relative pressure  $p/p^0 = 0.95$ .

## 2.6 Electron Microscopy

In this dissertation, Scanning Electron Microscopy, Transmission Electron Microscopy and Scanning Transmission Electron Microscopy were used to obtain knowledge about the catalysts morphology and the distribution of the metal nanoparticles. Moreover, Electron Tomography was used to determine the exact three-dimensional dispersion of the metal nanoparticles.



### 2.6.1 Scanning Electron Microscopy

Scanning Electron Microscopy (SEM) is a technique used to study the morphology and chemical composition of nano- and microstructures. The method can be used to acquire images of the analyzed sample's topology by the use of secondary electrons or backscattered electrons. The instrument uses a tungsten filament or a field emission gun (FEG) to generate an electron beam of 1-30 keV, which is systematically scanning the sample in a raster pattern.<sup>56</sup> The focusing of the beam is accomplished with a magnetic field by electromagnetic lenses and apertures in the instrument under high-vacuum. The focused beam interacts with the sample, which result in both inelastic or elastic scattering events.<sup>57</sup>

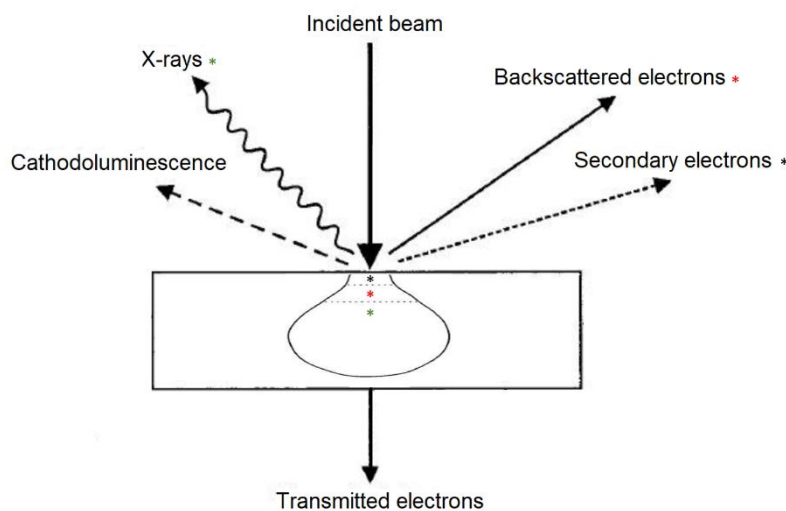


**Figure 2.3.:** Overview of the generated signals from the electron beam interaction with a sample in a scanning electron microscope. The stars of different colors show the penetration depths in the sample. Adapted from Goodhew et al.<sup>56</sup>

Inelastic scattering includes a variety of interactions between the incident electron beam and the sample, but importantly for imaging, it gives rise to the secondary electrons (SE), see Figure 2.3. SE is the most common signal used to make images. The ionized atoms of the sample generate the SE, which hold energies less than 50 eV. The SE only escapes from a nanometer region within the sample's surface, which gives high-resolution images of the topography. The images depend on the amount of SE that hits the scintillator, which is the detector converting the energies. The sample needs to be tilted in order to obtain the highest amount of SE and a low voltage electron beam results in the most detailed topographic information. The surface contrasts in the

images are a result of the angle the sample has to the detector, where brighter areas are facing the detector perpendicular.<sup>3</sup> The lateral resolution is typically around 10 nm.<sup>57</sup>

Elastic scattering occurs when the atomic nucleus or outer shell electrons in the sample deflect the electron beam, which results in backscattered electrons (BSE), see Figure 2.3. Using BSE to produce images is less common, but they provide both topographic and compositional information about the sample. The directional change of the scattered BSE has a wide angle, in general more than 90°. The BSE penetrates deeper into the sample and often undergo multiple scattering events before they escape from the surface, holding energies of more than 50 eV. The resulting lateral resolution is 1.0  $\mu\text{m}$ , which is not as high as with the use of SE.<sup>57</sup>

Most scanning electron microscopes have detectors for both SE and BSE.<sup>56</sup> In Figure 2.3, the additional signals generated from the electron beam's interaction with the sample can be seen, which includes Auger electrons, characteristic X-rays and cathodoluminescence.

## **Experimentals**

SEM samples were prepared by dispersion of the sample powders on a piece of carbon tape followed by sputter coating of a thin conductive gold layer to avoid charging. Images were taken with a Quanta 200 ESEM FEG microscope operated at 20 keV from FEI. The samples were prepared and the images were recorded with the help of fellow PhD student Rouzana Pulikkal Thumbayil and Postdoc Farnoosh Goodarzi.

### **2.6.2 Transmission Electron Microscopy**

A Transmission Electron Microscopy (TEM) instrument can characterize the internal structures of solid materials. With TEM it is possible to attain information about the size, the shape and the composition of a sample.<sup>3</sup> The instrument uses a high voltage electron beam to illuminate the sample, which when transmitted through generates an image or a diffraction pattern.<sup>56</sup> An illustration of a TEM instrument is shown in Figure 2.4.

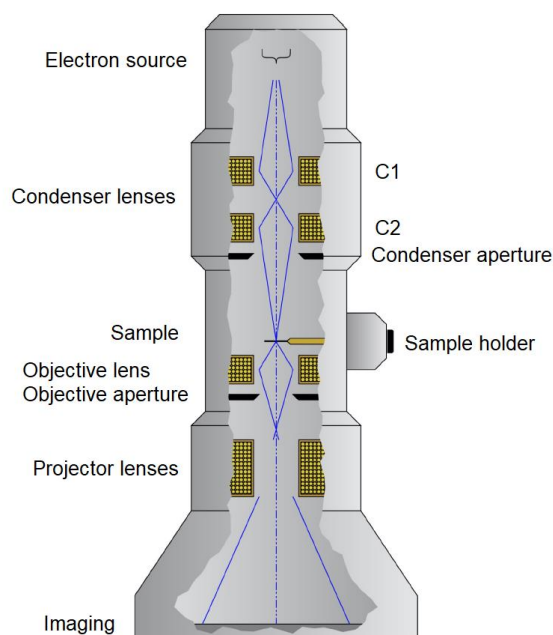


**Figure 2.4.:** *Illustration of a transmission electron microscope including components and the electron beam path. Adapted from Spurgeon et al.<sup>58</sup>*

The electron source is found at the top of the instrument, which typically is a thermionic or field electron emission gun, e.g. from a tungsten or LaB<sub>6</sub> source. The voltage applied in TEM is usually between 100-300 keV, depending on the thickness of the analyzed sample. Two or more electromagnetic condenser lenses are positioned below the electron gun, C1 and C2, which are used to focus the emitted electron beam. C1, the spot size, is used to control the gun crossover and the C2, the intensity, controls the convergence angle together with the condenser aperture. The size of the condenser aperture can restrict the fraction of electrons illuminating the sample. The sample is introduced through an airlock below by a sample holder. To obtain an image the objective aperture is inserted focusing the beam in the image plane of the objective lens; this is the image mode. To obtain the diffraction pattern the objective aperture is removed and the beam is focused on the back focal plane of the objective lens; this is the diffraction mode. The objective aperture is chosen to restrict the fraction of contributing electrons, i.e. exclusion of unscattered electrons. Subsequently, the projector lenses placed below are used to magnify the image or diffraction pattern displayed on the viewing screen. Here magnification up to one million times is easily achieved. A Charge Coupled Device (CCD) array camera placed below the viewing screen is usually acquiring the images. The resolution of a typical TEM instrument is about 0.5 nm, although this requires a careful alignment of the electron beam prior to analysis.<sup>3</sup>

Moreover, the sample has to be thin enough to let the electrons transmit through it, usually < 100 nm.<sup>56</sup>

The resulting images acquired from TEM are bright field (BF) images, which originate from electrons transmitted through the sample at an angle <10 mrad. If the objective aperture is moved off-angle or the incident beam is tilted, the image is obtained from the diffracted electron beam.<sup>3</sup> This results in dark field (DF) images. In some cases, it can be beneficial to acquire DF images since contrast and resolution are increased.

The images acquired with TEM can have three different origins of contrast, the mass-thickness contrast, the diffraction contrast and the phase contrast. Mass-thickness contrast originates from differences in thickness or density in a sample. The contrast appears as darker regions where the sample is thicker or of higher density. This is because thicker or denser parts of a sample scatter electrons more strongly and fewer electrons are transmitted through the sample, making it appear dark in the image. In a thin area, few electrons are deflected in the sample and the resulting image will appear brighter in this region. Diffraction contrast originates from crystalline samples that fulfill Bragg's law and diffract the electrons, see Equation 2.1 in Chapter 2.2. The diffraction contrast appears as dark regions in the images, but these disappear when the sample is tilted and Bragg's law is not satisfied. Phase contrast originates from the interference of waves with different phases. These appear as fringes in the image. These fringes are visible as dark or bright pattern spots in the image, corresponding to columns of atoms.<sup>56</sup>

## **Experimentals**

The TEM instrument used was a FEI Tecnai T20 G2 microscope, which was operated at 200 keV. The samples were dispersed on a 300-mesh holey or lacey carbon copper grid prior to analysis. The average nanoparticle size distributions were determined based on representative TEM images and >100 nanoparticles.

### **2.6.3 Scanning Transmission Electron Microscopy**

Scanning Transmission Electron Microscopy (STEM) is a technique building on the principles of both SEM and TEM to acquire elemental compositions and high-resolution images of samples.<sup>56</sup> In STEM, the electron beam is focused to a fine probe scanning the sample and images are created from the electrons transmitted through the sample. Resolution below Ångstrom can be achieved with STEM making it possible to take images of single atoms or atom columns.<sup>57</sup> These images are often taken with Z-contrast,

a High Angle Annular Dark Field (HAADF) detector. In HAADF, the detector only collects electrons scattered with an angle higher than  $>50$  mrad. Here, the Bragg effects can be avoided, thus a higher resolution and unaffected image contrast from small alterations in the objective lens defocus can be attained.<sup>59</sup> Multiple detectors are usually attached to the instrument such as an Energy Dispersive Spectrometer (EDS). The semiconductor Si detector is placed in line with the sample holder where it can collect scattered X-rays. Since the energy of the X-ray is element characteristic, the element can be identified from it. From EDS it is possible to get the quantitative composition or a compositional image/map of a sample. It is not possible to detect light elements, generally lighter than Na.<sup>56</sup>

## Experimentals

The HAADF images and EDS data of the prepared samples were obtained with a FEI Titan 80-300ST field emission gun TEM operated at 300 keV. AZtec software was used to process the EDS data. Additionally, HAADF images were obtained with a Jeol JEM-ARM300F operated at 300 kV at the Diamond Light Institute, as part of the proposal 20892 and 20650.

### 2.6.4 Electron Tomography

A TEM instrument is used to acquire two-dimensional images of three-dimensional samples. Thus, TEM images cannot be used to validate spatial distributions. Here, electron tomography can create a three-dimensional model with nanometer scale resolution from a series of two-dimensional projections. Electron tomography is performed by collecting a series of TEM images by tilting the sample to an angle of  $\pm \sim 70^\circ$ .<sup>60</sup> The projections from the tilt-series can then be digitally reconstructed to a three-dimensional data set, which can be visualized in a movie.<sup>61</sup> The tomographic reconstruction is performed with the Simultaneous Iterative Reconstruction Technique (SIRT), which is based on assumptions such as the incident beam is parallel. Thus, the reconstruction technique holds some constraints.<sup>57</sup> Further descriptions on the tomographic reconstruction can be found in the review by Jong *et al.* reporting the use of electron tomography for heterogeneous catalysis characterization.<sup>62</sup>

## Experimentals

The electron tomography was performed with a FEI Titan 80-300ST FEG TEM operated at 30 keV. The tomography was performed by collecting tilt-series of HAADF-STEM images with an angle increase of  $2^\circ$  between each image. The alignment and

reconstruction was made in Inspect 3D from FEI using SIRT. Segmentation and 3D visualization of the reconstructed samples were made in Avizo from FEI. The data were recorded together with PhD student Jes Ærøe Hyllested from DTU nanolab, who subsequently completed the tomographic reconstructions.

## 2.7 Solid-State Nuclear Magnetic Resonance

Solid-State Nuclear Magnetic Resonance (SS-NMR) spectroscopy can deliver valuable chemical information of solid samples. The analytical technique is ideal for the investigation of the nuclei's local structure in nanoscale-sized materials.<sup>63</sup> In this dissertation, SS-NMR was used to identify and compare the local environments of encapsulated POMs with bulk POMs. SS-NMR requires the investigated elements to possess a spin state above zero, with a preferred spin state of  $\frac{1}{2}$ .<sup>64</sup> Thus, some of the isotopes, which are accessible with SS-NMR spectroscopy, include  $^1\text{H}$ ,  $^{29}\text{Si}$ ,  $^{31}\text{P}$ ,  $^{51}\text{V}$ , among others.<sup>65</sup> A challenge with solid samples in SS-NMR is the anisotropic interactions, which cause significant line broadening compared to standard high-resolution NMR. This is in contrast to the liquid phase where a rapid molecular tumbling averages the anisotropic contributions, and only the isotropic chemical shift is observed. For solid samples, the fixed lattice and increased rigidity hinder any averaging, and instead of a well-defined peak at the isotropic chemical shift, a so-called powder line shape is observed. However, it is possible to introduce a liquid-like tumbling by application of the Magic-Angle Spinning (MAS) technique, where the samples are spun at an angle of  $54.74^\circ$  (the "magic angle") relative to the external magnetic field. This imposes a time modulation of the signal and the powder line shape is split into a manifold of spinning sidebands with a separation equal to the spinning frequency,  $nR$ .<sup>65</sup> Modern instruments utilizing small rotors can spin as high as 100 kHz, but more common spin rates are between 5 and 25 kHz depending on the application.

### Experimentals

$^{31}\text{P}$  and  $^{51}\text{V}$  MAS NMR spectra were recorded with a Bruker AVANCE III HD spectrometer operating at 14.1T magnetic field with a 4 mm o.d. CP/MAS BBFO probe. The  $^{31}\text{P}$  spectra were acquired with a simple bloch decay experiment (pulse-and-aquire) with high-power Spinal-64  $^1\text{H}$  decoupling, while a rotor-synchronized Hahn-echo sequence (spin echo) was used for the  $^{51}\text{V}$  spectra. All presented spectra were acquired with a spinning frequency of 15 kHz. Isotropic chemical shifts are reported relative to  $\text{NH}_4\text{H}_2\text{PO}_4$  (0.81

ppm) and  $\text{VO}(\text{Cl})_3$  (0.0 ppm) for  $^{31}\text{P}$  and  $^{51}\text{V}$ , respectively. Peak simulations were performed with the Solids Lineshape Analysis (SOLA) module in Topspin. The SS-NMR spectra were measured by and processed in collaboration with NMR technician Dr. Kasper Enemark-Rasmussen.

## **Chapter 3.      Hydrolytic Dehydrogenation of Ammonia Borane**

---

In this chapter, I describe my work with Co nanoparticles encapsulated in nitrogen-doped porous carbon matrices derived from the thermal decomposition of ZIF-67 and ZIF-8 crystals. Here, ZIF-67 and ZIF-8 crystals were used as sacrificial templates and metal precursors to synthesize a range of modified catalysts. The synthesized catalysts have been characterized and tested in a hydrolytic dehydrogenation of ammonia borane. This chapter is based on the publication Zacho *et al.*<sup>42</sup> in *Catalysis Science and Technology* (2018).

---

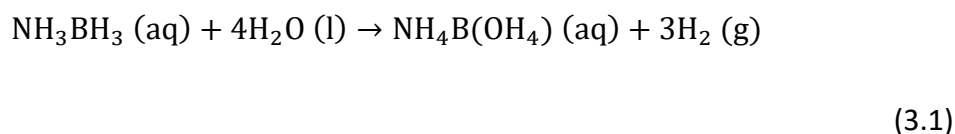


### 3.1 Introduction

The 2018 global CO<sub>2</sub> emissions from energy usage were once again at a record high, with a net increase of 2.0% from 2017-2018, the largest growth in seven years.<sup>66</sup> Recent articles built on data from 2019 stated that the CO<sub>2</sub> emissions again surpassed the preceding years. Although, the net increase of CO<sub>2</sub> emissions from 2018-2019 was reduced to a 0.6% increase.<sup>67</sup> The focus on strategies to decrease global CO<sub>2</sub> emissions has never been greater. The major sinner in the energy sector contributing to CO<sub>2</sub> emissions is fossil fuel consumption, which is why alternative clean energy strategies are in high demand. Several sources of clean energy have been developed and implemented, such as energy derived from solar cells and wind turbines.<sup>68</sup> Clean energy does contribute to a greater ratio of today's energy consumption, but in order to decrease CO<sub>2</sub> emissions and fulfill the market's need for energy, new alternatives are necessary to develop.

One promising future energy carrier is hydrogen (H<sub>2</sub>). H<sub>2</sub> has been proposed as a source to power fuel cells and produce electricity without the emission of greenhouse gases. H<sub>2</sub> has a high gravimetric energy density, but also a very low volumetric energy density. The interest in H<sub>2</sub> as an energy carrier is especially large in the automotive industry. However, in comparison to petroleum, H<sub>2</sub> is difficult to transport, handle and refuel. Two systems to store H<sub>2</sub> are promising in the current progressing research, physical-based systems and material-based systems.<sup>69–71</sup> The physical-based systems are the most mature, which include compressed, cryo-compressed and liquid H<sub>2</sub> storage. Nevertheless, the high pressures and cooling required in these systems are energy-intensive and can pose a safety threat. The safety concerns of the physical-based systems have led to further investigation of the material-based systems, which focus on storing H<sub>2</sub> under milder conditions. The material-based systems are categorized into solid-state storage (microporous materials, interstitial metal hydrides and complex hydrides) and chemical storage (liquid organics and chemical hydrogens).<sup>72</sup> In solid-state storage, the microporous materials are used as adsorbents for H<sub>2</sub> at ambient conditions. The interstitial metal hydrides have atomic H bound in the lattice and the complex hydrides have H<sub>2</sub> bound ionically or covalently in the structure. In chemical storage systems, chemical processes control the ability to store and release H<sub>2</sub>. The liquid organics stores H<sub>2</sub> in covalent C-H bonds and in the chemical hydrogens the H<sub>2</sub> is chemically bound within the material at ambient conditions, as in covalent N-H and B-H bonds.<sup>69</sup> The chemical hydrogens are particularly known for their incredible high H<sub>2</sub> densities. The focus in this part of my PhD dissertation has been on the commercially

available chemical hydrogen storage material, ammonia borane ( $\text{NH}_3\text{BH}_3$ ). The choice of ammonia borane is based on its high stability in air/water and its high volumetric/gravimetric density. Ammonia borane contains  $196 \text{ g kg}^{-1}$  or  $100\text{-}140 \text{ g l}^{-1} \text{ H}_2$ . When an efficient metal catalyst is applied to the hydrolytic dehydrogenation of ammonia borane, it is stoichiometrically possible to release three equivalents of  $\text{H}_2$ . The hydrolytic dehydrogenation reaction proceeds as written in Equation 3.1 with the addition of a metal catalyst to ammonia borane in water.<sup>73,74</sup>



As illustrated in Equation 3.1, the dehydrogenation of ammonia borane is producing a by-product. Methods to regenerate the by-products formed in the ammonia borane dehydrogenation back to ammonia borane require further development. Currently, one solution includes the addition of water, methanol and  $\text{LiAlH}_4/\text{NH}_4\text{Cl}$  as reducing agents to regenerate the by-products back to ammonia borane.<sup>75</sup> In this chapter of my PhD dissertation, I have focused on the development of a more efficient and stable catalyst for the hydrolytic dehydrogenation of ammonia borane. Literature reveals that heterogeneous catalysts investigated for the hydrolytic dehydrogenation of ammonia borane include catalysts with noble metal nanoparticles, base metal nanoparticles and multimetallic nanoparticles. The most active catalysts reported are the noble metal nanoparticle catalysts with Rh,<sup>76</sup> Pt,<sup>77</sup> Ru,<sup>78</sup> Ag,<sup>79</sup> and Pd<sup>80</sup> with TOFs reported up to  $2010 \text{ min}^{-1}$ .<sup>75</sup> However, as stated in Chapter 1, there are drawbacks such as the manufacturing cost and the scarcity of noble metals. The majority of base metal nanoparticle catalysts are holding nanoparticles of the more abundant metals, which include Ni,<sup>81</sup> Cu,<sup>82</sup> Co,<sup>83</sup> and Fe.<sup>84</sup> In multimetallic nanoparticle catalysts certain metal combinations can have synergistic effects, which increase their performance. However, the synthesis of these multimetallic catalysts is often complex, which is a disadvantage for scale-up and ultimately the cost. Due to the ferromagnetism of Ni, Co and Fe nanoparticles, these have been exploited as magnetic-separable catalysts. By using a ferromagnetic metal nanoparticle catalyst, the catalyst can be easily recovered from the liquid media using a permanent magnet.<sup>85–87</sup> As stated in Chapter 1, the metal incorporation within supports prepared by wet impregnation is not always resulting in a uniform quality and the metal nanoparticle size distributions can be difficult to reproduce. In general, a reproducible, simple catalyst synthesis in only a few steps is desired. Graphene supports have proved to be excellent supports for Co nanoparticles in the hydrolytic dehydrogenation of ammonia borane.<sup>88</sup> However, the synthesis of graphene often demands multiple steps

over several days.<sup>88–90</sup> The general complexity of current procedures to develop supported Co nanoparticle catalysts lead to my interest in the exploration of MOFs as sacrificial templates and metal precursors for the synthesis of new stable and simple synthesized catalyst for the hydrolytic dehydrogenation of ammonia borane. As specified in Chapter 1, MOFs can yield metal nanoparticles encapsulated in a porous carbon matrix upon thermal decomposition under inert atmosphere. The metal ions present in the MOFs are excellent precursors to form metal nanoparticles with a high dispersion. Zeolitic Imidazolate Frameworks (ZIFs), which are structures in a subclass of MOFs, are low-cost materials, which are simple to synthesize and modify to fit explicit desires. Examples of base metal containing ZIFs are ZIF-67 and ZIF-8, consisting of 2-methylimidazole and Co or Zn metal ions, respectively. It is also possible to impregnate the ZIF crystals with additional metals expanding their applications further. Examples of the utilization of ZIFs can be found in the creation of advanced carbon structures for electrochemistry purposes.<sup>24</sup> Here, the porosity of the carbon materials plays a key role for the catalytic activity. In this chapter, I will present a range of catalysts composed of Co nanoparticles in porous nitrogen-doped carbon matrices derived from the thermal decomposition of ZIF-67 and ZIF-8 crystals. Both ZIF-67 (Co) and ZIF-8 (Zn) have sodalite framework structures with 2-methylimidazole as the organic linker, which makes them isostructural. In the results and discussion part of this chapter, I will discuss the influence and choice of the temperature during synthesis and carbonization. Moreover, the influence of introducing Zn into the framework structure of ZIF-67, yielding a bimetallic hybrid (ZIF-67/8), will be discussed. Finally, parameters which can optimize the overall catalytic activity will also be included in the discussion.<sup>91,92</sup>

## **3.2 Experimental Details**

### **3.2.1 Material Preparations**

Reagents were acquired from a commercial source (Sigma-Aldrich), and used without additional purification. The reagents include: 2-methylimidazole (99%), cobalt(II) nitrate hexahydrate (99.9% trace metals basis), zinc(II) nitrate hexahydrate ( $\geq 99.0\%$ ), methanol (HPLC Plus,  $\geq 99.9\%$ ) and ammonia borane (97%).

### Synthesis of ZIF-67

The synthesis of ZIF-67 in methanol was modified from literature<sup>93</sup> and performed according to my previously published work Zacho *et al.*<sup>42</sup> 2-methylimidazole (3.244 g) and cobalt(II) nitrate hexahydrate (1.436 g) were each dissolved in 100 mL of methanol. Then the pink Co solution was transferred into the ligand solution. The solution was vigorously stirred for 12 min at the specific temperature (25°C or 60°C). The solution was left for 24 h at 25°C without stirring. The following day the purple product was collected by centrifugation (12000 rpm for 20 min), washed three times with methanol and dried at 80°C for 24 h. Based on the amount of Co, the yield of ZIF-67 was calculated to 75%.

### Synthesis of ZIF-67/8

The synthesis of the bimetallic hybrid ZIF-67/8 was prepared with a ratio of Co/Zn= 1. The synthesis was performed according to that of the pure ZIF-67, except for the incorporation of Zn into the framework. Thus, the difference was that the salt solution contained both zinc(II) nitrate hexahydrate (0.734 g) and cobalt(II) nitrate hexahydrate (0.718 g). The purple product was collected as stated above. The yield of ZIF-67/8 was calculated to 79%.

### Synthesis of Co/NC and CoZn/NC catalysts

The carbonizations of the synthesized ZIF-67 and ZIF-67/8 crystals were completed in a tube furnace under Ar atmosphere. The temperature was set to 700°C or 900°C for 2 h with a heating ramp of 5°C min<sup>-1</sup>. The names of the final catalysts were chosen according to the rough diameter size (nm) of the parent catalyst precursor, see Table 3.1.

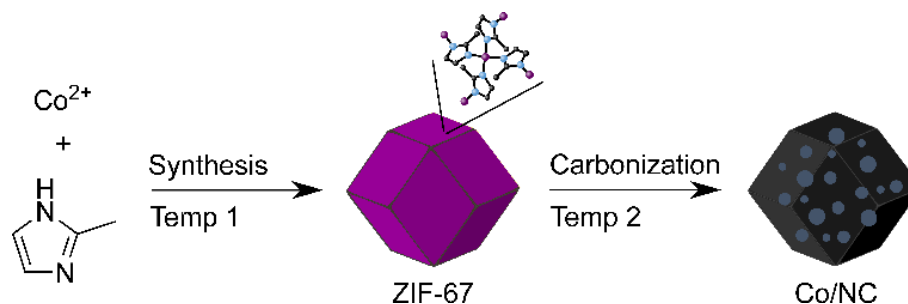


**Figure 3.1.:** A scheme of the synthesis procedure for ZIF-67 yielding a Co/NC catalyst.<sup>42</sup>  
Reproduced by the permission of The Royal Society of Chemistry.

### 3.2.2 Characterization Methods

In order to explain the catalytic performance of the catalysts, the prepared materials were characterized by multiple techniques. Atomic Absorption Spectroscopy (AAS) and XRF were used to determine the metal loadings. XRPD and N<sub>2</sub> physisorption were used to verify the crystal structure and determine the surface areas. SEM and TEM were used to identify the crystals' shape and size. Additionally, TEM was used to identify the Co nanoparticles average size and distribution. Finally, Thermal Gravimetric Analysis (TGA) was used to examine the thermal stability. TGA was done with a Mettler Toledo TGA/DSC 1 STAReSystem equipped with a GC100 STAReSystem Gas controller.

### 3.2.3 Catalytic Test Procedure

All catalysts were tested in an automated gas burette setup equipped with a pressure transducer. Here, the 250 mL burette, point **1** in Figure 3.2, made it possible to follow the displacement of a light silicon oil when H<sub>2</sub> gas was released.<sup>94</sup> An excess amount of silicon oil was kept in the working fluid reservoir, point **2**. In order to ensure that the oil would not reach the reaction compounds in the round-bottomed flask, an oil trap was installed, point **3**. During each experiment, LabView was used to control the setup and collect the data obtained from the pressure transducer point **4** and the thermocouple point **5**. LabView was used to record the change in pressure of the system upon release of H<sub>2</sub>. In each experiment, 10-20 mg of catalyst was added to the round-bottomed flask with a magnet, point **6**. The flask was sealed with a septum and connected to the gas burette system. Then through the septum, the solution of 50 mg ammonia borane in 10 mL water was injected quickly with a syringe to the prepared catalyst. No addition of NaBH<sub>4</sub> was performed, which is a common necessary procedure to activate several catalysts found in the literature.<sup>83,88,95</sup> The reactions were primarily stirred at room temperature with a magnetic stirrer, except for the temperature influence study. Here, an oil bath was used for heating. The data were collected continuously. The calibrations were made with a mass flow controller and the calculations of the released H<sub>2</sub> were based on the linear calibration lines.

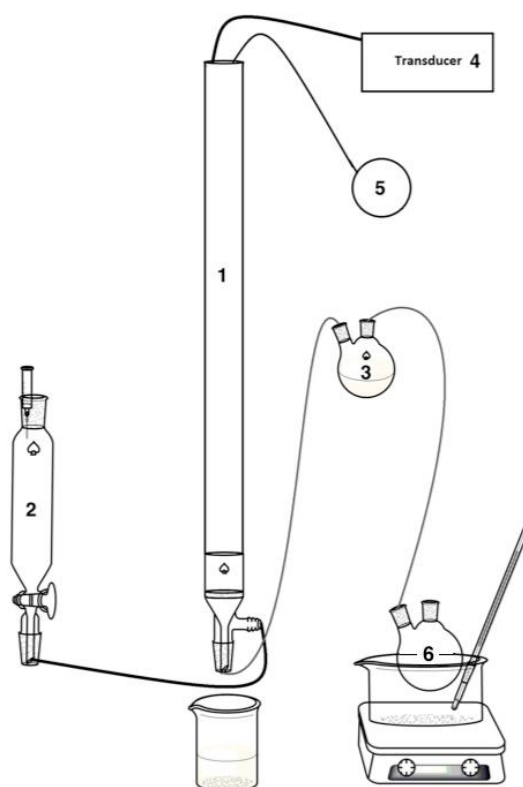


**Figure 3.2.:** *The automated gas burette system.*

### 3.3 Results and Discussion

#### 3.3.1 AAS and XRF

Table 3.1 provides an overview of the synthesized materials, both precursors and derived catalysts, and at which temperatures they were prepared. Temp 1 is the temperature the precursor ZIFs were synthesized at, and Temp 2 is the temperature the ZIFs were carbonized at in order to yield the derived catalysts. The high carbonization temperature of entry 4, ZIF-67/8-50, was chosen based on the boiling point of Zn at 907°C. Thus, this temperature was selected to ensure the removal of Zn from the framework by evaporation. The metal loadings were quantified from AAS and XRF, where standards of known Co concentrations were used to prepare a calibration line. The loadings of entry 1-2, Co/NC-500 and Co/NC-300, were 18 wt% Co. The metal loading of entry 3, CoZn/NC-50, was 4 wt% Co and for entry 4, Co/NC-50, it was 8 wt% Co. The difference in these metal loadings can be explained by the presence of Zn, which

remained in the CoZn/NC-50 catalyst, thus a lower Co wt% was obtained. XRF was used to verify the successful removal of Zn in Co/NC-50. Here, no peaks were present at a binding energy 8.6 and 9.6 keV, which is characteristic for  $K\alpha_1$  and  $K\beta_1$  of Zn, respectively. Additionally, XRF was used to verify the presence of Co at energies of 6.9 and 7.6 keV for all the prepared catalysts.

**Table 3.1.:** Overview of the prepared materials

Entry	Temp 1	Precursor <sup>a</sup>	Temp 2	Catalyst <sup>a</sup>
1	60°C	ZIF-67-500	750°C	Co/NC-500
2	25°C	ZIF-67-300	750°C	Co/NC-300
3	25°C	ZIF-67/8-50	750°C	CoZn/NC-50
4	25°C	ZIF-67/8-50	900°C	Co/NC-50

<sup>a</sup> The prepared materials are named according to the rough size of the parent crystals (denoted in nm).

### 3.3.2 XRPD

The diffraction patterns from the XRPD analysis of the precursor materials ZIF-67-500, ZIF-67-300 and ZIF-67/8-50 are presented in Figure 3.3. The diffraction patterns verified the characteristic ZIF-67 sodalite structure for all three materials. The prominent peaks of ZIF-67 were clear and well-resolved at the characteristic diffraction angles of  $2\theta$  equal  $7^\circ$  (001),  $13^\circ$  (112) and  $18^\circ$  (222).<sup>96,97</sup>

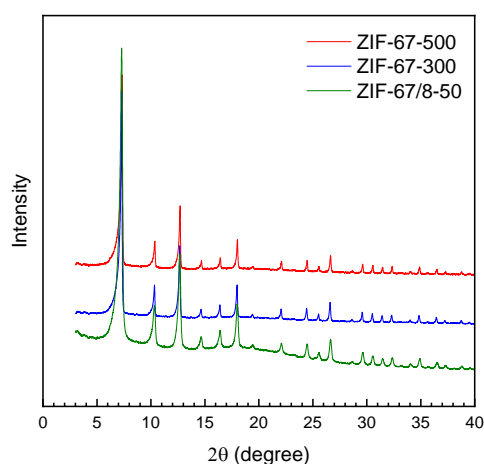


**Figure 3.3.:** The diffraction patterns of the prepared ZIF precursor materials.

The diffraction patterns of the corresponding catalysts after carbonization of the ZIF precursor materials can be seen in Figure 3.4. These catalysts include Co/NC-500, Co/NC-

300 and CoZn/C-50 carbonized at 750°C, as well as Co/NC-50 at 900°C. The diffraction patterns confirmed the full thermal decomposition of the crystalline ZIF structures. The patterns showed a broad diffraction band at 20° (002), which was attributed to graphitic carbon present in the amorphous carbon supports. It was expected that the graphitic carbon derived from Co-catalyzed carbon during the carbonization step.<sup>96,98</sup> Additionally, three peaks were visible at 2 $\theta$  degrees of 44° Co(111), 52° Co(200) and 75° Co(220).<sup>96</sup> These positions confirmed the presence of face-centered cubic Co nanoparticles in the prepared catalysts. In the diffraction pattern of CoZn/NC-50 carbonized at 750°C an additional peak could be seen at 42°, which was attributed Zn(101), providing evidence of the presence of Zn in the catalyst. However, the peaks were relatively weak. Therefore, determination of the average particle size by line-broadening analysis was not conducted.

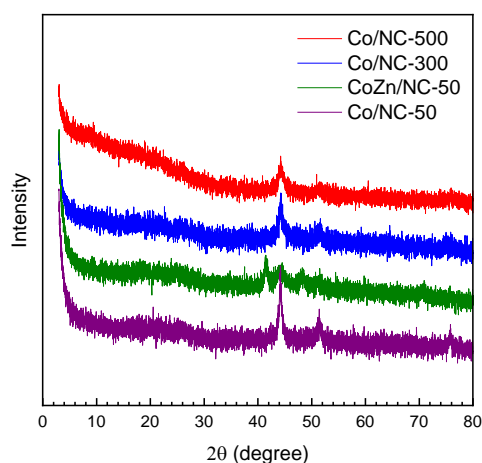


**Figure 3.4.:** *The diffraction patterns of the prepared catalysts after carbonization.*

### 3.3.3 N<sub>2</sub> Physisorption

The isotherms of the ZIF precursor materials, ZIF-67-500, ZIF-67-300 and ZIF-67/8-50 are presented in Figure 3.5. The isotherms were of Type I, which are typical for microporous materials such as MOFs.<sup>91</sup> ZIF-67 and ZIF-8 typically have average pore sizes of 0.34 nm.<sup>25</sup> ZIF-67-300 absorbed most N<sub>2</sub> at low relative pressures, which indicates that it had a higher content of micropores than ZIF-67-500. This was a result of the lower synthesis temperature 25°C vs. 60°C influencing the properties of the ZIF crystals. The isotherm of ZIF-67/8-50 revealed even less absorption of N<sub>2</sub> at low relative pressures. This lower micropore volume of the bimetallic ZIF-67/8-50 is attributed the partial substitution of Co by Zn in the framework, as Zn has a higher atomic weight. Additionally, ZIF-67/8-50



had increased absorption of  $N_2$  at high relative pressures. This higher mesopore volume can be attributed interparticle porosity between the small crystals.

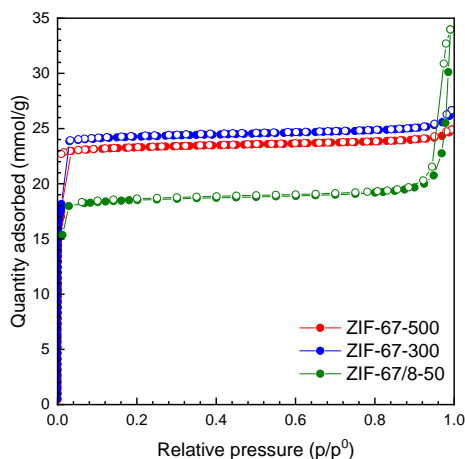


**Figure 3.5.:**  $N_2$  physisorption isotherms of the prepared ZIF precursor materials.

The isotherms of the resulting catalysts after carbonization of the ZIF precursor materials, Co/NC-500, Co/NC-300, CoZn/NC-50 and Co/NC-50, can be seen in Figure 3.6. The isotherms held characteristics of both Type I and IV, which indicates a combination of micropores and mesopores present in the catalysts.<sup>85</sup> Additionally, the isotherms possessed hysteresis due to delayed capillary condensation. Here, the H1 Hysteresis loop is typical in isotherms of materials having mesopores larger than  $\sim 4$  nm, see Figure 3.6 for pore size distributions.<sup>93</sup> The Hysteresis loop was largest for CoZn/NC-50 and Co/NC-50 implying an increased content of mesopores. The pore size distributions of Co/NC-500 and Co/NC-300 indicate that the majority of the pores was around 45 nm. The pore size distributions of CoZn/NC-50 and Co/NC-50 indicate that the majority of the pores was around 25 nm. However, the presence of pores around 3.5 nm applies to all four catalysts.

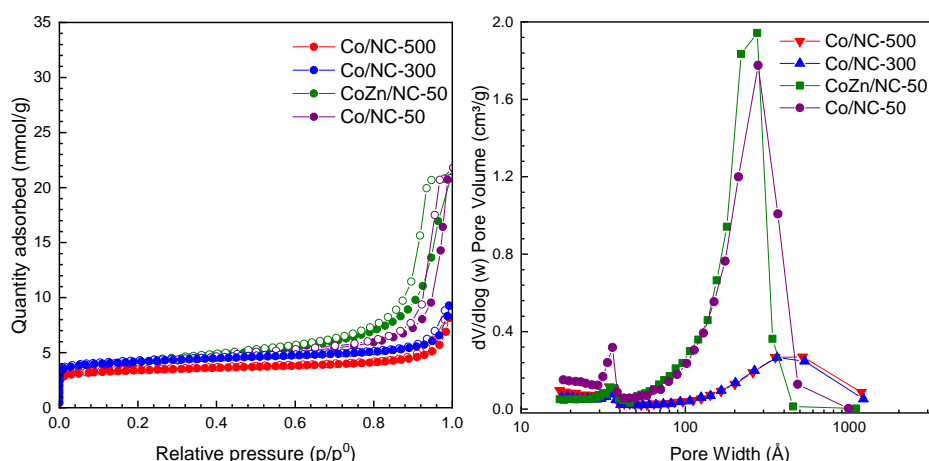


**Figure 3.6.:** (Left)  $N_2$  physisorption isotherms and (right) Pore size distributions of the prepared catalysts after carbonization of the ZIF precursor materials.

Table 3.2 presents the  $N_2$  physisorption analysis data. All ZIF structures, entries 1-3, showed a consistent trend of high specific surface areas (1379-1951  $m^2/g$ ). These specific surface areas were in agreement with the work presented by Zhang *et al.*<sup>99</sup> The relatively lower specific surface area ( $m^2/g$ ) of ZIF-67/8-50 was attributed the higher atomic weight of Zn. The thermal decomposition of the ZIFs resulted in a significant decrease in the resulting specific surface areas. This was a result of the great loss in ordered microporosity of the crystalline ZIFs upon thermal decomposition. Nevertheless, the specific surface areas of the derived carbon catalysts retained relatively high specific surface areas (290-356  $m^2/g$ ).

**Table 3.2.:** Overview of the data from  $N_2$  physisorption analysis.

Entr y	Material	$S_{BET}^a$ ( $m^2/g$ )	$S_{ext}^b$ ( $m^2/g$ )	$V_{micro}^b$ ( $cm^3/g$ )	$V_{tot}^d$ ( $cm^3/g$ )
1	ZIF-67-500	1951	67	0.779	0.842
2	ZIF-67-300	1848	72	0.811	0.884
3	ZIF-67/8-50	1379	90	0.603	0.719
4	Co/NC-500	290	74	0.085	0.210
5	Co/NC-300	356	96	0.103	0.233
6	CoZn/NC-50	335	179	0.065	0.423
7	Co/NC-50	312	184	0.058	0.482

<sup>a</sup> Specific surface area determined by the BET method, <sup>b</sup> external surface area and micropore volume determined by the t-plot method and <sup>d</sup> total pore volume determined by a single point read at  $p/p^0=0.95$ .

### 3.3.4 SEM

Representative SEM images of the prepared materials can be seen in Figure 3.7(a-f), the ZIF precursor materials (top) and the derived catalysts (bottom). From the SEM images of ZIF-67-500 and ZIF-67-300 the typical rhombic dodecahedral shape of ZIF-67 was visible, see Figure(a-b). Despite the relatively low resolution in SEM, the effect of the synthesis temperature on the ZIF-67 crystals was visible in these images, where different crystal sizes could be observed. Here, the ZIF-67 prepared at 60°C had average crystal sizes of 500 nm in diameter, whereas the ZIF-67 prepared at 25°C had sizes of 300 nm in diameter, see Figure 3.7(a-b), respectively. It is known that ZIF-8 possess the same framework as ZIF-67, but with a smaller average crystal size down to 50 nm in diameter.<sup>100</sup> Thus, by addition of  $\text{Zn}(\text{NO}_3)_2$ , the resulting bimetallic ZIF-67/8 had an average crystal size of only 50 nm, Figure 3.7(c). This will be clear from the high resolution TEM images in the following section, which illustrates single ZIF crystals at nanometer scale. The SEM images further revealed that after carbonization of the ZIF precursor materials, the Co/NC-500 and Co/NC-300 partly preserved the rhombic dodecahedral shape, though the structures shrunk and became more concave. Figure 3.7(f) revealed that the particles of CoZn/NC-50 agglomerated together in large aggregates. The same applied to Co/NC-50, which had a similar tendency, see Appendix A. Thus, the rhombic dodecahedral shape could not be identified in the bimetallic derived catalysts, which was speculated to be a consequence of the 50 nm small structures. This proved, that a minor change in the temperature could affect the resulting ZIF crystal sizes and the derived catalyst. A similar example from literature by Zou *et al.*<sup>93</sup> reported that by changing the solvent in the ZIF synthesis from methanol to water they could increase the ZIF crystal size. ZIFs are thus very dependent on the synthesis conditions, which also include alterations in the concentration of the reagents and dilution of the synthesis solution.<sup>25</sup>

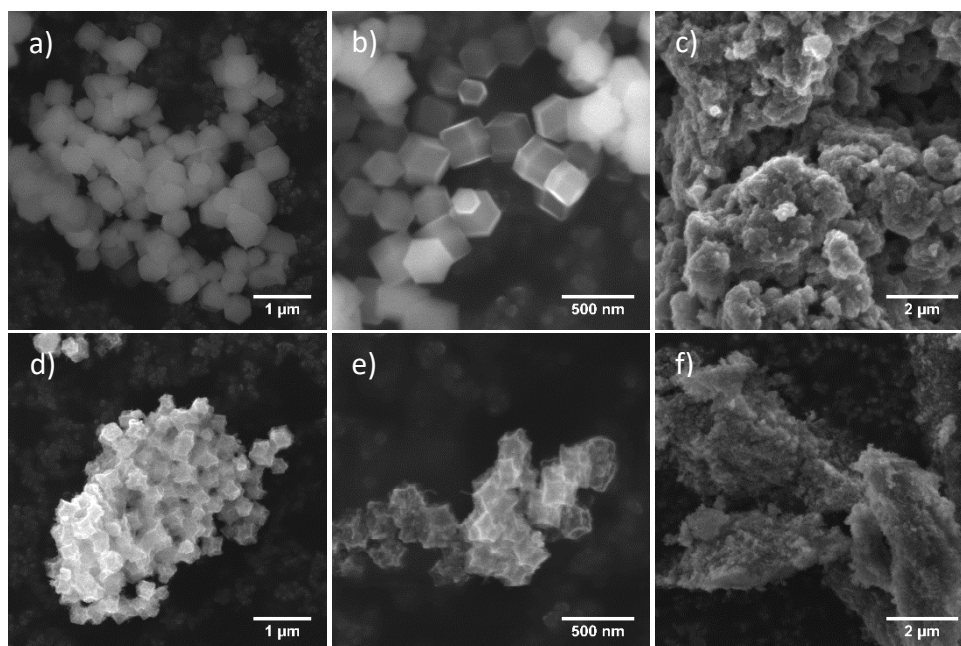


**Figure 3.7.:** SEM images of a) ZIF-67-500, b) ZIF-67-300, c) ZIF-67/8-50, d) Co/NC-500, e) Co/NC-300 and f) CoZn/NC-50.<sup>42</sup> Reproduced by the permission of the Royal Society of Chemistry.

### 3.3.5 TEM and TGA

Figure 3.8(a-c) and Figure 3.9(a-f) show representative TEM images of the prepared ZIF precursor materials and the derived catalysts, respectively. From the high resolution images obtained with TEM, single uniform crystals of ZIF-67 and ZIF-67/8 with the characteristic rhombic dodecahedral shapes were revealed. A large number of TEM images were acquired to determine the average crystal sizes of the ZIFs, which as mentioned previously, were used to name the materials. The average diameters of the crystals were in good agreement with the results obtained by SEM. From the TEM images in Figure 3.8(a-c), the crystal sizes can be clearly seen for ZIF-67-500 (500 nm), ZIF-67-300 (300 nm) and ZIF-67/8-50 (50 nm).

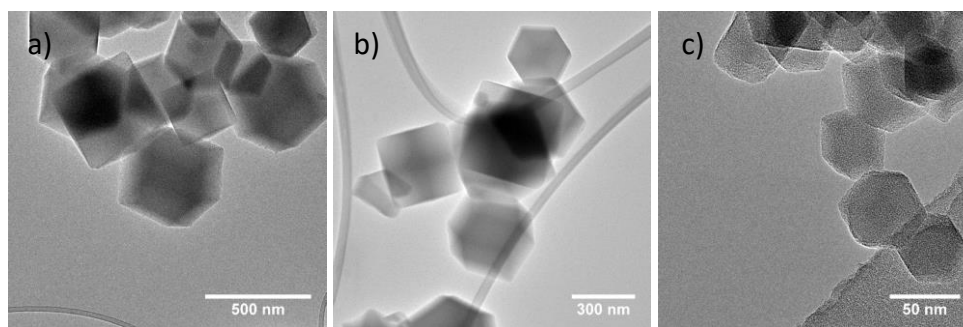


**Figure 3.8.:** TEM images of a) ZIF-67-500, b) ZIF-67-300 and c) ZIF-67/8-50.<sup>42</sup>  
 Reproduced by permission of The Royal Society of Chemistry.

The TEM images of the derived catalysts showed a high dispersion of Co nanoparticles, visible as dark spots due to the high atomic weight of Co, throughout the porous carbon supports, see Figure 3.9(a-f). The high dispersion of Co was noteworthy taking the high metal loadings of the carbon supports into account. Here, literature suggests that the pyridinic N in the carbon matrix might have an influence on the Co nanoparticles formed during carbonization, preventing agglomeration.<sup>25</sup> The Co nanoparticles in Co/NC-500 and Co/NC-300 were well-dispersed and in the range of 5-25 nm in diameter. The Co nanoparticles in CoZn/NC-50 and Co/NC-50 were significant smaller in the range of 5-15 nm, which was in accordance to the lower Co loading. The Co metal ions in the bimetallic ZIF-67/8-50 crystals had increased separation and spatial isolation due to the presence of Zn in the framework, which acted as a barrier expanding the interatomic distances. This could be a reason for the limited sintering of the Co nanoparticles in the Co/NC-50 catalyst, which was carbonized at a relatively high temperature.<sup>96</sup> The introduction of  $\text{Zn}(\text{NO}_3)_2$  to ZIF-67 made it possible to control the particle size of the ZIF crystals, the metal loading, and hence the resulting average Co nanoparticle size distribution. An apparent example was seen with the reference materials ZIF-67-500 and ZIF-67-300, carbonized at a high temperature of 900°C, which in the absence of Zn and the exposure to high temperatures resulted in increased sintering with Co nanoparticles at an average size of 100 nm in diameter, see Figure 3.9(e-f). Based on this observation, further optimization of the carbonization procedure might result in even smaller Co nanoparticles. However, a carbonization temperature of 750°C was chosen based on TGA experiments of the ZIF structures performed in Ar, see Figure 3.10(left). Here, decomposition of the ZIF structure started around 550°C, which means the carbonization was likely required to be carried out above this temperature. A required carbonization temperature above 550°C to decompose the ZIFs was in agreement with the work done by Li *et al.*<sup>96</sup> The graphitic carbon peaks, which were present in the

diffraction patterns of the catalysts could be verified with the TEM images. The TEM images showed visible carbon nanotubes protruding from the catalysts, which are pointed out for Co/NC-50 in Figure 3.9(d) and in Appendix A with a close-up TEM image. An additional TGA experiment of Co/NC-50 in air is shown in Figure 3.10(right). Here, the catalyst was stable up to 260°C in air.

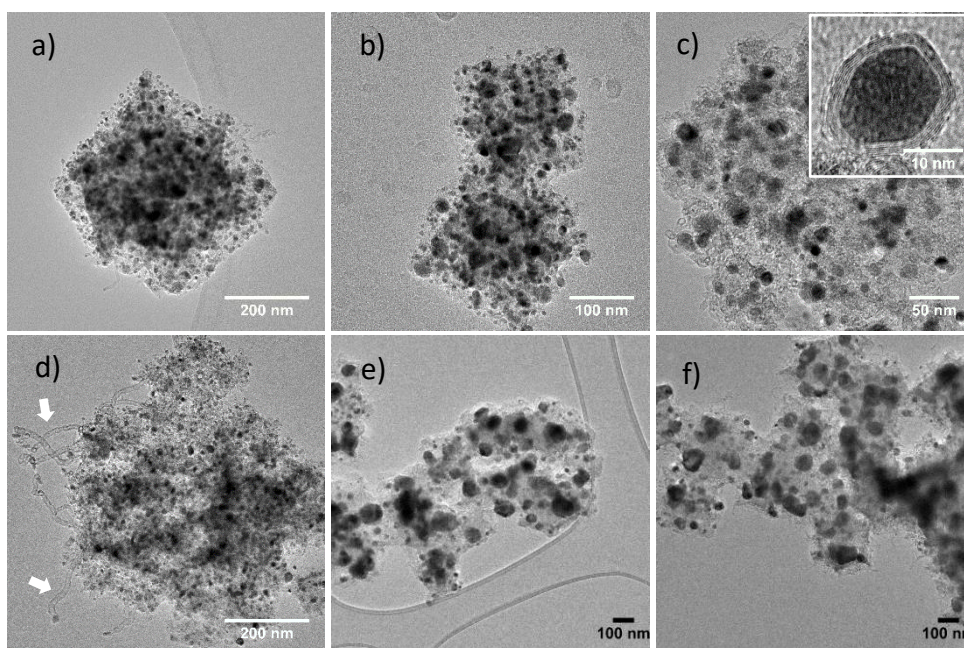


**Figure 3.9.:** TEM images of a) Co/NC-500, b) Co/NC-300, c) CoZn/NC-50, d) Co/NC-50, e) Co/NC-500 carbonized at 900°C and f) Co/NC-300 carbonized at 900°C.<sup>42</sup>

*Reproduced by permission of The Royal Society of Chemistry.*

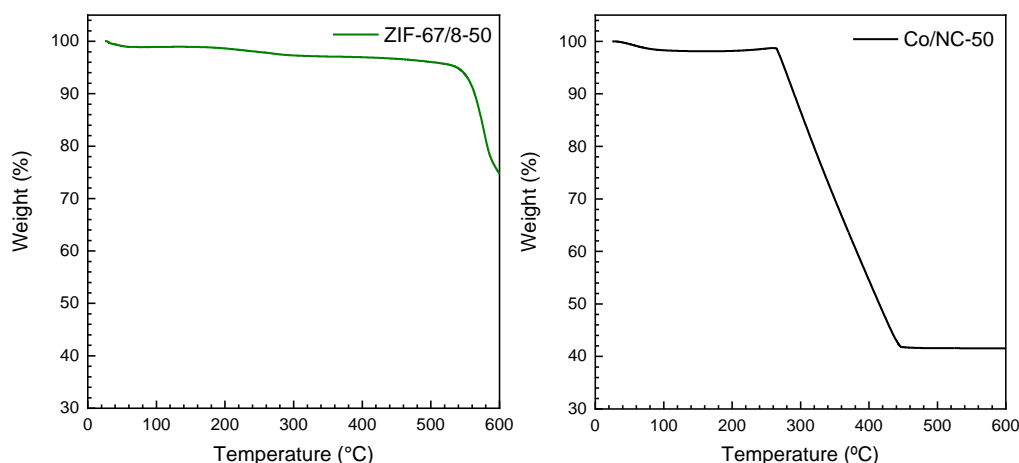


**Figure 3.10.:** (Left) TGA curve of ZIF-67/8-50 in Ar (600°C, 2h) and (right) Co/NC-50 in air (600°C, 2h) with a ramp of 5°C min<sup>-1</sup>.

### 3.3.6 The Hydrolytic Dehydrogenation of Ammonia Borane

Figure 3.11 shows the H<sub>2</sub> evolution curves for the different materials. The H<sub>2</sub> evolution curves show the volume of released H<sub>2</sub> from the catalytic hydrolytic dehydrogenation of ammonia borane, with volume of H<sub>2</sub> released (mL) as a function of time (min). For comparison of the catalytic activity, Table 3.3 compiles the TOFs (min<sup>-1</sup>) calculated from the initial rate and the Co loading (mol H<sub>2</sub> per mol Co min<sup>-1</sup>). From the TOFs it is noteworthy that Co/NC-500 had a lower TOF of 1.1 min<sup>-1</sup> in comparison to Co/NC-300 with a TOF of 2.7 min<sup>-1</sup>. Since the average Co nanoparticles size distribution were comparable (5-25 nm), the increased activity could be credited to the higher specific surface area and the pore volume of Co/NC-300. Moreover, the average particle size of the Co/NC-300 catalyst was lower, thus the diffusion path length in this material was shorter. This means that the diffusion of the reactants to the active sites was enhanced. This demonstrates how the crystal size of the parent ZIF precursor had an influence on the resulting catalyst structure and thus the overall catalytic activity. Recently, Zou *et al.*<sup>93</sup> reached similar conclusions for the oxygen reduction reaction. Table 3.3 entry 1-2 show that only 2.4-2.5 equivalents of H<sub>2</sub> out of 3.0 were released with Co/NC-500 and Co/NC-300. Although this is less than what is stoichiometric possible, it is still in the range of other base metal catalysts.<sup>75,95,101</sup> In comparison, the reference materials carbonized at 900°C possessed lower overall catalytic activities, as a result of the vastly agglomerated Co nanoparticles, Figure 3.11(right). Here, the reference catalysts were only able to release 1.15 equivalents of H<sub>2</sub>. The bimetallic CoZn/NC-50 catalyst had a low activity with a TOF of 1.8 min<sup>-1</sup> in comparison to Co/NC-50, which had the highest activity

with a TOF of  $7.6 \text{ min}^{-1}$ . The low activity of CoZn/NC-50 was speculated to be caused by limited diffusion due to blockage of the active Co sites or by the formation of an inactive CoZn alloy. The Co/NC-50 catalyst was able to release 2.9 equivalents of  $\text{H}_2$ , which was close to the maximum stoichiometric value of 3.0, corresponding to a yield of 97%. The results derived from the hydrolytic dehydrogenation of ammonia borane provided evidence that an improved catalytic performance could be achieved with a catalyst derived from a bimetallic ZIF-67/8 precursor. However, it was important that Zn was successfully removed by carbonization at  $900^\circ\text{C}$ .

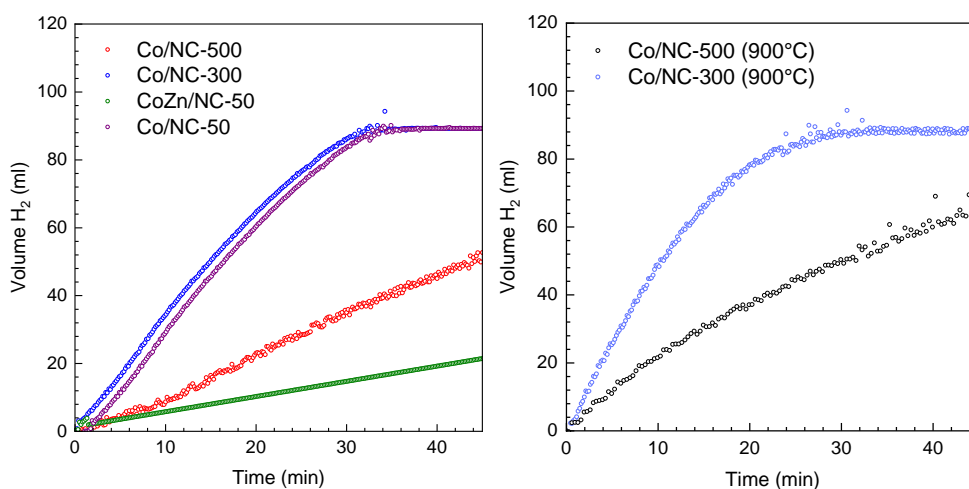


**Figure 3.11.:** Volume of released  $\text{H}_2$  for the hydrolytic dehydrogenation of ammonia borane at  $25^\circ\text{C}$ , (left) using 20 mg catalyst and (right) using 20 mg of reference catalysts Co/NC-300 and Co/NC-500 carbonized at  $900^\circ\text{C}$ .

**Table 3.3.:** Overview of the results from the catalytic dehydrogenation of AB.

Entry	Catalyst	Co wt% <sup>a</sup>	AB/Co <sup>b</sup>	$\text{H}_2/\text{AB}^b$	TOF <sup>c</sup> ( $\text{min}^{-1}$ )
1	Co/NC-500	18	26	2.4	1.1
2	Co/NC-300	18	26	2.5	2.7
3	CoZn/NC-50	4	60	2.7	1.8
4	Co/NC-50	8	126	2.9	7.6

<sup>a</sup> Determined by atomic absorption spectroscopy (AAS). <sup>b</sup> AB= ammonia borane (mol/mol). <sup>c</sup> TOF= turnover frequency (mol  $\text{H}_2$  per mol Co  $\text{min}^{-1}$ ).

As mentioned earlier, high TOF values have been reported with Co nanoparticles supported on graphene (Co/graphene of  $13.9 \text{ min}^{-1}$ )<sup>88</sup> and graphene oxide modified by polyethylenimine (Co/PEI-GO of  $39.9 \text{ min}^{-1}$ ).<sup>83</sup> In both cases  $\text{NaBH}_4$  was required to



activate the catalysts and upon recycling the catalysts suffered from severe deactivation. After five runs, only 60-65% of the initial catalytic activity was retained in the two cases from the literature. Figure 3.12(left) shows the hydrogen evolution curve of Co/NC-50 over five runs, which show a slight decrease in activity, see Appendix B for an image of the Co/NC-50 catalyst collected by a permanent magnet. However, with a TOF of 6.3  $\text{min}^{-1}$  after the fifth recycling, the catalyst impressively retained 83% of its initial catalytic activity. The TEM images of the five times recycled Co/NC-50 catalyst can be seen in Figure 3.12(middle and right). The deactivation could originate from particle aggregation and oxidation of the surface.<sup>102</sup> Wang *et al.* has investigated the use of Co nanoparticles in porous nitrogen-doped carbon materials obtained by the thermal decomposition of Co(salen) under Ar atmosphere for the hydrolytic dehydrogenation of ammonia borane.<sup>95</sup> Their best performing catalyst, which was the most comparable catalyst to this work, obtained a TOF of 5.6  $\text{mol H}_2$  per  $\text{mol Co min}^{-1}$ . They reported successful catalyst recycling up to 10 times.

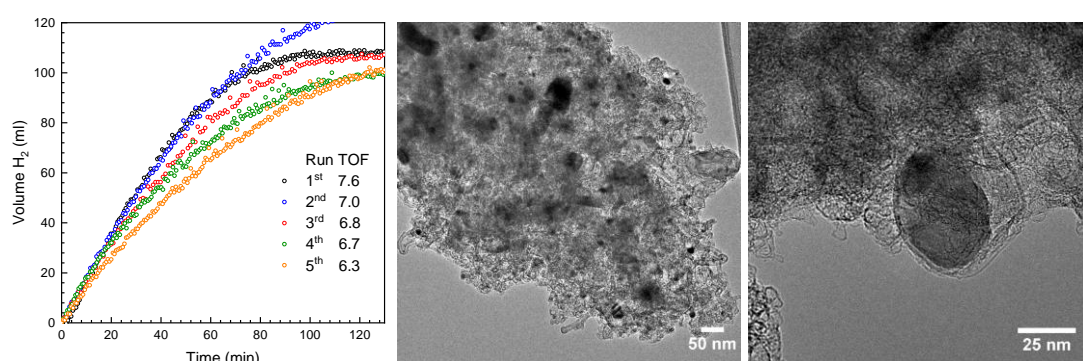


**Figure 3.12.:** (Left) volume of released  $\text{H}_2$  for the hydrolytic dehydrogenation of ammonia borane at 25°C using 10 mg of Co/NC-50 catalyst for five recycle tests. The TOFs are reported in  $\text{mol H}_2$  per  $\text{mol Co min}^{-1}$ . (Middle and right) TEM images of five times recycled Co/NC-50.<sup>42</sup> Reproduced by permission of The Royal Society of Chemistry.

A temperature study was performed with Co/NC-50 to illustrate the temperature's effect on the catalytic activity at 25-50°C, see Figure 3.13(left). The initial reaction rate was highly dependent on the temperature. All three equivalents of  $\text{H}_2$  were released within 25 min at a temperature  $\geq 45^\circ\text{C}$ . The corresponding Arrhenius plot can be seen in Figure 3.13(right) with a calculated activation energy of  $E_a$  44.9  $\text{kJ mol}^{-1}$ , calculated from the slope of the linear fit. Activation energies in the range of 38-67  $\text{kJ mol}^{-1}$  have been reported by Yang *et al.*<sup>73</sup> placing the Co/NC-50 in the better end of the given activation energies.

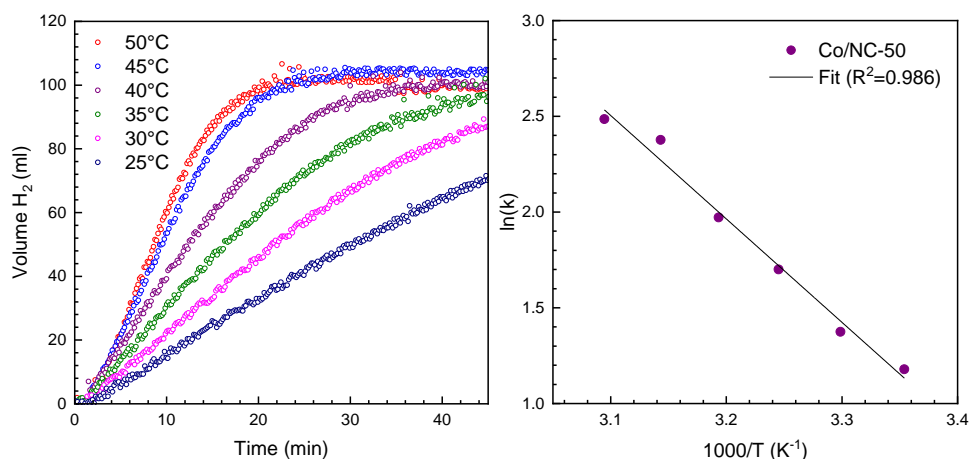


**Figure 3.13.:** (Left) a temperature study with increasing temperature from 25-50°C and (right) the resulting Arrhenius plot.

Finally, further improvement of the catalytic activity was achieved by addition of base in accordance to previous studies.<sup>91</sup> The reaction was run in NaOH or KOH (0.1M) with the best performing catalyst Co/NC-50 present. The addition of a base resulted in an increased reaction rate and a TOF of 11.0 min<sup>-1</sup> in KOH and a TOF of 12.7 min<sup>-1</sup> in NaOH, see Figure 3.14. Wang *et al.*<sup>91</sup> suggested based on a mechanistic study that this increase in activity was a result of increased electron density around the metal surface deriving from OH<sup>-</sup> electron donation, which in the end facilitated interactions with ammonia borane.

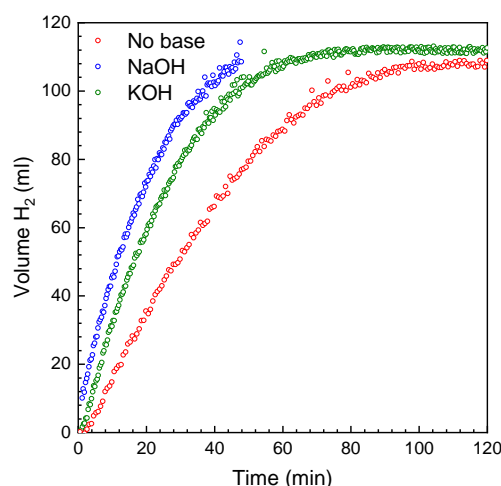


**Figure 3.14.:** *Volume of released  $H_2$  for the hydrolytic dehydrogenation of ammonia borane at 25°C using 10 mg of catalyst Co/NC-50 with the addition of 0.1M KOH or NaOH.*

### 3.4 Summary

Chapter 3 was based on my publication in *Catalysis Science & Technology*,<sup>42</sup> where the purpose was to synthesize a stable base-metal nanoparticle catalyst for the hydrolytic dehydrogenation of ammonia borane. To accomplish this, I exploited ZIF-67 as a sacrificial template and metal precursor for the synthesis of Co nanoparticles in a porous nitrogen-doped carbon matrix. Several alterations in the catalyst preparations were performed, in order to control the structural features of the catalysts. Moreover, the effect of these alterations on the catalytic performance was investigated. The ZIF precursors were modified by a change in the synthesis temperature (25°C and 60°C) and subsequent carbonization temperature (750°C and 900°C) to obtain a range of different catalysts. It was found that an alteration in the synthesis temperature could change the size of the ZIF precursor crystals and the subsequent catalyst particles formed. Here, a temperature of 25°C provided 300 nm in diameter ZIF-67 crystals and 60°C provided 500 nm in diameter ZIF-67 crystals. After the carbonization of the ZIF-67 crystals, the catalyst particles retained part of the distinctive rhombic dodecahedral shape. Introducing  $Zn(NO_3)_2$  to the synthesis of the ZIF-67 crystals formed bimetallic ZIF-67/8 crystals with a resulting lower average size of 50 nm in diameter. These derived catalyst particles formed large undefinable agglomerates, where the shapes were not distinguishable.

The ZIF-67 crystals were carbonized at 750°C based on data from TGA experiments. In order to investigate the effect of the carbonization temperature, two reference catalysts carbonized at 900°C were prepared. These reference catalysts suffered from severe Co nanoparticles agglomeration. However, with the ZIF-67/8 crystals it was different, since a carbonization temperature of 900°C was required to remove Zn. Even after being exposed to such a high carbonization temperature, the resulting Co/NC-50 catalyst preserved a good Co nanoparticle dispersion and a low size distribution of 5-15 nm in diameter. In total six catalysts were tested in the hydrolytic dehydrogenation of ammonia borane, where two of these included the reference catalysts. It was concluded that the average particle size of the Co nanoparticles and the structural features of the carbon support had a significant effect on the catalytic activity. The highest catalytic activity was acquired with the bimetallic ZIF-67/8 derived catalyst Co/NC-50. The catalyst, Co/NC-50, was able to yield a TOF of 7.6 mol H<sub>2</sub> per mol Co min<sup>-1</sup> with an apparent  $E_a = 44.9 \text{ kJ mol}^{-1}$  at ambient conditions. Moreover, the catalyst could retain 83% of its initial catalytic activity after the 5<sup>th</sup> recycling. Finally, further optimization of the catalytic activity was possible by addition of a base to the reaction mixture, either 0.1M KOH (TOF = 11.0 min<sup>-1</sup>) or 0.1M NaOH (TOF = 12.7 min<sup>-1</sup>). Hopefully, these results can inspire to the synthesis of novel heterogeneous catalyst deriving from MOFs used as sacrificial metal precursors. Moreover, I hope that these results can bring knowledge about how different alterations of MOFs influence the overall catalytic activity in dehydrogenations and contribute in the current development of future alternative energy technologies.



## Chapter 4. Carbon Monoxide Oxidation

---

In this chapter, I describe my work with  $\text{Co}_3\text{O}_4$  nanoparticles encapsulated in mesoporous metal oxide shells defined as nanorattle catalysts. These catalysts derived from thermal treatments of ZIF-67 and ZIF-8 crystals, which were used as sacrificial templates and metal precursors. A variety of catalysts with controlled properties were prepared, which have been characterized and tested in a carbon monoxide oxidation reaction. This chapter is based on two of the publications Zacho *et al.*<sup>1</sup> from *Catalysis Communications* (2019) and Zacho *et al.*<sup>43</sup> from *Topics in Catalysis* (2019).

---

## 4.1 Introduction

Toxic pollutants such as carbon monoxide (CO), hydrocarbons (HCs) and nitrogen oxides (NO<sub>x</sub>) are emitted from automotive engines upon incomplete combustion.<sup>3</sup> These toxic compounds are both harmful to human health and to the environment. Motor vehicle exhaust accounts for around 90% of CO emissions in high traffic-congested cities.<sup>103</sup> Especially, the high level of CO emitted to the atmosphere represents a severe problem. Therefore, a variety of techniques have been developed to remove CO from motor vehicle exhaust, with the most effective being catalytic oxidation. Here, CO is catalytically oxidized to CO<sub>2</sub> at the exhaust outlet of an automotive engine by using a catalytic converter, a three-way-catalyst (TWC), see Equation 4.1.



Currently, 99% of CO emissions from automobile exhaust can be removed with a TWC.<sup>103</sup> The TWC targets all three main pollutants, which in addition to CO includes oxidation of HCs to CO<sub>2</sub> and reduction of NO<sub>x</sub> to N<sub>2</sub> plus additional water. The catalytic oxidation is performed by the use of a noble metal catalyst, which most often is Pt, Pd and Rh based.<sup>104,105</sup> However, as stated in Chapter 1, due to scarcity and high manufacturing cost of noble metal catalysts, the use of the more abundant base metals are studied as alternative metal catalysts. Examples from literature show that efficient oxidation of CO can be achieved with catalysts composed of metal oxides from base metals, such as FeO<sub>x</sub>, CoO<sub>x</sub>, NiO and CuO<sub>x</sub>.<sup>106</sup> The catalysts are typically comprised of nanoparticles on different supports, such as SiO<sub>2</sub>, ZrO<sub>2</sub>, CeO<sub>2</sub> or TiO<sub>2</sub>.<sup>107,108</sup> However, these catalysts often suffer from increased nanoparticle sintering at high temperatures, which results in the loss of their unique properties.<sup>103,109</sup> Thus, the development of sinter-stable base metal oxide catalysts for CO oxidation is of great interest.

A variety of advanced nanomaterial catalysts can be synthesized of different metal and metal oxide nanoparticles encapsulated within a hollow, yolk(multi)shell or nanorattle type structure.<sup>11,110</sup> These are often prepared from hard<sup>111</sup> or soft templates.<sup>112–114</sup> CO oxidation has been studied as a model reaction by advanced nanomaterial catalysts in order to create a sinter-stable solution. Here, CO oxidation is an excellent model reaction to prove the concept of encapsulation.<sup>11</sup> In literature, a range of highly sinter-stable catalysts have already been synthesized by sophisticated methods. These

catalysts are primarily noble metal nanoparticles encapsulated in hollow structures, such as Au nanoparticles encapsulated in hollow structures of  $\text{SiO}_2$ ,  $\text{ZrO}_2$  and  $\text{TiO}_2$ .<sup>115,116</sup> However, the synthesis methods are often sophisticated with multiple steps and expensive reagents. Furthermore, these methods struggle with obtaining uniform materials in high yields. In the synthesis of yolk-shell  $\text{Au@TiO}_2$ , a sol-gel based templating method is used. Here, citrate-stabilized Au nanoparticles are first coated with  $\text{SiO}_2$ . The silica acts as a sacrificial layer to form a layer of  $\text{TiO}_2$  grown on top of it, followed by etching of the  $\text{SiO}_2$  with an aqueous solution of  $\text{NaOH}$ . This method holds complications such as difficult control of shell thickness.<sup>116</sup> In general, simple and effective methods for stabilizing nanoparticles in advanced nanomaterial structures are missing.

The lack of simple and effective methods to create advanced sinter-stable catalysts lead to the focus of this chapter, using MOFs as sacrificial templates and metal precursors to create advanced nanorattle type structures. In comparison to a yolk-shell structure, a nanorattle structure includes more than one encapsulated metal or metal oxide nanoparticle. Moreover, the hollow structure of nanorattle catalysts results in high surface areas, high porosities and low densities.<sup>117</sup> The idea is to first use ZIF-67 (Co) and ZIF-8 (Zn) crystals as a template to grow a shell of mesoporous  $\text{SiO}_2$  around it. Then either calcination of this structure to yield  $\text{Co}_3\text{O}_4$  nanoparticles within a mesoporous  $\text{SiO}_2$  shell or carbonization of this structure to yield Co nanoparticles in a porous carbon matrix within a mesoporous  $\text{SiO}_2$  shell can be performed. Additionally, the calcination can be done subsequently to the carbonization step to form well-dispersed  $\text{Co}_3\text{O}_4$  nanoparticles within the mesoporous  $\text{SiO}_2$  shell, see Figure 4.1.  $\text{Co}_3\text{O}_4$  nanoparticles are highly attractive metal oxides for CO oxidation. This is due to the weak Co-O bond resulting in easy availability of reactive oxygen. In literature,  $\text{Co}_3\text{O}_4$  nanoparticle based catalysts have been proved catalytically active down to  $-77^\circ\text{C}$ .<sup>106</sup> This is typically done under super dry conditions, since the presence of water is detrimental to the catalytic performance. The encapsulation of the  $\text{Co}_3\text{O}_4$  nanoparticles in a hydrophobic  $\text{SiO}_2$  shell might actually be beneficial in this case. However, this chapter will focus on CO oxidation at ambient conditions. In this chapter, ZIF-67@ $\text{SiO}_2$  precursors will be exposed to different thermal treatments to investigate the effect on the derived catalysts. Moreover, several catalysts will be synthesized from different Co/Zn ratios, to control the properties in the final catalysts. These catalysts will be tested in CO oxidation to investigate the effect of different alterations on the catalytic performance.



## 4.2 Experimental Details

### 4.2.1 Material Preparations

Reagents were acquired from a commercial source (Sigma-Aldrich), and were utilized without additional purifications. The reagents include: 2-methylimidazole (99%), cobalt(II) nitrate hexahydrate (99.9% trace metals basis), zinc(II) nitrate hexahydrate ( $\geq 99.0\%$ ), hexadecyltrimethylammonium bromide (CTAB  $\geq 98\%$ ), tetraethyl orthosilicate (TEOS, 99.99% trace metals basis), concentrated ammonia solution (aqueous, 25-28%), methanol (HPLC Plus,  $\geq 99.9\%$ ) and absolute ethanol ( $\geq 99.8\%$ ).

#### Synthesis of ZIF-67/8

The ZIF crystals were synthesized according to my previously published articles Zacho *et al.*<sup>1,42,43</sup> Here, the Co/Zn ratios were altered to obtain different ZIF crystal sizes and metal loadings. Zn was subsequently removed by evaporation under high temperatures. See Chapter 3.2.1 for detailed synthesis procedures and Table 4.1 below for Co/Zn ratios and reagents amounts (g).

**Table 4.1.:** Overview of the Co/Zn ratios in the prepared ZIF-67/8 with listed amounts.

	unit	Co <sub>1</sub> @SiO <sub>2</sub> (Zn <sub>1</sub> )	Co <sub>1</sub> @SiO <sub>2</sub> (Zn <sub>0</sub> )	Co <sub>0</sub> @SiO <sub>2</sub> (Zn <sub>1</sub> )	Co <sub>1</sub> @SiO <sub>2</sub> (Zn <sub>3</sub> )	Co <sub>3</sub> @SiO <sub>2</sub> (Zn <sub>1</sub> )
Co/Zn	ratio	1:1	1:0	0:1	1:3	3:1
Co(NO <sub>3</sub> ) <sub>2</sub> ·6H <sub>2</sub> O	g	0.718	1.436	-	0.359	1.070
Zn(NO <sub>3</sub> ) <sub>2</sub> ·6H <sub>2</sub> O	g	0.734	-	1.436	1.101	0.367
2-methylimidazole	g	3.244	3.244	3.244	3.244	3.244

#### Synthesis of ZIF-67/8@SiO<sub>2</sub>

The SiO<sub>2</sub> shell synthesis was modified from the literature.<sup>118</sup> ZIF-67/8 (1.0 g) in the given Co/Zn ratio was dispersed in absolute ethanol (400 mL) and water (660 mL), followed by the addition of 2-methylimidazole (5.0 g) and sonication of the solution for 30 min. CTAB (3.04 g) was added and sonication for 30 min was repeated. Then TEOS (7 mL) was added dropwise to the solution under stirring. Depending on the desired thickness of the SiO<sub>2</sub> shell, the core-shell material was collected after 2-24 h, with a longer period resulting in a thicker SiO<sub>2</sub> shell. The Co<sub>1</sub>@SiO<sub>2</sub> (Zn<sub>0</sub>) catalyst from the publication in Topics in Catalysis<sup>43</sup> was left for 2 h resulting in an average shell thickness of 50 nm. The Co<sub>1</sub>@SiO<sub>2</sub> (Zn<sub>0</sub>) (600/300) catalyst from the publication in Catalysis Communications<sup>1</sup> was left for

24 h resulting in an average shell thickness of 100 nm. The core-shell material was collected by centrifugation (8000 rpm for 10 min), washed three times with absolute ethanol and dried 80°C for 24 h.

### **Synthesis of $\text{Co}_x\text{@SiO}_2(\text{Zn}_y)$**

The prepared ZIF-67/8@SiO<sub>2</sub> was then either carbonized and then calcined or just directly calcined. The carbonizations were completed in a tube furnace under flowing Ar at 600°C (ZIF-67) or at 900°C (ZIF-67/8) for 2 h. The calcinations were completed in a muffle furnace in static air at 300°C or 550°C for 2 h. The heating ramp for the carbonization and calcination procedures was 5°C min<sup>-1</sup>. The 900°C carbonization for ZIF-67/8 was chosen based on previous findings in Chapter 3, which confirmed the successful removal of Zn by evaporation. The final name of the catalyst Co<sub>1</sub>@SiO<sub>2</sub> (Zn<sub>1</sub>) indicates a Co/Zn ratio of 1:1 present in the ZIF-67/8 precursor crystals, see Table 4.2 for an overview.

### **Synthesis of $\text{Co}_1\text{/SiO}_2(\text{Zn}_0)$**

The synthesis of the SiO<sub>2</sub> spheres were based on the so-called Stöber process.<sup>119</sup> A reference catalyst was prepared with incipient wetness impregnation of SiO<sub>2</sub> spheres. SiO<sub>2</sub> spheres were prepared by dissolving CTAB (1.5 g) in absolute ethanol (300 mL), water (500 mL) and an aqueous solution of concentrated ammonia 25-28% (10 mL). The solution was mixed at 25°C followed by the fast addition of TEOS (10 mL) to the solution under vigorous stirring. The white product was collected by centrifugation (12000 rpm for 10 min), washed three times with absolute ethanol and dried at 80°C for 24 h.

The white powder of SiO<sub>2</sub> spheres was calcined in a muffle furnace in static air at 550°C for 2 h with a heating ramp of 5°C min<sup>-1</sup>.

The final SiO<sub>2</sub> spheres were impregnated by incipient wetness with an aqueous solution of cobalt(II) nitrate hexahydrate equivalent to 15.8 wt% Co (22 wt% Co<sub>3</sub>O<sub>4</sub>).

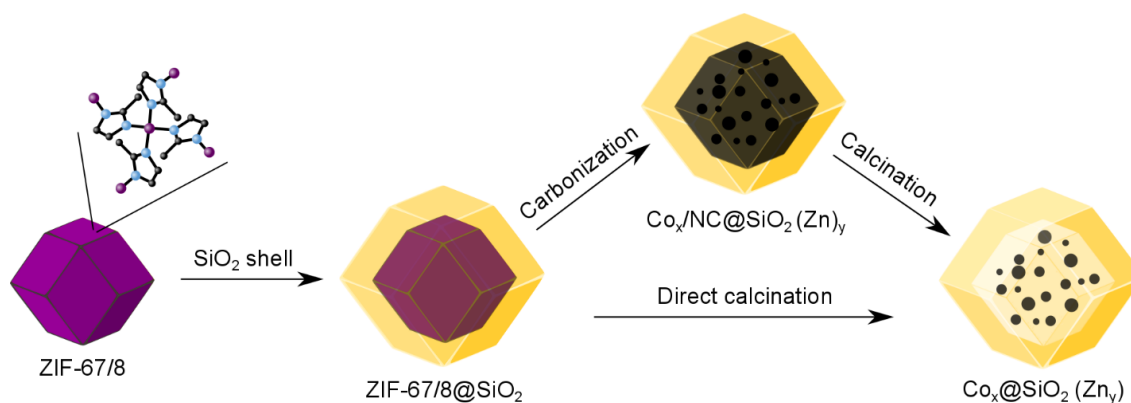


**Figure 4.1.:** A schematic of the synthesis procedure for yielding  $\text{Co}_x\text{@SiO}_2(\text{Zn}_y)$  catalysts.<sup>1</sup> Reproduced by permission of Elsevier.

## 4.2.2 Characterization Methods

In order to explain the performance of the catalysts in a CO oxidation reaction, the prepared materials were characterized by several techniques. XRF was used to determine the metal loadings. XRPD and  $\text{N}_2$  physisorption were used to confirm the structures. TGA was used to determine the optimal calcination temperature. XPS was used to identify the chemical state and support the encapsulation of Co. SEM and TEM were used to identify the shape and size of the nanorattle particles. Additionally, TEM was used to identify the Co and  $\text{Co}_3\text{O}_4$  nanoparticle size distribution. STEM and Electron Tomography were used to confirm the nanoparticles' three-dimensional dispersion in the metal oxide shell.

## 4.2.3 Catalytic Test Procedure

The prepared catalysts were tested in the CO oxidation reaction at atmospheric pressure in a plug flow reactor setup, equipped with a quartz fixed-bed reactor, a mass flow controller and an online Rosemount BINOS 100 non-dispersion infrared detector for quantification of CO and  $\text{CO}_2$ . In an experiment, 20 mg of fractionated catalyst (180–355  $\mu\text{m}$ ) was mixed with 100 mg of quartz (180–355  $\mu\text{m}$ ) and loaded in a 4 mm in diameter tubular quartz reactor fixed by two pieces of quartz wool, see Figure 4.2. The fractionation of the catalyst reduces external mass and heat transfer securing high reproducibility. In order to measure and control the temperature of the catalyst bed, a thermocouple was placed directly after the bed. The catalytic tests were performed with a flow of 1% CO in 78.3%  $\text{N}_2$  and 20.7%  $\text{O}_2$  (AGA regulator) and 50  $\text{mL min}^{-1}$  controlled

by a Brooks 4800 series mass flow controller. In a catalytic test, the temperature of the catalyst bed was heated from 30-300°C and then 300-30°C by a ramp of 2°C min<sup>-1</sup>.

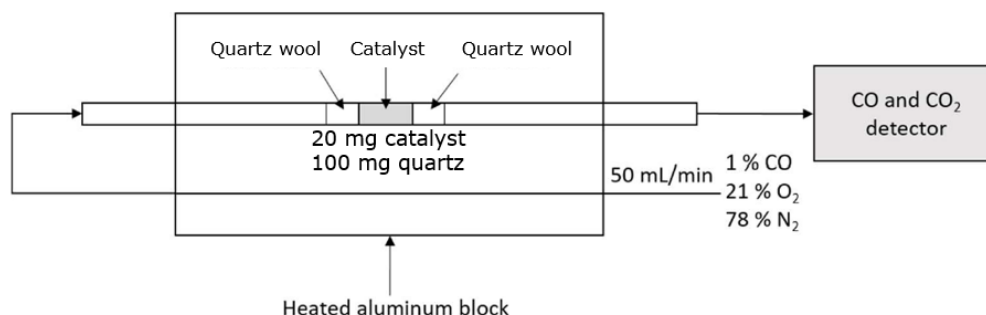


**Figure 4.2.:** A simplified overview of the tubular quartz reactor with the catalyst bed.

## 4.3 Results and Discussion

### 4.3.1 XRF and TGA

Table 4.2 provides an overview of the first set of prepared materials. The Co/Zn ratios were 1:0 in all these catalysts as the metal precursors were exclusively of Co, either ZIF-67@SiO<sub>2</sub> (Co) or cobalt(II) nitrate hexahydrate incipient wetness impregnated SiO<sub>2</sub>. The metal loadings were quantified from XRF, where standards of known metal concentrations were used to prepare a calibration line. All catalysts from Table 4.2 held a Co loading of 15.8 wt%, corresponding to a Co<sub>3</sub>O<sub>4</sub> loading of 21.5 wt%. The precursors were exposed to different thermal treatments based on TGA experiments, see Figure 4.3. The TGA curves of the ZIF-67@SiO<sub>2</sub> and Co<sub>1</sub>/NC@SiO<sub>2</sub> (Zn<sub>0</sub>) materials illustrate that in order to fully decompose the organic template, the ZIF-67@SiO<sub>2</sub> precursor requires a higher calcination temperature (400°C) in comparison to the prior carbonized Co<sub>1</sub>/NC@SiO<sub>2</sub> (Zn<sub>0</sub>) structure (300°C). Therefore, alterations in the temperature of the carbonization and/or calcination of the materials were performed. Here, Co<sub>1</sub>@SiO<sub>2</sub> (Zn<sub>0</sub>) (-/550), entry 1, and the reference material Co<sub>1</sub>/SiO<sub>2</sub> (Zn<sub>0</sub>) (-/550), entry 5, were directly calcined at 550°C. Co<sub>1</sub>/NC@SiO<sub>2</sub> (Zn<sub>0</sub>) (600/-), entry 2, was only carbonized at 600°C, which meant the carbon matrix was preserved. Co<sub>1</sub>@SiO<sub>2</sub> (Zn<sub>0</sub>) (600/550) and Co<sub>1</sub>@SiO<sub>2</sub> (Zn<sub>0</sub>) (600/300) were carbonized at 600°C prior to the calcination, which was completed at two different temperatures (550°C and 300°C). Here, the alterations were performed

to examine what impact a carbonization step prior to calcination had on the resulting nanorattle catalysts. Moreover, the influence of the calcination temperature on the resulting metal nanoparticles' size distribution and three-dimensional dispersion in the nanorattle was examined.

**Table 4.2.:** Overview of the prepared  $\text{Co}_x\text{@SiO}_2$  ( $\text{Zn}_y$ ) with altered thermal treatments.

Entry	Precursor	Catalyst <sup>a</sup>	Carbonization temperature	Calcination temperature
1	ZIF-67@SiO <sub>2</sub>	Co <sub>1</sub> @SiO <sub>2</sub> (Zn <sub>0</sub> ) (-/550)	-	550°C
2	ZIF-67@SiO <sub>2</sub>	Co <sub>1</sub> /NC@SiO <sub>2</sub> (Zn <sub>0</sub> ) (600/-)	600°C	-
3	ZIF-67@SiO <sub>2</sub>	Co <sub>1</sub> @SiO <sub>2</sub> (Zn <sub>0</sub> ) (600/550)	600°C	550°C
4	ZIF-67@SiO <sub>2</sub>	Co <sub>1</sub> @SiO <sub>2</sub> (Zn <sub>0</sub> ) (600/300)	600°C	300°C
5	SiO <sub>2</sub> spheres	Co <sub>1</sub> /SiO <sub>2</sub> (Zn <sub>0</sub> ) (-/550)	-	550°C

<sup>a</sup> The names of the prepared materials are distinguished by the ratio of Co/Zn in the catalyst precursors and the thermal treatment temperatures. The at-sign (@) indicates encapsulated in and the slash-sign (/) indicates supported on.

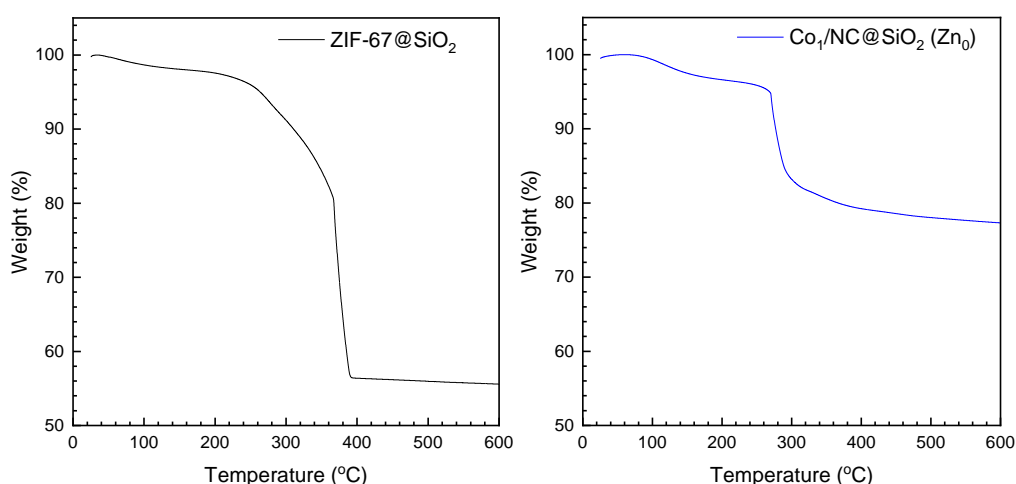


**Figure 4.3.:** (Left) TGA curve ZIF-67@SiO<sub>2</sub> in air (600°C, 2h) and (right) Co<sub>1</sub>/NC@SiO<sub>2</sub> (Zn<sub>0</sub>) in air (600°C, 2h) with a ramp of 5°C min<sup>-1</sup>.

Table 4.3 provides an overview of the second set of prepared materials with metal loadings quantified from XRF. These ZIF-67/8 precursors were synthesized with different Co/Zn ratios (3:1, 1:3, 1:1, 0:1, 1:0). The ZIF-67/8 precursor crystals were carbonized at 900°C to remove Zn by evaporation. Calcination was then conducted at a temperature of 300°C to remove carbon and form Co<sub>3</sub>O<sub>4</sub> nanoparticles, which was decided from the TGA experiments previously described, see Figure 4.3. The metal loadings varied according to the Co/Zn ratio

in the ZIF-67/8 precursor crystals. The nanorattle catalyst  $\text{Co}_0@\text{SiO}_2$  ( $\text{Zn}_1$ ), entry 4, which derived from pure ZIF-8 (Zn) crystals still contained 5.1 wt% of Zn. Here, prolonged carbonization at 900°C was expected to remove the remaining Zn by evaporation. The nanorattle catalyst  $\text{Co}_1@\text{SiO}_2$  ( $\text{Zn}_0$ ), entry 5, which derived from pure ZIF-67 (Co) crystals contained 15.8 wt% of Co. The nanorattle catalyst  $\text{Co}_1@\text{SiO}_2$  ( $\text{Zn}_1$ ), entry 3, had the lowest Co loading with 9.3 wt% of Co and 0.1 wt% of Zn left. The nanorattle catalyst  $\text{Co}_1@\text{SiO}_2$  ( $\text{Zn}_3$ ), entry 2, had a 9.8 wt% of Co and 0.2 wt% Zn. A prolonged carbonization of this nanorattle catalyst would be suggested as well due to the high Zn content in the ZIF-67/8 precursor. The nanorattle catalyst  $\text{Co}_3@\text{SiO}_2$  ( $\text{Zn}_1$ ), entry 1, had the highest Co loading with 26.9 wt% of Co in the catalyst with no measured Zn.

**Table 4.3.:** Overview of the prepared  $\text{Co}_x@\text{SiO}_2$  ( $\text{Zn}_y$ ) with Co/Zn ratio alterations.

Entry	Precursor	Catalyst <sup>a</sup>	Nanorattle size nm	Co loading wt%	Zn loading wt%
1	ZIF-67/8@SiO <sub>2</sub>	Co <sub>3</sub> @SiO <sub>2</sub> (Zn <sub>1</sub> )	150	26.9	0.0
2	ZIF-67/8@SiO <sub>2</sub>	Co <sub>1</sub> @SiO <sub>2</sub> (Zn <sub>3</sub> )	50	9.8	0.2
3	ZIF-67/8@SiO <sub>2</sub>	Co <sub>1</sub> @SiO <sub>2</sub> (Zn <sub>1</sub> )	150	9.3	0.1
4	ZIF-8@SiO <sub>2</sub>	Co <sub>0</sub> @SiO <sub>2</sub> (Zn <sub>1</sub> )	40	0.0	5.1
5	ZIF-67@SiO <sub>2</sub>	Co <sub>1</sub> @SiO <sub>2</sub> (Zn <sub>0</sub> )	350	15.8	0.0

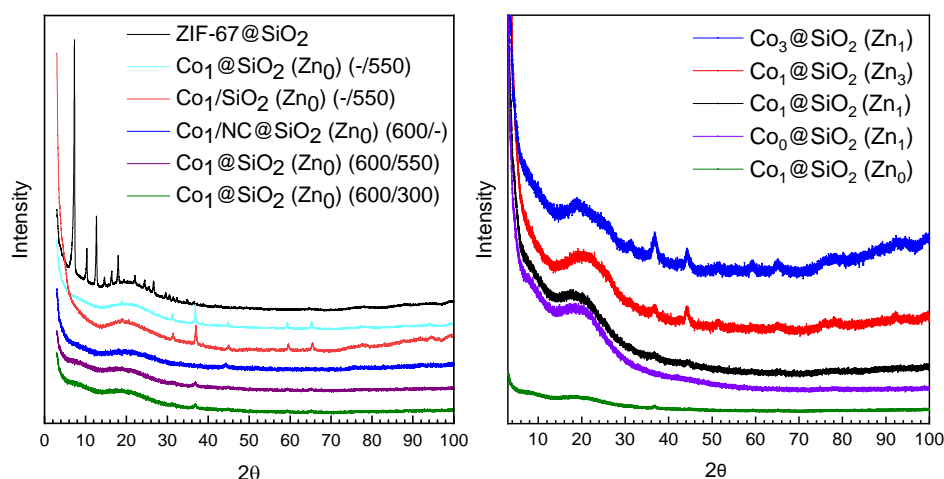
<sup>a</sup> The names of the prepared materials are distinguished by the ratio of Co/Zn in the catalyst precursors. The at-sign (@) indicates encapsulated in. The average nanorattle size is determined from TEM images, see section 4.3.4.

### 4.3.2 XRPD and XPS

The diffraction patterns from XRPD analysis of all the prepared materials can be seen in Figure 4.4. Figure 4.4(left) shows the diffraction pattern of ZIF-67@SiO<sub>2</sub>, which confirmed the characteristic ZIF-67 sodalite structure. An additional broad peak at  $2\theta$  degrees of 20° was present from amorphous SiO<sub>2</sub>, which derived from the metal oxide shell. The diffraction patterns of the resulting nanorattle catalysts deriving from thermal treatments of ZIF-67@SiO<sub>2</sub> showed weak diffraction peaks of either Co or Co<sub>3</sub>O<sub>4</sub> after carbonization and/or calcination. As the crystalline peaks of ZIF-67 were completely replaced by Co or Co<sub>3</sub>O<sub>4</sub> peaks it confirmed the complete decomposition of the ZIF framework. The diffraction pattern of the only carbonized catalyst, Co<sub>1</sub>/NC@SiO<sub>2</sub> (Zn<sub>0</sub>) (600/-), showed a weak peak at  $2\theta$  degrees of 44.3° from Co(111) confirming the presence of Co nanoparticles. In comparison, the four calcined catalysts, Co<sub>1</sub>@SiO<sub>2</sub> (Zn<sub>0</sub>) (-/550), Co<sub>1</sub>@SiO<sub>2</sub> (Zn<sub>0</sub>) (600/550), Co<sub>1</sub>@SiO<sub>2</sub> (Zn<sub>0</sub>) (600/300) and Co<sub>1</sub>/SiO<sub>2</sub> (Zn<sub>0</sub>) (-/550),

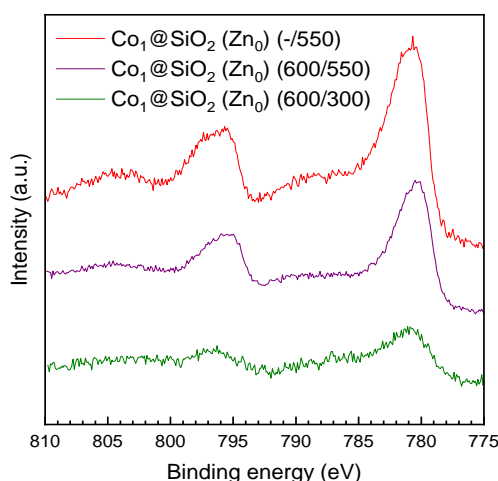
revealed weak peaks at  $2\theta$  degrees of  $19.0^\circ$  (111),  $31.3^\circ$  (220),  $36.8^\circ$  (311),  $38.6^\circ$  (222),  $44.9^\circ$  (422),  $59.4^\circ$  (511) and  $65.3^\circ$  (440) confirming the presence of  $\text{Co}_3\text{O}_4$  nanoparticles. The most intense peak were from  $\text{Co}_3\text{O}_4$ (311) at a  $2\theta$  degree of  $36.8^\circ$ . The nanorattle catalysts, which were prepared by direct calcination showed significantly sharper peaks at a position of  $36.8^\circ$  from  $\text{Co}_3\text{O}_4$ (311). This indicated that larger  $\text{Co}_3\text{O}_4$  nanoparticles were formed upon direct calcination at  $550^\circ\text{C}$  of the catalysts  $\text{Co}_1@\text{SiO}_2$  ( $\text{Zn}_0$ ) (-/550) and  $\text{Co}_1/\text{SiO}_2$  ( $\text{Zn}_0$ ) (-/550). However, the intensities of the  $\text{Co}_3\text{O}_4$ (311) peaks only provided an indication of a difference in metal nanoparticles sizes, the peaks were in general too weak to estimate the size of the nanoparticles by line broadening analysis.

Figure 4.4(right) shows the diffraction patterns of the nanorattle catalysts prepared with altered Co/Zn ratios. These catalysts all possessed the broad peak of amorphous  $\text{SiO}_2$  at a  $2\theta$  degrees of  $20^\circ$  confirming the metal oxide shell. Moreover, all diffraction patterns, except the ZIF-8 (Zn) derived  $\text{Co}_0@\text{SiO}_2$  ( $\text{Zn}_1$ ), showed a peak at  $2\theta$  degrees of  $36.8^\circ$  from  $\text{Co}_3\text{O}_4$ (311). The diffraction pattern of  $\text{Co}_0@\text{SiO}_2$  ( $\text{Zn}_1$ ) showed solely the broad peak of amorphous  $\text{SiO}_2$  with no distinctive peaks from ZnO. This might be due to the low loading of Zn remaining (5.1 wt%) after carbonization. It appeared as if  $\text{Co}_3@\text{SiO}_2$  ( $\text{Zn}_1$ ) had the most intensive peak from  $\text{Co}_3\text{O}_4$ (311), which might be due to the relatively high loading of Co (26.9 wt%) resulting in a higher degree of  $\text{Co}_3\text{O}_4$  nanoparticles agglomeration.



**Figure 4.4.:** The diffraction patterns of (left) the prepared ZIF-67@SiO<sub>2</sub> precursor material and the derived nanorattle catalysts after different carbonization and/or calcination temperatures and (right) the Co<sub>x</sub>@SiO<sub>2</sub> (Zn<sub>y</sub>) nanorattle catalysts prepared with different Co/Zn ratios.

XPS analysis indicated no change in the chemical state of  $\text{Co}_3\text{O}_4$  in the final three nanorattle catalysts prepared from  $\text{ZIF-67@SiO}_2$  at different temperatures, see Figure 4.5. The catalysts all had the two characteristic peaks from  $\text{Co}_3\text{O}_4$  with the most intense peak at a binding energy of 779.7 eV. No distinctive satellite peaks were present, which for  $\text{CoO}$  includes a peak at 786 eV. XPS analysis was also used to reveal the amount of Co detectable from the surface. Here, about 5 wt% of Co could be detected by XPS analysis, which according to the high loading of Co (15.8 wt%) in the three catalysts verified the encapsulation of  $\text{Co}_3\text{O}_4$  nanoparticles within the  $\text{SiO}_2$  shells. The 5 wt% of Co detectable was attributed single  $\text{Co}_3\text{O}_4$  nanoparticles present in the mesoporous  $\text{SiO}_2$  shell or exposed  $\text{Co}_3\text{O}_4$  nanoparticles in potentially damaged shell structures. As the  $\text{SiO}_2$  shells were mesoporous,  $\text{Co}_3\text{O}_4$  signals might also still be detectable despite complete encapsulation.



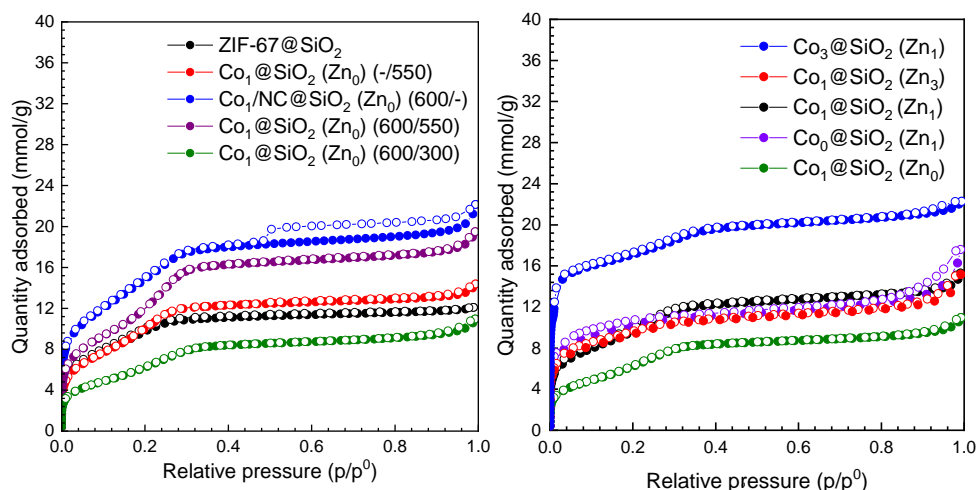
**Figure 4.5.:** *The XPS analysis of  $\text{Co}_1\text{@SiO}_2 (\text{Zn}_0)$  at the different carbonization and/or calcination temperatures: (-/550), (600/550) and (600/300).*

### 4.3.3 $\text{N}_2$ Physisorption

The isotherms of the  $\text{ZIF-67@SiO}_2$  precursor material and the derived nanorattle catalysts can be seen in Figure 4.6(left). Additionally, the isotherms of the nanorattle catalysts prepared with different Co/Zn ratios can be seen in Figure 4.6(right). The precursor material and nanorattle catalysts were all of Type IV isotherm, which verified them as mesoporous materials supporting the presence of mesoporous  $\text{SiO}_2$  shells. The small Hysteresis loop was attributed to capillary condensation characteristic of mesopores. The isotherms of  $\text{Co}_1/\text{NC@SiO}_2 (\text{Zn}_1)$  with the preserved carbon matrix within the  $\text{SiO}_2$  shell possessed a different H4 Hysteresis loop closing around  $p/p^0$  of



0.46, characteristic for the adsorbate  $N_2$  at 77K. As mentioned in Chapter 2, a H4 Hysteresis loop is typical for micro-mesoporous carbons. Thus, the difference in the Hysteresis loop is attributed to the restricted microporosity of the preserved N-doped carbon matrix.



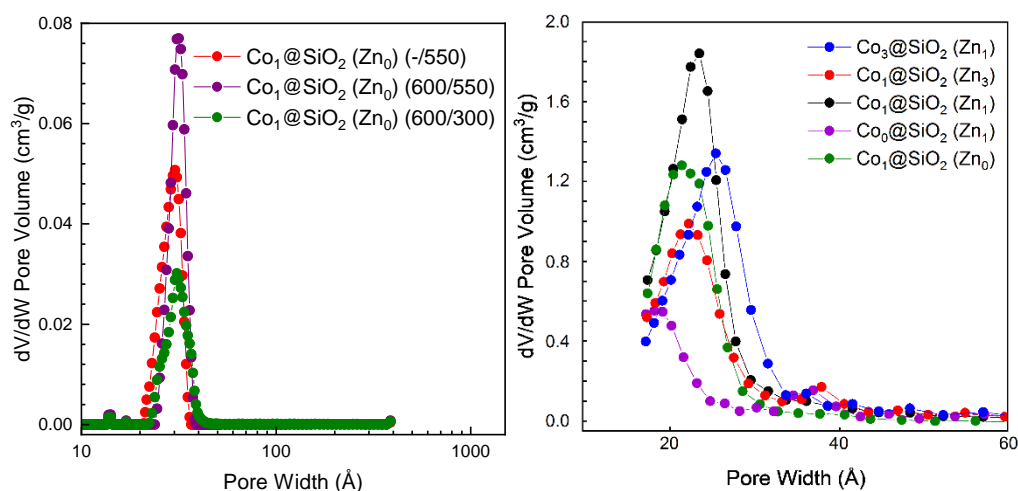
**Figure 4.6.:**  $N_2$  physisorption isotherms of (left) the prepared ZIF-67@SiO<sub>2</sub> precursor material and the derived nanorattle catalysts after different carbonization and/or calcination temperatures and (right) the Co<sub>x</sub>@SiO<sub>2</sub> (Zn<sub>y</sub>) nanorattle catalysts prepared with different Co/Zn ratios.

Table 4.4 presents the  $N_2$  physisorption analysis data. The precursor material ZIF-67@SiO<sub>2</sub>, entry 1, had a specific surface area around 802 m<sup>2</sup> g<sup>-1</sup>. The relatively low surface area of the precursor material was speculated to be caused by the remaining CTAB blocking the pores of the uncalcined SiO<sub>2</sub> shell, which limited the physisorption in the ZIF. All catalysts had high specific surface areas between 634-1418 m<sup>2</sup> g<sup>-1</sup>, deriving mainly from the external surface area of the SiO<sub>2</sub> shells. The minor deviations in specific surface areas were credited to the variations in size and shell thickness of the nanorattle catalyst particles. Entry 5 and entry 10, were similar nanorattle catalysts of Co<sub>1</sub>@SiO<sub>2</sub> (Zn<sub>0</sub>) deriving from a ZIF-67@SiO<sub>2</sub> precursor carbonized at 600°C and calcined at 300°C. These catalysts differed only in the thickness of their SiO<sub>2</sub> shells, 100 nm in diameter for entry 5 and 50 nm in diameter for entry 10. However, no significant deviation was measured in the specific surface area and total pore volume. All catalysts held high total pore volumes deriving mainly from the mesoporous SiO<sub>2</sub>. Figure 4.7 shows the pore size distributions of all Co<sub>x</sub>@SiO<sub>2</sub> (Zn<sub>y</sub>) nanorattle catalysts, which revealed small mesopores present of 2-3 nm in diameter.

**Table 4.4.:** Overview of results from N<sub>2</sub> physisorption analysis.

Entry	Material	$S_{\text{BET}}^a$ (m <sup>2</sup> /g)	$S_{\text{ext}}^b$ (m <sup>2</sup> /g)	$V_{\text{micro}}^b$ (cm <sup>3</sup> /g)	$V_{\text{tot}}^c$ (cm <sup>3</sup> /g)
1	ZIF-67@SiO <sub>2</sub>	802	n/a	n/a	0.411
2	Co <sub>1</sub> @SiO <sub>2</sub> (Zn <sub>0</sub> ) (-/550)	903	n/a	n/a	0.463
3	Co <sub>1</sub> NC/@SiO <sub>2</sub> (Zn <sub>0</sub> ) (600/-)	1271	n/a	n/a	0.690
4	Co <sub>1</sub> @SiO <sub>2</sub> (Zn <sub>0</sub> ) (600/550)	1040	n/a	n/a	0.623
5*	Co <sub>1</sub> @SiO <sub>2</sub> (Zn <sub>0</sub> ) (600/300)	626	n/a	n/a	0.340
6	Co <sub>3</sub> @SiO <sub>2</sub> (Zn <sub>1</sub> )	1418	627	0.322	0.742
7	Co <sub>1</sub> @SiO <sub>2</sub> (Zn <sub>3</sub> )	739	578	0.072	0.448
8	Co <sub>1</sub> @SiO <sub>2</sub> (Zn <sub>1</sub> )	860	746	0.002	0.481
9	Co <sub>0</sub> @SiO <sub>2</sub> (Zn <sub>1</sub> )	832	456	0.154	0.491
10*	Co <sub>1</sub> @SiO <sub>2</sub> (Zn <sub>0</sub> )	634	583	n/a	0.340

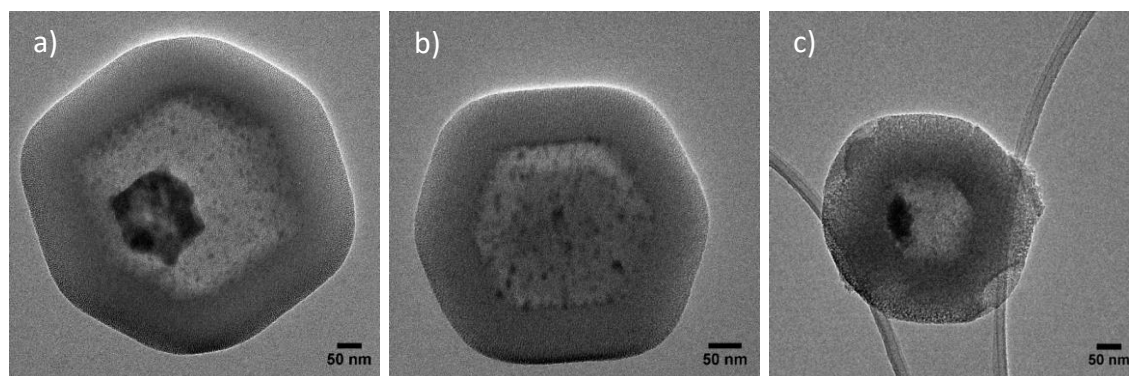
<sup>a</sup> Specific surface area determined by the BET method, <sup>b</sup> external surface area and micropore volume determined by the t-plot method and <sup>c</sup> total pore volume determined by a single point read at  $p/p^0=0.95$ . \* Entry 5 and 10 are similar materials with a difference in SiO<sub>2</sub> shell thickness, 100 nm and 50 nm in diameter, respectively.

**Figure 4.7.:** Pore size distributions of the Co<sub>x</sub>@SiO<sub>2</sub> (Zn<sub>y</sub>) nanorattle catalysts.

#### 4.3.4 SEM and TEM

Representative SEM and TEM images of all prepared nanorattle catalysts can be seen in Figure 4.8(a-f) and Figure 4.9(a-e). The SEM and TEM images in Figure 4.8(a-f) show the ZIF-67@SiO<sub>2</sub> derived Co<sub>1</sub>@SiO<sub>2</sub> (Zn<sub>0</sub>) nanorattle catalysts and the reference catalyst. The

TEM images of the nanorattle catalysts Figure 4.8(a-d) confirmed a successful creation of porous  $\text{SiO}_2$  shells encapsulating  $\text{Co}_3\text{O}_4$  nanoparticles, which were visible as dark spots in TEM due to the higher atomic weight of Co in comparison to the  $\text{SiO}_2$  shell. It was noteworthy that the nanorattle catalyst particles were replications of the hexagonal dodecahedral shape of ZIF-67, since most synthesized nanorattle catalysts are spherical.<sup>11</sup> Based on numerous representative TEM images it appeared as if the directly calcined  $\text{Co}_1@\text{SiO}_2$  ( $\text{Zn}_0$ ) (-/550) suffered from severe sintering deriving nanoparticles up to 75 nm in diameter. The severe agglomerations of  $\text{Co}_3\text{O}_4$  discovered with TEM were in agreement with XRPD, which showed one of the most intense peaks of  $\text{Co}_3\text{O}_4(311)$  in the diffraction pattern of  $\text{Co}_1@\text{SiO}_2$  ( $\text{Zn}_0$ ) (-/550). Figure 4.8(f) shows a SEM image of  $\text{Co}_1@\text{SiO}_2$  ( $\text{Zn}_0$ ) (-/550) with visible agglomerated  $\text{Co}_3\text{O}_4$  nanoparticles proving the large agglomerates were even noticeable with SEM. In comparison, the TEM images acquired of  $\text{Co}_1/\text{NC}@\text{SiO}_2$  ( $\text{Zn}_0$ ) (600/-) illustrated small nanoparticles below 25 nm in diameter, see Figure 4.8(b). This substantiated the formation of dispersed nanoparticles within the N-doped carbon matrix in the  $\text{SiO}_2$  shell upon carbonization. Here, the Co nanoparticles were small and well-dispersed due to confinement in the porous carbon matrix.  $\text{Co}_1/\text{NC}@\text{SiO}_2$  ( $\text{Zn}_0$ ) (600/-) nanorattles were subsequently calcined in air at either 550°C or 300°C in order to obtain the active  $\text{Co}_3\text{O}_4$  nanoparticles for the CO oxidation reaction, Figure 4.8(c-d). The calcination temperature had an influence on the size distribution of the  $\text{Co}_3\text{O}_4$  nanoparticles. TEM images of  $\text{Co}_1@\text{SiO}_2$  ( $\text{Zn}_0$ ) (600/500) illustrated nanoparticles up to 65 nm in diameter, whereas  $\text{Co}_1@\text{SiO}_2$  ( $\text{Zn}_0$ ) (600/300) typically illustrated nanoparticles of only 20 nm in diameter. However, both nanorattle catalysts, which were exposed to a prior carbonization step, appeared to have reduced agglomeration of  $\text{Co}_3\text{O}_4$  nanoparticles, in comparison to the directly calcined nanorattle catalysts. Figure 4.8(e) shows a TEM image of the reference catalyst  $\text{Co}_1@\text{SiO}_2$  ( $\text{Zn}_0$ ) (-/550), which clearly revealed the external coverage of the  $\text{SiO}_2$  sphere with  $\text{Co}_3\text{O}_4$  nanoparticles. Additional TEM images of the nanorattle catalysts can be found in the Appendix B.



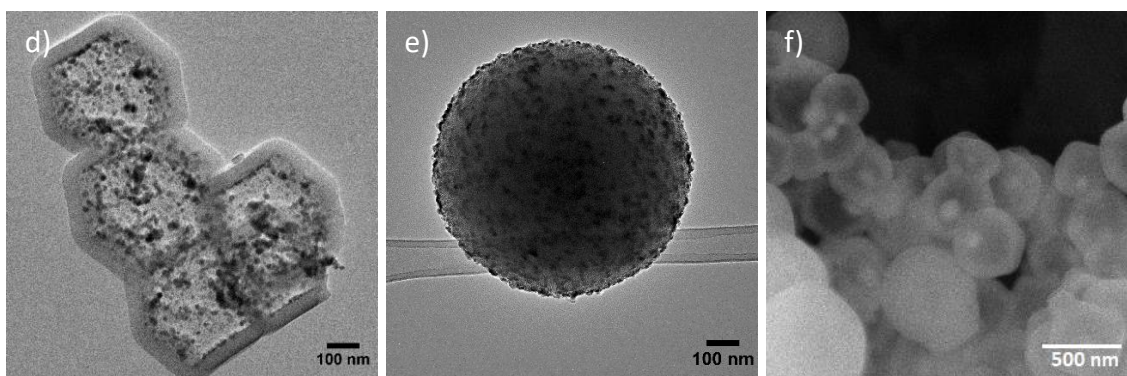


**Figure 4.8.:** TEM images of  $\text{Co}_1@\text{SiO}_2 (\text{Zn}_0)$  a) (-/550), b) NC (600/-), c) (600/550), d) (600/300), reference catalyst e)  $\text{Co}_1/\text{SiO}_2 (\text{Zn}_0)$  (-/550) and SEM image of d)  $\text{Co}_1@\text{SiO}_2 (\text{Zn}_0)$  (-/550).<sup>1</sup> Reproduced by permission of Elsevier.

The TEM images in Figure 4.9(a-e) show the nanorattle catalysts prepared with different Co/Zn ratios. The TEM images proved the successful formation of the nanorattle catalysts with encapsulated nanoparticles in porous  $\text{SiO}_2$  shells. Similar to the previous nanorattle catalysts in Figure 4.8, the  $\text{Co}_x@\text{SiO}_2 (\text{Zn}_y)$  nanorattle catalysts prepared with different Co/Zn ratios were replications of the hexagonal dodecahedral ZIF shape. From the XRF analysis it was proved that a change in the Co/Zn ratio altered the Co loadings in the nanorattle catalysts. From TEM analysis seen in Figure 4.9(a-e) it was furthermore proved that a change in the Co/Zn ratio altered the ZIF crystal sizes and the resulting nanorattle catalyst particle sizes. In agreement with previous findings in Chapter 3, it was revealed that a pure ZIF-8 (Zn) structure possessed crystal sizes of 40 nm and a pure ZIF-67 (Co) structure possessed crystal sizes of 350 nm. Additional alterations in the Co/Zn ratio revealed that a ratio of 1:3 derived nanorattle catalysts of 50 nm in diameter, whereas a Co/Zn ratio of 3:1 derived nanorattle catalysts of 150 nm in diameter. Thus, it was possible to modify the size of the nanorattle catalyst particles within a range of 40-350 nm by a simple synthesis modification of the ZIF precursor material's Co/Zn ratio. An overview of the nanorattle catalyst sizes in relation to their Co/Zn ratios can be seen in Table 4.3, (0:1= 40 nm, 1:3= 50 nm, 1:1= 150 nm, 3:1= 150 nm and 1:0= 350 nm). The suggested approach to alter the particle sizes can additionally be combined with sophisticated methods from literature to further alter the size of precursor ZIFs.<sup>42,120</sup> To further decrease the ZIF crystal size it is possible to add n-butylamine to the ZIF synthesis. Moreover, to further increase the ZIF crystal size it is possible to simply increase the synthesis temperature or change the solvent in the ZIF synthesis, in agreement with Chapter 3. In general, the nanorattle catalysts Figure 4.9(a-c), which were prepared from a bimetallic ZIF-67/8@ $\text{SiO}_2$  precursor material appeared to possess



smaller  $\text{Co}_3\text{O}_4$  nanoparticles. This impact was attributed to the increased separation and spatial isolation of the Co metal ions during the thermal treatments, where Zn metal ions limited the degree of Co agglomeration. The  $\text{Co}_3\text{O}_4$  nanoparticles of  $\text{Co}_x\text{@SiO}_2$  ( $\text{Zn}_y$ ) with Co/Zn ratios of 3:1, 1:3 and 1:1 all held size distributions of 2-20 nm, see Figure 4.9(a-c). In comparison, the nanorattle catalyst prepared from pure ZIF-67 (Co) crystals showed a higher size distribution of 2-25 nm. Thus, the introduction of Zn to the frameworks of ZIFs reduced the degree of  $\text{Co}_3\text{O}_4$  nanoparticles sintering. The nanorattle catalyst prepared from pure ZIF-8 (Zn) crystals showed no presence of  $\text{Co}_3\text{O}_4$  nanoparticles in the TEM image, as expected, see Figure 4.9(d). This proposed method for preparing nanorattle catalysts offers the possibility to acquire a high  $\text{Co}_3\text{O}_4$  loading while maintaining a low  $\text{Co}_3\text{O}_4$  nanoparticles size distribution, which can be challenging with incipient wetness impregnation. Being able to control the metal loading while keeping a specific nanoparticle size distribution is of great importance since it can be crucial to the catalysis. An example is for the Co catalyzed Fischer Tropsch synthesis.<sup>121</sup>

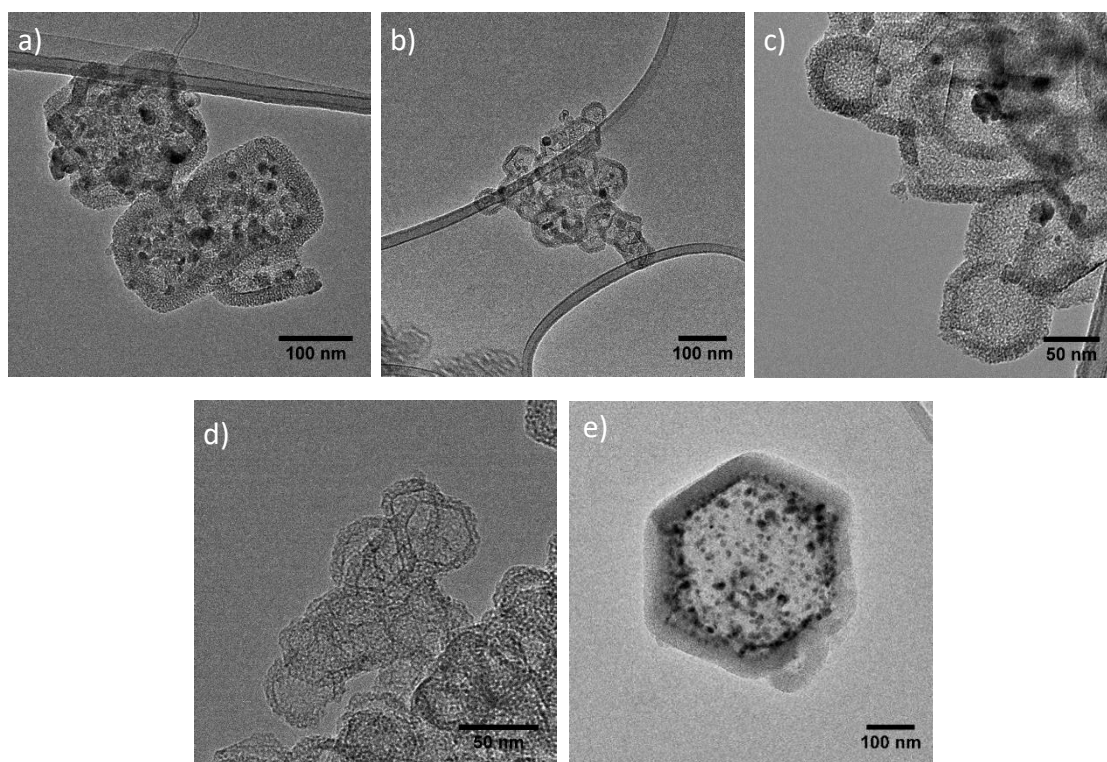


**Figure 4.9.:** TEM images of a)  $\text{Co}_3\text{@SiO}_2$  ( $\text{Zn}_1$ ), b)  $\text{Co}_1\text{@SiO}_2$  ( $\text{Zn}_3$ ), c)  $\text{Co}_1\text{@SiO}_2$  ( $\text{Zn}_1$ ), d)  $\text{Co}_0\text{@SiO}_2$  ( $\text{Zn}_1$ ) and e)  $\text{Co}_1\text{@SiO}_2$  ( $\text{Zn}_0$ ). Reproduced material from: Zacho et al.<sup>43</sup>, *Synthesis of Nano-engineered Catalysts Consisting of  $\text{Co}_3\text{O}_4$  Nanoparticles Confined in Porous  $\text{SiO}_2$* , *Topics in Catalysis*, 2019, by permission of Springer.

### 4.3.5 Electron Tomography and EDS

Electron tomography and EDS were used to investigate and understand the three-dimensional dispersion of Co and  $\text{Co}_3\text{O}_4$  nanoparticles in the mesoporous nanorattle catalysts post carbonization,  $\text{Co}_1/\text{NC@SiO}_2$  ( $\text{Zn}_0$ ) (600/-), and post calcination,  $\text{Co}_1@\text{SiO}_2$  ( $\text{Zn}_0$ ) (600/300). As mentioned in Chapter 2, with TEM, two-dimensional projections are acquired of three-dimensional objects, which makes it difficult to verify the dispersion of nanoparticles in a support. Electron tomography was performed in scanning TEM (STEM) mode where tilt-series of images from  $-68^\circ$  to  $68^\circ$  and  $-72^\circ$  to  $70^\circ$  were collected for the nanorattle catalysts  $\text{Co}_1/\text{NC@SiO}_2$  ( $\text{Zn}_0$ ) (600/-) and  $\text{Co}_1@\text{SiO}_2$  ( $\text{Zn}_0$ ) (600/300), respectively, by utilization of a HAADF detector. The tomographic reconstruction of  $\text{Co}_1/\text{NC@SiO}_2$  ( $\text{Zn}_0$ ) (600/-) confirmed the distribution of Co nanoparticles (blue) inside porous N-doped carbon placed within a mesoporous  $\text{SiO}_2$  shell, see Figure 4.10(a), Figure 4.11(c) and Movie S1:

<https://www.kemi.dtu.dk/-/media/Institutter/Kemi/Video/SimoneZacho/MovieS1>. The tomographic reconstruction of  $\text{Co}_1@\text{SiO}_2$  ( $\text{Zn}_0$ ) (600/300) verified the complete removal of the N-doped carbon by calcination at  $300^\circ\text{C}$  for 2h deriving  $\text{Co}_3\text{O}_4$  nanoparticles (red) on the internal surface of the mesoporous  $\text{SiO}_2$  shell, see Figure 4.10(b), Figure 4.11(d) and Movie S2:

<https://www.kemi.dtu.dk/-/media/Institutter/Kemi/Video/SimoneZacho/MovieS2>. The elemental maps obtained with EDS substantiated the confinement of the Co and  $\text{Co}_3\text{O}_4$  nanoparticles. Here, highly dispersed Co nanoparticles were found in a C core of  $\text{Co}_1/\text{NC@SiO}_2$  ( $\text{Zn}_0$ ) (600/-) and Co were dispersed in a hexagonal dodecahedral formation on the internal surface of the  $\text{SiO}_2$  shell with absence of C in the core of  $\text{Co}_1@\text{SiO}_2$  ( $\text{Zn}_0$ ) (600/300), see Figure 4.10(c) and Figure 4.10(d). Thus, electron tomography and EDS substantiated the successful encapsulations of Co and  $\text{Co}_3\text{O}_4$  nanoparticles in porous  $\text{SiO}_2$  shells.

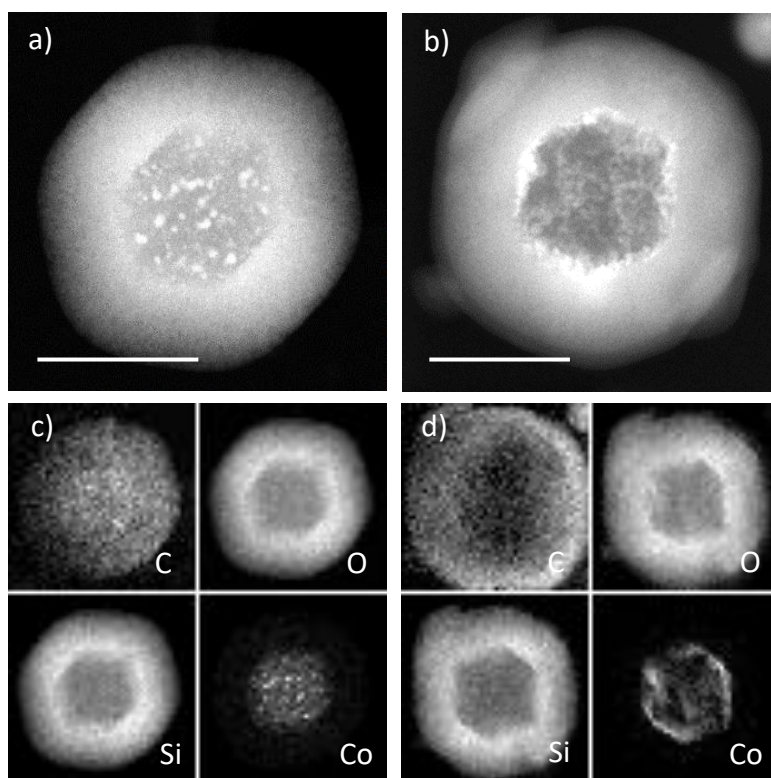


**Figure 4.10.:** Projected STEM-HAADF images of the nanorattle catalysts (a)  $\text{Co}_1/\text{NC}@ \text{SiO}_2 (\text{Zn}_0)$  (600/-) and (b)  $\text{Co}_1@ \text{SiO}_2 (\text{Zn}_0)$  (600/300), the scale bar is 100 nm. STEM-EDS elemental maps attained from the same nanorattle catalyst particle (c)  $\text{Co}_1/\text{NC}@ \text{SiO}_2 (\text{Zn}_0)$  (600/-) and (d)  $\text{Co}_1@ \text{SiO}_2 (\text{Zn}_0)$  (600/300), which were investigated by electron tomography.<sup>1</sup> Reproduced by permission of Elsevier.

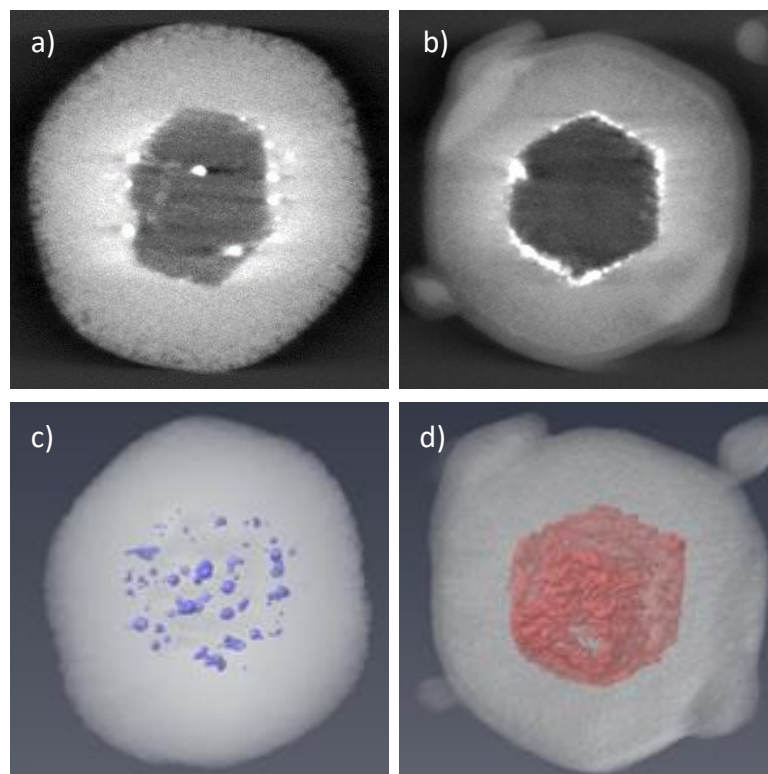


**Figure 4.11.:** STEM-HAADF slice images at the center of the nanorattle catalyst particles (a)  $\text{Co}_1/\text{NC}@ \text{SiO}_2 (\text{Zn}_0)$  (600/-) and (b)  $\text{Co}_1@ \text{SiO}_2 (\text{Zn}_0)$  (600/300) acquired from the tomographic reconstruction volume displayed in (c, d). (c) Co nanoparticles (blue) dispersed in the  $\text{SiO}_2$  shell and (d)  $\text{Co}_3\text{O}_4$  nanoparticles (red) dispersed on the internal surface of the  $\text{SiO}_2$  shell.<sup>1</sup> Reproduced by permission of Elsevier.

#### 4.3.6 The Carbon Monoxide Oxidation

The CO oxidation light-off curves for the ZIF-67@ $\text{SiO}_2$  derived nanorattle catalysts  $\text{Co}_1@ \text{SiO}_2 (\text{Zn}_0)$  prepared at the different conditions (-/550), (600/500), (600/300) can be seen in Figure 4.12(a). In the light-off curves the CO conversion (%) is plotted as a function of the temperature ( $^{\circ}\text{C}$ ). All three nanorattle catalysts held the same metal loading of 15.8 wt% Co based on XRF and the same amount of catalyst (20 mg) was used in each experiment, which makes the light-off curves directly comparable. No noteworthy difference was found in the catalytic performance of  $\text{Co}_1@ \text{SiO}_2 (\text{Zn}_0)$  (-/550) and  $\text{Co}_1@ \text{SiO}_2 (\text{Zn}_0)$  (600/550), which both reached 50% conversion at  $160^{\circ}\text{C}$ . However, it was evident from the light-off curves that the nanorattle catalyst  $\text{Co}_1@ \text{SiO}_2 (\text{Zn}_0)$  (600/300) had a higher catalytic activity reaching 50% conversion at  $134^{\circ}\text{C}$ . Thus, the



lower calcination temperature of 300°C, which resulted in less sintered Co<sub>3</sub>O<sub>4</sub> nanoparticles improved the overall catalytic performance in the CO oxidation reaction. This is in agreement with previous findings in the literature reporting that a decrease in the calcination temperature can have a significant influence on the properties of the catalyst and therefore the catalytic performance.<sup>122</sup> Thus, a prior carbonization step at 600°C, which made it possible to reduce the final calcination temperature from 500°C to 300°C had a substantial effect on the degree of sintering and the final catalytic activity of the nanorattle catalyst. A control experiment was performed with Co<sub>1</sub>/NC@SiO<sub>2</sub> (Zn<sub>0</sub>) (600/-) to prove the necessity of a post calcination step at 300°C to activate the nanorattle catalyst, see Figure 4.12(b). The initial activity in the first heating cycle was relatively poor with a 50% conversion at 208°C. However, subsequent to the heating cycle reaching 300°C, the nanorattle catalyst performed exactly as Co<sub>1</sub>@SiO<sub>2</sub> (Zn<sub>0</sub>) (600/300) reaching 50% conversion at 134°C, see Figure 4.12(d). This control experiment proved the need of a calcination step to oxidize Co to Co<sub>3</sub>O<sub>4</sub> nanoparticles and activate the nanorattle catalyst. The reference catalyst Co<sub>1</sub>/SiO<sub>2</sub> (Zn<sub>0</sub>) (-/550) prepared with a simple incipient wetness impregnation of mesoporous SiO<sub>2</sub> spheres was additionally tested in the CO oxidation reaction, see Figure 4.12(c). The reference catalyst had the poorest performance with a 50% conversion at 205°C. The performance was attributed to the poor stability of the metal nanoparticles, which upon high temperatures were likely to sinter. In the reference catalyst Co<sub>1</sub>/SiO<sub>2</sub> (Zn<sub>0</sub>) (-/550) no encapsulation or confinement of the Co<sub>3</sub>O<sub>4</sub> nanoparticles within a porous structure was introduced to hinder possible agglomeration. Thus, this experiment supported that small and well-dispersed Co<sub>3</sub>O<sub>4</sub> nanoparticles within porous structures ensure a high sinter stability is crucial to reach high catalytic performance.

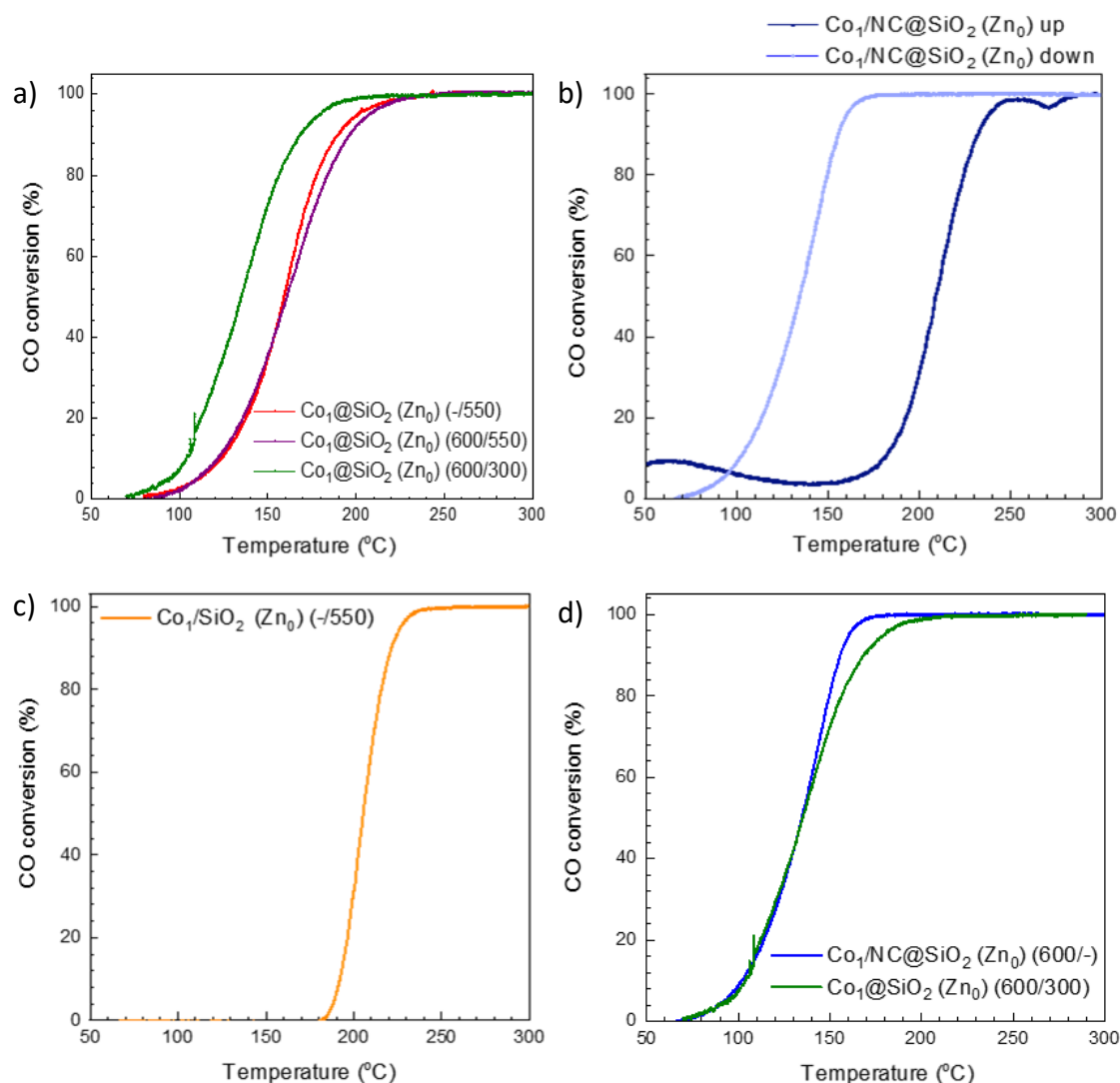


**Figure 4.12.:** CO oxidation light-off curves of the nanorattle catalysts a)  $\text{Co}_1/\text{SiO}_2 (\text{Zn}_0)$  prepared at  $(-/550)$ ,  $(600/500)$ ,  $(600/300)$ , b)  $\text{Co}_1/\text{NC}@\text{SiO}_2 (\text{Zn}_0)$   $(600/-)$  in the first heating cycle ramping up/down, c) reference catalyst  $\text{Co}_1/\text{SiO}_2 (\text{Zn}_0)$   $(-/550)$  and d)  $\text{Co}_1/\text{NC}@\text{SiO}_2 (\text{Zn}_0)$   $(600/-)$  after the first heating cycle compared to  $\text{Co}_1/\text{SiO}_2 (\text{Zn}_0)$   $(600/300)$ .

To investigate the effect of altering the Co/Zn ratios of the ZIF-67/8@SiO<sub>2</sub> precursor materials, CO oxidation reactions were performed, see Figure 4.13 for the light-off curves. The CO oxidations were performed with 20 mg of each of the four nanorattle catalysts  $\text{Co}_3@\text{SiO}_2 (\text{Zn}_1)$ ,  $\text{Co}_1@\text{SiO}_2 (\text{Zn}_3)$ ,  $\text{Co}_1@\text{SiO}_2 (\text{Zn}_1)$  and  $\text{Co}_1@\text{SiO}_2 (\text{Zn}_0)$ . The light-off curve of  $\text{Co}_0@\text{SiO}_2 (\text{Zn}_1)$  was excluded since the nanorattle catalyst showed no activity as no Co metal was incorporated. From the light-off curves, it was illustrated

that all nanorattle catalysts were active in the CO oxidation reaction.  $\text{Co}_3\text{O}_4/\text{SiO}_2$  ( $\text{Zn}_1$ ) had the highest activity with a 50% conversion at 120°C. This high performance was attributed to the high Co loading of 26.9 wt% present in the nanorattle catalyst, which held small and dispersed nanoparticles.  $\text{Co}_1\text{O}_x/\text{SiO}_2$  ( $\text{Zn}_0$ ) had the second-highest activity with a 50% conversion at 134°C, which was in correlation to its Co loading of 15.8 wt%. This performance was identical to the similar nanorattle catalyst  $\text{Co}_1\text{O}_x/\text{SiO}_2$  ( $\text{Zn}_0$ ) (600/300) described previously, which held a 50 nm in diameter thicker  $\text{SiO}_2$  shell. Thus, a difference of 50 nm in the shell thickness did not affect the mass transfer to such extend a decrease in the catalytic activity was detected.  $\text{Co}_1\text{O}_x/\text{SiO}_2$  ( $\text{Zn}_1$ ) had a 50% conversion at 147°C in accordance with the lower Co loading of 9.3 wt%. The nanorattle catalyst prepared with high Zn content,  $\text{Co}_1\text{O}_x/\text{SiO}_2$  ( $\text{Zn}_3$ ), which had a similar Co loading of 9.8 wt% reached 50% conversion at 170°C. This was the poorest performance of all the nanorattle catalysts containing  $\text{Co}_3\text{O}_4$  nanoparticles. As the  $\text{Co}_3\text{O}_4$  nanoparticles size distribution in  $\text{Co}_1\text{O}_x/\text{SiO}_2$  ( $\text{Zn}_3$ ) was similar to the other nanorattle catalysts, the lower activity was speculated to be caused by the remaining 0.2 wt% Zn. The Zn present in the catalyst might have blocked the access to the  $\text{Co}_3\text{O}_4$  nanoparticles active sites. TOFs were calculated from the Co loadings to compare the activity of the nanorattle catalysts. Here, it was found that  $\text{Co}_x/\text{SiO}_2$  ( $\text{Zn}_y$ ) prepared with Co/Zn ratios of 3:1, 1:1 and 1:0 performed identically with calculated TOFs of  $1.2 \cdot 10^{-1} \text{ mol CO min}^{-1} \text{ mol Co}$  calculated from the CO conversion at 120°C. In comparison,  $\text{Co}_1\text{O}_x/\text{SiO}_2$  ( $\text{Zn}_3$ ), which had a higher amount of Zn remaining in the nanorattle catalyst performed much poorer with a TOF of  $1.3 \cdot 10^{-2} \text{ mol CO min}^{-1} \text{ mol Co}$ . This proved that a prolonged carbonization step was required to obtain a competitive catalytic activity with the catalyst deriving from a Zn-rich ZIF-67/8 precursor.

In comparison to literature, low-temperature CO oxidation below -76° under dry conditions with  $\text{Co}_3\text{O}_4$  is well-known. Here, Jia *et al.*<sup>123</sup> reported a nanocomposite of  $\text{Co}_3\text{O}_4$ - $\text{SiO}_2$  with an activity below -76°C in the CO oxidation reaction. Nevertheless, most activity was lost at 80°C due to the adsorption of water causing an unusual temperature-dependent activity curve. At higher temperatures, the catalysts provided similar light-off temperatures between 132-160°C, as presented in this chapter. Xu *et al.*<sup>124</sup> reported a ceria based catalyst  $\text{Co}_3\text{O}_4$ - $\text{CeO}_2$ , which performed full CO to  $\text{CO}_2$  oxidation at a temperature of only 45°C. The high activity was attributed to the combination of  $\text{Co}_3\text{O}_4$  with the redox active  $\text{CeO}_2$ , which is often used in literature.<sup>125–127</sup> Therefore, the introduction of ceria to the nanorattle catalysts developed in this work could be of interest. With the developed synthesis procedure presented, it might be possible to use a similar approach to encapsulate  $\text{Co}_3\text{O}_4$  nanoparticles in porous  $\text{CeO}_2$  shells or to impregnate current ZIFs with Ce. Here, a substitution of TEOS with cerium(III) nitrate

hexahydrate to form a porous  $\text{CeO}_2$  shell could be investigated. As described in the introduction  $\text{TiO}_2$  is also highly used in CO oxidation reactions. Here, the substitution of TEOS with titanium isopropoxide (TIP) to form a  $\text{TiO}_2$  shell could be employed. In relation to this work, the substitution of TEOS with TIP was performed to synthesize two nanorattle catalysts of  $\text{Co}_3\text{O}_4$  nanoparticles within  $\text{TiO}_2$  shells. In the preparation of the nanorattle catalyst  $\text{Co}_x@\text{TiO}_2 (\text{Zn}_y)$  it was found that the calcination temperature influenced the phase of  $\text{TiO}_2$ , which up to  $400^\circ\text{C}$  yielded a higher surface area anatase and above  $600^\circ\text{C}$  yielded rutile. The current calcinations were performed at  $550^\circ\text{C}$  yielding a mixture of the two phases. Further synthesis optimization would be suggested to yield the higher surface area anatase  $\text{TiO}_2$ . Supporting information describing the full synthesis procedure of the  $\text{Co}_1@\text{TiO}_2 (\text{Zn}_0)$  and  $\text{Co}_1@\text{TiO}_2 (\text{Zn}_1)$  nanorattle catalysts can be seen in the Appendix B. Overall, the catalytic performances in the CO oxidation reaction were increased in comparison to their  $\text{SiO}_2$  counterparts, which was attributed the synergistic effects of the  $\text{TiO}_2$  shell with  $\text{Co}_3\text{O}_4$  facilitating the promotion of oxidation.<sup>116</sup> A 50% conversion at  $136^\circ\text{C}$  was reached with a  $\text{Co}_1@\text{TiO}_2 (\text{Zn}_0)$  (13 wt% Co) nanorattle catalyst and a 50% conversion at  $138^\circ\text{C}$  with a  $\text{Co}_1@\text{TiO}_2 (\text{Zn}_1)$  (6.6 wt% Co) nanorattle catalyst. These activities were significantly improved as the Co loadings in the  $\text{TiO}_2$  based nanorattle catalysts were lower than for their  $\text{SiO}_2$  counterparts. The  $\text{Co}_3\text{O}_4$  nanoparticle size distributions were between 5-40 nm in the  $\text{Co}_1@\text{TiO}_2 (\text{Zn}_0)$  (13 wt% Co) and 5-7 nm in the  $\text{Co}_1@\text{TiO}_2 (\text{Zn}_1)$  (6.6 wt% Co). However, the nanoparticles were difficult to distinguish from the  $\text{TiO}_2$  shells in the TEM images, due to their similar atomic weights, see Appendix B. These findings proved that the presented procedure can be easily adapted to derive sinter-stable nanorattle catalysts with tunable properties.

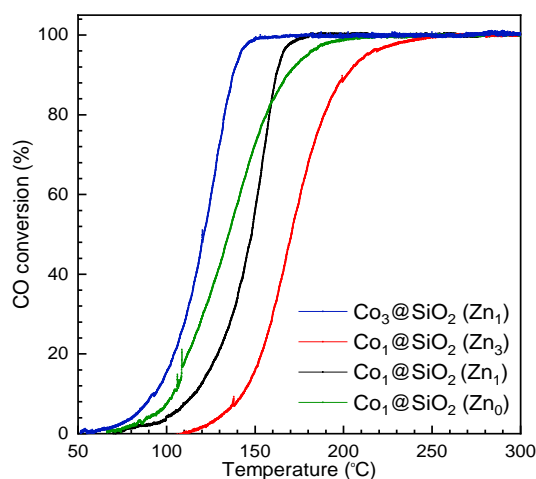


**Figure 4.13.:** CO oxidation light-off curves of the nanorattle catalysts  $\text{Co}_x/\text{SiO}_2 (\text{Zn}_y)$  prepared with different Co/Zn ratios.

**Table 4.5.:** Overview of the results from the CO oxidation reactions.

Entry	Material	T <sub>50</sub> (°C) <sup>a</sup>
1	Co <sub>1</sub> /SiO <sub>2</sub> (Zn <sub>0</sub> ) (-/550)	160
2	Co <sub>1</sub> /SiO <sub>2</sub> (Zn <sub>0</sub> ) (600/550)	160
3	Co <sub>1</sub> /SiO <sub>2</sub> (Zn <sub>0</sub> ) (600/300)	134
4	Co <sub>1</sub> NC/SiO <sub>2</sub> (Zn <sub>0</sub> ) (600/-) up	208
5	Co <sub>1</sub> NC/SiO <sub>2</sub> (Zn <sub>0</sub> ) (600/-) down	134
6	Co <sub>1</sub> /SiO <sub>2</sub> (Zn <sub>0</sub> ) (-/550)	205
7	Co <sub>3</sub> /SiO <sub>2</sub> (Zn <sub>1</sub> )	120
8	Co <sub>1</sub> /SiO <sub>2</sub> (Zn <sub>3</sub> )	170
9	Co <sub>1</sub> /SiO <sub>2</sub> (Zn <sub>1</sub> )	147
10	Co <sub>1</sub> /SiO <sub>2</sub> (Zn <sub>0</sub> )	134

<sup>a</sup> T<sub>50</sub> is the temperature (°C) reached at a CO conversion of 50% to CO<sub>2</sub>.

## 4.4 Summary

Chapter 4 was based on my two publications from Catalysis Communications<sup>1</sup> and Topics in Catalysis<sup>43</sup>, where the idea was to synthesize sinter-stable nanorattle catalysts with controllable properties tested in a CO oxidation reaction as a proof of concept. To accomplish this, I exploited ZIF-67 and ZIF-8 as sacrificial templates and metal precursors to form high surface area mesoporous SiO<sub>2</sub> shells with encapsulated Co<sub>3</sub>O<sub>4</sub> nanoparticles. Here, several modifications of the thermal treatments were performed, in order to control the three-dimensional dispersion and size distribution of the Co<sub>3</sub>O<sub>4</sub> nanoparticles. Moreover, alterations in the Co/Zn ratio of the precursor ZIF crystals were performed. The effect of these modifications was tested in the CO oxidation reaction. The alterations in the thermal treatment of the nanorattle catalysts revealed that the introduction of a prior carbonization step to the calcination could lower the calcination temperature from 500°C to 300°C. This resulted in reduced nanoparticles sintering leading to an improved activity of the Co<sub>1</sub>/SiO<sub>2</sub> (Zn<sub>0</sub>) (600/300) nanorattle catalyst in the CO oxidation reaction, reaching a 50% conversion at 134°C in comparison to the Co<sub>1</sub>/SiO<sub>2</sub> (Zn<sub>0</sub>) (600/550) nanorattle catalyst reaching a 50% conversion at 160°C. Additionally, the three-dimensional dispersion of the encapsulated Co and Co<sub>3</sub>O<sub>4</sub> nanoparticles in SiO<sub>2</sub> shells were illustrated by electron tomography. From the modifications in the Co/Zn ratios of the ZIF precursor crystals, it was found that it was possible to control different properties of the resulting nanorattle catalysts. Nanorattle

catalysts were synthesized with different particle sizes between 40-350 nm. Moreover, the Co loadings of the nanorattle catalysts were altered between 0-27 wt%. Even at high Co loadings, these nanorattle catalysts held small-sized and well-dispersed nanoparticles of 2-20/2-25 nm in diameter. The catalytic performance was dependent on the Co loading, where the nanorattle catalysts  $\text{Co}_x/\text{SiO}_2$  ( $\text{Zn}_y$ ) prepared with a Co/Zn ratio of 3:1, 1:1, 1:0 all showed similar performance in the CO oxidation reaction with a calculated TOF of  $1.2 \cdot 10^{-1} \text{ min}^{-1}$ . A Co/Zn ratio of 1:3 in the precursor ZIF crystal resulted in a less efficient catalyst for the CO oxidation reaction as a result of remaining Zn in the nanorattle catalyst. Thus, it is important to make sure all the Zn has been evaporated in the carbonization. The use of MOFs as sacrificial templates and metal precursors opens up a new pathway to prepare sinter-stable nanorattle catalysts with tunable properties. Hopefully, the great control and simplicity of this synthesis procedure can inspire further pathways to prepare novel sinter-stable catalysts with improved catalytic performances in the CO oxidation reaction.



## **Chapter 5.      Selective Oxidation of Methanol to Formaldehyde**

---

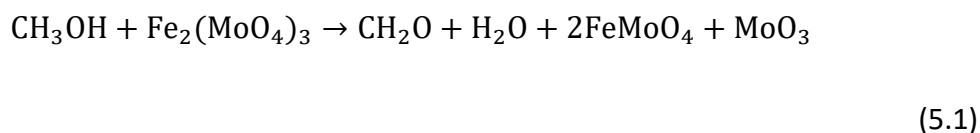
In this chapter, I describe my work with encapsulation of iron molybdate catalysts in mesoporous silica spheres and zeolites in order to attain a non Mo-leaching catalyst. These catalysts are prepared by impregnations of porous hollow SiO<sub>2</sub> spheres and desilicated silicalite-1 zeolites, which hold different average pore sizes. These encapsulated iron molybdate catalysts were characterized and tested for the selective oxidation of methanol to formaldehyde, where the current industrial catalyst suffers from a short lifetime due to Mo leaching. This chapter is based on my work performed in collaboration with PhD student Joachim Thrane, Assistant Professor Martin Høj and Professor Anker Degn Jensen from DTU Chemical Engineering, Department of Chemical and Biochemical Engineering. In this collaboration, I prepared the synthesized catalysts and PhD student Joachim Thrane performed the catalytic tests.

---

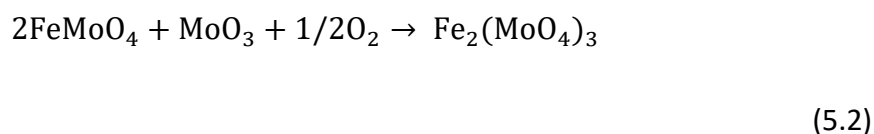


## 5.1 Introduction

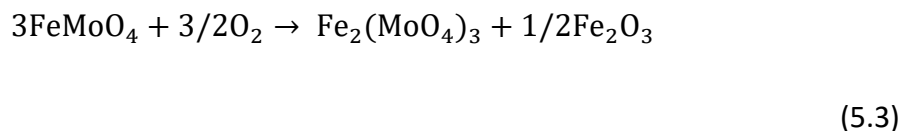
In 2017 the production of formaldehyde had increased to roughly 52 million tons. This amount is predicted to grow further in the coming years.<sup>128,129</sup> Formaldehyde is a central C1 building block used in the production of high valued synthetic resins. In the industry, formaldehyde is primarily produced from methanol in a selective oxidation process, using a silver or an iron molybdate catalyst. Typically the iron molybdate catalyst is preferred over the silver based catalyst, as the reaction occurs at lower temperatures with an iron molybdate catalyst (<350°C) in comparison to a silver based catalyst (>500°C).<sup>130</sup> The iron molybdate catalysts consist of a crystalline  $\text{Fe}_2(\text{MoO}_4)_3$  phase and  $\text{MoO}_3$ , catalyzing methanol to formaldehyde with a yield of 88-92% according to Equation 5.1.<sup>17</sup> The crystalline  $\text{Fe}_2(\text{MoO}_4)_3$  phase is subsequent regenerated by the reaction with  $\text{MoO}_3$ , see Equation 5.2.



In the industrial iron molybdate catalyst an excess of crystalline  $\text{MoO}_3$  ( $\text{Mo}/\text{Fe} > 1.5$ ) is necessary as Mo leaching is a major problem. Mo segregates from  $\text{Fe}_2(\text{MoO}_4)_3$  by the formation of volatile species with methanol at the reaction conditions (270-400°C). These volatile Mo species formed at hot spots of high methanol concentrations moves down the reactor bed where it accumulates. This eventually can lead to a significant pressure drop and finally, a reaction shutdown. Thus, the leaching result in not only a limited mechanical strength, but also a limited lifetime of the iron molybdate catalyst. The average lifetime of an iron molybdate catalyst in the industry is restricted to 1-2 years depending on the reaction conditions. The role of the crystalline excess of  $\text{MoO}_3$  has been widely discussed in literature, where crystalline  $\text{MoO}_3$  has been suggested to act as a reservoir to replenish an amorphous surface layer of active  $\text{MoO}_x$  on  $\text{Fe}_2(\text{MoO}_4)_3$ .<sup>131,132</sup> In contrary, it has also been suggested that the presence of crystalline  $\text{MoO}_3$  is required to re-oxidize the surface back to the active  $\text{Fe}_2(\text{MoO}_4)_3$  phase according to Equation 5.2.<sup>17,130</sup>



Therefore, in the case of crystalline  $\text{MoO}_3$  depletion, the formation of hematite follows according to Equation 5.3.<sup>17</sup>



In either case, as the content of crystalline  $\text{MoO}_3$  is reduced as a result of leaching, an increased formation of the iron-rich  $\text{FeMoO}_4$  and  $\text{Fe}_2\text{O}_3$  phases arises, which are more selective towards CO and  $\text{CO}_2$ , respectively. Thus, a typical iron molybdate catalyst has a Mo/Fe= 2-3 to guarantee excess of crystalline  $\text{MoO}_3$ . This excess of crystalline  $\text{MoO}_3$ , independent of its exact role, ultimately ensures a sufficient catalytic activity, a selectivity towards formaldehyde and a prolonged catalyst lifetime. Traditionally iron molybdate catalysts are made from either co-precipitation or a hydrothermal method from highly soluble and accessible reagents; iron nitrate nonahydrate as a source of Fe and ammonium heptamolybdate tetrahydrate as a source of Mo.<sup>130,133</sup> The crystalline  $\text{Fe}_2(\text{MoO}_4)_3$  phase is nearly always achieved during calcination, as it is the most thermodynamically stable phase.

The short lifetime of the iron molybdate catalyst, as a result of Mo leaching, has amplified the interest for the development of a more stable catalyst with limited Mo leaching. The work presented in this chapter aimed to synthesize an iron molybdate catalyst with enhanced stability towards leaching. Additionally, this iron molybdate catalyst should remain highly active and selective for the selective oxidation of methanol to formaldehyde. Encapsulation within porous nanomaterials has been proposed to be an effective method to develop non-leaching catalysts in literature.<sup>11</sup> Encapsulation of the iron molybdate catalyst within a porous structure might prevent fast diffusion of the volatile species away from the leached catalyst, which ultimately increases the chance of catalyst regeneration. In general, the encapsulation can be addressed by two approaches; 1) the synthesis of the porous structure first followed by the synthesis of the active catalyst within it or 2) the synthesis of the active catalyst first followed by the synthesis of the porous structure encapsulating it. In this work, the first approach was chosen, the so-called ship-in-a-bottle method. This approach was chosen due to the high stability of silica in acidic media. The iron molybdate catalyst is synthesized at a low pH due to the acidic iron(III) precursor solution, whereas the preparation of silica often requires alkaline synthesis conditions.<sup>134</sup> Therefore, the different porous silica-based structures, hollow  $\text{SiO}_2$  spheres and desilicated silicalite-1, were prepared first followed by impregnation with the iron molybdate precursors to form the crystalline  $\text{Fe}_2(\text{MoO}_4)_3$

and  $\text{MoO}_3$  phases, see Figure 5.1 for a schematic of the synthesis route to yield the  $\text{FeMo@SiO}_2$  catalyst. The dimensions of the porous structures are crucial when developing non-leaching iron molybdate catalysts. The porous structure has to hold the right dimensions since it needs to ensure enhanced confinement of Mo, as well as maintaining mass transfer of the substrates and products within the porous material. In this chapter, mesoporous hollow  $\text{SiO}_2$  spheres with pore opening diameters of 2.30 nm and desilicated MFI framework zeolite silicalite-1 with pore dimensions down to 0.51 x 0.55 nm, were used to encapsulate the iron molybdate catalyst. Other zeolites were initially screened as supports, such as hollow silicalite-1 zeolites and steam-assisted recrystallized zeolites prepared according to Dai *et al.*<sup>135</sup> and Rasmussen *et al.*<sup>136</sup> However, based on characterization and initial screenings of the derived iron molybdate impregnated porous supports, I decided not to proceed with these catalysts. The chosen encapsulated iron molybdate catalysts, in hollow  $\text{SiO}_2$  spheres and desilicated silicalite-1 zeolites, were characterized and then tested at DTU Chemical Engineering in their reactor setup for the selective oxidation of methanol to formaldehyde. The encapsulated iron molybdate catalysts were compared to an industrial iron molybdate catalyst to determine the effect of encapsulation on the overall activity and stability.

## 5.2 Experimental Details

### 5.2.1 Material Preparations

Reagents were acquired from a commercial source (Sigma-Aldrich), and used without additional purifications. The reagents include: iron(III) nitrate nonahydrate (99.99% trace metals basis), ammonium molybdate tetrahydrate (99.99% trace metals basis), tetraethyl orthosilicate (TEOS, 99.99% trace metals basis), hexadecyltrimethylammonium bromide (CTAB  $\geq 98\%$ ), concentrated ammonia solution (aqueous, 25-28%), Tetrapropylammonium hydroxide solution (TPAOH, 1.0 M in  $\text{H}_2\text{O}$ ) and absolute ethanol ( $\geq 99.8\%$ ).

#### Synthesis of Hollow $\text{SiO}_2$

The synthesis of the  $\text{SiO}_2$  spheres were based on the so-called Stöber process.<sup>119</sup> In a 2 L round-bottomed flask CTAB (1.5 g) was suspended in absolute ethanol (300 mL), water (500 mL) and an aqueous solution of concentrated ammonia 25-28% (10 mL). The

solution was mixed at 25°C followed by the fast addition of TEOS (10 mL) to the solution under vigorously stirring. The solution was left stirring at 25°C for 24 h. The white product was collected by centrifugation (12000 rpm for 10 min), washed three times with absolute ethanol and dried at 80°C for 24 h.

The core of the SiO<sub>2</sub> shells was removed by desilication. The white powder of SiO<sub>2</sub> spheres were dissolved in water (1600 mL) at 90°C for 48 h. The white product was collected by centrifugation (12000 rpm for 10 min), washed three times with absolute ethanol and dried 80°C for 24 h.

The final hollow SiO<sub>2</sub> spheres were calcined in a muffle furnace in static air at 550°C for 2 h with a heating ramp of 5°C min<sup>-1</sup>.

### **Synthesis of Desilicated Silicalite-1 Zeolite**

The synthesis of the desilicated silicalite-1 (D S1), (Top-down approach), was based on a modified literature procedure.<sup>137,138</sup> First silicalite-1 zeolites were prepared by a dropwise addition of TEOS (44.65 mL) to a 1M solution of TPAOH (72.65 mL) under stirring in a Teflon beaker. Then the solution was stirred for 1 h followed by hydrothermal crystallization in a 300 mL Teflon-lined stainless steel autoclave. The autoclave was heated to 180°C for 24 h at autogenous pressure. The product was collected by centrifugation (12000 rpm for 10 min), washed with water to a neutral pH and dried at 80°C for 24 h.

The white powder of silicalite-1 was then calcined in a muffle furnace in static air at 550°C for 20 h with a heating ramp of 5°C min<sup>-1</sup>.

The desilication of the silicalite-1 was prepared by dispersion of the silicalite-1 powder (2.0 g) in a solution of CTAB (1.4 g) in aqueous ammonia (200 mL) followed by 3 h of stirring at 25°C. The solution was then transferred to a Teflon-lined stainless steel autoclave. The autoclave was heated to 140°C for 24 h at autogenous pressure. The product was collected by centrifugation (12000 rpm for 10 min), washed with water to a neutral pH and dried at 80°C for 24 h.

The white powder of desilicated silicalite-1 was calcined in a muffle furnace in static air at 550°C for 5 h with a heating ramp of 5°C min<sup>-1</sup>.

## Impregnation with FeMo

The hollow  $\text{SiO}_2$  spheres or the desilicated silicalite-1 zeolites were impregnated by incipient wetness impregnation and/or vacuum impregnation to obtain a Fe/Mo ratio above 2. The vacuum impregnation was executed with a Fischer Scientific Chemical Diaphragm pump with a maximum vacuum of 2 mbar. The vacuum impregnation proceeded as followed:

Hollow  $\text{SiO}_2$  spheres or desilicated silicalite-1 zeolites (50 mg) was dispersed in a schlenk flask with ammonium molybdate tetrahydrate (4.0 g) dissolved in 10 mL of water. Then vacuum was applied to the system for 5 min to empty the pores of air. The vacuum was released to fill the pores with the precursor solution. The product was collected by centrifugation (12000 rpm for 10 min), washed three times with water and dried at  $80^\circ\text{C}$  for 24 h. The following day the procedure was repeated with the iron precursor. Here, the product was dispersed in a schlenk flask with iron(III) nitrate nonahydrate (0.25 g) dissolved in 10 mL of water. Here, the vacuum was similarly applied to the system for 5 min. The product was collected by centrifugation (12000 rpm for 10 min), washed three times with water and dried at  $80^\circ\text{C}$  for 24 h.

The FeMo impregnated hollow  $\text{SiO}_2$  spheres of desilicated silicalite-1 zeolites were calcined in a muffle furnace in static air at  $500^\circ\text{C}$  for 2 h with a heating ramp of  $5^\circ\text{C min}^{-1}$  to yield the final encapsulated iron molybdate catalysts.

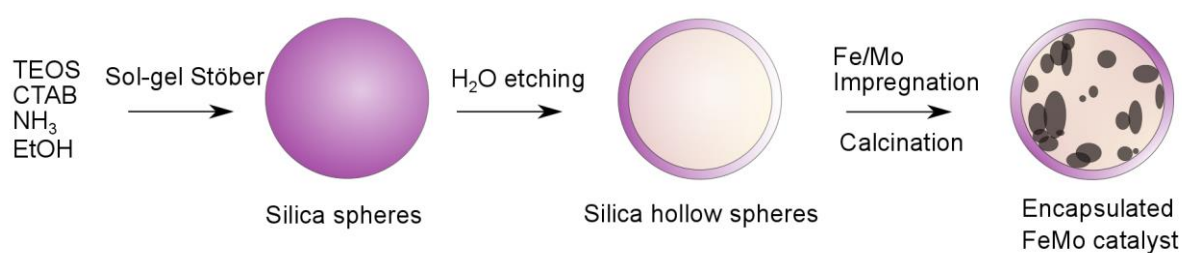


**Figure 5.1.:** A schematic of the synthesis procedure for yielding  $\text{FeMo@SiO}_2$ .

## 5.2.2 Characterization Methods

In order to explain the performance of the catalysts in the selective oxidation of methanol to formaldehyde, the prepared materials were characterized by several techniques. XRF was used to determine the Mo/Fe ratios and supported by Inductively Coupled Plasma (ICP) mass spectrometry. XRPD and Raman spectroscopy were used to confirm the iron molybdate structures. N<sub>2</sub> physisorption was used to determine the pore characteristics of the catalysts. SEM and TEM were used to identify the shape and the size of the encapsulated iron molybdate catalysts. Raman spectroscopy and ICP were performed by laboratory technicians at Haldor Topsøe according to Viegard *et al.*<sup>17</sup>

## 5.2.3 Catalytic Test Procedure

The selective oxidation of methanol to formaldehyde was tested by PhD student Joachim Thrane at DTU Chemical Engineering according to literature.<sup>17,131</sup> In brief, the catalysts were tested in a packed bed reactor. Prior to the test, the prepared catalyst powder was sieved to a 150-250  $\mu\text{m}$  fraction. Then 25 mg of the fractionated catalyst and 150 mg of SiC (fraction of 150-300  $\mu\text{m}$ ) to aid heat transfer were placed in a bed in the reactor (ID = 4 mm). The bed was positioned between two pieces of quartz wool to keep it in place. The reactor was then positioned in an oven. The feed gas contained a mixture of 5 vol.% MeOH and 10 vol.% O<sub>2</sub> in N<sub>2</sub>, where N<sub>2</sub> and O<sub>2</sub> were bubbled through a flask of MeOH. The flowrate of the feed was 150 NmL min<sup>-1</sup>, where the concentration of MeOH was controlled by cooling of the bubble-flask to 5°C. The temperature was measured with a thermocouple at the top of the catalyst bed controlled by a Siemens PLC running a PID loop. Here, LabView was used as interface. The effluent was analyzed by a Thermo Scientific Trace Ultra GC holding a TCD and FID detector. Quantifications were performed for MeOH, DME, DMM and MF by the FID detector, and CO and CO<sub>2</sub> by the TCD detector. The temperature in the reactor bed was ramped in steps to 350°C and the activity was measured up to 100h.

## 5.3 Results and Discussion

### 5.3.1 Catalytic Test Procedure

Table 5.1 provides an overview of the prepared materials and their impregnation technique. The metal loadings were quantified from XRF, where standards of known Fe/Mo ratios were used to prepare a calibration line. The FeMo loadings in the silica-based porous materials were 63-74 wt%. All iron molybdate catalysts held an excess of  $\text{MoO}_3$  ( $\text{Mo/Fe} > 1.5$ ) with Mo/Fe ratios typically above 2.0 as required, in order to compare them to the industrial catalyst with a Mo/Fe ratio of approximately 2.6. These quantified Mo/Fe ratios were confirmed by ICP performed at Haldor Topsøe. The Mo/Fe ratios for entry 3 and entry 4, FeMo@D S1, are not identical even though the vacuum impregnation was performed similarly with the same precursor amounts. The Mo/Fe ratios are added to the names of the FeMo@D S1 catalysts, entry 3 and entry 4, in brackets. This suggests that the impregnation technique is not 100% reproducible, as discussed in Chapter 1.

**Table 5.1.:** Overview of the prepared encapsulated FeMo catalysts.

Entry	Catalyst	Impregnation technique	Fe/Mo ratio
1	FeMo/SiO <sub>2</sub>	Incipient wetness impregnation	2.24
2	FeMo@SiO <sub>2</sub>	Vacuum impregnation	2.78
3	FeMo@D S1 (2.56)	Vacuum impregnation	2.56
4	FeMo@D S1 (2.39)	Vacuum impregnation	2.39

The names of the prepared materials are distinguished by the origin of the encapsulating silica or zeolite and the ratio of Fe/Mo in the catalyst. The at-sign (@) indicates encapsulated in and the slash-sign (/) indicates only partly encapsulated (supported on). D S1 is an abbreviation of desilicated silicalite-1.

### 5.3.2 XRPD and Raman spectroscopy

Figure 5.2 shows the diffraction patterns from XRPD of the fresh catalyst FeMo/SiO<sub>2</sub> and samples of the used catalyst taken from the feed inlet and outlet. The fresh FeMo/SiO<sub>2</sub> catalyst had the characteristic peaks of  $\text{Fe}_2(\text{MoO}_4)_3$  and  $\text{MoO}_3$  at  $2\theta$  degrees of 25.65° for  $\text{Fe}_2(\text{MoO}_4)_3$ , and 12.75°, 23.35° and 27.34° for  $\text{MoO}_3$ . However, the peaks were difficult to distinguish as a broad peak at  $2\theta$  degrees of 20° from the amorphous SiO<sub>2</sub> spheres was overlapping. The diffraction pattern of the FeMo/SiO<sub>2</sub> catalyst collected from the inlet of the methanol gas feed, which was recorded after the selective oxidation of methanol to formaldehyde, indicated leaching of Mo. It was very clear from

the diffraction pattern, which did not hold the same characteristic peaks of the iron molybdate catalyst, that severe leaching of Mo must have occurred. The peaks were in general too weak to be distinguished and the phases present of the used FeMo/SiO<sub>2</sub> catalyst (inlet) could not be identified. It is noteworthy that the Mo had not leached from the catalyst positioned at the outlet of the bed, which could be explained by the lower concentration of methanol it was exposed to. The knowledge gained from XRPD of the used incipient wetness impregnated iron molybdate catalyst led to the further impregnations by vacuum.

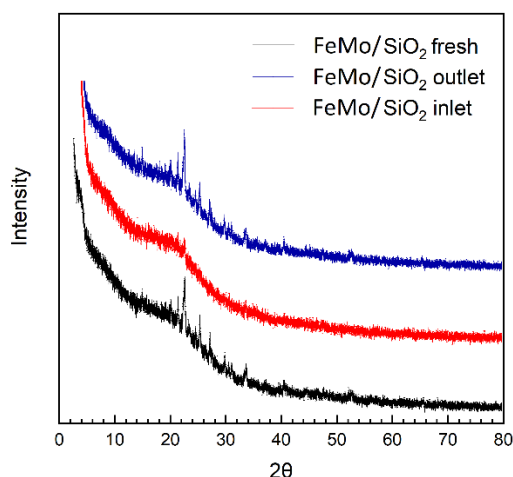


**Figure 5.2.:** *The diffraction patterns of the prepared FeMo/SiO<sub>2</sub> before the catalytic test and after, samples are taken from the feed gas inlet and outlet.*

To ensure the encapsulation of FeMo in the porous structures, the subsequently prepared catalysts were impregnated by vacuum to first empty the pores of air and fill them with the aqueous solution of the metal precursors. The diffraction patterns from XRPD analysis of the prepared materials FeMo@SiO<sub>2</sub>, FeMo@D S1 (2.56) and the desilicated silicalite-1 support can be seen in Figure 5.3. The diffraction pattern of the catalyst FeMo@SiO<sub>2</sub> shows the characteristic peaks of Fe<sub>2</sub>(MoO<sub>4</sub>)<sub>3</sub> and MoO<sub>3</sub> at  $2\theta$  degrees of 12.75°, 23.35°, 25.65° and 27.34°. <sup>17</sup> An additional peak positioned at a  $2\theta$  degree equal to 20° was also visible deriving from amorphous SiO<sub>2</sub>. However, the characteristic peaks of Fe<sub>2</sub>(MoO<sub>4</sub>)<sub>3</sub> and MoO<sub>3</sub> could not be identified from the diffraction pattern of FeMo@D S1 (2.56). As the crystalline framework of the silicalite-1 zeolite holds very distinctive peaks in XRPD, the peaks can disguise the presence of Fe<sub>2</sub>(MoO<sub>4</sub>)<sub>3</sub> and MoO<sub>3</sub>, as seen in Figure 5.3. As XRPD only revealed the crystalline framework of the silicalite-1 zeolite, Raman spectroscopy was used to supplement the confirmation of Fe<sub>2</sub>(MoO<sub>4</sub>)<sub>3</sub> and MoO<sub>3</sub> presence in the desilicated silicalite-1 zeolite.



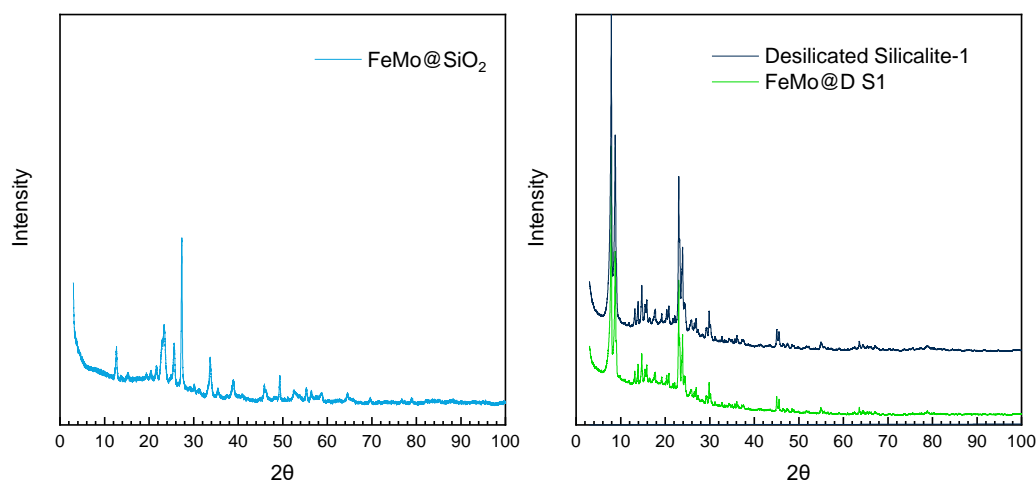


**Figure 5.3.:** The diffraction patterns of the prepared FeMo@SiO<sub>2</sub> and the FeMo@D S1 (2.56) as well as the desilicated silicalite-1 support.

The Raman spectra of the FeMo@D S1 (2.56) catalyst can be seen in Figure 5.4. From the Raman spectra, bands at 665, 818 and 993 cm<sup>-1</sup> from MoO<sub>3</sub> could be identified. Additionally, bands belonging to Fe<sub>2</sub>(MoO<sub>4</sub>)<sub>3</sub> were present at 782 and 966 cm<sup>-1</sup>.<sup>17</sup> Thus, the presence of the iron molybdate phases were confirmed by Raman spectroscopy.

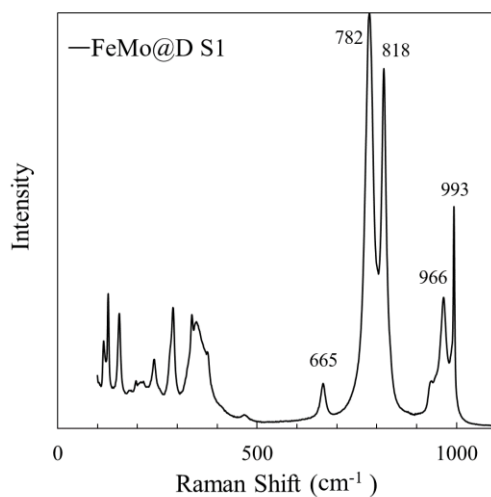


**Figure 5.4.:** The Raman spectra of the FeMo@D S1 (2.56) catalyst.

### 5.3.3 N<sub>2</sub> Physisorption

The isotherms of the FeMo@SiO<sub>2</sub> and FeMo@D S1 (2.56) catalysts can be seen in Figure 5.5. The isotherm of the FeMo@SiO<sub>2</sub> catalyst was of Type IV, typical for mesoporous materials, which supported the encapsulation of FeMo in mesoporous SiO<sub>2</sub> spheres. The small hysteresis was attributed to capillary condensation, which is characteristic for mesopores. The isotherm of the FeMo@D S1 catalyst was of Type I, which is typical for microporous materials as zeolites. The isotherm held a small Hysteresis loop at  $p/p^0$  of 0.15, which is characteristic for N<sub>2</sub> in MFI micropores. This hysteresis has been explained in literature as a fluid-to-crystal-like phase transition.<sup>139</sup> Another H4 Hysteresis loop was present closing around  $p/p^0$  of 0.45, which was assigned to intraparticle voids and mesopores in the desilicated zeolite. The presence of intraparticle voids and mesopores in the desilicated silicalite-1 derived from the desilication procedure in aqueous alkaline solution and CTAB. Here, the role of the alkaline solution and CTAB is explained in literature by Mielby *et al.*<sup>138</sup> reporting that the alkaline solution dissolves Si-O-Si bonds in the silicalite-1 and the surfactant CTAB is added to protect the silicalite-1 structure from nonuniform leaching.

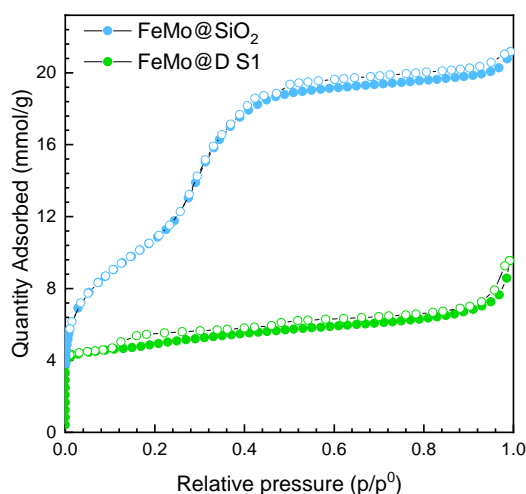


**Figure 5.5.:** The N<sub>2</sub> physisorption isotherms of FeMo@SiO<sub>2</sub> and FeMo@D S1 catalysts.

Table 5.2 presents the N<sub>2</sub> physisorption analysis data. The FeMo@SiO<sub>2</sub> catalyst, entry 1, had a high specific surface area of 1008 m<sup>2</sup> g<sup>-1</sup>, where the majority of it (941 m<sup>2</sup> g<sup>-1</sup>) was attributed to the external surface area of the SiO<sub>2</sub> shell. The high pore volume derived from the mesoporous SiO<sub>2</sub> and the pores held an average diameter of 2.30 nm. The FeMo@D S1 (2.56), entry 2, had a high specific surface area of 411 m<sup>2</sup> g<sup>-1</sup> in comparison to a standard non-desilicated silicalite-1, deriving from the additional mesopores

introduced by desilication of the microporous structure.<sup>137</sup> Furthermore, the pore volumes were increased in comparison to a standard silicalite-1, however, a large percentage of the pore volume was still ascribed to the micropore volume.<sup>140</sup> The average diameter of the pores was measured to 0.56 nm, which is similar to the value found in the literature.<sup>141</sup>

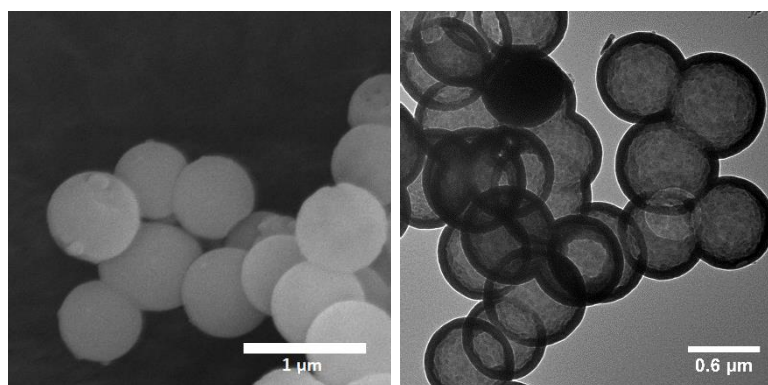
**Table 5.2.:** Overview of results from N<sub>2</sub> physisorption analysis.

Entry	Catalyst	$S_{\text{BET}}^{\text{a}}$ (m <sup>2</sup> /g)	$S_{\text{ext}}^{\text{b}}$ (m <sup>2</sup> /g)	$V_{\text{micro}}^{\text{b}}$ (cm <sup>3</sup> /g)	$V_{\text{tot}}^{\text{c}}$ (cm <sup>3</sup> /g)	Pore width (Å)
1	FeMo@SiO <sub>2</sub>	1008	941	n/a	0.697	23.0
2	FeMo@D S1	411	173	0.095	0.267	5.6

<sup>a</sup> Specific surface area determined by the BET method, <sup>b</sup> external surface area and micropore volume determined by the t-plot method and <sup>c</sup> total pore volume determined by a single point read at  $p/p^0=0.95$ .

### 5.3.4 SEM and TEM

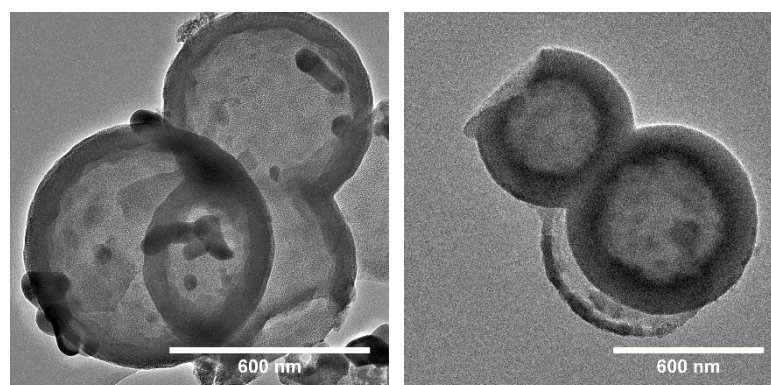
Representative SEM and TEM images of the prepared hollow SiO<sub>2</sub> spheres can be seen in Figure 5.6. The SEM and the TEM images of the hollow SiO<sub>2</sub> spheres showed uniform spheres of 600 nm in diameter. The hollow structures were verified with TEM, as the images illustrated darker outer spheres verifying the presence of a shell with a thickness of around 100 nm in diameter.



**Figure 5.6.:** SEM image and TEM image of the hollow SiO<sub>2</sub> spheres.

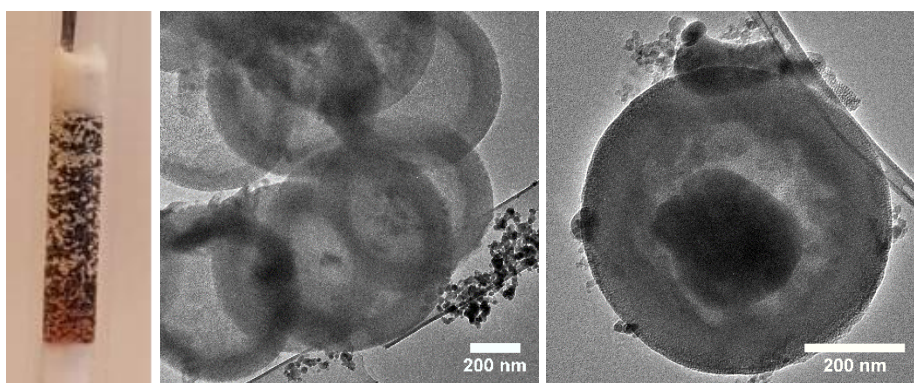
TEM images of the FeMo/SiO<sub>2</sub> and the FeMo@SiO<sub>2</sub> catalysts can be seen in Figure 5.7. The TEM image of the FeMo/SiO<sub>2</sub> prepared by incipient wetness revealed the presence of crystalline FeMo phases on the surface of the hollow SiO<sub>2</sub> spheres. In comparison, the

FeMo@SiO<sub>2</sub> prepared by vacuum impregnation appeared to encapsulate the FeMo fully. The FeMo appeared as dark spots of 10-100 nm in diameter in the TEM images due to the high atomic weight of Fe and Mo. In order to ensure full encapsulation of the FeMo and potentially limit the Mo leaching, vacuum impregnation was chosen as the desired technique to impregnate the hollow SiO<sub>2</sub> spheres and the desilicated silicalite-1. To support this decision, TEM images from the inlet and the outlet of the reactor bed of the FeMo/SiO<sub>2</sub> catalyst prepared by incipient wetness impregnation used in the selective oxidation were examined, see Figure 5.8.



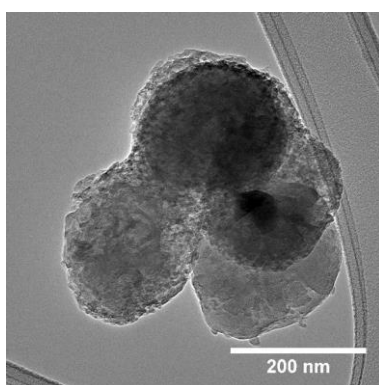
**Figure 5.7.:** TEM images of (left) the FeMo/SiO<sub>2</sub> and (right) the FeMo@SiO<sub>2</sub> catalyst.

Figure 5.8 shows an image of the reactor bed and TEM images of the used FeMo/SiO<sub>2</sub> catalyst. The methanol feed was introduced from the bottom of the bed (inlet). It is clear from the image, Figure 5.8(left), that a colour change at the inlet from yellow to brown of the iron molybdate catalyst had occurred after 100h on stream. This indicated leaching of the Mo, which leaves iron-rich phases of FeMoO<sub>4</sub> and Fe<sub>2</sub>O<sub>3</sub> in the inlet also commonly observed for the industrial catalyst.<sup>17</sup> TEM images were acquired of the used catalyst positioned at the inlet (Figure 5.8(middle)) and the outlet (Figure 5.8(right)) of the reactor bed. The TEM image of the FeMo/SiO<sub>2</sub> from the inlet of the bed showed no FeMo remaining at the hollow SiO<sub>2</sub> surfaces, whereas the TEM image of the FeMo/SiO<sub>2</sub> from the outlet of the bed had preserved FeMo on the surface. Thus, the TEM images suggested significant leaching of Mo from the FeMo/SiO<sub>2</sub> catalyst positioned at the inlet of the reactor bed where the methanol concentration was the highest. The FeMo/SiO<sub>2</sub> catalyst positioned at the outlet of the bed was shielded from Mo leaching. Thus, the Mo leaching resulted in an uneven degradation of the reactor bed.



**Figure 5.8.:** (Left) an image of the packed reactor bed, a TEM image (middle) of the used FeMo/SiO<sub>2</sub> from the inlet of the catalyst bed, and (right) of the FeMo/SiO<sub>2</sub> catalyst from the outlet of the catalyst bed.

The TEM image in Figure 5.9 shows the FeMo@D S1 (2.56) catalyst. Here, the desilicated silicalite-1 crystals of 200 nm can be seen with mesopores within the structures deriving from the desilication process. Based on a range of TEM images, dark spots of FeMo up to 100 nm was visible in the TEM images, which appeared to be primarily encapsulated within the zeolites. Additional SEM and TEM images of all the encapsulated iron molybdate catalysts can be found in the Appendix C.



**Figure 5.9.:** TEM image of the FeMo@D S1 (2.56).

### 5.3.5 The Selective Oxidation of Methanol to Formaldehyde

Figure 5.10 and Table 5.3 present the activities and selectivities of the catalysts, FeMo@SiO<sub>2</sub>, FeMo@D S1 (2.56), FeMo@D S1 (2.39) and the industrial reference catalyst, for the selective oxidation of methanol to formaldehyde. The conversions and

selectivities were corrected for reversible by-product formation according to Thrane *et al.*<sup>131</sup>, which is described in brief in Appendix C. Thus, Figure 5.11 illustrates the corrected conversion vs. corrected selectivity to formaldehyde vs. time on stream (TOS). The activity and selectivity were evaluated at 350°C for a period of up to 100h, which is simulated accelerated deactivation conditions to test the stability of the catalysts. The poor activity and selectivity of the catalyst FeMo/SiO<sub>2</sub> were not included in Figure 5.10 and Table 5.3, as the encapsulation of FeMo was not successful with the incipient wetness impregnation. The activities and selectivities of all the prepared encapsulated iron molybdate catalysts, as well as the industrial reference catalyst, decreased with the time on stream. However, all catalysts, except FeMo@D S1 (2.56), reactivated after approximately 50-80 h on stream. This small reactivation was previously reported with the industrial catalyst by Viegaard *et al.*<sup>17</sup>, which suggested that the reactivation begins when all excess crystalline MoO<sub>3</sub> had evaporated. Thus, this indicated that FeMo@D S1 (2.56) still had preserved crystalline MoO<sub>3</sub> in the catalyst, which could be a result of restricted Mo leaching due to encapsulation. In general, the selectivities remained high after 100 h for all catalysts (96.9%-99.0%) with low amounts of over-oxidated products CO and CO<sub>2</sub> formed. The majority of the by-products formed were dimethyl ether (DME), 1,1-dimethoxymethane (DMM) and methyl formate (MF), which are reversible and partly reversible by-products commonly formed. The non-corrected activities can be seen plotted in Appendix C. The FeMo@D S1 (2.56) catalyst showed the highest activity under the tested reaction conditions with a corrected conversion from 61.3%-18.6% after 0-100 h. In comparison, the industrial reference catalyst with the most similar Mo/Fe ratio had a corrected conversion from 46.0%-10.4% after 0-100 h. Despite the high measured activity of the FeMo@D S1 (2.56) catalyst in the selective oxidation, the catalyst still suffered from deactivation after 100 h. This suggested that the encapsulation in desilicated silicalite-1 did not hinder all Mo from leaching. The FeMo@D S1 (2.39) catalyst prepared by the same procedure showed significantly lower activity for the selective oxidation with a corrected conversion measured from 44.9%-11.0% after 0-100 h. The performance of the FeMo@D S1 (2.39) catalyst was similar to the industrial reference catalyst, which suggested that this catalyst did not sufficiently limit the leaching of Mo as indicated with the FeMo@D S1 (2.56) catalyst. However, the activity of the iron molybdate catalyst did not decrease by becoming encapsulated in desilicated silicalite-1. Therefore, it was determined that the encapsulation in desilicated silicalite-1 was not the perfect solution to the Mo leaching problem, as the synthesis was not fully reproducible. The difference in activities of the FeMo@D S1 catalysts was suggested to derive from variations in the surface area and pore volume as well as the vacuum impregnation. Unfortunately, it was not possible to further examine the used FeMo@D S1 catalysts after the selective oxidation as the amount of

catalyst left was too little (<25 mg). The FeMo@SiO<sub>2</sub> catalyst had a corrected conversion from 32.7%-15.9% with the lowest overall activity. This was attributed to the much larger pore size in the FeMo@SiO<sub>2</sub> catalyst of 2.30 nm in comparison to the FeMo@D S1 catalyst of 0.56 nm in diameter. Based on all results obtained in this work a pore size of 0.56 nm in diameter or lower is suggested to be required to limit any leaching of volatile Mo species. The deactivation of iron molybdate catalysts has been examined thoroughly in literature,<sup>17,130</sup> where alternative catalysts have been suggested for the selective oxidation of methanol to formaldehyde.<sup>131,142</sup> However, encapsulation of the iron molybdate catalyst in porous materials has not before been investigated as a solution to the leaching of Mo, as presented in this work. The encapsulation in porous materials might not be the most stable and perfect solution in the industrial selective oxidation of methanol to formaldehyde. However, this work can hopefully inspire and contribute to the development of future non-leaching catalysts.

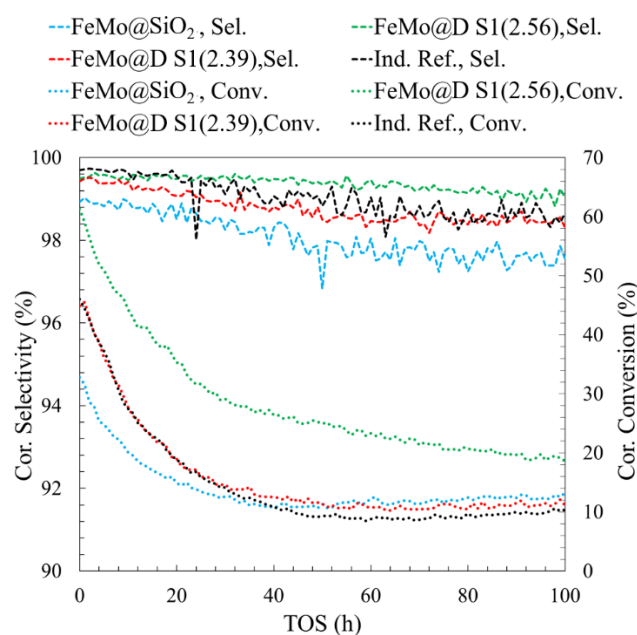


**Figure 5.10.:** The corrected selectivity (%) vs. corrected conversion (%) vs. TOS (h) for the encapsulated FeMo catalysts and an industrial reference catalyst in the selective oxidation of methanol to formaldehyde. The tests were performed with 25 mg of catalyst mixed with 150 mg SiC at 350°C, 150 NmL min<sup>-1</sup>, 5% MeOH and 10% O<sub>2</sub> in N<sub>2</sub>.



**Table 5.3.:** Overview of the corrected conversions and selectivities of the catalysts for the selective oxidation of methanol to formaldehyde.

Entry	Catalyst	Corrected conversion (%)	Corrected selectivity (%)
1	Industrial reference catalyst	46.0-10.4	99.7-98.7
2	FeMo@SiO <sub>2</sub>	32.7-15.9	98.9-96.9
3	FeMo@D S1 (2.56)	61.3-18.6	99.5-99.0
4	FeMo@D S1 (2.39)	44.9-11.0	99.4-98.3

The corrected conversions and selectivities are presented in a range from the initial activity to the final activity measured.

## 5.4 Summary

Chapter 5 was based on my work performed in collaboration with PhD student Joachim Thrane, Assistant Professor Martin Høj and Professor Anker Degn Jensen from DTU Chemical Engineering, Department of Chemical and Biochemical Engineering. Here, the idea was to synthesize a non-leaching iron molybdate catalyst for the selective oxidation of methanol to formaldehyde. To accomplish this, I synthesized porous materials of different pore sizes, hollow SiO<sub>2</sub> spheres and desilicated silicalite-1 zeolites, intended to encapsulate the iron molybdate catalyst to limit leaching of Mo by restricting its fast diffusion through the pores of the materials. The iron molybdate catalysts were prepared by either incipient wetness impregnation or vacuum impregnation. The vacuum impregnation technique was chosen as the best approach to introduce FeMo into the porous materials as it resulted in successful encapsulation. The derived catalysts obtained the correct crystalline Fe<sub>2</sub>(MoO<sub>4</sub>)<sub>3</sub> and MoO<sub>3</sub> phases verified by XRPD and Raman spectroscopy. All prepared catalysts held an excess of crystalline MoO<sub>3</sub>, with Mo/Fe ratios between 2.24-2.78 confirmed by XRF and ICP. The performance of the catalysts, FeMo@SiO<sub>2</sub>, FeMo@D S1 (2.56) and FeMo@D S1 (2.39) were all compared with the industrial reference catalyst under simulated accelerated deactivation conditions to test the stability of the catalysts. The catalysts all held high corrected selectivities towards formaldehyde of 99.5-96.9% similar to the industrial reference catalyst. However, the corrected conversions varied for the catalysts. Here, the FeMo@D S1 (2.56) showed the highest activity with a corrected conversion from 61.3%-18.6% at 350°C from 0-100 h. This performance indicated that encapsulation was successful and it limited the leaching of Mo to some degree. However, the synthesis procedure of the FeMo@D S1 catalyst had issues with reproducibility, as the catalyst



FeMo@D S1 (2.39) prepared similarly did not perform as expected, but performed similarly to the industrial reference catalyst. Thus, the encapsulation in desilicated silicalite-1 was promising but required a reproductive synthesis procedure. The FeMo@SiO<sub>2</sub> catalyst with an average pore size of 2.30 nm in diameter appeared to hold too large pore sizes to restrict Mo from leaching. Thus, based on these findings, a small pore size of <0.56 nm was suggested to be necessary to restrict Mo from leaching. This work illustrated how encapsulation of iron molybdate catalysts in small pore sized porous materials to some degree limits the leaching of Mo. Hopefully, this work can inspire the design of future non-leaching catalysts by encapsulating the active catalyst within nano-engineered porous materials.

## **Chapter 6.      Phenyl Acetate Fries Rearrangement and OxFA Process**

---

In this chapter, I describe my work with encapsulation of heteropolyoxometalates in zeolites in order to attain non-leaching high surface area heterogeneous catalysts. The heteropolyoxometalates include  $\text{H}_3\text{PW}_{12}\text{O}_{40}$ ,  $\text{H}_3\text{PMo}_{12}\text{O}_{40}$  and  $\text{H}_8\text{PV}_5\text{Mo}_7\text{O}_{40}$  encapsulated in recrystallized silicalite-1 zeolites. The encapsulated catalysts were characterized and tested in a phenyl acetate Fries rearrangement reaction and for the production of formic acid from biomass by selective catalytic oxidation (the OxFA process). The phenyl acetate Fries rearrangement was chosen as a model reaction to test the encapsulated  $\text{H}_3\text{PW}_{12}\text{O}_{40}$  and  $\text{H}_3\text{PMo}_{12}\text{O}_{40}$  catalysts as acidic heterogeneous catalysts. The OxFA process was chosen to test the encapsulated  $\text{H}_8\text{PV}_5\text{Mo}_7\text{O}_{40}$  catalyst as a redox-active heterogeneous catalyst. The chapter is based on my work performed in collaboration with PhD student Anna Bukowski, PhD student Dorothea Voss and Dr. Ing. Jakob Albert at the Institute of Chemical Engineering, Friedrich-Alexander University (FAU), in Erlangen Germany. In this collaboration, Dr. Ing. Jakob Albert was my external supervisor. Anna Bukowski and Dorothea Voss assisted me with the OxFA process tests.

---

## 6.1 Introduction

Polyoxometalates (POMs) are polyatomic anions consisting of three or more transition metal atoms in their highest oxidation state linked by oxygen atoms. Typically, the metal atoms are from group five (e.g.  $V^{5+}$ ) or six (e.g.  $Mo^{6+}$  or  $W^{6+}$ ). POMs include the two major groups; isopolyoxometalates- isopoly acids (IPAs), and heteropolyoxometalates- heteropoly acids (HPAs). The most commonly applied heteropolyoxometalate structure in catalysis is the Keggin-type with the anion formula  $[XM_{12}O_{40}]^{3-}$ .<sup>143</sup> Here, X is a heteroatom like P or Si. The M is a transition metal like W or Mo, also called the addenda atom. The HPA anion is comprised of a central tetrahedron  $XO_4$  with twelve octahedral  $MO_6$  surrounding it,<sup>144</sup> see Figure 6.1.

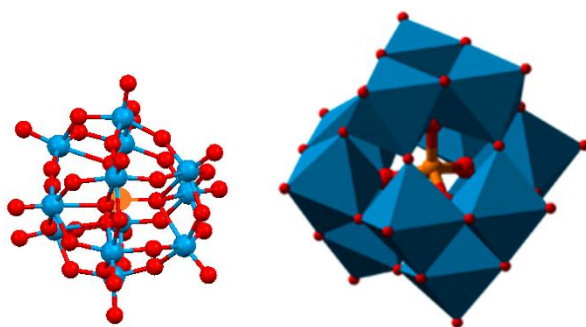


**Figure 6.1.:** The structure of a Keggin-type heteropolyoxometalate built by octahedral  $MO_6$  units surrounding a central  $XO_4$  unit. Adapted from Lefebvre et al.<sup>145</sup>

Some of the so-called addenda atoms M can be substituted with other transition metals like V, Cr or Mn, which results in the general anion formula  $[XY_nM_{12-n}O_{40}]^{(3+n)-}$ . The HPAs are typically more stable than IPAs due to the central  $XO_4$  unit's interaction with the  $MO_6$  units in the HPAs. Besides the higher thermal stabilities of the Keggin-type HPAs (465°C for  $H_3PW_{12}O_{40}$ ), the Keggin-type HPAs are also favored because of their more simple preparation methods.<sup>143</sup> The HPAs are well-known for their high Brønsted acidity and tunable redox-properties i.e. their high oxidation abilities. Moreover, the HPAs are characterized by their fast reversible multi-electron transfer, high proton mobility and high solubility in polar solvents.<sup>144</sup> In aqueous media, HPAs are strongly dissociated acids that are stronger than most mineral acids. The acid strength, as well as their stability in aqueous solution, decreases as illustrated;  $H_3PW_{12}O_{40}$  (HPW) >  $H_3PMo_{12}O_{40}$  (HPA-0) >  $H_8PV_5Mo_7O_{40}$  (HPA-5).<sup>146</sup> In general, the stability of HPA-n (n= amount of substituted V) decreases with increasing substitution of  $V^{5+}$  into the  $H_3PMo_{12}O_{40}$  structures. The

opposite is applicable for the oxidation potential of the HPAs, which decreases as  $\text{H}_8\text{PV}_5\text{Mo}_7\text{O}_{40}$  (HPA-5) >  $\text{H}_3\text{PMo}_{12}\text{O}_{40}$  (HPA-0) >  $\text{H}_3\text{PW}_{12}\text{O}_{40}$  (HPW). Depending on the desired application, different structures of HPAs are therefore preferable. Examples of the use of HPAs are acid catalyzed reactions such as the phenyl acetate Fries rearrangement and selective catalytic oxidations such as the production of formic acid from biomass, the OxFA process. In the phenyl acetate Fries rearrangement reaction, the highest activity is achieved with a homogeneous HPW catalyst,<sup>147</sup> whereas in the OxFA process, superior activity is achieved with a homogeneous HPA-5 catalyst.<sup>144,148</sup> The typical drawbacks of homogeneous catalysts, as for bulk HPA catalysts, are the difficulties with separation from the reaction media and catalyst recycling.<sup>143</sup> In order to improve catalyst separation and recycling in HPA catalyzed reactions, heterogeneous HPAs have been developed by supporting or encapsulating the HPA structures on/within porous materials such as MOFs or zeolites.<sup>145,149</sup> Moreover, the supported and encapsulated HPAs have much larger specific surface areas compared to the bulk HPAs with low specific surface areas of  $1\text{--}5\text{ m}^2\text{ g}^{-1}$ .

The most common way to synthesize a heterogeneous HPA catalyst has been by impregnating the HPA structure on a support material, such as  $\text{SiO}_2$ ,  $\alpha\text{-Al}_2\text{O}_3$  or activated carbon. The acid strength of the HPW catalyst has proven to decrease when introduced on different supports as illustrated;  $\text{SiO}_2 > \alpha\text{-Al}_2\text{O}_3 > \text{activated carbon}$ .<sup>150</sup> The interaction with  $\text{SiO}_2$  is minimum due to its inert character, however support materials of more basic character can decompose the HPA. The degree of interaction varies with the support, the type of HPA impregnated and the HPA loading. However, as the supported HPAs easily dissolve when in polar media, this is not an optimum solution. More sophisticated methods have been used to introduce HPA catalysts on different porous materials. Here, zeolites have been of interest as various framework structures of different channel and cage sizes exist. Since the zeolites possess very small interconnected pores, the introduction of HPAs by impregnation is not possible. An example is the faujasite (FAU) zeolite with pore sizes down to 0.73 nm in diameter, whereas the Keggin-type HPAs are around 1.3 nm in diameter.<sup>145,151,152</sup> One solution is to form the HPA structures in the already prepared zeolite structure, the ship-in-a-bottle method. As Keggin-type HPAs are synthesized under very acidic conditions, the zeolite structure has to be stable at a  $\text{pH} < 1$ . The pioneering work with encapsulation of HPA structures in zeolites Y was performed by Mukai *et al.*<sup>153–156</sup> Mukai *et al.*<sup>153–156</sup> have reported the synthesis of HPA-0 structures encapsulated in zeolite Y from a solution of  $\text{MoO}_3$  and  $\text{H}_3\text{PO}_4$  in the presence of dealuminated zeolite Y, which prior to the synthesis was ion-exchanged and calcined. Here, it was necessary to remove the excess of the HPA-0 structure formed on the surface of the zeolites by washing steps with hot water ( $80^\circ\text{C}$ ). These encapsulated HPA-

0 catalysts were tested in the simple esterification of acetic acid with ethanol. In this esterification, the performance of the encapsulated HPA catalyst was lower than that of the parent HPA-0, but it was higher in comparison to a simple HPA impregnated zeolite Y. The leaching-stability of the encapsulated HPA catalyst was improved by partial substitution of protons with Cs cations into the HPA-0 structures, which decreased its solubility in polar media. The use of HPA salts as catalysts has also been reported widely, as water-insoluble HPA salts can be obtained by the incorporation of large monovalent cations as  $\text{Cs}^+$ . However, the activity of these HPA salts as acidic catalysts always derives from residual protons remaining.<sup>143</sup> Another approach to encapsulate HPA structures inside a zeolite is to synthesize the zeolite structure around the already prepared HPAs. As already mentioned, the HPAs are synthesized under very acidic conditions at pH-levels below 1, whereas zeolites often are synthesized under alkaline conditions detrimental to the HPAs. A limited number of methods have been reported following the strategy of synthesizing the zeolite around the HPAs.<sup>157,158</sup> Additionally, the reported methods were doubtful as the HPAs were introduced in alkaline solutions up to a pH of 10. Moreover, physical characterizations to confirm the presence of the HPA structures were limited. In addition to encapsulation in zeolites, the encapsulation of HPAs in MOFs has been reported widely. Here, the introduction of the HPA structure has been reported with both impregnation of the MOF support material or by *in situ* synthesis within the MOF support material. Additionally, synthesis procedures where the MOFs are synthesized in the presence of HPA moieties have also been reported.<sup>159</sup> The majority of the encapsulated HPAs in MOFs have been performed with the MIL-101 framework due to its high porosity, large pore openings and cavities.<sup>152,160–162</sup> The stability of MIL-101 is sufficient under the acidic conditions where HPAs are formed. However, the thermal stability of MIL-101 limits the applications of the encapsulated HPA catalysts as the MIL-101 framework typically decomposes below 300°C.<sup>163,164</sup> Alc  nis *et al.* reported a method to successfully encapsulate HPW in MIL-101 by direct addition of the HPW to the synthesis solution of MIL-101. The MIL-101 encapsulated HPW catalyst showed remarkable activity in the esterification of n-butanol with acetic acid in comparison to the HPW impregnated MIL-101.<sup>152</sup>

Most of the reported methods to support or encapsulate HPA catalysts still suffer from problems with either low loadings or leaching in aqueous media due to HPAs high solubility in polar solvents.<sup>135,143</sup> The aim of the collaboration with FAU was to find a method to efficiently encapsulate and confine the homogeneous HPA catalysts (HPW, HPA-0 and HPA-5) in a porous support to yield a recyclable and non-leaching heterogeneous catalyst in solution. The choice of porous materials to encapsulate the HPAs was based on the pore sizes of the materials and conclusions from literature. In

the initial screening of porous supports, hollow SiO<sub>2</sub> spheres were synthesized, as described in Chapter 5. However, as the pore diameter of 2.3 nm obtained in the mesoporous SiO<sub>2</sub> synthesized by CTAB appeared to be too large to limit any leaching, myristyltrimethylammonium bromide, which has a shorter hydrophobic tail was used instead as a surfactant template. This resulted in mesoporous SiO<sub>2</sub> spheres with an average pore size of 1.8 nm in diameter. Zeolite Y (FAU) was also tested as a porous support as it holds a small average pore size down to 0.73 nm in diameter. Recrystallized silicalite-1 zeolites were also prepared by a hydrothermal treatment in TPAOH to yield large mesopores and cavities in the zeolite structure. This was done to increase the mass transfer within the microporous zeolite structure while maintaining the pore dimensions down to 0.51 x 0.55 nm of the MFI structure.<sup>141</sup> This approach was modified from a procedure reported by Dai *et al.*<sup>135</sup>. Unfortunately, the zeolite encapsulated HPAs reported by Dai *et al.*<sup>135</sup> obtained a limited HPA loading of 3 wt%. As HPAs in general are too large (1.3 nm) to diffuse into the pores of the MFI zeolite structure, the HPAs were synthesized *in situ* inside the zeolite structure. Thus, the HPA precursors were introduced in steps in the pores by vacuum impregnation. As high-silica zeolites are often hydrophobic they can be difficult to fill with aqueous solutions. Encapsulated HPA-0 in the three different porous materials were prepared, characterized and screened in a simple esterification reaction of formic acid and ethanol. Based on the esterification results the recrystallized silicalite-1 zeolite was chosen as the most promising porous material for successful encapsulation of HPAs. Supporting information on the encapsulated HPA-0 structures in hollow SiO<sub>2</sub> spheres and zeolite Y can be found in Appendix D. The encapsulated HPW and HPA-0 structures in recrystallized silicalite-1 were further optimized and tested in the acid-catalyzed phenyl acetate Fries rearrangement reaction and the encapsulated HPA-5 in recrystallized silicalite-1 was tested for the catalytic oxidation of biomass, the OxFA process. These two reactions will be introduced in the following sections.

### The Phenyl Acetate Fries Rearrangement

Aromatic ketones such as hydroxyacetophenones are important intermediates in the production of pharmaceuticals as well as fine and specialty chemicals. The common way to produce these aromatic ketones is by Fries rearrangement of aryl esters like phenyl acetate. The conventional production of aromatic ketones from aryl esters is catalyzed by a stoichiometric amount of a soluble Lewis acid (e.g. AlCl<sub>3</sub>) or a mineral acid (e.g. H<sub>2</sub>SO<sub>4</sub>). However, the conventional route results in a high amount of corrosive waste as the metal halides and products form complexes, which require separation by hydrolysis.<sup>165</sup> The use of solid catalysts, such as Keggin-type HPAs, has proved to not only

yield a superior activity in the phenyl acetate Fries rearrangement, but it also offers a more environmentally and economically friendly approach.<sup>147</sup> The Fries rearrangement can be effectively catalyzed by the strong Brønsted acidity of HPAs, which are stronger acids than the conventional catalysts used, such as the mineral acids. HPAs are also stronger acids than zeolites like H-beta, which is the most commonly used acidic zeolite in the Fries rearrangement reaction.<sup>147</sup> Due to the higher acidic strength of the HPAs, the Fries rearrangement can be completed at a lower catalyst concentration, lower temperature and with less by-product formation. Moreover, HPAs are stable and safer to handle in comparison to mineral acids. The highest activity is obtained with a homogeneous HPW catalyst, which among the HPAs is the most thermally stable and strongest acid, as previously described. A schematic overview of the phenyl acetate (PhOAc) Fries rearrangement can be seen in Figure 6.2. Here, 2-hydroxyacetophenone (2HAP), phenol (PhOH) and 4-acetoxyacetophenone (4AAP) are considered as the primary products and 4-hydroxyacetophenone (4HAP) as the secondary product. The reaction involves the formation of an acylium ion intermediates generated from the ester and the acid catalyst.<sup>166</sup> 2HAP is suggested to be formed by an intramolecular rearrangement of phenyl acetate. 4AAP and phenol are suggested to be formed by the self-acylation of 2x phenyl acetate. 4HAP is suggested to be the product of an intermolecular acylation of phenyl acetate and phenol. The yield of phenol is often higher than 4AAP, as part of phenol derives from the phenyl acetate hydrolysis and/or decomposition. Small amounts of acetic acid and acetic anhydrides can also be produced.<sup>165</sup>

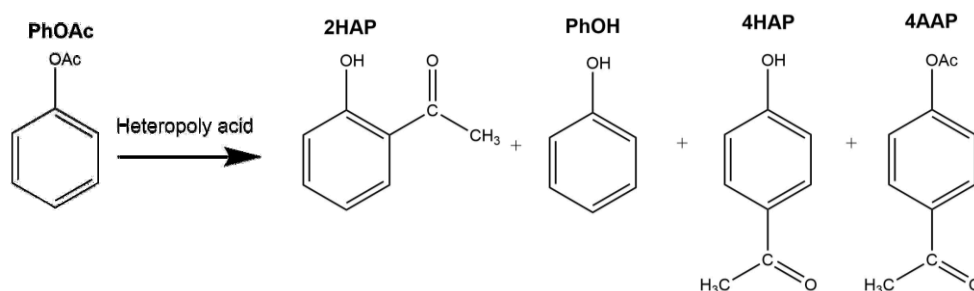


**Figure 6.2.:** A schematic overview of the phenyl acetate Fries rearrangement, which can be acidic catalyzed to aromatic ketones by heteropoly acids.

Typically, the phenyl acetate Fries rearrangement reaction is performed with the homogeneous HPW catalyst with a 0.6-5 wt% HPA charge at 130-150°C for 2 h in a liquid phase batch reaction. The reaction is completed in neat phenyl acetate or in a polar solvent like nitrobenzene. The catalyst is often pretreated at 130-200°C under vacuum

to obtain the anhydrous catalyst, which is a stronger acid.<sup>147</sup> The highest conversion reported by Kozhevnikov *et al.*<sup>147</sup> was obtained with the homogeneous HPW catalyst in 75% nitrobenzene at 150°C for 2 h converting 45.8% phenyl acetate with the highest selectivity towards 4HAP (24%), excluding phenol (52%). HPW catalysts supported on SiO<sub>2</sub> have also been studied in the Fries rearrangement, where the reaction is carried out in the non-polar solvent dodecane. The reactions of phenyl acetate in dodecane are reported to be heterogeneously catalyzed. However, the heterogeneity of the supported HPW catalyst is doubtful, as the supported HPW catalyst revealed leaching. The highest conversion with a supported catalyst was achieved with 40 wt% HPW supported on SiO<sub>2</sub> in 64% dodecane at 160°C for 2 h converting 18% phenyl acetate with the highest selectivity towards 4AAP (14%), excluding phenol (66%). However, as the wt% charge of HPAs and different conditions in the Fries rearrangement reactions were reported, it can be difficult to directly compare them.<sup>147</sup> A higher wt% charge of the catalyst increases the conversion, as a result of less catalyst being deactivated by product inhibition.

Deactivation of the homogeneous HPA catalyst, as well as supported HPA catalyst, has been reported for the Fries rearrangement at the given reaction conditions. The deactivation derives mainly from product inhibition of the acidic active sites restricting the conversion or by the formation of coke, which ultimately blocks the active sites.<sup>167</sup> Thus, gas-phase or continuous fixed-bed reactions have been studied as alternative approaches to the batch conditions, which could restrict product inhibition by continuous removal of the products. The coke cannot be calcined off as traditionally done at 500-550°C due to the thermal stability of HPAs. Other approaches to restrict coke formation have been investigated. A method applicable to supported HPA catalysts includes the synthesis of smaller crystals increasing product diffusion or doping with Pd. A catalyst doping of 2.1 wt% Pd proved to increase the recyclability of an HPW catalyst supported on SiO<sub>2</sub>, although it did not change the initial activity of the catalyst.<sup>150</sup> Moreover, by doping with Pd, a reduced calcination temperature to successfully remove coke under aerobic conditions can be achieved. This was reported for a Pd doped HPW catalyst supported on SiO<sub>2</sub>, which was regenerated at 350°C.<sup>147</sup>

### The OxFA process

Formic acid is important in the processing of textiles, leather, rubber and for animal feed preservation.<sup>168</sup> As the demand for renewable alternatives to fossil fuel feedstocks for chemical production is increasing, the catalytic OxFA process offers a solution to convert biomass to formic acid.<sup>169,170</sup> The OxFA process can use a variety of biogenic raw



materials, which selectively can be converted into liquid formic acid with only gaseous  $\text{CO}_2$  as a by-product. The conventional production of formic acid is exclusively based on fossil resources. The most common synthesis route is the methyl formate hydrolysis route from  $\text{CO}$ , water and methanol with methyl formate as an intermediate in the presence of a catalyst (e.g.  $\text{KOCH}_3$ ).<sup>171,172</sup> The OxFA process is effectively catalyzed by the Brønsted acidic and redox-active V substituted heteropoly acids (HPA-n). The reactivity derives from both the dissolved  $\text{V}^{5+}$  species and the HPA-n itself.<sup>171</sup> The highest activity is obtained with an HPA-5, which has five V atoms substituted into the structure. It has been reported by Albert *et al.*<sup>144,148</sup> that the reason for HPA-5's superior activity is due to an increased formation of pervanadyl cation  $\text{VO}_2^+$  species in the acidic media with increasing V substitution. The redox potential is higher for the pervanadyl cation than the HPA-n itself, which further explains the higher activity of HPA-5. A schematic overview of the OxFA process can be seen in Figure 6.3. Here, oxidative cleavage of the C-C bonds in the biomass substrate by HPA-n electron and oxygen transfer is first completed to form formic acid and  $\text{CO}_2$ , while the HPA-n catalyst is simultaneously reduced. Then in the second step, the reduced catalyst is reoxidized *in situ* by molecular  $\text{O}_2$  or compressed air.<sup>144,173</sup> The HPA-0 and HPA-1 are not used in the OxFA process as temperatures above  $100^\circ\text{C}$  are necessary to reoxidize the HPA-n ( $n=0-1$ ), which causes formic acid decomposition.

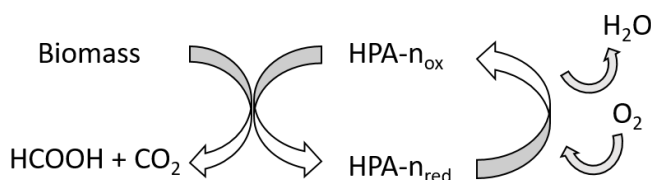


**Figure 6.3.:** A schematic overview of the OxFA process, which catalytically converts biomass to formic acid by V substituted heteropoly acids. Adapted from Reichert *et al.*<sup>174</sup>

In general, the OxFA process is performed with the homogeneous HPA-5 catalyst at  $90^\circ\text{C}$ , over 6-24 h and at 20-60 bar to ensure sufficient  $\text{O}_2$  to reoxidize the HPA-5.<sup>174</sup> An advantage in the OxFA process is that the applied biomass does not need to be pre-dried as the solvent is water. Glucose is often used as a model substrate to test the redox activity of synthesized HPA catalysts.<sup>148</sup> However, more complex biomass structures can also be used by the addition of a solubilizer and accelerator like p-toluene sulfonic acid (p-TSA) to dissolve non water-soluble substrates.<sup>175</sup> In general, a yield of up to 70% formic acid has been reported from biomass oxidation in a monophasic acidic aqueous

solution, typically with glucose as a substrate. However, in a biphasic system (water/organic phase) where the formed formic acid is *in situ* extracted into the organic phase, a higher yield of up to 85% with a selectivity towards formic acid of 85% is attainable with glucose as a substrate.<sup>36</sup> Additionally, the more complex biomass-derived substrates, such as beech wood, can attain a yield of up to 61% with a selectivity towards formic acid of 68% in the OxFA process after 48 h catalyzed by homogeneous HPA-5.<sup>168,171,176</sup>

## 6.2 Experimental Details

### 6.2.1 Material Preparations

Reagents were acquired from a commercial source (Sigma-Aldrich), and were utilized without additional purifications. The reagents include: sodium tungstate dihydrate (99.99% trace metals basis), sodium phosphate dibasic dihydrate ( $\geq 98.0\%$ ), molybdenum(VI) oxide (99.97% trace metals basis), vanadium(V) oxide (99.95% trace metals basis), tetraethyl orthosilicate (TEOS, 99.99% trace metals basis), tetrapropylammonium hydroxide solution (TPAOH, 1.0 M in H<sub>2</sub>O), hydrochloric acid (ACS reagent, 37%), phosphoric acid ( $\geq 85\%$ ) and absolute ethanol ( $\geq 99.8\%$ ).

#### Synthesis of Recrystallized Silicalite-1 Zeolite

The synthesis of the silicalite-1 zeolites was prepared as described in Chapter 5, subsection 5.2.1. The recrystallization of the prepared silicalite-1 zeolites (Top-down approach) was performed as described in the following section modified from literature.<sup>177</sup>

Silicalite-1 powder (10 g) and TPAOH (60.5 mL) were mixed in a Teflon beaker. The solution was then transferred to a stainless steel autoclave and heated to 170°C for 24 h at autogenous pressure. The product was collected by centrifugation (12000 rpm for 10 min) and washed with water to a neutral pH. The product was dried at 80°C for 24 h.

The white powder of recrystallized silicalite-1 was calcined in a muffle furnace in static air at 550°C for 20 h with a heating ramp of 5°C min<sup>-1</sup>.

**Vacuum Impregnation with  $\text{H}_3\text{PW}_{12}\text{O}_{40}$** 

All vacuum impregnations were executed with a Fischer Scientific Chemical Diaphragm pump with a maximum vacuum of 2 mbar. The impregnation method was modified from a procedure reported by Booth *et al.*<sup>178</sup> Sodium tungstate dehydrate (5.0 g) and sodium phosphate dibasic dihydrate (0.8 g) were dissolved in 7.5 mL of water at 110°C in a schlenk flask. The solution was cooled and recrystallized silicalite-1 (500 mg) was dispersed in the solution. Vacuum was applied to the system for 5 min to empty the pores of the zeolites. The vacuum was released to fill the pores with the precursor solution. Hydrochloric acid (4 mL) was added dropwise to the solution and it was stirred at 95°C for 1 h. The product was collected by centrifugation (12000 rpm for 10 min) and washed five times with 80°C water. The product was dried at 80°C for 24 h.

The following day, in order to make sure all excess HPA on the surface of the zeolite was removed, the product was dispersed in water (18 mL) and phosphoric acid (2 mL) at 100°C for 1 h. The product was collected by centrifugation (12000 rpm for 10 min) and washed five times with 80°C water. The product was dried at 80°C for 24 h. The product HPW@Recryst S1 was a white powder.

**Vacuum Impregnation with  $\text{H}_3\text{PMo}_{12}\text{O}_{40}$** 

The impregnation method was modified by a procedure by Mukai *et al.*<sup>154</sup> Recrystallized silicalite-1 (1.0 g) and molybdenum(VI) trioxide (3.6 g) were dissolved in 35 mL of water in a schlenk flask and stirred at 25°C for 24 h. Vacuum was applied to the system for 5 min to empty the pores of the zeolites. The vacuum was released to fill the pores with the precursor solution. Phosphoric acid (240  $\mu\text{L}$ ) was added dropwise to the solution and it was stirred at 95°C for 3 h. The product was collected by centrifugation (12000 rpm for 10 min) and washed five times with 80°C water. The product was dried at 80°C for 24 h.

The following day, the product was dispersed in water (18 mL) and phosphoric acid (2 mL) at 100°C for 1 h. The product was collected by centrifugation (12000 rpm for 10 min) and washed five times with 80°C water. The product was dried at 80°C for 24 h. The product HPA-0@Recryst S1 was a gray powder.

**Vacuum Impregnation with  $\text{H}_5\text{PV}_5\text{Mo}_7\text{O}_{40}$** 

The impregnation method was modified by a procedure by Zubrzycki *et al.*<sup>179</sup> Molybdenum(VI) trioxide (1.689 g) and vanadium(V) oxide were dissolved in 67.5 mL of water in a schlenk flask and stirred at 110°C for 2 h. Then recrystallized silicalite-1 (500 mg) was dispersed in the solution and vacuum was applied to the system for 5 min to

empty the pores of the zeolites. The vacuum was released to fill the pores with the precursor solution. A 0.12M phosphoric acid solution (9.78 mL, 80  $\mu$ L phosphoric acid in 9.7 mL of water) was added dropwise to the solution and it was stirred at 110°C for 3 h. The solution was left with stirring at 25°C for 24 h. The product was collected by centrifugation (12000 rpm for 10 min) and washed five times with 80°C water. The product was dried at 80°C for 24 h.

The following day, the product was dispersed in water (18 mL) and phosphoric acid (2 mL) at 100°C for 1 h. The product was collected by centrifugation (12000 rpm for 10 min) and washed five times with 80°C water. The product was dried at 80°C for 24 h. The product HPA-5@Recryst S1 was a white/gray powder.

#### Preparation of the reference HPAs, $\text{H}_3\text{PW}_{12}\text{O}_{40}$ , $\text{H}_3\text{PMo}_{12}\text{O}_{40}$ and $\text{H}_5\text{PV}_5\text{Mo}_7\text{O}_{40}$

The homogeneous reference  $\text{H}_3\text{PW}_{12}\text{O}_{40}$  was commercially available and bought from Sigma-Aldrich as tungstophosphoric acid hydrate (cryst. EMPLURA). The homogeneous references  $\text{H}_3\text{PMo}_{12}\text{O}_{40}$  and  $\text{H}_5\text{PV}_5\text{Mo}_7\text{O}_{40}$  were prepared in collaboration with PhD students Dorothea Voss and Julian Mehler at FAU by a procedure according to Albert *et al.*<sup>144</sup> and Odyakov *et al.*<sup>180</sup>

#### Preparation of the initial screened supports Hollow $\text{SiO}_2$ and Zeolite Y

The synthesis procedures can be found in Appendix D.

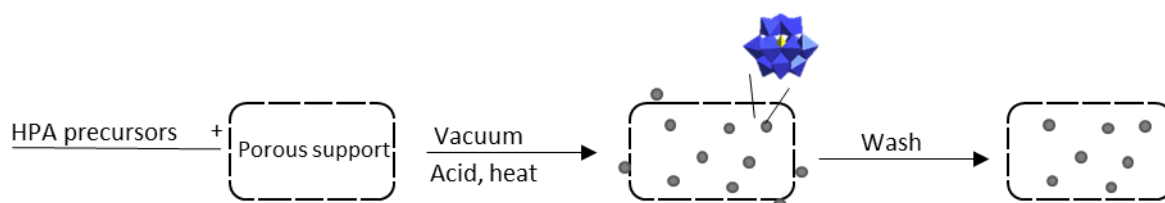


**Figure 6.4.:** A schematic of the vacuum impregnation of HPAs in recrystallized silicalite-1 zeolites.

### 6.2.2 Characterization Methods

In order to explain the performance of the catalysts in the phenyl acetate Fries rearrangement reaction and the OxFA process, the prepared materials were characterized by several techniques. XRF was used to determine the HPA loadings and the substitution of V in HPA-n. ICP was used to test for leaching in the reaction medium

in the OxFA process reaction. XPS was used to support the encapsulation of HPAs. XRPD and FTIR were used to confirm the HPA structures. SS-NMR was used as an additional technique to support XRPD and FTIR in the validation of the HPA structures. N<sub>2</sub> physisorption was used to determine the surface areas of the encapsulated HPA catalysts. STEM and EDS were used to identify the morphology of the encapsulated HPA catalysts and the distribution of W, Mo and V in the recrystallized silicalite-1 zeolites. ICP was measured by laboratory technician Dr. Nicola Taccardi at FAU in Erlangen, Germany according to Albert *et al.*<sup>144</sup>

### 6.2.3 Catalytic Test Procedure

#### Phenyl Acetate Fries Rearrangement

The phenyl acetate Fries rearrangement reactions were performed at DTU in batch reactions by a modified procedure according to Kozhevnikova *et al.*<sup>165</sup>

The Fries rearrangement reactions were performed in a carousel (12 Plus Reaction Station by Radleys) in 20 mL volume glass tubes equipped with sealing caps. The carousel was placed on a magnetic stirrer with a hotplate. In a typical experiment 60 mg bulk HPA was added to the glass tube with phenyl acetate (7.511 mL) and a permanent magnet. To ensure inert conditions, a balloon with N<sub>2</sub> was attached to the cap by a syringe. The reaction mixture was heated to 150°C and samples of 0.1 mL were taken in time intervals of 30 min: 0 min, 30 min, 1 h, 1.5 h and 2 h. The hot filtration experiment was performed with two reactions in glass tubes being tested simultaneously. Here, samples were taken after 5 min from both glass tubes, followed by a hot filtration of one of the catalysts in the glass tubes. This was done to compare the activity after 2 h to detect possible leaching. One experiment was performed with the homogeneous HPW catalyst in nitrobenzene as a solvent. Here, instead of a neat phenyl acetate solution, a mixture of phenyl acetate (1.635 mL) and nitrobenzene (4.375 mL) was added to the catalyst, which was equivalent to a solution of 75% nitrobenzene. The samples were quantified with gas chromatography (GC) using an Agilent 7890A GC-FID-MS with a 5975C VL MSD with triple-Axis Detector. The GC was equipped with a CP-Chirasil-Dex CB column. The samples prior to measurements were diluted to 1 mL with dichloromethane. The conversions and selectivities were calculated from the carbon balances derived from the GC spectra chromatograms.

## The OxFA process

The OxFA process reactions were performed at FAU together with PhD students Anna Bukowski and Dorothea Voss, according to the procedure reported by Albert *et al.*<sup>144,174,181,182</sup> In brief, the selective oxidations were completed in 20 mL Hastelloy C276 autoclaves. In a typical experiment HPA-5 catalyst (190 mg), glucose/molasses (180 mg), water (10 g) and a permanent magnet were added to the autoclave. The autoclave was closed, purged twice with 20 bar oxygen and a pre-pressure of 15-20 bar O<sub>2</sub> was filled into the autoclaves. The stirring was set to 300 rpm and the heating to 90°C. When the temperature of 90°C was reached, the oxygen pressure was adjusted to 30 bar and the reaction was started by adjusting the stirring speed to 1000 rpm. The reaction was stopped after 24 h by decreasing the stirring speed to 300 rpm and switching the heating off. When the autoclaves were cooled down samples of the gas phase and the liquid phase were prepared and analyzed by GC and high-performance liquid chromatography (HPLC).

The analysis of the gaseous by-products was completed with a Varian GC 450 equipped with a 2 m x 0.75 mm ID ShinCarbon ST column. The yield was calculated as  $n(\text{CO}_2)/n(\text{C-atoms substrate})$ . The liquid products were quantified with an HPLC from Jasco equipped with a 300 mm x 8 mm SH1011 Shodex column. The eluent was a 5 mmol aqueous sulphuric acid mixture. The yields were calculated as  $n(\text{product})/n(\text{C-atoms substrate})$ . The elemental composition of molasses was determined by CHNS analysis to C<sub>0.88</sub>H<sub>1.85</sub>O<sub>1</sub> and was bought commercially from Suedzucker AG.

## 6.3 Results and Discussion

### 6.3.1 XRF and XPS

Table 6.1 provides an overview of the prepared materials and their HPA loadings. The HPA loadings were quantified from XRF, where standards of known SiO<sub>2</sub> and HPAs mixture ratios were prepared to make calibration lines. The highest loading was prepared with HPW@Recryst S1 of 30 wt% HPW. This could be explained by the overall higher solubility of the used HPW sodium salt precursors. The HPA-0@Recryst S1 held a loading of 5 wt% HPA-0 and HPA-5@Recryst S1 held a loading of 2 wt% HPA-5. The lower solubility of MoO<sub>3</sub> and V<sub>2</sub>O<sub>5</sub> was suggested to be the cause of the relatively lower loadings. The amount of V-substitution in the prepared HPA-5 catalyst was determined

from the calculation of  $n(V)/n(Mo)$ . Attempts to incorporate a higher loading of HPA-5 into the recrystallized silicalite-1 zeolites were made but without success. It was found that a decreased amount of recrystallized silicalite-1 introduced to the vacuum impregnation resulted in a higher HPA loading. This is suggested to be a result of poor mixing when a large amount of zeolite was applied, which resulted in inefficient pore fillings with the in general low soluble precursors. XPS analysis of the encapsulated HPA catalysts revealed that between 0-0.5 wt% of the HPAs were detectable from the surface of the encapsulated catalysts. Thus, this provided evidence of successful encapsulations.

**Table 6.1.:** Overview of the prepared encapsulated HPA catalysts.

Entry	HPA	Catalyst	HPA loading wt%
1	H <sub>3</sub> PW <sub>12</sub> O <sub>40</sub>	HPW@Recryst S1	30
2	H <sub>3</sub> PMo <sub>12</sub> O <sub>40</sub>	HPA-0@Recryst S1	5
3	H <sub>8</sub> PV <sub>5</sub> Mo <sub>7</sub> O <sub>40</sub>	HPA-5@Recryst S1	2

The at-sign (@) indicates encapsulated in. Recryst S1 is an abbreviation of recrystallized silicalite-1.

### 6.3.2 XRPD and FTIR

The diffraction patterns from XRPD and the FTIR spectra of the HPW@Recryst S1 catalyst, the recrystallized silicalite-1 zeolite and the bulk HPW can be seen in Figure 6.5. The diffraction pattern of HPW@Recryst S1 showed the characteristic peaks of both the recrystallized silicalite-1 zeolite structure as well as the crystalline HPW structure. This was expected as the loading of HPW was relatively high (30 wt% HPW). The diffraction pattern of the catalyst HPW@Recryst S1 held the characteristic peaks of the crystalline HPW at  $2\theta$  degrees equal to  $25.2^\circ$  and  $34.4^\circ$ .<sup>183</sup> The FTIR spectra of the catalyst HPW@Recryst S1 held the typical bands of adsorption at  $1080\text{ cm}^{-1}$  (P-O),  $983\text{ cm}^{-1}$  (W=O<sub>t</sub>),  $898\text{ cm}^{-1}$  (W-O<sub>c</sub>-W) and  $797\text{ cm}^{-1}$  (W-O<sub>e</sub>-W), which confirmed the incorporation of crystalline HPW.<sup>183</sup> The FTIR adsorption bands of the recrystallized silicalite-1 zeolites were in general broad and had overlapping bands with those of the bulk HPW.

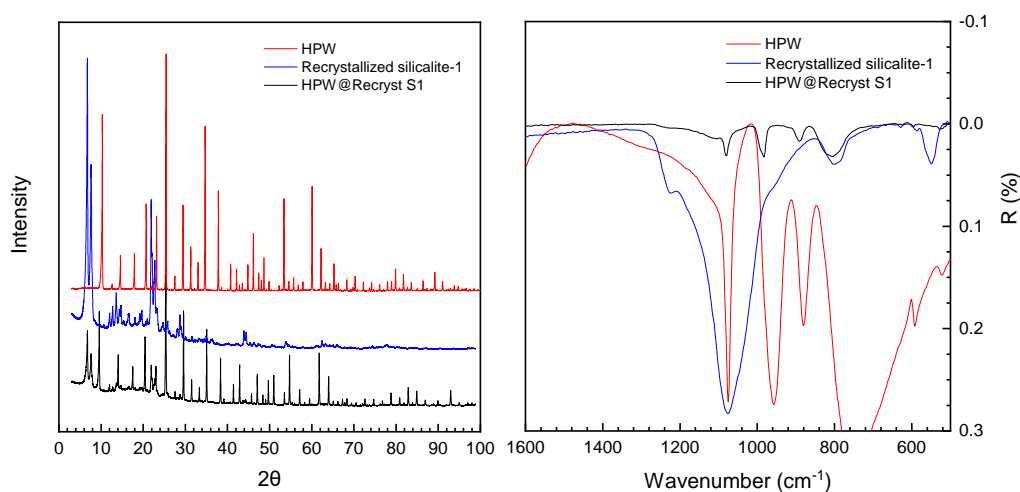


**Figure 6.5.:** The diffraction patterns and FTIR of the prepared HPW@Recryst S1, the recrystallized support and the reference bulk HPW.

The diffraction patterns from XRPD and the FTIR spectra of the HPA-0@Recryst S1 catalyst, the recrystallized silicalite-1 zeolite and the bulk HPA-0 can be seen in Figure 6.6. The diffraction pattern of HPA-0@Recryst S1 showed relatively weak peaks, which derived from the recrystallized silicalite-1 zeolite structure. The diffraction pattern of the bulk HPA-0 held peaks at  $2\theta$  degrees equal to  $8.9^\circ$ ,  $26.0^\circ$  and  $27.6^\circ$ .<sup>184</sup> The absence of crystalline HPA-0 peaks might be a result of the low loading of HPA-0 (5 wt% HPA-0) and a high dispersion in the cavities of the zeolites, as reported by Ferreira *et al.*<sup>185</sup> The FTIR spectra of the catalyst HPA-0@Recryst S1 held only the characteristic absorption bands of recrystallized silicalite-1. The FTIR spectra of the bulk HPA-0 held bands at  $1054\text{ cm}^{-1}$  (P-O<sub>a</sub>),  $952\text{ cm}^{-1}$  (Mo-O<sub>d</sub>),  $878\text{ cm}^{-1}$  (Mo-O<sub>b</sub>-Mo) and  $739\text{ cm}^{-1}$  (Mo-O<sub>c</sub>-Mo), which are characteristic of crystalline HPA-0.<sup>144</sup> Thus, based on XRPD and FTIR the presence of HPA-0 could not be determined.



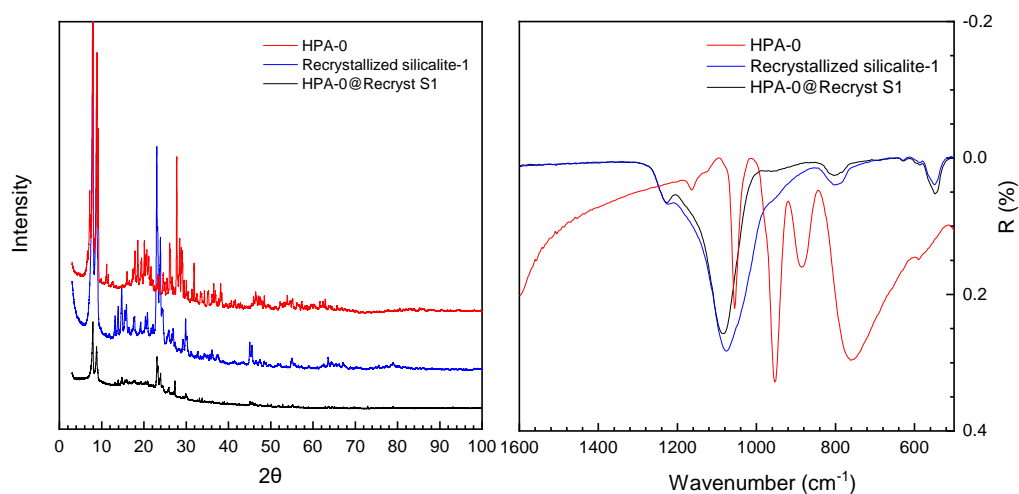


**Figure 6.6.:** *The diffraction patterns and FTIR of the prepared HPA-0@Recryst S1, the recrystallized support and the reference bulk HPA-0.*

The diffraction patterns from XRPD and the FTIR spectra of the HPA-5@Recryst S1 catalyst, the recrystallized silicalite-1 zeolite and the bulk HPA-5 can be seen in Figure 6.7. The diffraction pattern of HPA-5@Recryst S1 showed the characteristic peaks solely from the recrystallized silicalite-1 zeolite structure. The diffraction pattern of the bulk HPA-5 held peaks at  $2\theta$  degrees equal to  $8.8^\circ$ ,  $26.7^\circ$  and  $29.0^\circ$ .<sup>184</sup> The absence of crystalline HPA-5 peaks might be a result of the low loading of HPA-5 (2 wt% HPA-5) and a high dispersion in the cavities of the zeolite.<sup>185</sup> Additionally, the FTIR spectra of the catalyst HPA-5@Recryst S1 held only the characteristic absorption bands of recrystallized silicalite-1. The FTIR spectra of the bulk HPA-5 held bands at  $1045\text{ cm}^{-1}$  ( $\text{P-O}_a$ ),  $948\text{ cm}^{-1}$  ( $\text{Mo-O}_d$ ),  $864\text{ cm}^{-1}$  ( $\text{Mo-O}_b\text{-Mo}$ ) and  $730\text{ cm}^{-1}$  ( $\text{Mo-O}_c\text{-Mo}$ ), which are characteristic of crystalline HPA-5.<sup>144</sup> Thus, based on XRPD and FTIR the presence of HPA-5 could not be determined.

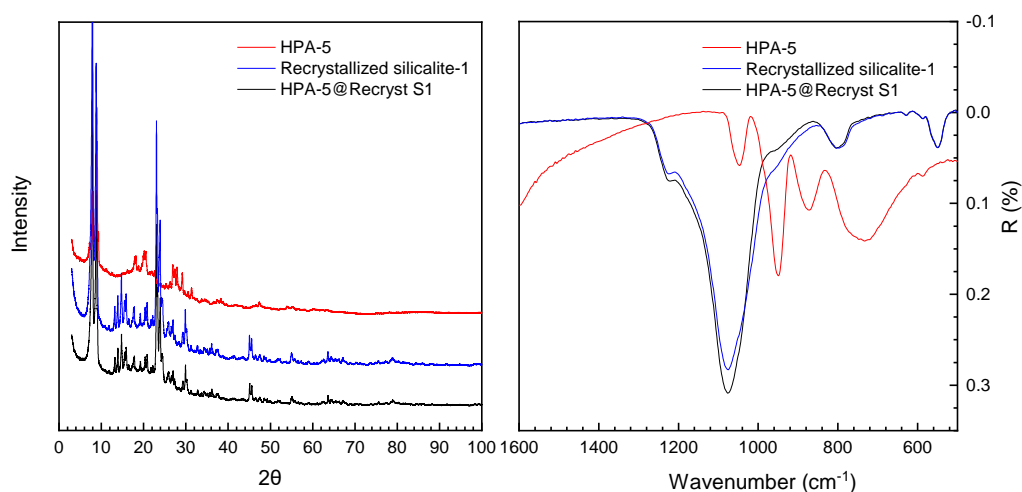


**Figure 6.7.:** The diffraction patterns and FTIR of the prepared HPA-5@Recryst S1, the recrystallized support and the reference bulk HPA-5.

### 6.3.3 Solid-State NMR

$^{31}\text{P}$  and  $^{51}\text{V}$  magic-angle spinning (MAS) SS-NMR were used to study the chemical interactions of the HPAs with the recrystallized silicalite-1 zeolites of the HPA@Recryst S1 catalysts. Moreover, SS-NMR was used as an additional technique to support XRPD and FTIR in the validation of the HPA structures. Kozhevnikov *et al.*<sup>143</sup> have reported that in the majority of supported HPAs measured by SS-NMR, an interaction between the support and the HPAs has been detected, where the HPA loading has a significant influence on the degree of interaction. Figure 6.8 illustrates the  $^{31}\text{P}$  SS-NMR spectra of the bulk HPAs and the encapsulated HPA@Recryst S1 catalysts. The spectrum of the bulk HPW showed a peak at -15 ppm characteristic for the intact HPW Keggin structure. In the spectrum of the encapsulated HPW@Recryst S1 catalyst, a peak was detected at -14 ppm. Kozhevnikov *et al.*<sup>143</sup> reported peaks at both -15 ppm and -14 ppm from the Keggin structure found in a  $\text{SiO}_2$  supported HPW catalyst. Typically, the peak found at -14 ppm was detected in supported HPW catalysts with loadings below 30%, which was suggested to derive from the “interacting” species  $(\text{SiOH}_2^+)(\text{H}_2\text{PW}_{12}\text{O}_{40}^-)$ .<sup>143</sup> Another publication by Kozhevnikov *et al.*<sup>186</sup> reported that the “interacting” species could be  $\text{H}_6\text{P}_2\text{W}_{18}\text{O}_{62}$  or  $\text{H}_6\text{P}_2\text{W}_{21}\text{O}_{71}$  depending on the HPW loading, to which they credited the increased performance acquired in a liquid-phase dealkylation of alkylphenols. The peak found at -14 ppm from the HPW@Recryst S1 catalyst with a loading of 30 wt% HPW was thus assumed to derive from the HPW interacting with the zeolite support. The  $^{31}\text{P}$  SS-NMR spectrum of the bulk HPA-0 showed a peak at -3.5 ppm, which is characteristic for the HPA-0 structure. However, the  $^{31}\text{P}$  SS-NMR spectra of the HPA-0@Recryst S1 catalyst

solely revealed a peak around -0.1 ppm. This peak might derive from decomposed HPA-0, which is suggested by Kozhevnikov *et al.*<sup>143</sup> Kozhevnikov *et al.*<sup>143</sup> reported that at lower supported HPA-0 loadings, the HPA-0 cannot retain the Keggin structure and it decomposes due to strong interactions with the silanol groups of the support. Rocchiccioli-Deltcheff *et al.*<sup>187</sup> supported this statement as they reported that at a high loading of supported HPA-0 the performance of the catalyst was equivalent to that of the bulk HPA-0 in a methanol oxidation/dehydration reaction. However, at a low loading, the acidity of HPA-0 was decreased due to interactions with the support and in some cases, the Keggin structure was decomposed to  $\text{MoO}_3$ . Nevertheless, it was reported that the catalyst even at lower loadings still maintained its redox activity. Thus, the peak found at -0.1 ppm in the  $^{31}\text{P}$  SS-NMR spectra of the HPA-0@Recryst S1 was attributed to a potentially decomposed HPA-0 structure. The spectrum of bulk HPA-5 showed a peak at -1.7 ppm characteristic for HPA-5,<sup>188</sup> whereas the spectrum of the HPA-5@Recryst S1 catalyst showed a peak at -3.9 ppm as well as a minor peak at -3.2 ppm. Albert *et al.*<sup>144</sup> reported peaks between -3.0 ppm and -4.0 ppm obtained from HPA-2 by  $^{31}\text{P}$  liquid-state NMR (LS-NMR), which was equivalent to SS-NMR. Additionally, Evtuguin *et al.*<sup>188</sup> reported the presence of peaks at -3.2 ppm for all HPA-*n* (*n* = 1-5). Moreover, at higher V substitution the presence of more than one peak could be seen with  $^{31}\text{P}$  LS-NMR.<sup>188</sup> This indicated that the HPA-5@Recryst S1 catalyst held an HPA-*n* structure, but it might have possessed a lower V-substitution than first expected based on XRF.

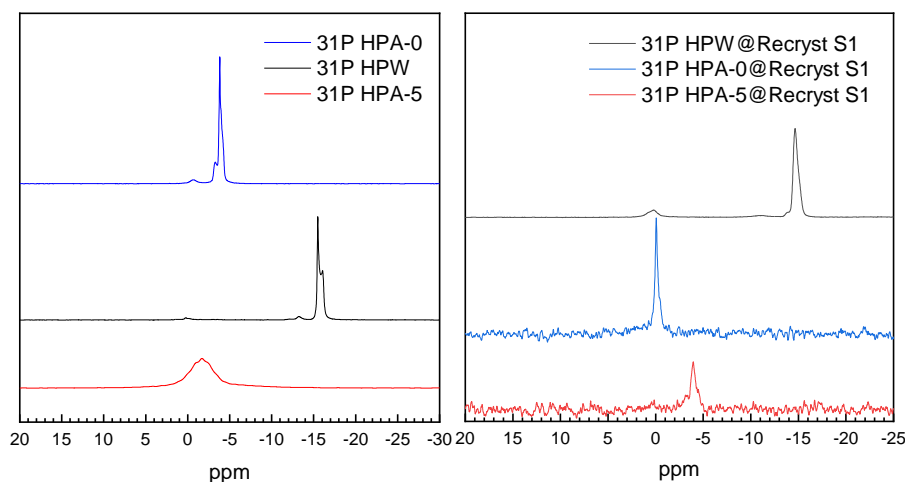


**Figure 6.8.:** The  $^{31}\text{P}$  SS-NMR spectra of the homogeneous bulk HPAs and the HPA@Recryst S1 catalysts. Isotropic chemical shifts are reported relative to  $\text{NH}_4\text{H}_2\text{PO}_4$  (0.81 ppm) for  $^{31}\text{P}$ .

The  $^{51}\text{V}$  SS-NMR spectra of the bulk HPA-5 and the HPA-5@Recryst S1 catalyst are presented in Figure 6.9. Albert *et al.*<sup>144</sup> reported peaks in the range of -530 to -540 ppm obtained from  $^{51}\text{V}$  LS-NMR of HPA-2, which is in good agreement with the  $^{51}\text{V}$  SS-NMR spectrum of the HPA@Recryst S1 catalyst (-529 ppm). Evtuguin *et al.*<sup>188</sup> reported a similar  $^{51}\text{V}$  LS-NMR peak at -532 ppm in spectra of HPA-*n* (*n*= 1-5), with a higher amount of peaks deriving from increased V-substitution. Therefore, the HPA-5@Recryst S1 catalyst was expected to possess a lower V substituted HPA-*n* than *n*= 5, which according to the  $^{31}\text{P}$  and  $^{51}\text{V}$  SS-NMR spectra was speculated to be HPA-2. For simplifications, the catalyst will still be referred to as HPA-5@Recryst S1. While the  $^{51}\text{V}$  SS-NMR spectrum for HPA-5@Recryst S1 catalyst contained relative narrow peaks, the  $^{51}\text{V}$  SS-NMR spectrum for bulk HPA-5 exhibited a manifold of spinning sidebands due to the large chemical shift anisotropy interaction experienced by the  $^{51}\text{V}$  nuclei. The absence of a similar spinning sideband pattern for the HPA-5@Recryst S1 catalyst was most likely due to increased mobility, which might indicate that the HPA-*n* was located inside a void with freedom to move. The determined  $^{51}\text{V}$  isotropic chemical shift for bulk HPA-5 was -578 ppm.

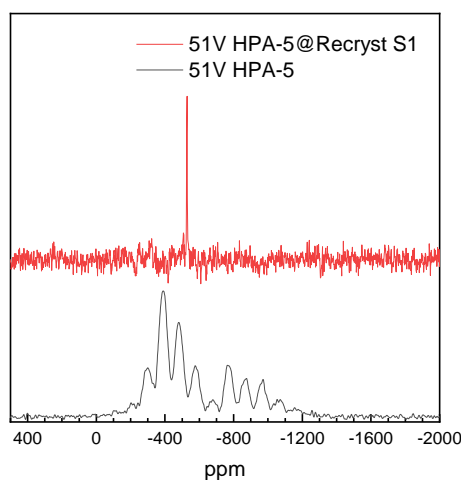


**Figure 6.9.:** The  $^{51}\text{V}$  SS-NMR spectra of the homogeneous bulk HPA-5 and the HPA-5@Recryst S1 catalyst. Isotropic chemical shifts are reported relative to  $\text{VO}(\text{Cl})_3$  (0.0 ppm) for  $^{51}\text{V}$ .

The spectra acquired with  $^{31}\text{P}$  SS-NMR supported the presence of HPW in the HPW@Recryst S1 catalyst in agreement with XRPD and FTIR. It was not possible to detect HPA-0 in the spectra acquired with  $^{31}\text{P}$  SS-NMR of the HPA-0@Recryst S1 catalyst, which was speculated to be a result of the HPA-0 Keggin structure becoming unstable at lower loadings ( $\leq 10$  wt% HPA-0). This was in agreement with XRPD and FTIR, where no

distinctive peaks or bands from HPA-0 were found. This was unfortunate, as the synthesis of encapsulated HPA-0 in the initial screening of porous supports did suggest a successful vacuum impregnation of zeolite Y with HPA-0 in accordance with FTIR, where peaks at  $952\text{ cm}^{-1}$  and  $739\text{ cm}^{-1}$  were more distinctive. FTIR of HPA-0@SiO<sub>2</sub> and HPA-0@Zeolite Y can be seen in Appendix D. As partially decomposed HPA-0 catalysts, according to Rocchiccioli-Deltcheff *et al.*,<sup>187</sup> still can have preserved catalytic activity, the HPA-0@Recryst S1 catalyst was still tested in the Fries rearrangement reaction. The spectra acquired with <sup>31</sup>P and <sup>51</sup>V SS-NMR supported the presence of HPA-n in the HPA-5@Recryst S1 catalyst. However, based on <sup>31</sup>P and <sup>51</sup>V SS-NMR, the peaks were attributed to an HPA-n Keggin structure with a lower V substitution than 5, such as HPA-2.

### 6.3.4 N<sub>2</sub> Physisorption

The isotherms of the HPA@Recryst S1 catalysts and the recrystallized silicalite-1 zeolite can be seen in Figure 6.10. All isotherms of the HPA@Recryst S1 catalysts were of Type I, as for the recrystallized silicalite-1 zeolite. This is typical for microporous materials, such as zeolites. Small Hysteresis loops with a closure at  $p/p^0$  of 0.15 characteristic for N<sub>2</sub> in MFI micropores were visible, as described in Chapter 5, subsection 5.3.3. This Hysteresis loop was most distinctive in the HPW@Recryst S1 catalyst. The isotherms showed significant H4 Hysteresis loops, which were close to parallel at  $p/p^0 > 0.45$ . These were assigned to intraparticle voids and mesopores in the recrystallized silicalite-1, which were only accessible through the inherent micropores of the zeolite. The intraparticle voids and mesopores derived from the recrystallization with TPAOH were similar to those introduced by the desilication process with CTAB described in Chapter 5. However, the acquired voids inside the silicalite-1 structure were much larger with the recrystallization process, which resulted in a much larger H4 Hysteresis loop. Wang *et al.*<sup>177</sup> reported that the intracrystalline voids resulted from a combined alkaline dissolution and a partial and local recrystallization process by TPA<sup>+</sup>, which they supported by thermal analysis and NMR.

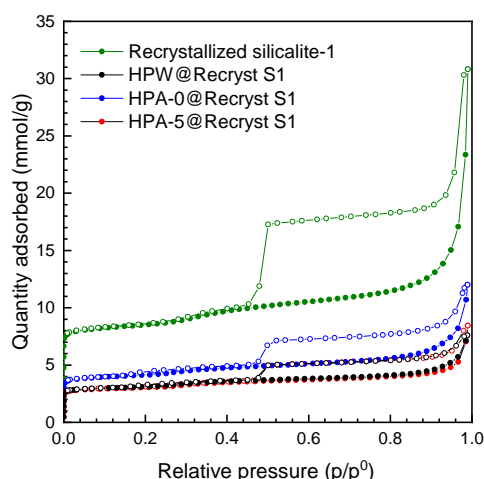


**Figure 6.10.:** The  $N_2$  physisorption isotherms of the HPA@Recryst S1 catalysts and the recrystallized silicalite-1 zeolite.

Table 6.2 presents the  $N_2$  physisorption analysis data. The recrystallized silicalite-1 zeolite had a high specific surface area of  $677 \text{ m}^2 \text{ g}^{-1}$  and a pore volume of  $0.73 \text{ cm}^3 \text{ g}^{-1}$ , where the majority of the surface area was attributed to the internal surface area deriving from the large voids and mesopores introduced by recrystallization. The HPA@Recryst S1 catalysts all held high specific surface areas of  $262\text{--}354 \text{ m}^2 \text{ g}^{-1}$ . The lower surface areas and pore volumes deriving mainly from mesopores of the HPA@Recryst S1 catalysts post to the incorporation of HPAs indicated that the voids were occupied by HPAs. The same tendency was observed in HPA impregnated dealuminated Y zeolites reported by Mukai *et al.*<sup>154</sup>

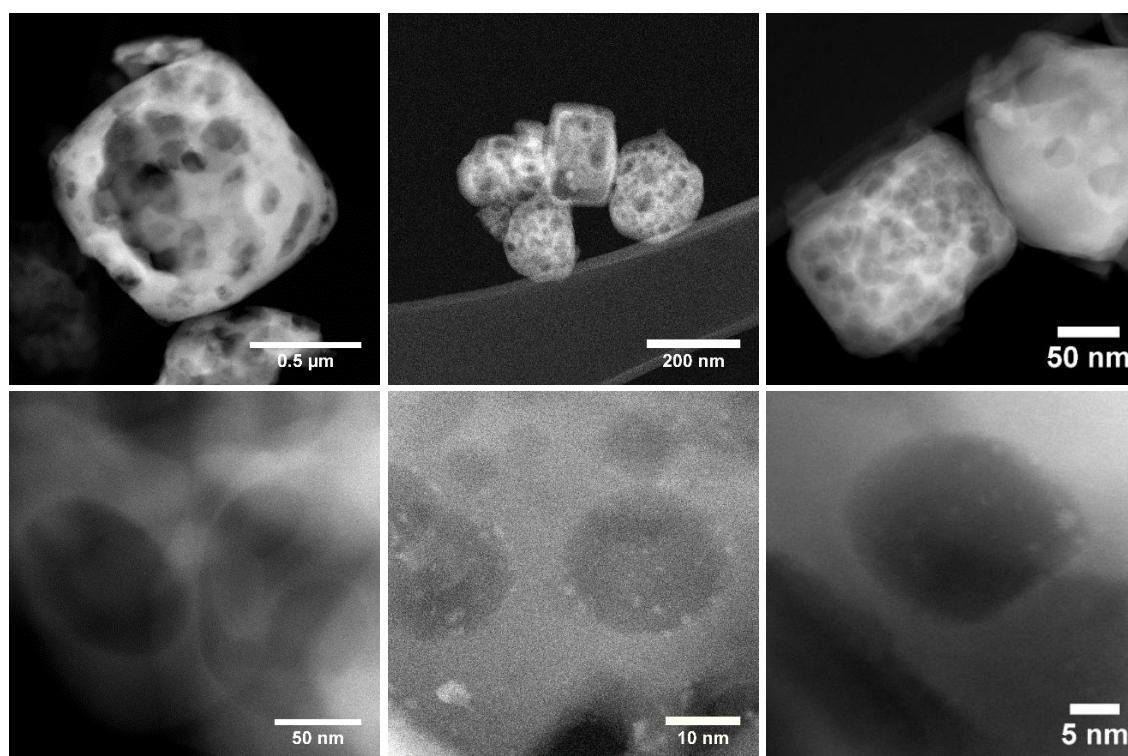
**Table 6.2.:** Overview of results from  $N_2$  physisorption analysis.

Entry	Material	$S_{\text{BET}}^a$ ( $\text{m}^2/\text{g}$ )	$S_{\text{ext}}^b$ ( $\text{m}^2/\text{g}$ )	$V_{\text{micro}}^b$ ( $\text{cm}^3/\text{g}$ )	$V_{\text{tot}}^c$ ( $\text{cm}^3/\text{g}$ )
1	Recrystallized silicalite-1	677	172	0.221	0.725
2	HPW@Recryst S1	269	62	0.081	0.221
3	HPA-0@Recryst S1	354	89	0.105	0.316
4	HPA-5@Recryst S1	262	60	0.079	0.215

<sup>a</sup> Specific surface area determined by the BET method, <sup>b</sup> external surface area and micropore volume determined by the t-plot method and <sup>c</sup> total pore volume determined by a single point read at  $p/p^0=0.95$ .

### 6.3.5 STEM and EDS

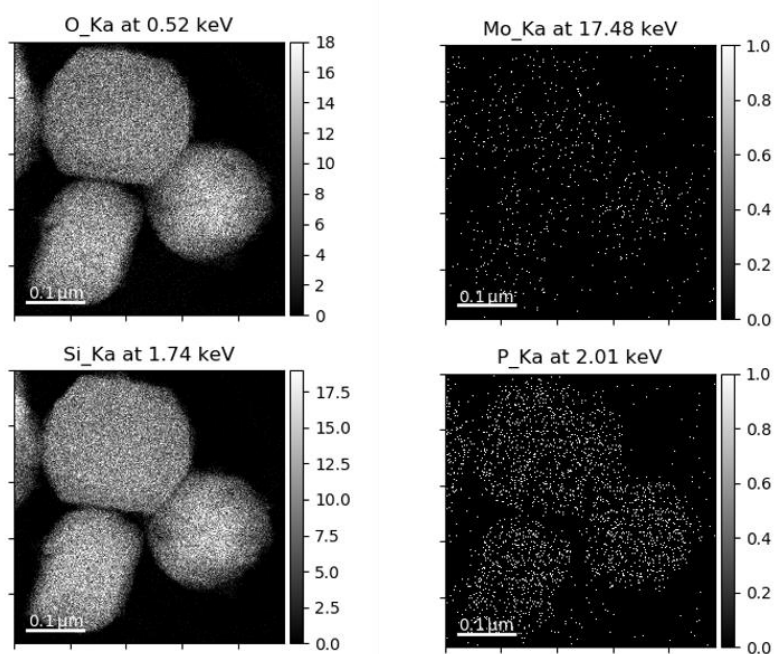
Representative STEM images (DF) of the prepared HPA@Recryst S1 catalysts can be seen in Figure 6.11. The STEM images clearly show the large mesopores and voids inside the recrystallized silicalite-1 zeolites. The zeolites were typically around 200 nm in diameter, however, zeolite crystals up to 700 nm in diameter were found. Small clusters of 1-2 nm in diameter could be seen in the STEM images, which were attributed to the small HPA structures of 1.3 nm or HPA moieties. The transition metal-based HPA structures appeared as bright spots in the voids of the zeolites in the STEM images, due to the high atomic weights of the HPAs. Additional STEM images can be seen in Appendix D.



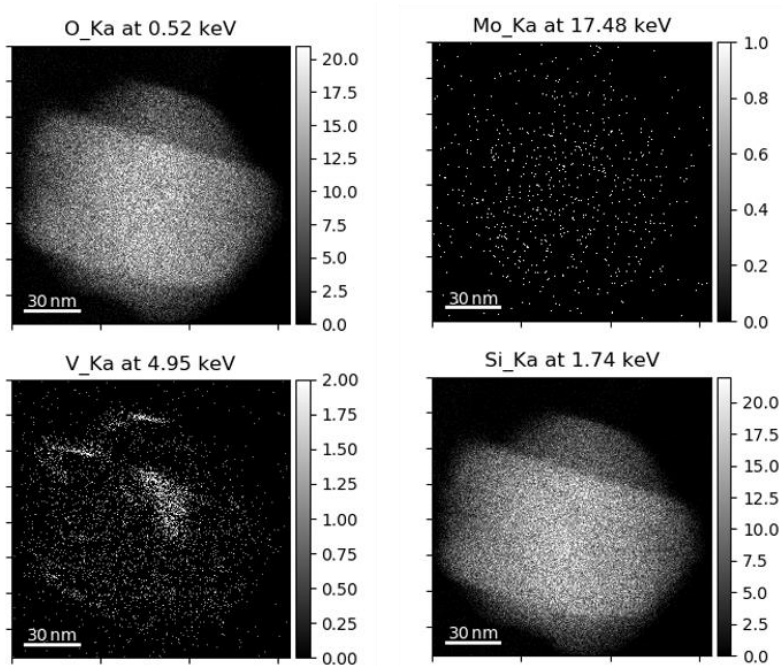
**Figure 6.11.:** *STEM (DF) images of (left) HPW@Recryst S1, (middle) HPA-0@Recryst S1, and (right) HPA-5@Recryst S1.*

Figure 6.12 and Figure 6.13 show the elemental mapping obtained by STEM (DF) EDS of the HPA-0@Recryst S1 catalyst and HPA-5@Recryst S1 catalyst, respectively. Figure 6.12 of HPA-0@Recryst S1 shows the zeolite comprising of Si and O, as well as finely dispersed Mo and P. Figure 6.13 of HPA-5@Recryst S1 additionally shows the composition of the zeolite, as well as finely dispersed Mo. It appears as if the V was dispersed throughout

the zeolite, but with agglomerated areas. Based on elemental mapping by EDS the second washing step was introduced in the synthesis procedure to make sure that no excess of V was present on the external surface of the zeolite in agglomerates.



**Figure 6.12.:** STEM (DF) EDS elemental mapping of HPA-0@Recryst S1.



**Figure 6.13.:** STEM (DF) EDS elemental mapping of HPA-5@Recryst S1.



### 6.3.6 The Phenyl Acetate Fries Rearrangement

Table 6.3 presents the activities of the bulk acidic HPA catalysts, the acidic HPA@Recryst S1 catalysts and HZSM-5 as a solid reference catalyst. All catalysts showed high selectivities towards phenol, which was expected according to literature.<sup>147</sup> The bulk HPW catalyst, entry 1, had a conversion of 12% with a selectivity towards 4AAP of 34%, excluding phenol of 59%. As suggested by Kozhevnikov *et al.*<sup>147</sup> this yield could be increased further if PhNO<sub>2</sub> was added as a solvent. The bulk HPW in 75% PhNO<sub>2</sub>, entry 2, had the highest conversion of 23% with a selectivity towards 4AAP of 26%, excluding phenol of 61%. This increased activity probably originated from less product inhibition when neat conditions were not applied, as the neat conditions can derive mass transfer and temperature gradient challenges.<sup>189</sup> HPA-0 and HPA-0@Recryst S1, entry 3 and 6, showed a poor activity in the phenyl acetate Fries rearrangement reactions with conversions of 5% and 4% with the primary selectivities towards phenol 98-99%, respectively. This was suggested by Kozhevnikova *et al.*<sup>165</sup> to be a result of catalyst reduction from the organic medium, as HPA-0 catalysts are strong oxidants.<sup>147</sup> Moreover, if the HPA-0@Recryst S1 catalyst with a loading of 5 wt% HPA-0 was partly decomposed to MoO<sub>3</sub> the low activity can be attributed to weak Lewis acidity. As a reference solid catalyst the acidic zeolite HZSM-5, entry 4, was tested in the Fries rearrangement reaction, which showed a negligible activity in comparison to the HPA based catalysts. The HPW@Recryst S1 with a loading of 30 wt% HPW, entry 5, showed surprisingly high activity with a conversion of 6% with a selectivity towards 4AAP of 21%, excluding phenol of 73%. Kozhevnikov *et al.*<sup>143</sup> reported that a maximum loading of 20 wt% HPW on a SiO<sub>2</sub> can be impregnated if the acidic strength should be maintained of the parent HPW. Thus, if this is correct 10% of the impregnated HPW was not contributing to the same extent as the bulk HPW. In this case, a 20 wt% loading HPW would be ideal. To prove the heterogeneity of the HPW@Recryst S1 catalyst a hot filtration test was performed, entry 7. Two reactions with the HPW@Recryst S1 catalyst, **a** and **b**, were simultaneously completed where the HPW@Recryst S1 catalyst from reaction **a** was filtered off after 5 min. The conversions after 5 min were 3% in both reactions **a** and **b**. After 2 h the conversion remained at 3% in reaction **a** with the absence of the HPW@Recryst S1 catalyst, however the conversion had increased to 6% in reaction **b**, as expected if the catalyst was heterogeneous. Based on the hot filtration test it was anticipated that the HPW@Recryst S1 catalyst was heterogeneous as no further activity was measured after removal of the catalyst in reaction **a**. Thus, the encapsulation in recrystallized silicalite-1 zeolites prohibited the leaching of HPW in the tested reaction media. However, catalyst recycling was not successful as product inhibition was a huge problem. Implementation of a procedure to regenerate the

catalyst after the reaction tests or to reduce deactivation by product inhibition, such as with Pd doping described previously,<sup>150</sup> is suggested as future work to introduce catalyst recycling.

The reaction conditions and catalyst amounts were not optimized in this work, which might explain the difference between the reported activities by Kozhevnikova *et al.*<sup>147</sup> and those reported in this chapter. Moreover, the pretreatment of the catalysts can have a huge effect on the activity of the HPAs, as excess water in the HPA structure can cause a decrease in the acidity. Here, a typical treatment under vacuum at 150°C was reported for the HPAs prior to the reaction in the work by Kozhevnikov *et al.*<sup>147</sup> In general, the homogeneous HPW catalyzed phenyl acetate Fries rearrangement was more effective as it produced less phenol, which was less valuable than the acetophenones. However, the encapsulation of HPW in recrystallized silicalite-1 zeolites was demonstrated as a successful non-leaching catalyst. As the encapsulation of HPA-0 in recrystallized silicalite-1 was unsuccessful, the synthesis procedure could be redesigned in regards to HPA loadings, since the loadings have a large effect on the stability of the Keggin structures. Moreover, the reaction conditions and pretreatment of the catalysts applied in the phenyl acetate Fries rearrangement reaction would be suggested to be optimized.

**Table 6.3.:** Overview of the activities obtained in the Fries rearrangement reaction.

Entry	Catalyst	Conversion (%)	Selectivity (%)			
			2HAP	PhOH	4HAP	4AAP
1	HPW	12	7	59	<1	34
2	HPW (PhNO <sub>2</sub> )	23	12	61	1	26
3	HPA-0	5	<1	98	-	2
4	HZSM-5	1	<1	>99	-	-
5	HPW@Recryst S1 <sup>a</sup>	6	4	73	2	21
6	HPA-0@Recryst S1 <sup>b</sup>	4	-	>99	-	<1
7	HPW@Recryst S1 (Hot filtration)	3*	4	74	-	22

Reaction conditions: 2 h, 150°C, PhOAc neat or in solvent PhNO<sub>2</sub> (75%). <sup>a</sup> 30wt%,

<sup>b</sup> 5wt%, \*catalyst was filtered off after 5 min and run for 2 h.

### 6.3.7 The OxFA Process

Table 6.4 shows the activity of the HPA-5@Recryst S1 catalyst in the OxFA process with glucose, entry 1, and molasses, entry 2, as substrates. A conversion of 27.8% glucose after 6 h was obtained with the HPA-5@Recryst S1 catalyst, which based on characterization by SS-NMR was assumed to be 2wt% HPA-2 encapsulated in recrystallized silicalite-1. The HPA-5@Recryst S1 catalyst was able to produce formic acid (FA) with a yield of 6.5% and a selectivity towards FA of 14.5%. Glycolaldehyde (yield of 1.7%) was also formed, which is an intermediate on the way to formic acid. Moreover, CO<sub>2</sub> was formed in large amounts with a yield of 36.6%. Thus, the HPA-5@Recryst S1 catalyst was able to convert glucose to FA, but with a lower selectivity than the homogeneous HPA-5 catalyst. The combined yield of FA and CO<sub>2</sub> was 43.0% for the HPA-5@Recryst S1 catalyst, where HPA-2 was reported by Albert *et al.*<sup>144</sup> to give a combined yield of 91.0% with a FA:CO<sub>2</sub> selectivity of 52:48. Furthermore, the bulk HPA-5 was reported to give a higher combined yield of 94.0% with a FA:CO<sub>2</sub> selectivity of 61:39%. As the loading of HPA-2 in the HPA-5@Recryst S1 catalyst was only 2 wt% and it was further encapsulated within the recrystallized silicalite-1 with small pore openings, a lower activity was expected in comparison to the homogeneous HPA-n catalysts reported in the literature by Reichert *et al.*<sup>174</sup> The small pores of the recrystallized silicalite-1 zeolites were expected to limit the mass transfer within the zeolites, which was likely to make the overall kinetics slower. Entry 2 showed that when molasses was applied as a real biomass substrate in the OxFA process with the HPA-5@Recryst S1 catalyst, no conversion was detected. In general, the oxidation of more complex biomass-derived substrates is slower and lower yields of FA can be expected in accordance to Reichert *et al.*<sup>176</sup> However, as no conversion of molasses was measured, it was expected to be caused by restricted mass transfer and size selectivity of the larger substrate into the average-sized 0.56 nm diameter pores of the MFI structured recrystallized silicalite-1 zeolites. However, based on ICP measurements of the liquid phase of the reaction medium after the OxFA process with glucose, traces of V were detected. Here, 15% of the V present in the HPA-5@Recryst S1 was measured to have leached. Thus, the HPA-5@Recryst S1 catalyst was not sufficiently stable towards leaching in water. The leaching of V could be a result of excess HPA-2 on the surface of the zeolites or due to too large pore openings of the zeolites to restrict the pervanadyl cations from leaching when HPA-2 dissociates in water. However, no leaching of V was detected in the resulting liquid phase of the reaction medium after the test with molasses. Thus, it was suggested that the small amount of V detected might also have derived from an excess of V, which was not removed sufficiently by the washing step in the synthesis of the applied catalyst batch. From these experiments it was found that

the HPA-5@Recryst S1 catalyst was able to oxidize glucose to FA, however, molasses was too large to fit the pore openings of the MFI framework. Thus, the application of HPAs encapsulated in recrystallized silicalite-1 zeolites is limited in the industrial OxFA process as the substrates are restricted to smaller molecules, such as glucose. Moreover, as leaching of V was detected in the reaction with glucose, it was concluded that the encapsulation of HPA-2 in recrystallized silicalite-1 zeolites did not provide a satisfactory synthesis approach to confine the highly soluble V species. Stabilization of the highly soluble HPA-5 catalyst by substitution of Cs cations into the structure would be suggested to improve its leaching-stability. Additionally, further optimization of the synthesis procedure to incorporate HPA-5 with a high loading would be proposed to optimize the catalytic activity. Hopefully the results obtained in this work can contribute to further development of heterogeneous non-leaching HPA-n catalysts by encapsulation in advanced porous materials.

**Table 6.4.:** Overview of the activities obtained in the OxFA process.

Entry	Catalyst	Substrate	Combined yield FA+ CO <sub>2</sub> (%)	FA yield (%)	FA Selectivity (%)
1	HPA-5@Recryst S1	Glucose	43.0	6.5	14.5
2	HPA-5@Recryst S1	Molasses	-	-	-

Batch reaction with the reaction conditions: 6 h, 90°C, 30 bar O<sub>2</sub> and 1000 rpm. 10 g H<sub>2</sub>O, 0.180 g glucose or molasses and 0.190 g HPA-5@Recryst S1 catalyst with an HPA-2 loading of 2 wt%. Formic acid is abbreviated (FA).

## 6.4 Summary

Chapter 6 was based on my work performed in collaboration with PhD student Anna Bukowski, PhD student Dorothea Voss and Dr. Ing. Jakob Albert at the Institute of Chemical Engineering, Friedrich-Alexander University (FAU), in Erlangen Germany. Here, the idea was to encapsulate different heteropolyoxometalates in zeolites in order to attain non-leaching high surface area heterogeneous catalysts. To accomplish this, I prepared different encapsulated heteropolyoxometalates HPW, HPA-0 and HPA-5 in recrystallized silicalite-1 zeolites by vacuum impregnation. XRPD and SS-NMR verified a successful encapsulation of crystalline HPW in the HPW@Recryst S1 catalyst. It was not possible to confirm the encapsulation of crystalline HPA-0 in the HPA-0@Recryst S1 catalyst. The HPA-0 structures were assumed to be partly decomposed due to strong interactions with the silanol groups of the zeolites, which can occur at lower HPA-0

loadings. SS-NMR revealed that the HPA-5@Recryst S1 catalyst more likely held encapsulated HPA-2 Keggin structures. HPA structures around 1-2 nm were visible in high-resolution STEM (DF) and based on elemental mappings by EDS, the Mo and V appeared to be dispersed throughout the zeolites. The catalysts HPW@Recryst S1 and HPA-0@Recryst S1 were tested in a phenyl acetate Fries rearrangement reaction. Here, the HPA-0@Recryst S1 had a poor activity in the phenyl acetate Fries rearrangement reaction with a conversion of 4% with the primary selectivity towards phenol (99%). This activity was similar to that of the homogeneous HPA-0, which was expected to be a result of catalyst reduction from the organic medium, as HPA-0 catalysts are strong oxidants. The HPW@Recryst S1 catalyst showed significant activity with a conversion of 6% with a selectivity towards 4AAP of 21%, excluding phenol of 73%. Based on hot filtration tests it was anticipated that the HPW@Recryst S1 catalyst was heterogeneous and the confinement in recrystallized silicalite-1 zeolites restricted the HPW from leaching in polar media. However, it was not possible to recycle the catalyst due to product inhibition. Here, optimization as Pd doping of the HPW@Recryst S1 catalyst to introduce recycling could be attempted. The catalyst HPA-5@Recryst S1 was tested in the OxFA process. Here, the HPA-5@Recryst S1 catalyst was able to convert glucose to FA with a yield of 6.5% with a selectivity towards FA of 14.5%. The HPA-5@Recryst S1 catalyst was not able to convert molasses, which was expected to be caused by mass transfer limitations and size selectivity restricting the larger molasses substrates of entering the average MFI pore openings of 0.56 nm in diameter. A 15% leaching of the V present in the HPA-5@Recryst S1 catalyst was detected, which revealed that encapsulation in recrystallized silicalite-1 did not offer a sufficient synthesis method to confine the highly soluble V species. To decrease the solubility of HPA-5 in polar media substitution of Cs cations into the HPA-5 structures would be suggested to increase the stability of the encapsulated catalyst. Moreover, an optimized synthesis method to incorporate higher HPA-n loadings and ensure no excess of V is present at the surface of the support is suggested. Hopefully, these results can contribute to the further development of heterogeneous non-leaching HPA catalysts by encapsulation in nano-engineered porous materials.

## Chapter 7. Conclusion

The objective of this dissertation was to prepare different novel heterogeneous catalysts with high thermal stabilities and prevented leaching, and to test these in existing catalytic processes. The catalysts were prepared by encapsulation of catalytically active metals in nano-engineered porous materials. The metals were introduced by the use of sacrificial metal precursors or metal impregnation. In Chapter 3 (p. 35-55) and Chapter 4 (p. 57-81) the catalysts were prepared from sacrificial metal precursors in order to obtain thermally stable catalysts, and in Chapter 5 (p. 83-100) and Chapter 6 (p. 101-128) the catalysts were prepared by metal impregnation of nanoporous materials in order to obtain non-leaching catalysts.

In Chapter 3 the use of Co-based ZIF-67 and Zn-based ZIF-8 structures as sacrificial templates and metal precursors for the synthesis of Co nanoparticles encapsulated in porous nitrogen-doped carbon matrices was described. Modifications of these catalysts were introduced by varying the synthesis temperature (25°C and 60°C), carbonization temperature (750°C and 900°C) and the incorporation of Zn to give bimetallic ZIF-67/8 metal precursors. The Zn was later removed by evaporation at 900°C. In general, it was found that lower ZIF synthesis temperatures and the introduction of Zn (ZIF-67/8) favored the formation of smaller crystals and subsequent small catalyst particles. Additionally, a high carbonization temperature increased the sintering of Co nanoparticles compared to the same catalyst prepared at a lower temperature. However, this was not the case for the catalyst, Co/NC-50, which was derived from 50 nm ZIF-67/8 crystals. The Co/NC-50 catalyst preserved a good dispersion of Co nanoparticles after carbonization at 900°C, and a narrow particle size distribution of 5-

15 nm in diameter. The prepared catalysts were tested in the hydrolytic dehydrogenation of ammonia borane. Here, the Co/NC-50 catalyst proved the most active and released the highest amount of H<sub>2</sub> with a TOF of 12.7 min<sup>-1</sup> in 0.1M NaOH. The high activity was attributed to the narrower particle size distribution of the Co nanoparticles and the high surface area carbon support, which was obtained from small ZIF-67/8 crystals. Furthermore, the Co/NC-50 catalyst could be recycled with 83% of the initial activity retained after 5 cycles. Chapter 3 illustrated that ZIFs could be used as sacrificial templates and metal precursors to obtain stable, high surface area carbon catalysts with high dispersion of small Co nanoparticles.

In Chapter 4, the use of ZIF-67 and ZIF-8 structures as sacrificial templates and metal precursors for the synthesis of Co<sub>3</sub>O<sub>4</sub> nanoparticles encapsulated in mesoporous SiO<sub>2</sub> shells was presented. These nanorattle catalysts were modified by thermal treatments (carbonization and/or calcination) and variations in the Co/Zn ratios of the ZIF-67/8 precursors (3:1, 1:3, 1:1, 0:1, 1:0). It was found that the introduction of a carbonization step prior to the calcination step lowered the required calcination temperature from 500°C to 300°C. The calcination of the ZIF-67/8 crystals yielded Co<sub>3</sub>O<sub>4</sub> nanoparticles on the internal surface of the mesoporous SiO<sub>2</sub> shell. The lower calcination temperature resulted in reduced sintering yielding small and well-dispersed Co<sub>3</sub>O<sub>4</sub> nanoparticles of 2-20 nm in diameter. Moreover, by altering the Co/Zn ratios it was possible to control the nanorattle particle sizes (40-350 nm) and the Co loadings (0-27 wt%). All nanorattle catalysts containing Co<sub>3</sub>O<sub>4</sub> nanoparticles were tested in a CO oxidation reaction where most of the catalysts showed similar performance in the oxidation of CO to CO<sub>2</sub> with a TOF of  $1.2 \cdot 10^{-1}$  min<sup>-1</sup>. However, for the nanorattle catalyst prepared with a Co/Zn ratio of 1:3, a poor performance was observed due to insufficient removal of the high amount of Zn. Chapter 4 described how ZIFs could be exploited as sacrificial templates and metal precursors to obtain sinter-stable nanorattle catalysts with Co<sub>3</sub>O<sub>4</sub> nanoparticles well-dispersed on the internal surface of mesoporous SiO<sub>2</sub> shells.

In Chapter 5, the preparation of encapsulated iron molybdate catalysts in nanoporous materials was described. Here, hollow SiO<sub>2</sub> spheres with an average pore size of 2.30 nm in diameter and desilicated silicalite-1 zeolites with an average pore size of 0.56 nm in diameter were designed to confine and prevent leaching of Mo. The active metals were introduced by vacuum impregnation of the nanoporous materials to form the iron molybdate phases *in situ*. All encapsulated iron molybdate catalysts were tested for the selective oxidation of methanol to formaldehyde under simulated accelerated deactivation conditions to test the stability towards leaching. The catalyst, FeMo@D S1 (2.56), consisting of iron molybdate in the ratio Mo/Fe= 2.56 encapsulated in desilicated

silicalite-1, showed the highest conversion of methanol measured from 61.3%-18.6% at 350°C from 0-100 h with a high selectivity towards formaldehyde of 99.5%-99.0%. The catalyst, FeMo@D S1 (2.56) showed increased stability towards Mo leaching compared to the industrial iron molybdate catalyst. However, the synthesis procedure using vacuum impregnation proved challenging to reproduce. In Chapter 5 it was demonstrated how nano-engineered porous materials can be used in the design of non-leaching catalysts. It was described how the active metals could easily be encapsulated in nanoporous materials by metal impregnation, however, reproduction of the catalysts proved challenging as it was difficult to precisely control the Mo/Fe ratio.

In Chapter 6, heteropolyoxometalates encapsulated in nanoporous materials were prepared by metal impregnation of recrystallized silicalite-1 zeolites. The aim was to convert the HPA catalysts, HPW, HPA-0 and HPA-5, into heterogeneous catalysts with high surface area and prevented leaching in polar media. The encapsulation of HPW proved to be successful. However, the encapsulation of HPA-0 suffered from partial decomposition at low loadings, due to strong interactions with the zeolite support. In the synthesis of the encapsulated V-substituted HPA-5, the lower V substituted HPA-2 structure was obtained instead. The Brønsted acidic catalysts, HPW@Recryst S1 and HPA-0@Recryst S1, were tested in the phenyl acetate Fries rearrangement reaction. The catalyst, HPW@Recryst S1, showed significant activity in the Fries rearrangement reaction with a conversion of 6% with the highest product selectivity towards 4AAP of 21%, excluding the by-product phenol. A hot filtration test of the catalyst provided evidence that it was heterogeneous and stable towards leaching. The redox-active V-substituted catalyst, HPA-5@Recryst S1, was tested for the selective oxidation of biomass to formic acid. The catalyst, HPA-5@Recryst S1, was able to convert glucose to formic acid with a yield of 6.5% and a selectivity towards formic acid of 14.5%. Unfortunately, the encapsulation was not sufficient to prevent leaching completely, as 15% V was detected in the liquid phase after the reaction. Chapter 6 described the encapsulation of HPW in recrystallized silicalite-1 zeolites by metal impregnation to derive a non-leaching catalyst. However, in the encapsulation of the more unstable Keggin structures, HPA-0 and HPA-2, metal impregnation of recrystallized silicalite-1 zeolites proved to be an inadequate method, as only low loadings could be introduced.

The results reported in this dissertation demonstrated the benefits and challenges of encapsulating active metals in nano-engineered porous materials using sacrificial metal precursors and metal impregnation. Heterogeneous catalysts prepared from sacrificial metal precursors offer great control of the derived metal nanoparticle size distributions, dispersions and loadings, which can be used to improve thermal stability.



Heterogeneous catalysts prepared by metal impregnation of nano-engineered porous materials offer a simple way to encapsulate a range of active metals. However, the method suffers from challenges with reproducibility and depending on the encapsulated active metal leaching may occur.

Further investigation of heterogeneous catalysts prepared from the encapsulation of active metals in nano-engineered porous materials is necessary for the industrial application of these. The majority of existing synthesis procedures are costly to up-scale, and reproducibility can be a challenge. Encapsulated active metals are currently more adequate as catalytic model systems, to achieve more knowledge of how encapsulation of active metals affects the stability and activity in catalytic processes. The results obtained in this dissertation describes some of the advantages and disadvantages of encapsulating catalytically active metals in nanoporous materials. This knowledge can be valuable in the further development of novel thermally stable and non-leaching heterogeneous catalysts.

## Bibliography

1. Zacho, S. L., Hyllested, J., Kasama, T. & Mielby, J. Controlling the dispersion of Co<sub>3</sub>O<sub>4</sub> nanoparticles inside mesoporous nanorattle catalysts. *Catal. Commun.* **125**, 6–9 (2019).
2. Chorkendorff, I. & Niemantsverdriet, J. W. *Concepts of Modern Catalysis and Kinetics*. (John Wiley and Sons Ltd, 2003).
3. Rothenberg, G. *Catalysis: Concepts and Green Applications*. (Wiley-VCH Verlag GmbH & Co. KGaA, 2008).
4. Knözinger, H. & Kochloefl, K. *Ullmann's Encyclopedia of Industrial Chemistry*. *Ullmann's encyclopedia of industrial chemistry* (2012).
5. Ostwald, W. Definition der Katalyse. *Z. Phys. Chem.* **15**, 705–706 (1894).
6. Hagen, J. *Industrial catalysis: a practical approach*. (Wiley-VCH Verlag GmbH & Co. KGaA, 2006).
7. Misono, M. Basis of Heterogeneous Catalysis. *Studies in Surface Science and Catalysis*. **176**, 1–23 (2013).
8. Pan, Y., Shen, X., Yao, L., Bentalib, A. & Peng, Z. Active Sites in Heterogeneous Catalytic Reaction on Metal and Metal Oxide: Theory and Practice. *Catalysts* **8**, 478 (2018).
9. Korotchenkov, G. S. & Védrine, J. C. *Metal Oxides in Heterogeneous Catalysis*. *Metal Oxides in Heterogeneous Catalysis* (2018).
10. Boudart, M. Turnover Rates in Heterogeneous Catalysis. *Chem. Rev.* **95**, 661–666 (1995).
11. Prieto, G. *et al.* Hollow Nano- and Microstructures as Catalysts. *Chem. Rev.* **116**, 14056–14119 (2016).
12. Arulmani, S., Anandan, S. & Ashokkumar, M. *Nanomaterials for Green Energy*. (Elsevier, 2018).

13. Dibenedetto, A. & Aresta, M. *Inorganic micro-and nanomaterials: Synthesis and Characterization*. (2013).
14. Ricco, R., Malfatti, L., Takahashi, M., Hill, A. J. & Falcaro, P. Applications of Magnetic Metal-Organic Framework Composites. *J. Mater. Chem. A* **1**, 13033–13045 (2013).
15. Jia, X., Khan, W., Wu, Z., Choi, J. & Yip, A. C. K. Modern synthesis strategies for hierarchical zeolites: Bottom-up versus top-down strategies. *Adv. Powder Technol.* **30**, 467–484 (2019).
16. Hansen, T. W., Delariva, A. T., Challa, S. R. & Datye, A. K. Sintering of Catalytic Nanoparticles : Particle Migration or Ostwald Ripening? *Accounts Chem. Res.* **46**, 1720–1730 (2013).
17. Viegard, K. R. *et al.* Deactivation Behavior of an Iron-Molybdate Catalyst during Selective Oxidation of Methanol to Formaldehyde. *Catal. Sci. Technol.* **8**, 4626–4637 (2018).
18. Sharmin, E. & Zafar, F. *Metal-Organic Frameworks*. Intech (IntechOpen, 2016).
19. Bruce, D. W., O'Hare, D. & Walton, R. I. *Porous Materials*. (John Wiley & Sons, 2010).
20. Furukawa, H., Cordova, K. E., O'Keeffe, M. & Yaghi, O. M. The chemistry and applications of metal-organic frameworks. *Science (80-. )*. **341**, 974 (2013).
21. ZIF-8. *University of Liverpool, ChemTube3D*. <https://www.chemtube3d.com/mof-zif8/> (2019).
22. Zhou, H. C. J. & Kitagawa, S. Metal-Organic Frameworks (MOFs). *Chem. Soc. Rev.* **43**, 5415–5418 (2014).
23. Sun, Y. & Zhou, H. C. Recent progress in the synthesis of metal-organic frameworks. *Sci. Technol. Adv. Mater.* **16**, 1–11 (2015).
24. Liu, B., Shioyama, H., Akita, T. & Xu, Q. Metal-Organic Framework as a Template for Porous Carbon. *J. Am. Chem. Soc.* **130**, 5390–5391 (2008).
25. Oar-Arteta, L., Wezendonk, T., Sun, X., Kapteijn, F. & Gascon, J. Metal Organic Frameworks as Precursors for the Manufacture of Advanced Catalytic Materials.

- Mater. Chem. Front.* **1**, 1709–1745 (2017).
26. Slowing, I. I., Vivero-Escoto, J. L., Wu, C. W. & Lin, V. S. Y. Mesoporous silica nanoparticles as controlled release drug delivery and gene transfection carriers. *Adv. Drug Deliv. Rev.* **60**, 1278–1288 (2008).
  27. International Zeolite Association, I. [www.europe.iza-structure.org/IZA-SC/ftc\\_table.php](http://www.europe.iza-structure.org/IZA-SC/ftc_table.php). <http://www.iza-structure.org/databases/> (2020).
  28. Yates, D. J. C. Studies on the surface area of zeolites, as determined by physical adsorption and X-ray crystallography. *Can. J. Chem.* **46**, 1695–1701 (1968).
  29. Cruciani, G. Zeolite upon heating: Factors governig their thermal stability and structural changes. *J. Phys. Chem. Solids* **67**, 1973–1994 (2006).
  30. FAU zeolite. AZ<sup>TM</sup> Industrial Applications. <https://www.asiazeolite.com/industrial> (2019).
  31. Serp, P. & Machado, B. *Nanostructured Carbon Materials*. (Cambridge University Press, 2015).
  32. Kaneko, K., Ishii, C., Ruike, M. & kuwabara, H. Origin of superhigh surface area and microcrystalline graphitic structures of activated carbons. *Carbon N. Y.* **30**, 1075–1088 (1992).
  33. Bai, L. *et al.* Synthesis of Metallic Nanocrystals : From Noble Metals to Base Metals. *Materials (Basel)*. **12**, 1497 (2019).
  34. White, R. J., Luque, R., Budarin, V. L., Clark, J. H. & Macquarrie, D. J. Supported metal nanoparticles on porous materials . Methods and applications. *Chem. Soc. Rev.* **38**, 481–494 (2009).
  35. Zhang, L., Feng, C., Gao, S., Wang, Z. & Wang, C. Palladium Nanoparticle Supported on Metal-Organic Framework derived N-Decorated Nanoporous Carbon as an Efficient Catalyst for the Suzuki Coupling Reaction. *Catal. Commun.* **61**, 21–25 (2015).
  36. Zhong, W., Liu, H., Bai, C., Liao, S. & Li, Y. Base-Free Oxidation of Alcohols to Esters at Room Temperature and Atmospheric Conditions using Nanoscale Co-Based Catalysts. *ACS Catal.* **5**, 1850–1856 (2015).

37. Cao, X. *et al.* Metal Oxide-Coated Three-Dimensional Graphene Prepared by the Use of Metal-Organic Frameworks as Precursors. *Angew. Chemie - Int. Ed.* **53**, 1404–1409 (2014).
38. Malonzo, C. D. *et al.* Thermal Stabilization of Metal-Organic Framework-Derived Single-Site Catalytic Clusters through Nanocasting. *J. Am. Chem. Soc.* **138**, 2739–2748 (2016).
39. Cao, X., Tan, C., Sindoro, M. & Zhang, H. Hybrid Micro-/Nano-structures derived from Metal–Organic Frameworks: Preparation and Applications in Energy Storage and Conversion. *Chem. Soc. Rev.* **46**, 2660–2677 (2017).
40. McNamara, N. D., Kim, J. & Hicks, J. C. Controlling the Pyrolysis Conditions of Microporous/Mesoporous MIL-125 to Synthesize Porous, Carbon-Supported Ti Catalysts with Targeted Ti Phases for the Oxidation of Dibenzothiophene. *Energy and Fuels* **30**, 594–602 (2016).
41. Shen, Y. Carbothermal Synthesis of Metal-Functionalized Nanostructures for Energy and Environmental Applications. *J. Mater. Chem. A* **3**, 13114–13188 (2015).
42. Zacho, S. L., Mielby, J. & Kegnæs, S. Hydrolytic dehydrogenation of ammonia borane over ZIF-67 derived Co nanoparticle catalysts. *Catal. Sci. Technol.* **8**, 4741–4746 (2018).
43. Zacho, S. L., Gajdek, D., Mielby, J. & Kegnæs, S. Synthesis of Nano-engineered Catalysts Consisting of Co<sub>3</sub>O<sub>4</sub> Nanoparticles Confined in Porous SiO<sub>2</sub>. *Top. Catal.* **62**, 621–627 (2019).
44. Hollas, J. M. Modern spectroscopy. in *Modern spectroscopy* 479–501 (Wiley-VCH Verlag GmbH & Co. KGaA, 2004).
45. [www.Malvernpanalytical.com/en/products/technology/x-ray-fluorescence](http://www.Malvernpanalytical.com/en/products/technology/x-ray-fluorescence). *Malvern panalytical* (2020).
46. Kramar, U. X-Ray Fluorescence Spectrometers. *Encycl. Spectrosc. Spectrom.* 695–706 (2017).
47. Chorkendorff, I. & Niemantsverdriet, J. W. *Concepts of Modern Catalysis and Kinetics*. (2003).

- 
48. [www.labcompare.com/Spectroscopy/165-Infrared-Spectroscopy-IR-FTIR/](http://www.labcompare.com/Spectroscopy/165-Infrared-Spectroscopy-IR-FTIR/). *Labcompare* (2020).
  49. Chorkendorff, I. & Niemantsverdriet, J. W. *Concepts of Modern Catalysis and Kinetics*. (2003).
  50. Thommes, M. *et al.* Physisorption of gases, with special reference to the evaluation of surface area and pore size distribution (IUPAC Technical Report). *Pure Appl. Chem.* **87**, 1051–1069 (2015).
  51. Brunauer, S., Deming, L. S., Deming, W. E. & Teller, E. On a Theory of the Van der Waals Adsorption of Gases. *J. Am. Chem. Soc.* **62**, 1723–1732 (1940).
  52. Atkins, B. Y. & Paula, D. *Atkins' Physical Chemistry 9th edition*. (Oxford University Press, 2010).
  53. Sing, K. S. W. Adsorption Methods for the Characterization of Porous Materials. *Adv. Colloid Interface Sci.* **76–77**, 3–11 (1998).
  54. de Boer, J. H., Linsen, B. G., van der Plas, T. & Zondervan, G. J. Studies on Pore Systems in Catalysts. The t Method. *J. Catal.* **4**, 319–323 (1965).
  55. Landers, J., Gor, G. Y. & Neimark, A. V. Density Functional Theory Methods for Characterization of Porous Materials. *Colloids Surfaces A Physicochem. Eng. Asp.* **437**, 3–32 (2013).
  56. Goodhew, P. J., Humphreys, J. & Beanland, R. *Electron Microscopy and Analysis*. (Taylor & Francis, 2000).
  57. Zhou, W. & Lin, Z. *Scanning Microscopy for Nanotechnology*. (Springer, 2006).
  58. Spurgeon, S. R. [www.inspirehep.net/record/1774177/plots](http://www.inspirehep.net/record/1774177/plots). *InspireHep* 1 <http://arxiv.org/abs/2001.00947> (2020).
  59. Williams, D. B. & Carter, C. B. *Transmission Electron Microscopy*. (Springer, 2009).
  60. Kübel, C. *et al.* Recent advances in electron tomography: TEM and HAADF-STEM tomography for materials science and semiconductor applications. *Microsc. Microanal.* **11**, 378–400 (2005).

61. Midgley, P. A. & Weyland, M. 3D Electron Microscopy in the Physical Sciences: The Development of Z-Contrast and EFTEM Tomography. *Ultramicroscopy* **96**, 413–431 (2003).
62. Friedrich, H., De Jongh, P. E., Verkleij, A. J. & De Jong, K. P. Electron Tomography for Heterogeneous Catalysts and Related Nanostructured Materials. *Chem. Rev.* **109**, 1613–1629 (2009).
63. Dybowski, C. & Bai, S. Solid-State NMR Spectroscopy. *Anal. Chem.* **80**, 4295–4300 (2008).
64. Raja, P. M. V & Barron, A. R. *Physical Methods in Chemistry and Nano Science*. (2014).
65. Hunger, M. *Solid-State NMR Spectroscopy*. (Springer, 2009).
66. [www.bp.com/content/dam/bp/business-sites/en/global/corporate/pdfs/energy-economics/statistical-review/bp-stats-review-2019-full-report.pdf](http://www.bp.com/content/dam/bp/business-sites/en/global/corporate/pdfs/energy-economics/statistical-review/bp-stats-review-2019-full-report.pdf). *BP Statistical Review of World Energy 2019* 1–69 (2019).
67. [www.latimes.com/environment/story/2019-12-03/carbon-dioxide-emissions-fossil-fuels-record-high-2019](http://www.latimes.com/environment/story/2019-12-03/carbon-dioxide-emissions-fossil-fuels-record-high-2019). *Los Angeles Times* (2019).
68. Rebhan, E. Challenges for Future Energy Usage. *Eur. Phys. J. Spec. Top.* **176**, 53–80 (2009).
69. Klebanoff, L. E. *Hydrogen Storage Technology: Materials and Applications. Section II, 8. Development of Off-Board Reversible Hydrogen Storage Materials*. (Taylor & Francis, 2012).
70. Dincă, M. & Long, J. R. Hydrogen Storage in Microporous Metal-Organic Frameworks with Exposed Metal Sites. *Angew. Chemie - Int. Ed.* **47**, 6766–6779 (2008).
71. Veenstra, M. J. & Hobein, B. On-Board Physical Based 70 MPa Hydrogen Storage Systems. *SAE Int. J. Engines* **4**, 1862–1871 (2011).
72. [www.energy.gov/eere/fuelcells/hydrogen-storage](http://www.energy.gov/eere/fuelcells/hydrogen-storage). *U.S. Department of Energy's Office of Energy Efficiency and Renewable Energy* (2020).

- 
73. Yang, Y. *et al.* Catalytic Hydrolysis of Ammonia Borane by Cobalt Nickel Nanoparticles Supported on Reduced Graphene Oxide for Hydrogen Generation. *J. Nanomater.* **2014**, 1–9 (2014).
  74. Chen, W. *et al.* Reaction Mechanism and Kinetics for Hydrolytic Dehydrogenation of Ammonia Borane on a Pt/CNT Catalyst. *AIChE J.* **63**, 60–65 (2017).
  75. Zhan, W. W., Zhu, Q. L. & Xu, Q. Dehydrogenation of Ammonia Borane by Metal Nanoparticle Catalysts. *ACS Catal.* **6**, 6892–6905 (2016).
  76. Akbayrak, S., Tonbul, Y. & Özkar, S. Ceria Supported Rhodium Nanoparticles: Superb Catalytic Activity in Hydrogen Generation from the Hydrolysis of Ammonia Borane. *Appl. Catal. B Environ.* **198**, 162–170 (2016).
  77. Chen, W. *et al.* Unique Reactivity in Pt/CNT Catalyzed Hydrolytic Dehydrogenation of Ammonia Borane. *Chem. Commun.* **50**, 2142–2144 (2014).
  78. Du, C. *et al.* Facile Synthesis of Monodisperse Ruthenium Nanoparticles Supported on Graphene for Hydrogen Generation from Hydrolysis of Ammonia Borane. *Int. J. Hydrogen Energy* **40**, 6180–6187 (2015).
  79. Chen, J., Lu, Z. H., Wang, Y., Chen, X. & Zhang, L. Magnetically Recyclable Ag/SiO<sub>2</sub>-CoFe<sub>2</sub>O<sub>4</sub> Nanocomposite as a Highly Active and Reusable Catalyst for H<sub>2</sub> Production. *Int. J. Hydrogen Energy* **40**, 4777–4785 (2015).
  80. Akbayrak, S., Kaya, M., Volkan, M. & Özkar, S. Palladium(0) Nanoparticles Supported on Silica-Coated Cobalt Ferrite: A Highly Active, Magnetically Isolable and Reusable Catalyst for Hydrolytic Dehydrogenation of Ammonia Borane. *Appl. Catal. B Environ.* **147**, 387–393 (2014).
  81. Mahyari, M. & Shaabani, A. Nickel Nanoparticles Immobilized on Three-Dimensional Nitrogen-Doped Graphene as a Superb Catalyst for the Generation of Hydrogen from the Hydrolysis of Ammonia Borane. *J. Mater. Chem. A* **2**, 16652–16659 (2014).
  82. Kaya, M., Zahmakiran, M., Özkar, S. & Volkan, M. Copper(0) Nanoparticles Supported on Silica-Coated Cobalt Ferrite Magnetic Particles: Cost Effective Catalyst in the Hydrolysis of Ammonia-Borane with an Exceptional Reusability Performance. *ACS Appl. Mater. Interfaces* **4**, 3866–3873 (2012).
  83. Hu, J., Chen, Z., Li, M., Zhou, X. & Lu, H. Amine-Capped Co Nanoparticles for Highly



- Efficient Dehydrogenation of Ammonia Borane. *ACS Appl. Mater. Interfaces* **6**, 13191–13200 (2014).
84. Duman, S., Metin, O. & Özkar, S. B-N Polymer Embedded Iron(0) Nanoparticles as Highly Active and Long Lived Catalyst in the Dehydrogenation of Ammonia Borane. *J. Nanosci. Nanotechnol.* **13**, 4954–61 (2013).
85. Li, X., Zeng, C., Jiang, J. & Ai, L. Magnetic Cobalt Nanoparticles Embedded in Hierarchically Porous Nitrogen-Doped Carbon Frameworks for Highly Efficient and Well-Recyclable Catalysis. *J. Mater. Chem. A* **4**, 7476–7482 (2016).
86. Kramer, S., Mielby, J., Buss, K., Kasama, T. & Kegnæs, S. Nitrogen-Doped Carbon-Encapsulated Nickel/Cobalt Nanoparticle Catalysts for Olefin Migration in Allylarenes. *ChemCatChem* **9**, 2930–2934 (2017).
87. Kramer, S., Hejjo, F., Rasmussen, K. H. & Kegnæs, S. Silylative Pinacol Coupling Catalyzed by Nitrogen-Doped Carbon-Encapsulated Nickel/Cobalt Nanoparticles: Evidence for a Silyl Radical Pathway. *ACS Catal.* **8**, 754–759 (2018).
88. Yang, L. *et al.* Graphene Supported Cobalt(0) Nanoparticles for Hydrolysis of Ammonia Borane. *Mater. Lett.* **115**, 113–116 (2014).
89. Hummers, W. S. & Offeman, R. E. Preparation of Graphitic Oxide. *J. Am. Chem. Soc.* **80**, 1339 (1958).
90. Kovtyukhova, N. I. Layer-by-Layer Assembly of Ultrathin Composite Films from Micron-Sized Graphite Oxide Sheets and Polycations. *Chem. Mater.* **11**, 771–778 (1999).
91. Wang, C. *et al.* Hydrolysis of Ammonia-Borane over Ni/ZIF-8 Nanocatalyst: High Efficiency, Mechanism, and Controlled Hydrogen Release. *J. Am. Chem. Soc.* **139**, 11610–11615 (2017).
92. Yao, Q., Yang, K., Hong, X., Chen, X. & Lu, Z. Base-Promoted Hydrolytic Dehydrogenation of Ammonia Borane Catalyzed by Noble-Metal-Free Nanoparticles. *Catal. Sci. Technol.* **8**, 870–877 (2018).
93. Xia, W. *et al.* Well-Defined Carbon Polyhedrons Prepared from Nano Metal-Organic Frameworks for Oxygen Reduction. *J. Mater. Chem. A* **2**, 11606–11613 (2014).

- 
94. Zheng, F. *et al.* Automated Gas Burette System for Evolved Hydrogen Measurements. *Rev. Sci. Instrum.* **79**, 084103 (2008).
  95. Wang, H., Zhao, Y., Cheng, F., Tao, Z. & Chen, J. Cobalt Nanoparticles Embedded in Porous N-doped Carbon as Long-Life Catalysts for Hydrolysis of Ammonia Borane. *Catal. Sci. Technol.* **6**, 3443–3448 (2016).
  96. Yin, P. *et al.* Single Cobalt Atoms with Precise N-Coordination as Superior Oxygen Reduction Reaction Catalysts - Yin - 2016 - Angewandte Chemie International Edition. *Angew. Chem. Int. Ed.* **55**, 10800–10805 (2016).
  97. Feng, X. & Carreon, M. A. Kinetics of Transformation on ZIF-67 Crystals. *J. Cryst. Growth* **418**, 158–162 (2015).
  98. Meng, J. *et al.* General Oriented Formation of Carbon Nanotubes from Metal-Organic Frameworks. *J. Am. Chem. Soc.* **139**, 8212–8221 (2017).
  99. Chen, E., Yang, H. & Zhang, J. Zeolitic Imidazolate Framework as Formaldehyde Gas Sensor. *Inorg. Chem.* **53**, 5411–5413 (2014).
  100. Schejn, A. *et al.* Controlling ZIF-8 Nano- and Microcrystal Formation and Reactivity Through Zinc Salt Variations. *CrystEngComm* **16**, 4493–4500 (2014).
  101. Metin, Ö. & Özkar, S. Water Soluble Nickel(0) and Cobalt(0) Nanoclusters Stabilized by Poly(4-Styrenesulfonic acid-co-maleic acid): Highly Active, Durable and Cost Effective Catalysts in Hydrogen Generation from the Hydrolysis of Ammonia Borane. *Int. J. Hydrogen Energy* **36**, 1424–1432 (2011).
  102. Bennedsen, N. R., Kramer, S., Mielby, J. J. & Kegnæs, S. Cobalt–Nickel Alloy Catalysts for Hydrosilylation of Ketones Synthesized by Utilizing Metal–Organic Framework as Template. *Catal. Sci. Technol.* **8**, 2434–2440 (2018).
  103. Soliman, N. K. Factors Affecting CO Oxidation Reaction over Nanosized Materials: A review. *J. Mater. Res. Technol.* **8**, 2395–2407 (2019).
  104. Kummer, J. T. Use of Noble Metals in Automobile Exhaust Catalysts. *J. Phys. Chem.* **90**, 4747–4752 (1986).
  105. Lafyatis, D. S. *et al.* Ambient Temperature Light-Off for Automobile Emission Control. *Appl. Catal. B Environ.* **18**, 123–135 (1998).

106. Xanthopoulou, G. G., Novikova, V. A., A., K. Y. & P., A. A. Nanocatalysts for Low-Temperature Oxidation of CO: Review. *Eurasian Chem. J.* **17**, 17–32 (2015).
107. Khedr, M. H., Nasr, M. I., Abdel Halim, K. S., Farghali, A. A. & Soliman, N. K. CO Oxidation over Various Nanostructured Metal Oxides. *Int. J. Adv. Res.* **2**, 593–606 (2014).
108. Royer, S. & Duprez, D. Catalytic Oxidation of Carbon Monoxide over Transition Metal Oxides. *ChemCatChem* **3**, 24–65 (2011).
109. Corma, A. & Garcia, H. Supported Gold Nanoparticles as Catalysts for Organic Reactions. *Chem. Soc. Rev.* **37**, 2096–2126 (2008).
110. El-Toni, A. M. *et al.* Design, Synthesis and Applications of Core-Shell, Hollow Core, and Nanorattle Multifunctional Nanostructures. *Nanoscale* **8**, 2510–2531 (2016).
111. Mezzavilla, S., Baldizzone, C., Mayrhofer, K. J. J. & Schüth, F. General Method for the Synthesis of Hollow Mesoporous Carbon Spheres with Tunable Textural Properties. *ACS Appl. Mater. Interfaces* **7**, 12914–12922 (2015).
112. Wang, G. H. *et al.* Platinum-Cobalt Bimetallic Nanoparticles in Hollow Carbon Nanospheres for Hydrogenolysis of 5-Hydroxymethylfurfural. *Nat. Mater.* **13**, 293–300 (2014).
113. Wang, G. H. *et al.* Scalable One-Pot Synthesis of Yolk-Shell Carbon Nanospheres with Yolk-Supported Pd Nanoparticles for Size-Selective Catalysis. *Chem. Mater.* **30**, 2483–2487 (2018).
114. Lou, X. W., Archer, L. A. & Yang, Z. Hollow Micro-/Nanostructures: Synthesis and Applications. *Adv. Mater.* **20**, 3987–4019 (2008).
115. Arnal, P. M., Comotti, M. & Schüth, F. High-Temperature-Stable Catalysts by Hollow Sphere Encapsulation. *Angew. Chemie - Int. Ed.* **45**, 8224–8227 (2006).
116. Lee, I., Joo, J. B., Yin, Y. & Zaera, F. A Yolk@Shell Nanoarchitecture for Au/TiO<sub>2</sub> Catalysts. *Angew. Chemie - Int. Ed.* **50**, 10208–10211 (2011).
117. Zhang, Q., Lee, I., Joo, J. B., Zaera, F. & Yin, Y. Core-Shell Nanostructured Catalysts. *Acc. Chem. Res.* **46**, 1816–1824 (2013).
118. Zhan, G. & Zeng, H. C. ZIF-67-Derived Nanoreactors for Controlling Product

- Selectivity in CO<sub>2</sub> Hydrogenation. *ACS Catal.* **7**, 7509–7519 (2017).
119. Stöber, W., Fink, A. & Bohn, E. Controlled Growth of Monodisperse Silica Spheres in the Micron Size Range. *J. Colloid Interface Sci.* **26**, 62–69 (1968).
  120. Cravillon, J. *et al.* Controlling Zeolitic Imidazolate Framework Nano- and Microcrystal Formation: Insight into Crystal Growth by Time-Resolved in situ Static Light Scattering. *Chem. Mater.* **23**, 2130–2141 (2011).
  121. Nakhaei Pour, A., Hosaini, E., Tavasoli, A., Behroozsarand, A. & Dolati, F. Intrinsic Kinetics of Fischer-Tropsch Synthesis over Co/CNTs Catalyst: Effects of Metallic Cobalt Particle Size. *J. Nat. Gas Sci. Eng.* **21**, 772–778 (2014).
  122. Zheng, J., Chu, W., Zhang, H., Jiang, C. & Dai, X. CO oxidation over Co<sub>3</sub>O<sub>4</sub>/SiO<sub>2</sub> Catalysts: Effects of Porous Structure of Silica and Catalyst Calcination Temperature. *J. Nat. Gas Chem.* **19**, 583–588 (2010).
  123. Jia, C. J. *et al.* Co<sub>3</sub>O<sub>4</sub> - SiO<sub>2</sub> Nanocomposite: A Very Active Catalyst for CO Oxidation with Unusual Catalytic Behavior. *J. Am. Chem. Soc.* **133**, 11279–11288 (2011).
  124. Xu, X., Li, J. & Hao, Z. CeO<sub>2</sub>-Co<sub>3</sub>O<sub>4</sub> Catalysts for CO Oxidation. *J. Rare Earths* **24**, 172–176 (2006).
  125. Centeno, M. A., Reina, T. R., Ivanova, S., Laguna, O. H. & Odriozola, J. A. Au/CeO<sub>2</sub> catalysts: Structure and CO oxidation activity. *Catalysts* **6**, A15 (2016).
  126. Bekyarova, E., Fornasiero, P., Kašpar, J. & Graziani, M. CO Oxidation on Pd/CeO<sub>2</sub>-ZrO<sub>2</sub> Catalysts. *Catal. Today* **45**, 179–183 (1998).
  127. Kang, Y., Sun, M. & Li, A. Studies of the Catalytic Oxidation of CO over Ag/CeO<sub>2</sub> Catalyst. *Catal. Letters* **142**, 1498–1504 (2012).
  128. Merchant Research & Consulting Ltd. [www.mcgroup.co.uk/news/20140627/formaldehyde-production-exceed-52-mln-tonnes.html](http://www.mcgroup.co.uk/news/20140627/formaldehyde-production-exceed-52-mln-tonnes.html). *World Formaldehyde Prod. to Exceed 52 Mln Tonnes 2017*. *Merch. Res. Consult. Ltd.* (2020).
  129. [www.prnewswire.com/news-releases/global-formaldehyde-industry-300933750.html](http://www.prnewswire.com/news-releases/global-formaldehyde-industry-300933750.html). *Global Formaldehyde Industry by Global Industry Analysts* (2020).

130. Beale, A. M. *et al.* An iron molybdate catalyst for methanol to formaldehyde conversion prepared by a hydrothermal method and its characterization. *Appl. Catal. A Gen.* **363**, 143–152 (2009).
131. Thrane, J. *et al.* Alkali Earth Metal Molybdates as Catalysts for the Selective Oxidation of Methanol to Formaldehyde—Selectivity, Activity, and Stability. *Catalysts* **10**, 1–15 (2020).
132. Routray, K., Zhou, W., Kiely, C. J., Grünert, W. & Wachs, I. E. Origin of the Synergistic Interaction between MoO<sub>3</sub> and Iron Molybdate for the Selective Oxidation of Methanol to Formaldehyde. *J. Catal.* **275**, 84–98 (2010).
133. Vieira Soares, A. P., Farinha Portela, M. & Kiennemann, A. Methanol Selective Oxidation to Formaldehyde over Iron-Molybdate Catalysts. *Catal. Rev. - Sci. Eng.* **47**, 125–174 (2005).
134. Nikolenko, N. V., Kozhevnikov, I. V., Kostyniuk, A. O., Bayahia, H. & Kalashnykov, Y. V. Preparation of Iron Molybdate Catalysts for Methanol to Formaldehyde Oxidation based on Ammonium Molybdoferate(II) Precursor. *J. Saudi Chem. Soc.* **22**, 372–379 (2018).
135. Dai, C. *et al.* Synthesis of Yolk-Shell HPW@Hollow silicalite-1 for Esterification Reaction. *Chem. Commun.* **50**, 4846–4848 (2014).
136. Rasmussen, K. H., Goodarzi, F., Christensen, D. B., Mielby, J. & Kegnæs, S. Stabilization of Metal Nanoparticle Catalysts via Encapsulation in Mesoporous Zeolites by Steam-Assisted Recrystallization. *ACS Appl. Nano Mater.* **2**, 8083–8091 (2019).
137. Goodarzi, F. *et al.* Methanation of Carbon Dioxide over Zeolite-Encapsulated Nickel Nanoparticles. *ChemCatChem* **10**, 1566–1570 (2018).
138. Mielby, J. *et al.* Oxidation of Bioethanol using Zeolite-Encapsulated Gold Nanoparticles. *Angew. Chemie* **126**, 12721–12724 (2014).
139. Llewellyn, P. L. *et al.* Adsorption by MFI-Type Zeolites Examined by Isothermal Microcalorimetry and Neutron Diffraction. 1. Argon, Krypton, and Methane. *Langmuir* **9**, 1846–1851 (1993).
140. Yang, X., Huang, L., Li, J., Tang, X. & Luo, X. Fabrication of SiO<sub>2</sub>@Silicalite-1 and its use as a Catalyst Support. *RSC Adv.* **7**, 12224–12230 (2017).

141. McCusker, L. B., Olson, D. H. & Baerlocher, C. *Atlas of Zeolite Framework Types*. (Elsevier, 2007).
142. Vieira Soares, A. P., Farinha Portela, M., Kiennemann, A. & Millet, J. M. Iron-Molybdate Deactivation during Methanol to Formaldehyde Oxidation: Effect of Water. *React. Kinet. Catal. Lett.* **75**, 13–20 (2002).
143. Kozhevnikov, I. V. Catalysis by Heteropoly Acids and Multicomponent Polyoxometalates in Liquid-Phase Reactions. *Chem. Rev.* **98**, 171–198 (1998).
144. Albert, J., Lüders, D., Bösmann, A., Guldi, D. M. & Wasserscheid, P. Spectroscopic and Electrochemical Characterization of Heteropoly Acids for their Optimized Application in Selective Biomass Oxidation to Formic Acid. *Green Chem.* **16**, 226–237 (2014).
145. Lefebvre, F. Synthesis, Characterization and Applications in Catalysis of Polyoxometalate/Zeolite Composites. *Inorganics* **4**, 1–24 (2016).
146. Kozhevnikov, I. V. & Matveev, K. I. Homogeneous Catalysts based on Heteropoly Acids (Review). *Appl. Catal.* **5**, 135–150 (1983).
147. Kozhevnikov, I. V. Friedel-Crafts Acylation and Related Reactions Catalysed by Heteropoly Acids. *Appl. Catal. A Gen.* **256**, 3–18 (2003).
148. Ponce, S., Trabold, M., Drochner, A., Albert, J. & Etzold, B. J. M. Insights into the Redox Kinetics of Vanadium Substituted Heteropoly Acids through Liquid Core Waveguide Membrane Microreactor Studies. *Chem. Eng. J.* **369**, 443–450 (2019).
149. Wu, L. & Sadjadi, S. *Encapsulated Catalysts. Chapter 1: Originally Encapsulated Polyoxometalate Catalysts: Supramolecular Composition and Synergistic Catalysis*. (Elsevier Inc., 2017).
150. Sartori, G. & Maggi, R. Use of Solid Catalysts in Friedel-Crafts Acylation Reactions. *Chem. Rev.* **106**, 1077–1104 (2006).
151. Vilà-Nadal, L. & Cronin, L. Design and Synthesis of Polyoxometalate-Framework Materials from Cluster Precursors. *Nat. Rev. Mater.* **2**, 17054 (2017).
152. Juan-Alcañiz, J., Ramos-Fernandez, E. V., Lafont, U., Gascon, J. & Kapteijn, F. Building MOF Bottles around Phosphotungstic Acid Ships: One-Pot Synthesis of Bi-Functional Polyoxometalate-MIL-101 Catalysts. *J. Catal.* **269**, 229–241 (2010).

153. Mukai, S. R., Lin, L., Masuda, T. & Hashimoto, K. Key Factors for the Encapsulation of Keggin-Type Heteropoly Acids in the Supercages of Y-Type Zeolite. *Chem. Eng. Sci.* **56**, 799–804 (2001).
154. Mukai, S. R., Masuda, T., Ogino, I. & Hashimoto, K. Preparation of Encaged Heteropoly Acid Catalyst by Synthesizing 12-Molybdophosphoric Acid in the Supercages of Y-Type Zeolite. *Appl. Catal. A Gen.* **165**, 219–226 (1997).
155. Mukai, S. R. *et al.* A Stable ‘Ship in the Bottle’ Type 12-Molybdophosphoric Acid Encaged Y-Type Zeolite Catalyst for Liquid Phase Reactions. *React. Kinet. Catal. Lett.* **69**, 253–258 (2000).
156. Mukai, S. R., Shimoda, M., Lin, L., Tamon, H. & Masuda, T. Improvement of the Preparation Method of ‘Ship-in-the-Bottle’ Type 12-Molybdophosphoric Acid Encaged Y-Type Zeolite Catalysts. *Appl. Catal. A Gen.* **256**, 107–113 (2003).
157. Zendehtdel, M., Mobinikhaledi, A., Alikhani, H. & Jafari, N. Preparation of Heteropoly Acid/ Porous Hybrid Materials and Investigation of their Catalytic Behavior in the Synthesis of Perimidine. *J. chin. chem. soc.* **57**, 683–689 (2010).
158. Sun, C., Zhang, F. & Cao, J. A ‘Build-Bottle-around-Ship’ Method to Encapsulate Ammonium Molybdophosphate in Zeolite Y. An Efficient Adsorbent for Cesium. *J. Colloid Interface Sci.* **455**, 39–45 (2015).
159. Ye, J. J. & Wu, C. De. Immobilization of Polyoxometalates in Crystalline solids for Highly Efficient Heterogeneous Catalysis. *Dalt. Trans.* **45**, 10101–10112 (2016).
160. Balula, S. S., Granadeiro, C. M., Barbosa, A. D. S., Santos, I. C. M. S. & Cunha-Silva, L. Multifunctional Catalyst Based on Sandwich-Type Polyoxotungstate and MIL-101 for Liquid Phase Oxidations. *Catal. Today* **210**, 142–148 (2013).
161. Saikia, M., Bhuyan, D. & Saikia, L. Keggin Type Phosphotungstic Acid Encapsulated Chromium (III) Terephthalate Metal Organic Framework as Active Catalyst for Biginelli Condensation. *Appl. Catal. A Gen.* **505**, 501–506 (2015).
162. Maksimchuk, N. V. *et al.* Heterogeneous Selective Oxidation Catalysts Based on Coordination Polymer MIL-101 and Transition Metal-Substituted Polyoxometalates. *J. Catal.* **257**, 315–323 (2008).
163. Leus, K. *et al.* Systematic Study of the Chemical and Hydrothermal Stability of Selected ‘Stable’ Metal Organic Frameworks. *Microporous Mesoporous Mater.*

**226**, 110–116 (2016).

164. Bhattacharjee, S., Chen, C. & Ahn, W. S. Chromium Terephthalate Metal-Organic Framework MIL-101: Synthesis, Functionalization, and Applications for Adsorption and Catalysis. *RSC Adv.* **4**, 52500–52525 (2014).
165. Kozhevnikova, E. F., Quartararo, J. & Kozhevnikov, I. V. Fries Rearrangement of Aryl Esters Catalysed by Heteropoly Acid. *Appl. Catal. A Gen.* **245**, 69–78 (2003).
166. Jayat, F., Sabater Picot, M. J. & Guisnet, M. Solvent Effects in Liquid Phase Fries Rearrangement of Phenyl Acetate over a HBEA Zeolite. *Catal. Letters* **41**, 181–187 (1996).
167. Rohan, D., Canaff, C., Fromentin, E. & Guisnet, M. Acetylation of Anisole by Acetic Anhydride over a HBEA Zeolite - Origin of Deactivation of the Catalyst. *J. Catal.* **177**, 296–305 (1998).
168. Rauch, S., Piepenbreier, F., Voss, D., Albert, J. & Hartmann, M. LCA in Process Development: Case Study of the OxFA-Process. in *Sustainable Production, Life Cycle Engineering and Management* 105–113 (Springer, 2019).
169. Albert, J. & Wasserscheid, P. Expanding the Scope of Biogenic Substrates for the Selective Production of Formic Acid from Water-Insoluble and Wet Waste Biomass. *Green Chem.* **17**, 5164–5171 (2015).
170. Levi, P. G. & Cullen, J. M. Mapping Global Flows of Chemicals: From Fossil Fuel Feedstocks to Chemical Products. *Environ. Sci. Technol.* **52**, 1725–1734 (2018).
171. Preuster, P. & Albert, J. Biogenic Formic Acid as a Green Hydrogen Carrier. *Energy Technol.* **6**, 501–509 (2018).
172. Hietala, J. *et al.* *Ullmann's Encyclopedia of Industrial Chemistry. ICIS Chemical Business* (Wiley-VCH Verlag GmbH & Co. KGaA, 2016).
173. Khenkin, A. M. & Neumann, R. Oxidative C-C Bond Cleavage of Primary Alcohols and Vicinal Diols Catalyzed by H5PV2Mo10O40 by an Electron Transfer and Oxygen Transfer Reaction Mechanism. *J. Am. Chem. Soc.* **130**, 14474–14476 (2008).
174. Reichert, J. & Albert, J. Detailed Kinetic Investigations on the Selective Oxidation of Biomass to Formic Acid (OxFA Process) Using Model Substrates and Real



- Biomass. *ACS Sustain. Chem. Eng.* **5**, 7383–7392 (2017).
175. Albert, J., Wölfel, R., Bösmann, A. & Wasserscheid, P. Selective Oxidation of Complex, Water-Insoluble Biomass to Formic Acid using Additives as Reaction Accelerators. *Energy Environ. Sci.* **5**, 7956–7962 (2020).
176. Reichert, J., Brunner, B., Jess, A., Wasserscheid, P. & Albert, J. Biomass Oxidation to Formic Acid in Aqueous Media using Polyoxometalate Catalysts - Boosting FA Selectivity by In-Situ Extraction. *Energy Environ. Sci.* **8**, 2985–2990 (2015).
177. Wang, Y., Lin, M. & Tuel, A. Hollow TS-1 Crystals Formed via a Dissolution-Recrystallization Process. *Microporous Mesoporous Mater.* **102**, 80–85 (2007).
178. Booth, H. S. & Bailar, J. *Inorganic syntheses, Volume 1, Chapter VI.* (1939).
179. Zubrzycki, R., Epping, J. D. & Ressler, T. Role of Vanadium and Phosphorus in Substituted Keggin-Type Heteropolyoxo Molybdates Supported on Silica SBA-15 in Selective Propene Oxidation. *ChemCatChem* **7**, 1112–1121 (2015).
180. Odyakov, V. F. & Zhizhina, E. G. A Novel Method of the Synthesis of Molybdovanadophosphoric Heteropoly Acid Solutions. *React. Kinet. Catal. Lett.* **95**, 21–28 (2008).
181. Albert, J., Mendt, M., Mozer, M. & Voß, D. Explaining the Role of Vanadium in Homogeneous Glucose Transformation Reactions using NMR and EPR Spectroscopy. *Appl. Catal. A Gen.* **570**, 262–270 (2019).
182. Voß, D., Ponce, S., Wesinger, S., Etzold, B. J. M. & Albert, J. Combining Autoclave and LCWM Reactor Studies to Shed Light on the Kinetics of Glucose Oxidation Catalyzed by Doped Molybdenum-Based Heteropoly Acids. *RSC Advances* vol. 9 29347–29356 (2019).
183. Dias, J. A., Caliman, E., Dias, S. C. L., Paulo, M. & De Souza, A. T. C. P. Preparation and Characterization of Supported H<sub>3</sub>PW<sub>12</sub>O<sub>40</sub> on Silica Gel: A Potential Catalyst for Green Chemistry Processes. *Catal. Today* **85**, 39–48 (2003).
184. Almohalla, M., Rodriguez-Ramos, I. & Guerrero-Ruiz, A. Comparative Study of Three Heteropolyacids Supported on Carbon Materials as Catalysts for Ethylene Production from Bioethanol. *Catal. Sci. Technol.* **7**, 1892–1901 (2017).
185. Ferreira, P., Fonseca, I. M., Ramos, A. M., Vital, J. & Castanheiro, J. E. Esterification

- of Glycerol with Acetic Acid over Dodecamolybdophosphoric Acid Encaged in USY Zeolite. *Catal. Commun.* **10**, 481–484 (2009).
186. Kozhevnikov, I. V., Kloetstra, K. R., Sinnema, A., Zandbergen, H. W. & Van Bekkum, H. Study of Catalysts Comprising Heteropoly Acid H<sub>3</sub>PW<sub>12</sub>O<sub>40</sub> Supported on MCM-41 Molecular Sieve and Amorphous Silica. *J. Mol. Catal. A Chem.* **114**, 287–298 (1996).
187. Rocchiccioli-Deltcheff, C. *et al.* Structure and Catalytic Properties of Silica-Supported Polyoxomolybdates: Thermal Behavior of Unsupported and Silica-Supported 12-Molybdosilicic Acid Catalysts from IR and Catalytic Reactivity Studies. *J. Catal.* **126**, 591–599 (1990).
188. Evtuguin, D. V., Pascoal Neto, C., Rocha, J. & Pedrosa De Jesus, J. D. Oxidative Delignification in the Presence of Molybdovanadophosphate Heteropolyanions: Mechanism and Kinetic Studies. *Appl. Catal. A Gen.* **167**, 123–139 (1998).
189. De Martino, M. T., Abdelmohsen, L. K. E. A., Rutjes, F. P. J. T. & Van Hest, J. C. M. Nanoreactors for green catalysis. *Beilstein J. Org. Chem.* **14**, 716–733 (2018).

## Appendix A    Supporting information, Chapter 3

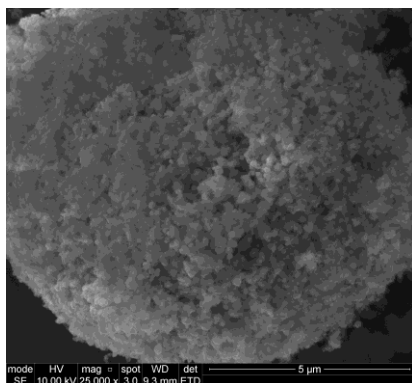


**Figure A.1.:** SEM image of Co/NC-50.<sup>42</sup> Reproduced by permission of The Royal Society of Chemistry.

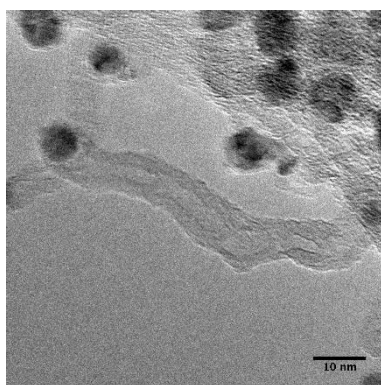


**Figure A.2.:** Close-up TEM image of a carbon nanotube protruding from the Co/NC-50.



**Figure A.3.:** Illustration of the magnetic Co/NC-50 catalyst collected by a permanent magnet.

## Appendix B Supporting information, Chapter 4

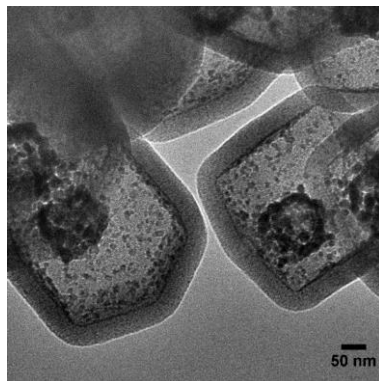


**Figure B.1.:** *TEM image of Co<sub>1</sub>@SiO<sub>2</sub> (Zn<sub>0</sub>) (-/550).<sup>1</sup> Reproduced by permission of Elsevier.*

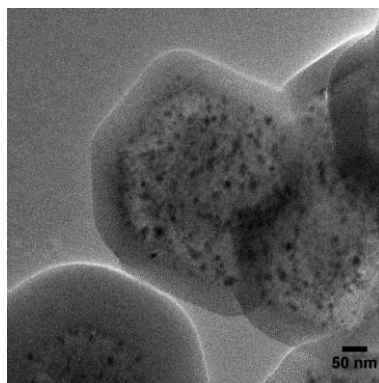


**Figure B.2.:** *TEM image of Co<sub>1</sub>/NC@SiO<sub>2</sub> (Zn<sub>0</sub>) (600/-).<sup>1</sup> Reproduced by permission of Elsevier.*

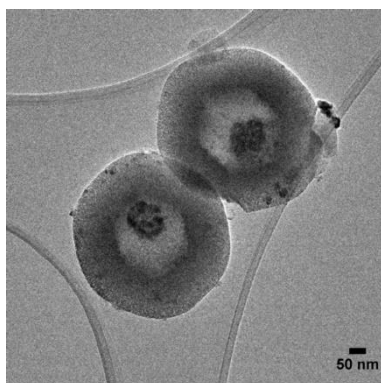


**Figure B.3.:** TEM image of  $\text{Co}_1@\text{SiO}_2 (\text{Zn}_0)$  (600/550).<sup>1</sup> Reproduced by permission of Elsevier.

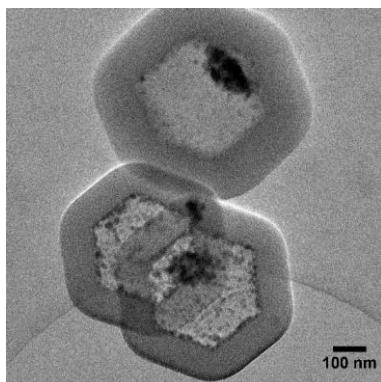


**Figure B.4.:** TEM image of  $\text{Co}_1@\text{SiO}_2 (\text{Zn}_0)$  (600/300).

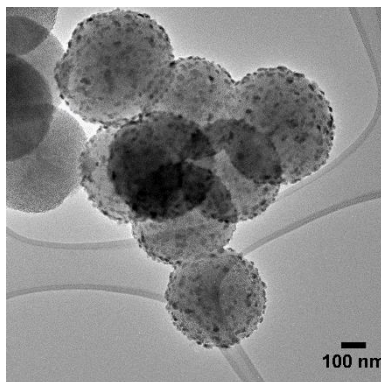


**Figure B.5.:** TEM image of  $\text{Co}_1/\text{SiO}_2 (\text{Zn}_0)$  (-/550).<sup>1</sup> Reproduced by permission of Elsevier.

### Synthesis of ZIF-67/8@TiO<sub>2</sub>

The ZIF-67/8 crystals were prepared according to the synthesis procedure found in Chapter 3.2.1 and 4.2.1. ZIF-67/8 (0.8 g) in the given Co/Zn ratio (1:0 or 1:1) was dispersed in absolute ethanol (97.4 mL) and sonicated for 30 min. Hexadecylamine (HAD) (0.8 g) and an aqueous solution of concentrated ammonia 25-28% (2 mL) were added followed by 1 h stirring. Then titanium isopropoxide (TIP) (2 mL) was dropwise added to the solution under stirring. The core-shell material was collected after 20 min by centrifugation (8000 rpm for 10 min), washed three times with water and absolute ethanol and dried at 80°C for 24 h.

### Synthesis of Co<sub>x</sub>@TiO<sub>2</sub> (Zn<sub>y</sub>)

The final catalysts were obtained with carbonization and calcination of the prepared ZIF-67/8@TiO<sub>2</sub> materials. The products were carbonized in a tube furnace under flowing Ar at 600°C (ZIF-67) or at 900°C (ZIF-67/8) for 2h. The products were calcined in a muffle furnace in static air at 550°C for 2 h. The heating ramp of the carbonization and calcination procedure was 5°C min<sup>-1</sup>. The 900°C carbonization for ZIF-67/8 was chosen based on previous findings in Chapter 3, which confirmed successful removal of Zn by evaporation. The final name of the catalyst Co<sub>1</sub>@TiO<sub>2</sub> (Zn<sub>1</sub>) indicates a Co/Zn ratio of 1:1 present in the ZIF-67/8 precursor crystals.

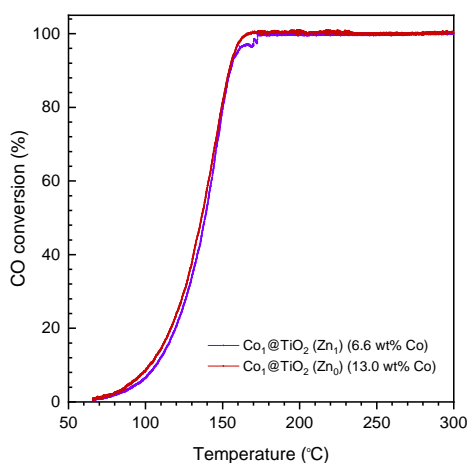


**Figure B.6.:** CO oxidation light-off curves of the nanorattle catalysts Co<sub>1</sub>/TiO<sub>2</sub> (Zn<sub>0</sub>) and Co<sub>1</sub>/TiO<sub>2</sub> (Zn<sub>1</sub>).

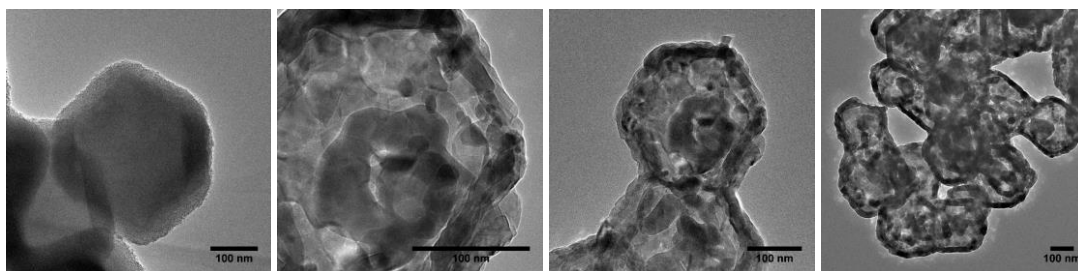


**Figure B.7.:** TEM images of  $\text{Co}_1@ \text{TiO}_2 (\text{Zn}_0)$  (left) before calcination and (additional images) after.

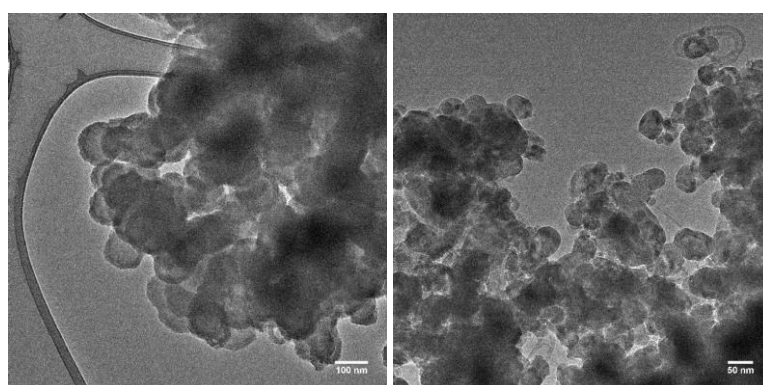


**Figure B.8.:** TEM images of  $\text{Co}_1@ \text{TiO}_2 (\text{Zn}_1)$  (left) before calcination and (right) after.

## Appendix C Supporting information, Chapter 5

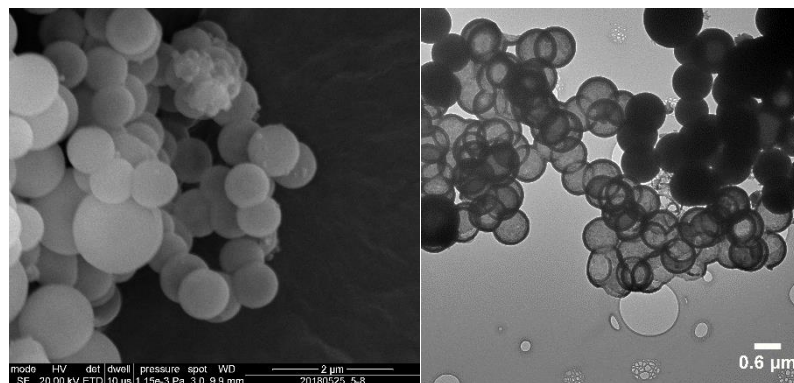


**Figure C.1.:** SEM image and TEM image of the hollow  $\text{SiO}_2$  spheres.

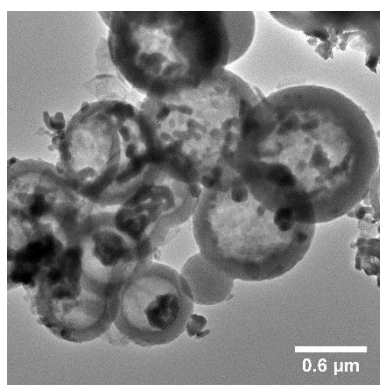


**Figure C.2.:** TEM image of the  $\text{FeMo}/\text{SiO}_2$  catalyst.

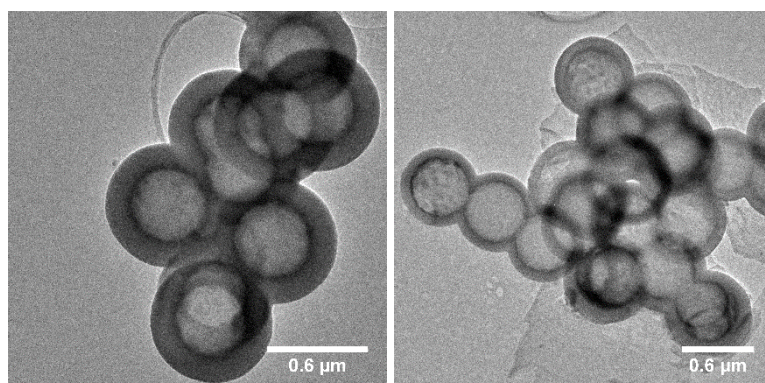


**Figure C.3.:** TEM images of the  $\text{FeMo}@/\text{SiO}_2$  catalyst.



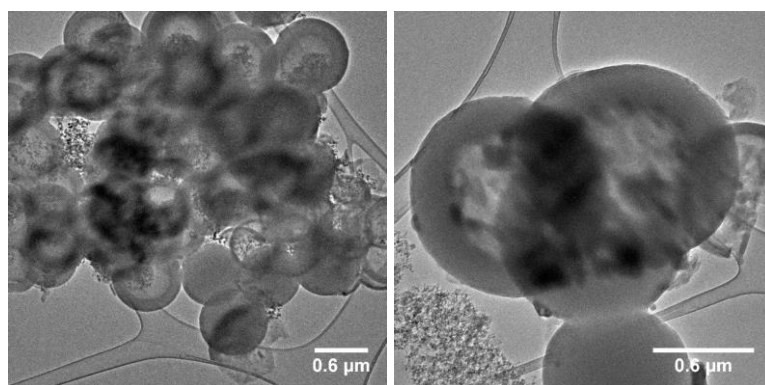


**Figure C.4.:** TEM images of (left) the used FeMo/SiO<sub>2</sub> from the inlet of the reactor bed and (right) the FeMo/SiO<sub>2</sub> catalyst from the outlet of the reactor bed.

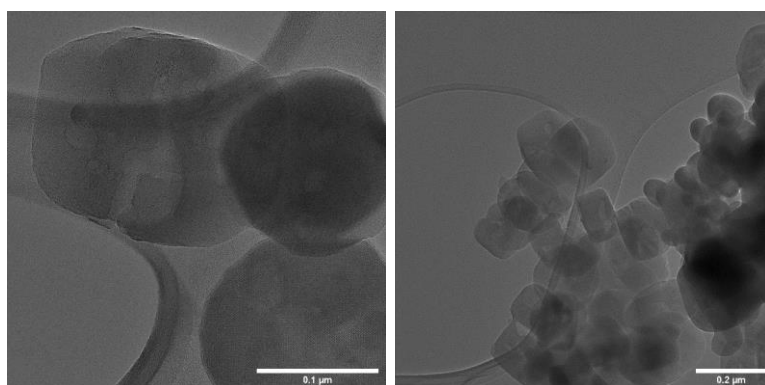


**Figure C.5.:** TEM images of FeMo@D S1 (2.56).

### Reversible by-product corrected conversion and selectivity

In Figure 5.11 the conversions and selectivities were corrected for reversible by-products as these would be converted back at an increased MeOH conversion. In general, DME, DMM and MF are reversible by-products, which are converted under industrial operation conditions. DME was considered as 2x MeOH, DMM was considered as 2x MeOH and 1x CH<sub>2</sub>O, and MF was considered as 1x MeOH and 1x CO. This made the comparison of the catalysts more clear.

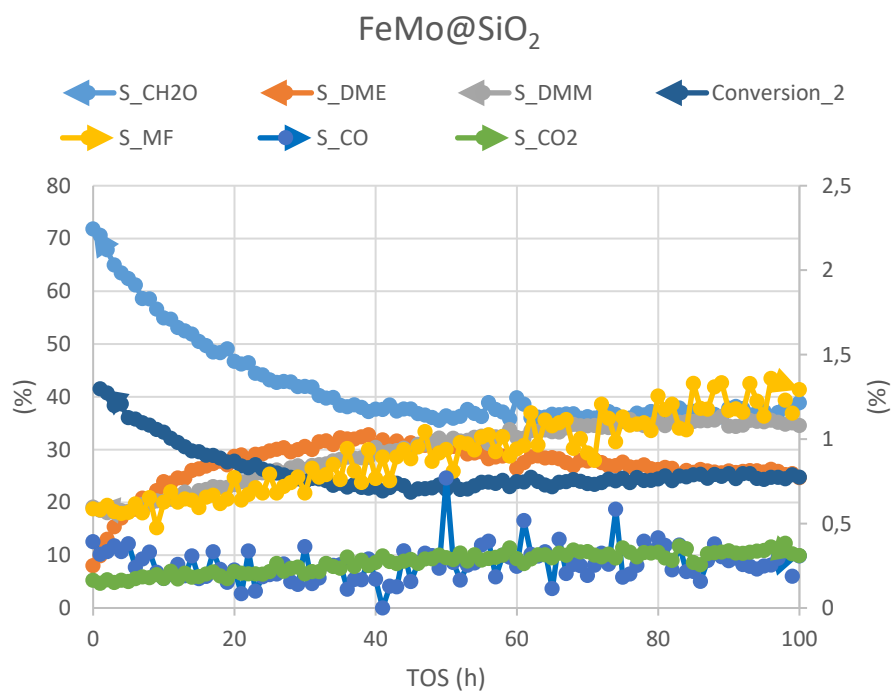


**Figure C.6.:** *Non-corrected activity of  $\text{FeMo@SiO}_2$  showing by-product formation.*

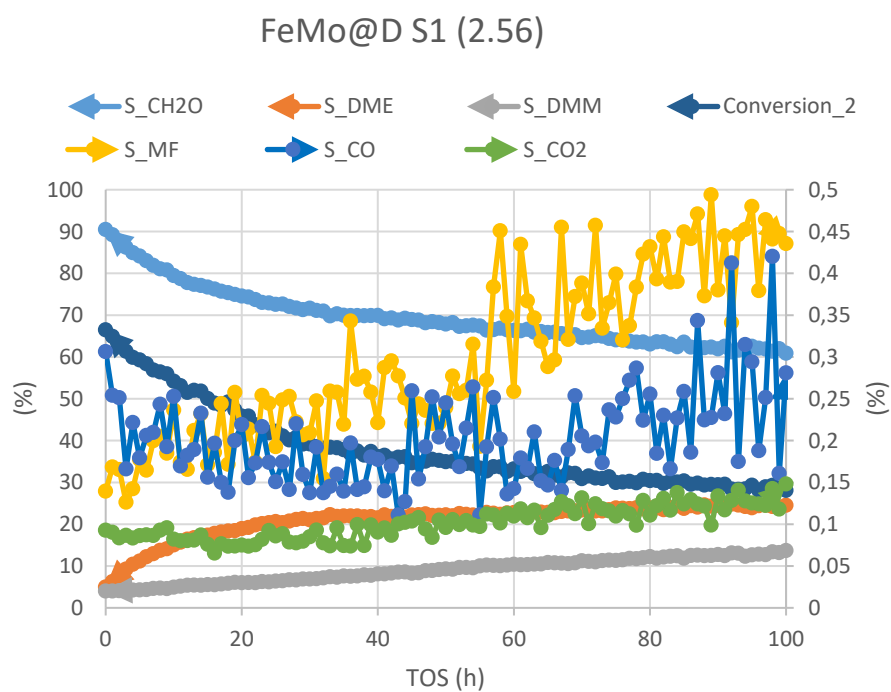


**Figure C.7.:** *Non-corrected activity of FeMo@D S1 (2.56) showing by-product formation.*

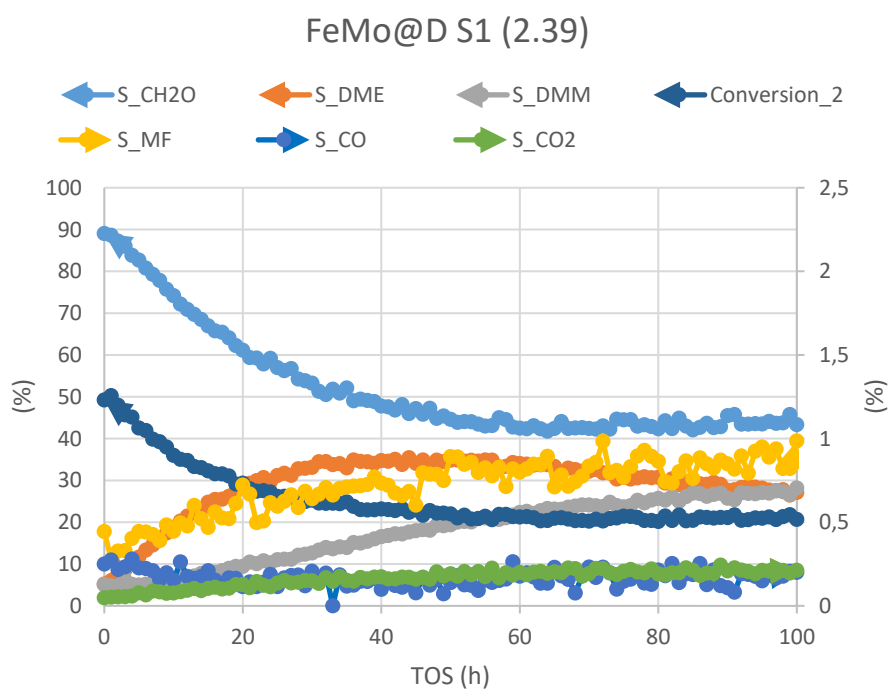


**Figure C.8.:** *Non-corrected activity of FeMo@D S1 (2.39) showing by-product formation.*

## Appendix D    Supporting information, Chapter 6

### Material Preparations

Reagents were acquired from a commercial source (Sigma-Aldrich), and were utilized without additional purifications. The reagents include: molybdenum(VI) oxide (99.97% trace metals basis), tetraethyl orthosilicate (TEOS, 99.99% trace metals basis), myristyltrimethylammonium bromide ( $\geq 99\%$ ), concentrated ammonia solution (aqueous, 25-28%), phosphoric acid ( $\geq 85\%$ ), sodium chloride (ACS reagent,  $\geq 99.0\%$ ), absolute ethanol ( $\geq 99.8\%$ ) and zeolite Y (HUSY, CBV720, Si/Al=30) from commercial source Zeolyst International.

### Synthesis of Hollow SiO<sub>2</sub>

The SiO<sub>2</sub> spheres were modified from the Stöber process from literature.<sup>119</sup> In a 2L round-bottomed flask myristyltrimethylammonium bromide (1.5 g) was dissolved in absolute ethanol (300 mL), water (500 mL) and an aqueous solution of concentrated ammonia 25-28% (10 mL). The solution was mixed at 25°C followed by the fast addition of TEOS (10 mL) to the solution under vigorously stirring. The solution was left stirring at 25°C for 24 h. The white product was collected by centrifugation (12000 rpm for 10 min), washed three times with absolute ethanol and dried at 80°C for 24 h.

Then the white powder of SiO<sub>2</sub> spheres were dissolved in water (1600 mL) at 90°C for 48 h. The white product was collected by centrifugation (12000 rpm for 10 min), washed three times with absolute ethanol and dried at 80°C for 24 h.

The final hollow SiO<sub>2</sub> spheres were calcined in a muffle furnace in static air at 550°C for 2 h with a heating ramp of 5°C min<sup>-1</sup>.

### Synthesis of Zeolite Y

The preparation of zeolite Y was performed according to Ferreira *et al.*<sup>185</sup>, which modified a procedure by Mukai *et al.*<sup>154</sup>. In brief, a commercial zeolite Y (HUSY) (CBV720, Si/Al=30) from Zeolyst International was ion exchanged to the sodium form by three treatments with 2M NaCl at 80°C. The the product was collected by centrifugation (12000 rpm for 10 min), washed three times with water and dried at 80°C for 24 h.

### Vacuum Impregnation with $\text{H}_3\text{PMo}_{12}\text{O}_{40}$

The impregnation method was modified by a procedure by Mukai *et al.*<sup>154</sup> where the hollow  $\text{SiO}_2$  or Zeolite Y (1.0 g) and molybdenum(VI) trioxide (3.6 g) were dissolved in 35 mL of water in a schlenk flask and stirred at 25°C for 24 h. Then vacuum was applied to the system for 5 min to empty the pores and fill them upon release. Then phosphoric acid (240  $\mu\text{L}$ ) was added dropwise to the solution and it was stirred at 95°C for 3h. The product was collected by centrifugation (12000 rpm for 10 min) and washed five times with 80°C water. The product was dried at 80°C for 24 h.

The following day, the product was dispersed in water (18 mL) and phosphoric acid (2 mL) at 100°C for 1 h. The product was collected by centrifugation (12000 rpm for 10 min) and washed five times with 80°C water. The product was dried at 80°C for 24 h. The product was a grey powder.

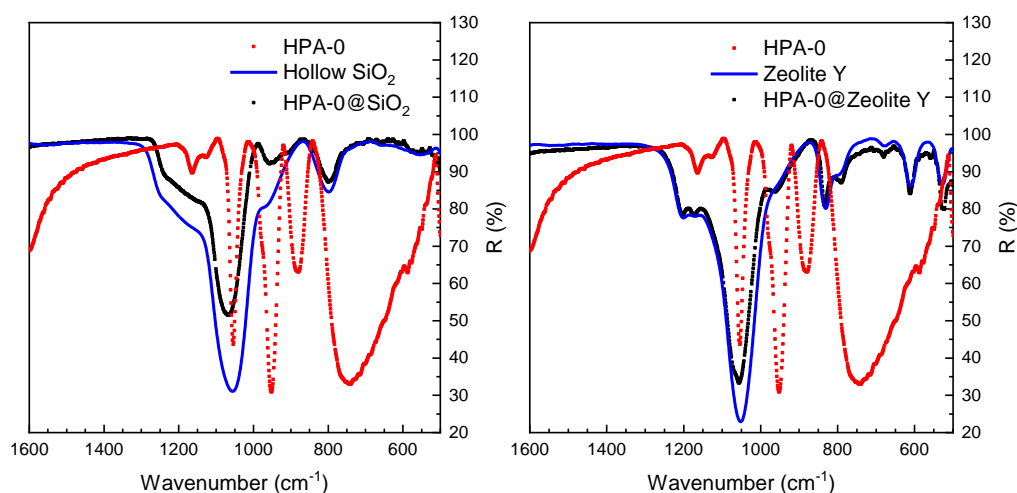


**Figure D.1.:** The FTIR of the prepared HPA-0@ $\text{SiO}_2$  and HPA-0@Zeolite Y, the supports and the reference bulk HPA-0.

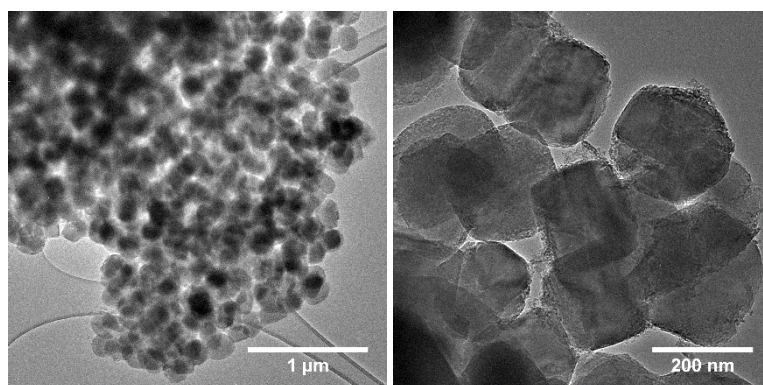


**Figure D.3.:** *TEM images of HPA-0@Recryst S1.*

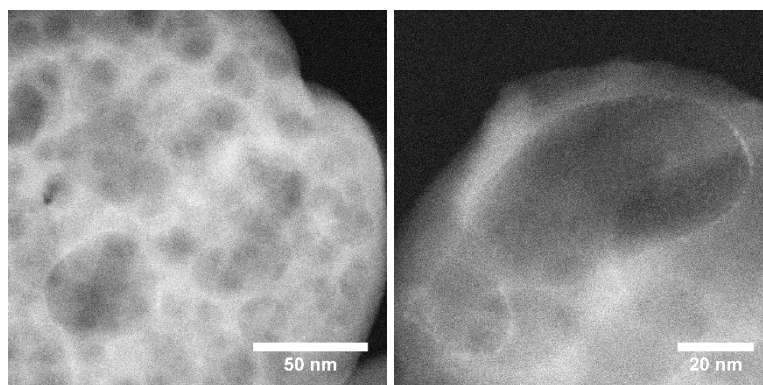


**Figure D.2.:** *STEM (DF) images of HPA-0@Recryst S1.*

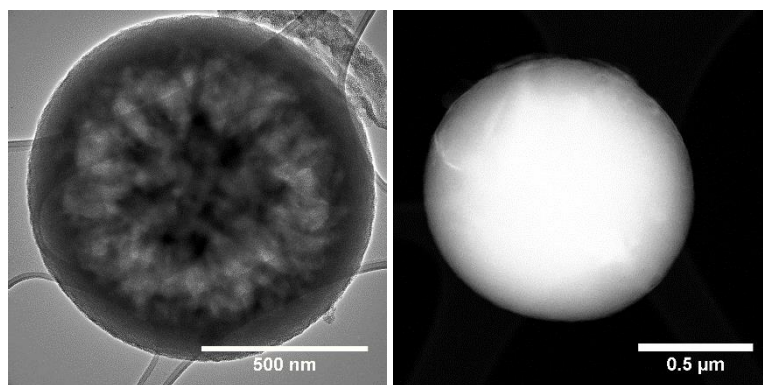


**Figure D.4.:** *TEM and STEM (DF) images of HPA-0@SiO<sub>2</sub>.*

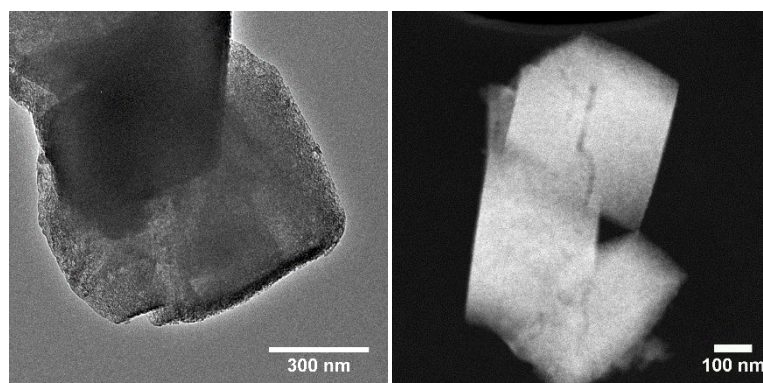


**Figure D.5.:** *TEM and STEM (DF) images of HPA-0@Zeolite Y.*



## Appendix E     Disseminations

Chapter 3 and Chapter 4 are based on my work published in the international and peer reviewed journals listed below. The content was allowed to be reproduced by the permission of The Royal Society of Chemistry (I), Springer (II) and Elsevier (III). The front page of the papers can be seen at page 166-168.

- I                Zacho, S. L., Mielby, J. and Kegnæs, S. Hydrolytic Dehydrogenation of Ammonia Borane over ZIF-67 Derived Co Nanoparticle Catalysts, *Catalysis Science and Technology*, **8** (18), 4741-4746 (2018).
  
- II               Zacho, S. L., Gajdek, D., Mielby, J. and Kegnæs, S. Synthesis of Nano-Engineered Catalysts Consisting of Co<sub>3</sub>O<sub>4</sub> Nanoparticles Confined in Porous SiO<sub>2</sub>, *Topics in Catalysis*, (2019).
  
- III              Zacho, S. L., Hyllested, J. Æ., Kasama, T. and Mielby, J. Controlling the Dispersion of Co<sub>3</sub>O<sub>4</sub> Nanoparticles inside Mesoporous Nanorattle Catalysts, *Catalysis Communications*, **125**, 6-9 (2019).

### **Supplementary disseminations related to the work described in this dissertation**

#### **Oral Presentations**

Metal-Organic Frameworks as Template and Metal Precursor for Heterogeneous Catalysts – *Presentation at University College London, October 27<sup>th</sup> 2017, London, England.*

Novel Heterogeneous Catalysts with Nano-Engineered Porosity – *DTU Chemistry PhD symposium, November 14<sup>th</sup> 2017, Holte, Denmark.*

ZIFs as Template and Self-Sacrificing Catalyst Precursors – *18<sup>th</sup> Nordic Symposium on Catalysis, August 27<sup>th</sup> 2018, Copenhagen, Denmark.*

Encapsulation of Nanoparticles and Clusters in Porous Materials – *New Year's Seminar with FAU, February 1<sup>st</sup> 2019, Lyngby, Denmark.*

## **Poster Presentations**

Modified ZIF-67 as Precursor for Microporous Carbon Co Nanoparticle Catalysts – *EuCheMS Inorganic Chemistry Conference (EICC-4), July 2-5, 2017 Copenhagen, Denmark.*

Hydrolytic Dehydrogenation of Ammonia Borane over MOF Derived Cobalt Nanoparticles Catalysts – *Europacat XIII, August 27-31, 2017, Florence, Italy.*

Novel Heterogeneous Catalysts with Nano-Engineered Porosity – *EFCATS School on Catalysis, June 25-29, 2018, Prague, Czech Republic.*

Novel Heterogeneous Catalysts with Nano-Engineered Porosity – *136<sup>th</sup>International Summer Course- BASF, August 11-17, 2019, Ludwigshafen, Germany.*

Encapsulation of Metal Nanoparticle Catalysts in Porous Silica-Based Shells – *Europacat XIV, August 18-23, 2019, Aachen, Germany.*

Encapsulation of Polyoxometalates in Porous Silica-Based Shells – *DTU Chemistry PhD symposium, November 8-9, 2019, Helsingør, Denmark.*

PAPER

View Article Online  
View Journal | View Issue



Cite this: *Catal. Sci. Technol.*, 2018, 8, 4741

Received 20th July 2018,  
Accepted 18th August 2018

DOI: 10.1039/c8cy01500g

rsc.li/catalysis

# Hydrolytic dehydrogenation of ammonia borane over ZIF-67 derived Co nanoparticle catalysts†

Simone Louise Zacho, Jerrik Mielby and Søren Kegnæs \*

In this work, we exploited zeolitic imidazolate framework ZIF-67 as a sacrificial precursor to prepare Co nanoparticles supported on nanoporous nitrogen-doped carbon. The catalysts were tested for hydrolytic dehydrogenation of ammonia borane and the size of the Co nanoparticles and the structural features of the carbon support were shown to have a large effect on the catalytic activity. Furthermore, we investigated the effect of adding Zn to the catalyst precursor (ZIF-67/8). The highest catalytic activity was obtained for ZIF-67/8 with a molar ratio of Co/Zn = 1, which was carbonized at 900 °C to remove Zn by evaporation. At room temperature, this catalyst resulted in a turnover frequency of 7.6 mol H<sub>2</sub> per mol Co min<sup>−1</sup> and an apparent activation energy of *E*<sub>a</sub> = 44.9 kJ mol<sup>−1</sup>. The turnover frequency was further increased to 12.7 min<sup>−1</sup> in 0.1 M NaOH.

## Introduction

Hydrogen produced from renewable resources holds great promise as a solution to future energy and environmental challenges.<sup>1</sup> In particular, hydrogen may power fuel cells, which can generate electricity without emission of greenhouse gasses. Unfortunately, the physical properties of hydrogen gas make transportation, handling and refuelling difficult. Much effort has therefore been devoted to the development of chemical hydrogen storage materials.<sup>2–5</sup> In these types of materials, chemical processes control hydrogen storage and release. This makes them different from metal hydrides<sup>6</sup> or carbon materials,<sup>7</sup> where temperature and pressure control storage and release. One compound, ammonia borane (H<sub>3</sub>NBH<sub>3</sub>), has attracted particular attention because of its high volumetric and gravimetric density. Ammonia borane is solid at room temperature, stable in air and water and contains around 196 g kg<sup>−1</sup> or 100–140 g l<sup>−1</sup> of H<sub>2</sub>.<sup>8</sup> In combination with an efficient catalyst, the hydrolytic dehydrogenation of ammonia borane is given by



In a protic solvent like H<sub>2</sub>O, up to three equivalents of H<sub>2</sub> can be released from ammonia borane and when an appropriate catalyst is used, hydrogen can be released under ambient conditions. In the past years, a number of efficient noble

metal catalysts have been developed for the hydrolytic dehydrogenation of H<sub>3</sub>NBH<sub>3</sub>, including both homogeneous<sup>9</sup> and heterogeneous catalysts based on Pt,<sup>10</sup> Rh,<sup>11</sup> Ru,<sup>12</sup> Ag<sup>13</sup> and Pd.<sup>14</sup> Considering the limited availability and high cost of noble metals, the development of equally active and more cost-effective non-noble metal catalysts is of great interest.<sup>15</sup> Among the non-noble metals, Co supported on carbon has recently been suggested as a promising catalyst because of its high activity<sup>16</sup> and magnetic properties. These properties make it easy to collect the supported nanoparticles from the liquid phase.<sup>17–19</sup> For instance, Wang *et al.*<sup>20</sup> recently embedded Co nanoparticles in porous nitrogen-doped carbon, which was synthesized by carbonization of a Co(salen) precursor under Ar atmosphere. The Co nanoparticles resulted in a turnover frequency (TOF) of 5.6 mol H<sub>2</sub> per mol Co min<sup>−1</sup> in the hydrolytic dehydrogenation of ammonia borane. The catalyst showed good stability over 10 runs collecting the catalyst using a permanent magnet after each run. The porosity of these type of carbon materials is a key factor for the catalytic activity.

Here, we report a method to prepare Co nanoparticles supported on a porous nitrogen-doped carbon matrix synthesized by carbonization. The method exploits metal organic frameworks (MOFs) as sacrificial precursors for both the cobalt nanoparticles and the nitrogen-doped carbon matrix support. Because of their remarkable chemical and structural properties, such as their high surface area and well-defined porosity, MOFs have recently attracted much interest for applications in gas adsorption, separation and heterogeneous catalysis.<sup>21,22</sup> Furthermore, MOFs have recently been used for preparation of high-surface area nanoporous carbons for electrochemical reactions.<sup>23</sup>

DTU Chemistry, Technical University of Denmark, Kemitorvet Building 207, DK-2800 Kgs. Lyngby, Denmark. E-mail: skk@kemi.dtu.dk

† Electronic supplementary information (ESI) available. See DOI: 10.1039/c8cy01500g



# Synthesis of Nano-engineered Catalysts Consisting of $\text{Co}_3\text{O}_4$ Nanoparticles Confined in Porous $\text{SiO}_2$

Simone Louise Zacho<sup>1</sup> · Dorotea Gajdek<sup>1</sup> · Jerrik Mielby<sup>1</sup> · Søren Kegnæs<sup>1</sup>

Published online: 18 January 2019  
© Springer Science+Business Media, LLC, part of Springer Nature 2019

## Abstract

Here we exploit zeolitic imidazolate frameworks ZIF-67 and ZIF-8 as precursors to obtain nanorattle catalysts with  $\text{Co}_3\text{O}_4$  nanoparticles confined inside porous  $\text{SiO}_2$  shells. The method is simple and uses zeolitic imidazolate frameworks as both structural templates and sacrificial precursors. Nanorattle catalysts of different sizes and metal loadings are designed by varying the Co/Zn ratio in the zeolitic imidazolate frameworks. It is possible to obtain different metal loadings by introduction and removal of Zn using evaporation. Moreover, all produced catalysts contained small  $\text{Co}_3\text{O}_4$  nanoparticles. Finally, the different catalysts are tested in CO oxidation to demonstrate the effect of variations as a proof of concept. Thus, the use of metal–organic frameworks to control properties in nanorattle catalysts proposes an alternative method for the preparation of novel catalysts and shows a new pathway for synthesis of nanostructured materials.

**Keywords** Metal–organic framework · Mesoporous materials · Templating · Nanorattle catalysts · CO oxidation

## 1 Introduction

The use of catalysts, both molecular and solid catalysts, are widespread in the chemical industry due to the facilitation of energy-efficient production [1]. The advantages of solid catalysts over molecular catalysts are often displayed as recyclability, high robustness and ease of catalyst separation [2–4]. Precious metal catalysts are widely used in solid catalysis and as oxidation catalysts in a variety of reactions and includes metals like Pt, Au, Ag, Ru and Pd [5–11]. However, precious metals are rare and expensive. Replacement of these expensive catalysts with much more abundant base metals such as the relative abundant Co is more advantageous from environmental and economic perspectives.

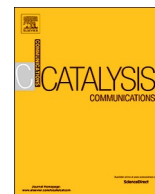
Recently, the use of base metal nanoparticles supported on different carriers has been demonstrated as powerful solid catalysts for a large range of oxidation reactions [8, 12].

In order to obtain maximum catalytic activity, the design of the catalyst is of great importance [13]. For supported metal nanoparticle catalysts, there has been a focus on the synthesis of materials with a small nanoparticle size to enhance catalytic efficiency due to the correlation between relative surface area and nanoparticle size. However, the reduction of the nanoparticle sizes can enhance the tendency for particle sintering and hereby lead to a decreased catalytic activity. Thus, the nano-engineering of sintering-stable supported nanoparticle catalysts has attracted attention over the years, and many strategies have been developed [14–22]. One design strategy has been related to the synthesis of nanostructured materials where the nanoparticles are confined in ultra-small containers forming nanoreactors or rattle core–shell materials [23–25]. The main advantage of nanoreactor materials are the ability to selectively allow certain substrates to enter into the nanoreactor and get converted over the nanoparticles. This can for certain reaction leads to improved catalytic activity, selectivity and stability compared to more conventional catalysts. Sun et al. have exemplified the use of rattle core–shell materials for the Fischer Tropsch synthesis, which is a great example on a Co-catalyzed reaction [26–29]. Despite the solvothermal route by Sun et al. is an easy and cost efficient method to prepare core–shell materials it does not offer full control of the core–shell

**Electronic supplementary material** The online version of this article (<https://doi.org/10.1007/s11244-019-01134-9>) contains supplementary material, which is available to authorized users.

✉ Søren Kegnæs  
skk@kemi.dtu.dk

<sup>1</sup> Department of Chemistry, Technical University of Denmark, 2800 Kgs. Lyngby, Denmark



## Short communication

Controlling the dispersion of  $\text{Co}_3\text{O}_4$  nanoparticles inside mesoporous nanorattle catalystsSimone L. Zacho<sup>a</sup>, Jes Æ. Hyllested<sup>b</sup>, Takeshi Kasama<sup>b</sup>, Jerrik Mielby<sup>a,\*</sup><sup>a</sup> DTU Chemistry, Technical University of Denmark, Kemitorvet 207, 2800 Kgs. Lyngby, Denmark<sup>b</sup> DTU Nanolab, Technical University of Denmark, Fysikvej 307, 2800 Kgs. Lyngby, Denmark

## ARTICLE INFO

## Keywords:

Metal-organic frameworks  
Mesoporous materials  
Templating  
Nanorattle catalysts  
CO oxidation

## ABSTRACT

Here we report a simple method to synthesize  $\text{Co}_3\text{O}_4$  nanoparticles inside mesoporous nanorattle catalysts. In this method, zeolitic imidazolate framework ZIF-67 is used as structural template for the preparation of a mesoporous metal oxide shell as well as sacrificial precursor to form  $\text{Co}_3\text{O}_4$  nanoparticles inside the shell. Furthermore, we demonstrate that the introduction of a carbonization step prior to the final calcination can decrease the required calcination temperature from 550 °C to 300 °C. This has a large effect on the dispersion and catalytic activity of  $\text{Co}_3\text{O}_4$  for CO oxidation and decreases the light-of temperature (temperature at 50% conversion) from 160 °C to 134 °C. Exploiting metal-organic frameworks as both structural template and sacrificial precursor offers precise control of size, shape and structure and opens up new exiting opportunities for design of advanced nanostructured catalysts.

## 1. Introduction

The rational design and synthesis of hollow nanostructured materials holds great promise for new and emerging technologies in fields ranging from energy storage [1–3], catalysis [4], adsorption [5], separation [6], sensing [7], photocatalysis [8] to drug delivery [9,10]. Besides their high porosity, high surface area and low density, the hollow nanomaterials offer a number of key advantages with respect to loading or functionalization of their interior [11]. Furthermore, hollow nanostructures may help to prevent aggregation, sintering and metal leaching [12]. In particular, these advantages have been intensely pursued in confined synthesis [13], nanoreactors [4,14] and controlled release [15].

There are several methods to prepare hollow nanomaterials. These methods are typically based on ‘templating’ using either hard [16] or soft templates [17–19]. Alternative template-free methods based on the Kirkendall effect [20], Ostwald ripening [21], selective dissolution [22] or recrystallization are also available [23]. All these methods have different advantages and disadvantages, but typically suffer from complicated synthesis procedures, expensive additives, poor yield or non-uniform materials. Subsequent loading or functionalization often causes further challenges and limitations. This has encouraged researchers to continue finding new and effective methods to synthesize hollow nanomaterials in simple and economically viable ways.

Metal-organic frameworks (MOFs) consist of metal ions or clusters that are coordinated by organic linkers to form three-dimensional structures. The tunable porosity of these structures gives rise to remarkable physical properties with many promising applications in gas storage, separation and catalysis [24,25]. Furthermore, MOFs have recently attracted much interest as sacrificial precursors for preparation of porous N-doped carbons for applications in electrochemistry [26,27]. Here we demonstrate how a type of MOFs known as zeolitic imidazolate frameworks (ZIFs) represents a promising platform for the design and synthesis of heterogeneous nanorattle catalysts. Furthermore, we show how the carbonization and/or calcination of the ZIFs controls the three-dimensional distributions of metal nanoparticles inside the nanorattles.

In the first step, ZIF-67 is synthesized from a solution of cobalt(II) nitrate and 2-methyl imidazole in methanol. We then exploit the ZIF-67 as structural template for the synthesis of a shell of mesoporous silica using tetra ethyl orthosilicate (TEOS) and cetyltrimethylammonium bromide (CTAB). The composite material is then calcined in order to decompose the ZIF-67 core into  $\text{Co}_3\text{O}_4$  and remove the organic template by combustion. This process requires a temperature of >550 °C. However, if the material is first carbonized under inert atmosphere, the ZIF-67 is decomposed into small Co nanoparticles stabilized by a N-doped carbon matrix inside the shell. Although this carbonization step is performed at 600 °C, the subsequent calcination to remove the N-doped carbon and oxidize Co into  $\text{Co}_3\text{O}_4$  already occur at 300 °C, see

\* Corresponding author.

E-mail address: [jjmie@kemi.dtu.dk](mailto:jjmie@kemi.dtu.dk) (J. Mielby).<https://doi.org/10.1016/j.catcom.2019.02.020>

Received 15 November 2018; Received in revised form 31 January 2019; Accepted 21 February 2019

Available online 08 March 2019

1566-7367/ © 2019 Elsevier B.V. All rights reserved.